TUNNELLING-INDUCED GROUND DISPLACEMENTS IN SAND

UNITED KINGDOM · CHINA · MALAYSIA

Bo Zhou

Department of Civil Engineering

University of Nottingham

A dissertation submitted for the degree of

Doctor of Philosophy

September, 2014

Declaration

I hereby declare that, except where specific reference is made to the works of others, the contents of this thesis are original and have not been submitted, in whole or in part, to any other university for any degree or qualification. This thesis, except where specific statement is made, is entirely the result of my own work and includes nothing which is the outcome of collaboration.

Bo Zhou
September 2014

Acknowledgements

I would like to deeply thank my supervisor, Dr. Alec Marshall, for his help, encouragement and guidance. I learnt a lot from him who is not only a good academic researcher but also a strong leader for our group.

I would like to sincerely thank my supervisor, Prof. Hai-Sui Yu, for his support and guidance. It is such a precious opportunity to work at the Nottingham Centre for Geomechanics (NCG).

I am really appreciative of many excellent suggestions that were provided by Dr. Dariusz Wanatowski. The suggestions improved this research.

Many thanks also to Prof. Robert Mair who said my research project was 'very important' during his presentation in Nottingham. It is a great honour and encouragement to me.

I am indebted for plenty of technical help provided by Craig Cox and James Meakin whose professional works considerably supported the centrifuge tests.

I am grateful to all of my fellow researchers at NCG. I got important help from Itai Elkayam, Wenbo Yang, Pinqiang Mo, Andrea Franza, Nian Hu, Jipeng Wang, Wei Cai and Yang Lu.

I have made many friends in Nottingham. Much appreciation for the unforgettable experiences. Foremost, I met Siming there, for which I feel so blessed.

I would like to thank the University of Nottingham for the full scholarship that gave me the opportunity to study in the UK.

Finally I would like to thank my loving parents and family. Their love gives me strength.

Abstract

Underground tunnelling causes stress relief in the surrounding soil and results in ground movement. To evaluate potential detrimental effects on nearby structures and infrastructure, it is important to understand the characteristics of these displacements, both magnitude and shape.

The geotechnical centrifuge testing is the main method for this research. In the centrifuge experiments, the tunnel was modelled using a water-filled flexible membrane, and tunnel volume loss was modelled by extracting water from the membrane. Surface and subsurface soil displacements were evaluated by analysing digital images taken of the soil through a transparent Perspex wall of the centrifuge container throughout the tests.

The main objective of these tests was to examine the effects that relative density and stratification have on greenfield soil displacements above tunnels in sandy ground. Data from a series of plane-strain centrifuge tests on tunnels in silica sand are presented. The relative density of the sand sample ranged from 90% to 50% in the tests. The soil displacement data were examined to determine features of greenfield settlement, both surface and subsurface. The effects that relative density and stratification have on the settlement trough shape is demonstrated and discussed. Some interesting features of tunnelling in sandy ground were revealed in the analysis.

Additionally, the cavity expansion method were used to study the volumetric deformation of soil caused by tunnelling. The trends of soil dilation angle with tunnel volume loss were examined. This solution also investigated the possibility of using triaxial test data to estimate the volumetric deformation above tunnels.

Furthermore, the centrifuge test results are compared to the prediction by discrete element method (DEM). The capability of DEM to accurately predict the effect of relative density on settlements is evaluated.

Keywords: tunnel, centrifuge, settlement, sand, relative density, stratified.

Contents

List of Figures

Nomenclature

Roman Symbols

a current cavity radius

a_0 original cavity radius

a acceleration

AC alternating current

A_i area of each wall

$\bar{v}_i$ velocity of each of the N walls which make up the membrane

$BSPP$ British standard pipe parallel

C cohesion

C cover, measured from surface of soil to crown of tunnel

c displacement measured at model tunnel crown

DAS data acquisition system

DC direct current

ΔF_i out-of-balance force in the radial direction of the tunnel

Δt explicit scheme time step

DEM discrete element method

$\dot{V_s}$ volume of the ground settlement

$\dot{V_t}$ reduced tunnel volume

D_t tunnel diameter

D_{50} average grain size diameter

e_{max} maximum void ratio

e_{min} minimum void ratio

F elastic modulus

F_a maximum load on the linear actuator

$F_{g,i}$ particle force acting on wall i

F_p load of piston onto the threaded rod

F_s shear force

G shear stiffness

g gravity (9.81 m/s^2)

G Gaussian curve

$GeoPIV$ PIV software for geotechnical testing

G_s specific gravity

$\hat{n}_i$ outer normal vector to the each of the N walls

h_i depth where acceleration is $80g$ = depth of model tunnel axis

H_w height from the base plate to the overflow hole

I_d relative density

V_0 initial volume of the excavation for tunnel

i horizontal offset from tunnel centreline to point of inflexion of curve fitted to settlement data

I moment of inertia

k cavity expansion parameter (= 1 for cylindrical cavity solution; = 2 for spherical cavity solution)

K coefficient of earth pressure

K^* trough width parameter based on x^*

K^*_{50} K^* for Test 50

$K^*_{50/90}$ K^* for Test 50/90

K^*_{90} K^* for Test 90

$K^*_{90/50}$ K^* for Test 90/50

K^{**} trough width parameter based on x^{**}

K trough width parameter

K_w water stiffness

L length

l_1 distance between the two strokes of piston and actuator

l_2 distance between the two strokes of piston and LVDT

$LVDT$ linear variable differential transformer

mG modified Gaussian curve

M_r reaction moment

$M_{w,i}$ mass of each wall defined to keep the critical time step as that defined by PFC^{3D}

n shape parameter used in modified Gaussian curve

N centrifuge acceleration scale

O_{RS} offset from R to top of soil

p current tunnel pressure

p_0 initial tunnel pressure

PIV particle image velocimetry

p' mean effective stress

P_s soil overburden pressure at the tunnel axis

PVC polyvinyl chloride

P_w water pressure at the axis level of the tunnel (at depth z_t)

Q volumetric rate of fluid extraction

q self weight of threaded rod

r an arbitrary distance from the cavity centre

r_0 initial distance from the cavity centre (when $p = p_0$)

R^2 coefficient of determination

R radius to baseplate (distance from the centrifuge axis to the baseplate of swing cradle)

r distance to the centrifuge axis

R_e effective radius = $(R_T + h_i/2)$

r_o overestimation of stress at base

rpm revolutions per minute

R_s radius of the soil surface (the distance from the soil surface to the centrifuge axis)

R_T Radius to top of soil = $(R - O_{RS}$

R_t radius of the model tunnel axis (the distance from the model tunnel axis to the centrifuge axis)

r_u underestimation of stress near surface

R_w radius of the overflow hole (the distance from the overflow hole to the centrifuge axis)

s displacement at sides of model tunnel

S_{max} maximum vertical displacement of soil at tunnel centreline

S_v vertical displacement of soil

$T_{\gamma-Vl}$ empirical parameter in order to fit $\psi - \gamma$ curves to $\psi_{rep} - V_{l,t}$ data

u displacement

V_0 initial volume of water in the tunnel

$V_{l,s}$ volume loss of soil

$V_{l,t}$ volume loss of tunnel

WHT width height thickness

x horizontal offset from tunnel centreline

x^* horizontal distance from $x = 0$ to point on fitted curve where $S_v = 0.606 S_{max}$

x^{**} horizontal distance from $x = 0$ to point on fitted curve where $S_v = 0.303 S_{max}$

Y cavity expansion analysis parameter related to C and ϕ

z depth measured from ground surface

z_i depth to the centre of wall i

z_t depth of tunnel axis

Greek Symbols

α cavity expansion analysis parameter related to ϕ

α shape parameter used in modified Gaussian curve

$\bar{\phi}'$ average friction angle

β cavity expansion analysis parameter related to ψ

β_{rep} cavity expansion analysis parameter related to ψ_{rep}

δ_F δ_p due to F_p

δ_l deflection of the threaded rod at the LVDT stroke

δ_p deflection of the threaded rod at the head joint of the piston

δ_q δ_p due to q

ϵ_r^e elastic radial strain

ϵ_θ^e elastic circumferential strain

ϵ_θ^p plastic circumferential strain

ϵ_r^p plastic radial strain

ϵ_r radial strain

ϵ_θ circumferential strain

ϵ_v volumetric strain

ϵ_{xx} axial strain in x direction

ϵ_{xz} shear strain

ϵ_{yy} axial strain in y direction

ϵ_{zz} axial strain in z direction

γ engineering shear strain

γ' unit weight of sands in water

γ unit weight

γ_w unit weight of water

μ inter-particle friction coefficient

ν Poisson's ratio

ω angular velocity

ϕ friction angle

ϕ'_{cv} critical state friction angle

ϕ'_{max} maximum friction angle

ψ dilation angle

ψ_{rep} representative dilation angle

ρ_s soil density

ρ_w water density

σ_{max} maximum permissible stress

σ_{norm} normalised tunnel pressure

$\sigma_{o,50g}$ pressure on the window by saturated sand at $50g$

$\sigma_{o,1g}$ pressure on the window by saturated sand at $1g$

σ_r radial stress

σ_t pressure in the model tunnel

σ_θ circumferential stress

τ_{max} maximum permissible shear

θ_F θ_p due to F_p

θ_p rotation of the threaded rod at the head joint of the piston

θ_q θ_p due to q

Chapter 1

INTRODUCTION

This research investigates the tunnelling-induced movements in sandy ground. The transport capacity of underground rail systems is considerably higher than that of private cars and public buses. Moreover, the underground is an environment-friendly transport method with micro air and noise pollution, which is significant for the world today. In some highly populated developing countries, the underground is the best solution of urban transport problems.

Underground tunnelling, as a kind of cavity excavation, causes stress relief within the surrounding soil. Such stress relief leads to movements of soil around the tunnel. When the movements propagate to the ground surface, the surface settlement occurs. The shape of ground settlement is termed settlement trough. The settlement could result in damages to nearby structures and infrastructure, such as cracks of buildings, leakage of pipelines and displacements of piles.

The Gaussian curve (Section 2.2.2.1, p.7) is a typical model to describe the settlement trough. It has been proved to well fit large amount of case study data in undrained clay, but it usually did not provide as good fit to settlement trough in sands, probably due to the contraction/dilation of sands. The Gaussian curve was consequently modified (Section 2.2.2.2, p.7) with altering the trough width parameter, i, for settlement trough in sands. Marshall et al. [2012] examined the effects of tunnel size, depth and volume loss on greenfield displacements above tunnels in dense sand (relative density, $I_d = 90\%$). There is, however, little research on ground displacements in sand with different relative densities and stratification. The lack of knowledge in this area would lead to potential damages to the buried structures above tunnels.

This research focuses on the examination of the effects that relative density and stratification have on settlements in sandy ground. The geotechnical centrifuge technology is the main research method. A plane-strain centrifuge model was developed and soil displacements were measured by an image-based technique. The main topic of each chapter in this thesis is summarised:

- the literature review related to this research is provided in Chapter 2 (p.4);
- the development of the centrifuge model and experimental methods are

shown in Chapter 3 (p.33);

- Chapter 4 (p.77) reports the centrifuge test results in Group 1 (Figure 3.6, p.42) and analyses the effect of relative density on settlements;
- the cavity expansion method is used to study the volumetric deformation of sand caused by tunnelling in Chapter 5 (p.140);
- the capability of discrete element method (DEM) to accurately predict the effect of relative density is evaluated in Chapter 6 (p.157); and
- Chapter 7 (p.167) reports the centrifuge test results in Group 2 (Figure 7.1, p.168) and examines the effect of stratification (layers with different I_d) on settlements.

The most important findings, applicability of results and recommendations are presented in Chapter 8 (p.192).

Chapter 2

BACKGROUND

2.1 Introduction

This chapter provides the literature review on tunnelling-induced ground displacements. A series of widely-cited research on this topic is covered and some results of them are used in this research. The literature on geotechnical centrifuge technology, as the main method of this research, is presented at last.

2.2 Ground movements caused by tunnelling

2.2.1 Overview

Underground excavation causes stress relief in the surrounding soil and results in ground movement. The movements in the three-dimensional area could be divided into two perpendicular parts: the transverse movement and the longitudinal movement. The greenfield settlement associated with tunnelling is shown in Figure 2.1. Greenfield is used to refer to land without structures. This research mainly focuses on the transverse settlement.

Mair and Taylor [1997] stated that there are five major components that lead to stress release and displacements in the soil around tunnels;

1. deformation of the ground towards the tunnel face due to stress relief;
2. the passage of the shield results in the radial ground movements, which possibly is due to presence of an overcutting edge (bead) used to help steering and maintain alignment of the shield;
3. the difference in diameter of the tail of the shield and the installed lining form the tail void, and hence the soil tends to move into the gap;
4. deflection of the lining as it starts to take the developing ground loading;
5. time dependent consolidation settlement for soft clays.

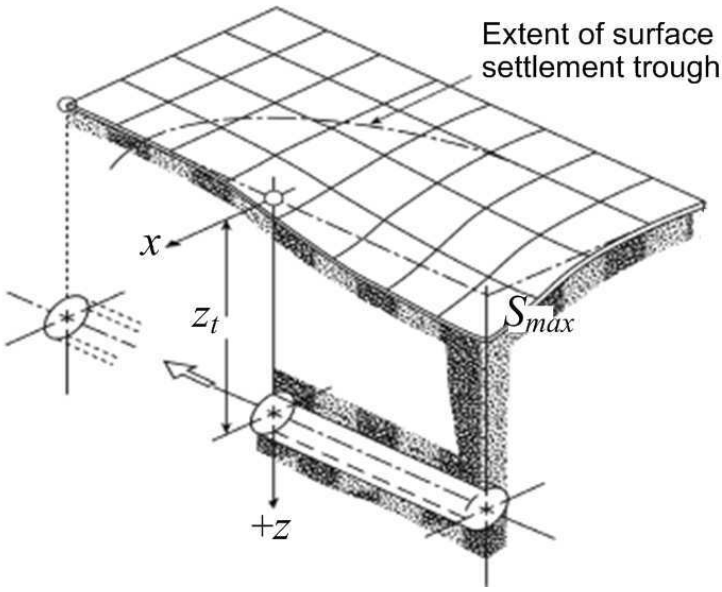

Figure 2.1: Surface settlement associated with underground tunnelling [Attewell et al., 1986]

For tunnelling in clay, the last component is important. The construction changes the stress regime around the tunnel. As the excess pore pressure equilibrates over time the ground volume would be changed. The effects of consolidation are not usually accounted due to the lack of relative high quality case study data and the limited monitoring work. However, compared to the undrained movements (components 1-4), the maximum settlement after consolidation may reach two to four times the short-term value (undrained movement).

For tunnelling in sands, the settlement could be accounted as short-term ground deformation, but could not be accounted as the undrained movements with constant volume. Marshall et al. [2012] showed that the constant volume assumptions are inaccurate owing to the contraction/dilation of sands. However, the constant volume assumption is still used in practice because it is difficult to estimate the volumetric deformation in sand. It is of interest to the examination of the volumetric strain caused by tunnelling.

2.2.2 Transverse settlement trough

2.2.2.1 Settlement trough in undrained clay

The transverse settlement trough is generally described as a Gaussian distribution curve:

$$S_v(x) = S_{max} \cdot exp\left(-\frac{x^2}{2 \cdot i^2}\right) \tag{2.1}$$

where S_v is the vertical settlement at a horizontal distance x from the tunnel centreline, S_{max} is the maximum settlement that is at the tunnel centreline and i is referred to as the trough width that is the distance from the tunnel centreline to the trough inflexion point. The settlement trough is determined by two parameters, S_max and i.

The Gaussian distribution trough was firstly proposed by Martos [1958]. Schmidt [1969], Peck [1969] and subsequently many other authors also provided an approximation to the settlement trough with Gaussian curves. Most authors have shown that the Gaussian distribution curve highly fitted the transverse settlement trough, such as in Heathrow Express Trail Tunnel [Bowers et al., 1996].

Marshall [2009] calculated the derivative and second derivative of $S_v(x)$ from Gaussian distribution curve, which is the slope and curvature of settlement trough (Figure 2.2).

The vertical settlement at inflexion point is fixed at:

$$S_v(x = i) = S_{max} \cdot exp\left(-\frac{i^2}{2 \cdot i^2}\right) = 0.606 S_{max} \tag{2.2}$$

2.2.2.2 Settlement trough in sand

The Gaussian distribution curve accurately described the settlement trough in undrained clay but did not always match well to the trough shape in drained

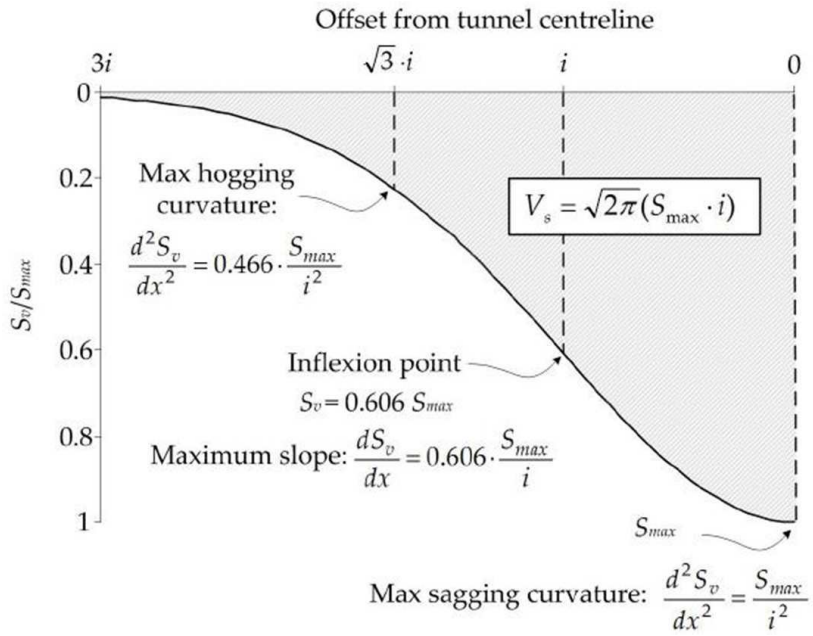

Figure 2.2: Settlement trough described by Gaussian distribution curve, after Marshall [2009]

soils [Celestino et al., 2000; Jacobsz et al., 2004; Vorster et al., 2005]. In order to obtain a better fit to the observed tunnelling-induced settlement data, Vorster et al. [2005] suggested a modified Gaussian curve of the following form:

$$\begin{aligned} S_v(x) &= \frac{n}{(n-1)+exp[\alpha(x^2/i^2)]} \cdot S_{max} \\ n &= e^{\alpha} \cdot \frac{2\alpha-1}{2\alpha+1} + 1 \end{aligned} \tag{2.3}$$

where n is the shape function parameter and α is a parameter to ensure that i, the trough width, has the same definition as in Gaussian distribution curve (Equation 2.1, p.7).

The modified Gaussian curve is determined by three parameters, S_{max}, i and α (n is a function of α). The third parameter, α, is the additional degree of freedom provided by the modified Gaussian curve compared to the Gaussian

curve, and therefore gives more flexibility to the curve shape. Figure 2.3 shows three modified Gaussian curves with the same values of S_{max} and i but different values of α. The additional parameter adjusts the vertical location of inflexion point where $x = i$. Note that the modified Gaussian curve becomes the Gaussian curve when $\alpha = 0.5$.

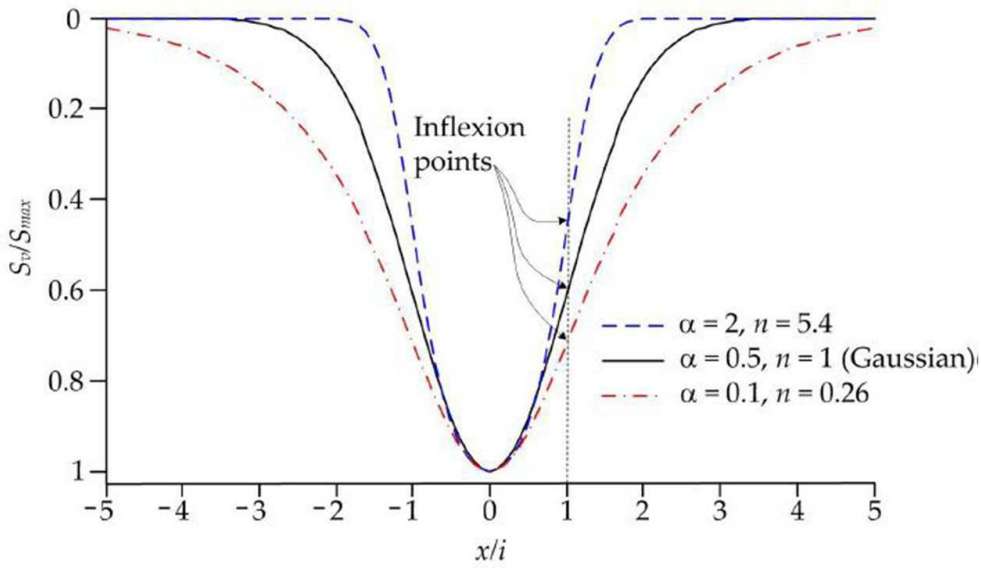

Figure 2.3: Features of modified Gaussian settlement trough, after Marshall [2009]

Marshall et al. [2012] showed that the modified Gaussian curve could provide a good fit to the settlement data in sand with a relative density of 90%.

2.2.3 Volume loss

2.2.3.1 Tunnel volume loss and soil volume loss

The volume loss is commonly used to describe the effect of tunnelling. There are two kinds of volume loss for tunnelling-induced ground displacements, the volume loss of tunnel, $V_{l,t}$, and the volume loss of soil, $V_{l,s}$. Both of them are expressed as a percent.

The volume loss of tunnel, $V_{l,t}$, refers to the ratio of the reduced tunnel volume

to the initial tunnel volume:

$$V_{l,t}[\%] = \frac{\dot{V}_t}{V_0} \cdot 100 \tag{2.4}$$

where $\dot{V}_t$ is the reduced tunnel volume due to the components 1 to 4 (Section 2.2.1, p.5), and V_0 is the initial volume of the excavation for tunnel. For a circular tunnel, $V_0 = 1/4 \cdot \pi D_t^2 \cdot L$, where D_t is the initial tunnel diameter.

Volume loss of soil, $V_{l,s}$, refers to the ratio of the volume of ground settlement to the initial tunnel volume:

$$V_{l,s}[\%] = \frac{\dot{V}_s}{V_0} \cdot 100 \tag{2.5}$$

where $\dot{V}_s$ is the volume of ground settlement.

The relationship between those two kinds of volume loss depends on the ground condition. For undrained conditions, the volume of soil above tunnels is constant, so that the volume of ground settlement is equal to the reduced tunnel volume and $V_{l,t} = V_{l,s}$. For drained conditions, the volume of soil changes, so that the volume of ground settlement is not equal to the reduced tunnel volume and $V_{l,t} \neq V_{l,s}$.

Mair and Taylor [1997] concluded the following based on projects conducted at the time:

1. volume losses in stiff clays such as London Clay using open-face tunnelling are generally between 1% and 2%;
2. resent project in London clay using sprayed concrete linings can produce volume losses between 0.5% and 1.5%;
3. earth pressure balance (EPB) and slurry machines can achieve a high degree of settlement control, particularly in sands with volume losses as low as 0.5% (in soft clays, short term volume loss of only 1-2% has been reported);

4. in mixed face conditions volume loss may be higher for EPB and slurry machines.

In the recent projects [Mair, 2008], as a result of good control of earth pressure with EPB tunnelling machines in a wide variety of ground conditions, low volume loss, well below 1%, are now readily achievable.

2.2.3.2 Tunnel volume loss with supporting pressure

The tunnel supporting pressure was observed to decrease quickly with an increase of tunnel volume loss to 1% and then remain relatively stable after 2% (e.g. Jacobsz [2002]; Vorster [2005]; Marshall [2009]), probably due to the arching in soils.

Centrifuge trapdoor tests were used to study the arching evolution caused by underground excavations [Iglesia et al., 1999]. Figure 2.4 presents a generalised ground reaction curve. Initially, the 'arch' starts to form and the loading on the underground structure decreases abruptly. The loading approaches a minimum value at a stage of maximum arching. An increase of loading is found during the transition from the maximum arching condition to the ultimate stage. The transition is termed loading recovery stage. As the surrounding soil continually converges toward the excavated zone, the arch will ultimately collapse.

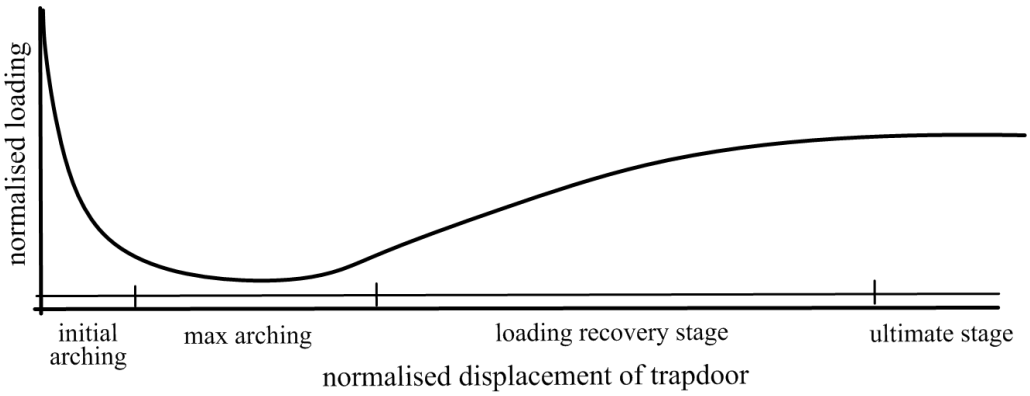

Figure 2.4: Generalised ground reaction curve, after Iglesia et al. [1999]

2.2.3.3 Tunnel collapse

Atkinson and Potts [1977] theoretically predicted the upper and lower bound for the tunnel collapse in sand. The lower bound prediction is given by:

$$\frac{\sigma_t}{2\gamma R} = \frac{\mu}{\mu^2 - 1}$$
$$\mu = \frac{1 + \sin(\phi_{max})}{1 - \sin(\phi_{max})} \tag{2.6}$$

where σ_t is the supporting pressure, γ is the soil unit weight, R is the tunnel radius, and ϕ_{max} is the maximum friction angle.

The upper bound is given by:

$$\frac{\sigma_t}{2\gamma R} = \frac{1}{4\cos(\phi_{max})}\left(\frac{1}{\tan(\phi_{max})} + \phi_{max} - \frac{\pi}{2}\right) \tag{2.7}$$

Note that an associated flow rule was used for these solutions (the vector of plastic deformation is normal to the yield surface and the dilation angle (ψ) is equal to the friction angle (ϕ_{max})).

Figure 2.5 shows the collapse mechanism for the upper bound.

2.2.4 Trough width

The trough width is usually evaluated by i that is the distance from the tunnel centre line to the inflexion point of settlement trough.

2.2.4.1 Surface trough width

There are a number of methods, empirical, experimental, analytical and numerical solutions, to estimate the trough width. Atkinson and Potts [1977] derived the

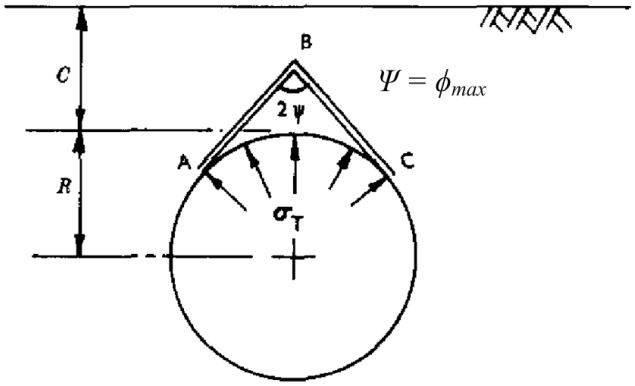

Figure 2.5: Collapse mechanism for the upper bound, after Atkinson and Potts [1977]

following equation from the centrifuge tests for tunnelling in dry sands:

$$i = 0.25(C + D_t) \tag{2.8}$$

where C is the depth to tunnel crown and D_t is the tunnel diameter.

Mair et al. [1982] proposed the relation for shallow tunnels in soft clay:

$$\frac{2i}{D_t} = \frac{z_t}{D_t} \tag{2.9}$$

where z_t is the depth of tunnel axial.

Both of them related the trough width to two parameters, the tunnel depth and size. Moreover, Clough and Schmidt [1981] estimated the trough width in soft clay by the two parameters, irrespective of the excavation method:

$$\frac{2i}{D_t} = \left(\frac{z_t}{D_t}\right)^{0.8} \tag{2.10}$$

The most common relationship between surface trough width and tunnel depth is proposed by O'Reilly, M. P. and New [1982]. The authors stated that there

is an approximately linear relationship between the trough width and the depth of tunnel. They also showed that the trough width is independent of the tunnel construction method, which is same as the most previous research. This linear relationship is, however, irrespective of the tunnel diameter, which is different with Equation 2.8-2.10. This relationship is not valid for very shallow tunnels where the tunnel depth to diameter ratio is less than one. Its equation is

$$i = K \cdot z_t \tag{2.11}$$

where K is the trough width parameter. Based on a mount of case study, the authors showed that the Equation 2.11 was appropriate, and suggested that K should be 0.4-0.5 for stiff fissured clay, 0.5-0.6 for glacial deposits, 0.6-0.7 for soft silty clay and 0.2-0.3 for sands above the water table. Mair and Taylor [1997] suggested that K should be 0.5 for clay and 0.25-0.45 for sands and gravels.

Selby [1988] and New and O'Reilly [1991] suggested that the trough width for layered ground could be estimated from K_i for the soil type in each layer of thickness z_i, as:

$$i = K_1 z_1 + K_2 z_2 (+...) \tag{2.12}$$

2.2.4.2 Subsurface trough width

It is necessary to estimate the subsurface displacements for the evaluation of the potential damage to the existing subsurface structures, such as piles and pipes.

O'Reilly, M. P. and New [1982] proposed that the Gaussian distribution curve is also appropriate for the estimation of subsurface displacements, based on the plane strain and undrained condition.

Mair et al. [1993] modified Equation 2.11 in order to predict both the surface and subsurface trough width:

$$i(z) = K(z_t - z) \tag{2.13}$$

where $i(z)$ is the trough width at an arbitrary depth of z.

The vale of K was found to vary with depth, z. Mair et al. [1993] reviewed a mount of field measurements and centrifuge test data for tunnelling in stiff and soft clays, and proposed the K associated with depth:

$$K(z) = \frac{0.175 + 0.325\,(1 - z/z_t)}{1 - z/z_t} \tag{2.14}$$

In Figure 2.6, the values of i from subsurface settlement measurements have been plotted against the depth, z, and both i and z have been normalised by the depth of the tunnel axis, z_t.

In this figure, the dash line was corresponding to the Equation 2.13 with a constant $K = 0.5$, while the solid line was corresponding to the Equation 2.13 with the value of K by Equation 2.14. The later prediction better fitted the data from field and centrifuge tests.

Grant and Taylor [2000] also showed that the centrifuge test data for clay strongly confirmed the prediction by Equation 2.13 and 2.14, but the authors noted that the prediction overestimated the trough width within the zone about $D_t/2$ around the tunnel. The Equations do not consider the tunnel size and cannot perform well close to the tunnel. Moh et al. [1996] analysed the data from the Taipei Rapid Transit Systems and modified the Equation 2.10 (p.13) to estimate the trough width associated with depth:

$$i(z) = \left(\frac{D_t}{2}\right)\left(\frac{z_t}{D_t}\right)^{0.8}\left(\frac{z_t - z}{z_t}\right)^{m} \tag{2.15}$$

where m is referred to as a 'subsurface trough width parameter'. For tunnels

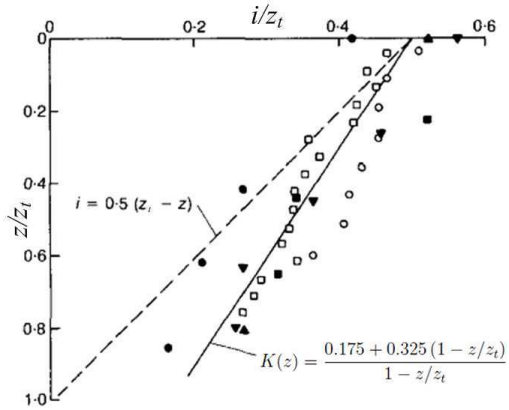

	Location	Soil type	D: m	z_0: m	Reference
●	Green Park	London Clay	4·1	29	Attewell & Farmer (1974)
▲	Regent's Park (northbound)	London Clay	4·1	20	Barratt & Tyler (1976)
▼	Regent's Park (southbound)	London Clay	4·1	34	Barratt & Tyler (1976)
■	Willington Quay	Soft clay	4·3	13.5	Glossop (1978)
○	Centrifuge* model 2DP	Soft clay	0·06	0·13	Mair (1979)
□	Centrifuge* model 2DV	Soft clay	0·06	0·22	Mair (1979)

Figure 2.6: Variation of trough width with depth for tunnels in clay, after Mair et al. [1993]

driven in silty sands, $m = 0.4$ will be appropriate, and for tunnels driven in silty clays, $m = 0.8$ is recommended. The authors stated that Equation 2.15 could well estimate the trough width close to tunnel because it considers the tunnel size. However, as Equation 2.10 by Clough and Schmidt [1981], Equation 2.15 is not widely used.

2.2.4.3 Trough width for non-Gaussian fitted curves

In the case of tunnelling in sand, the tunnel volume loss causes the volumetric deformation (dilation/contraction) in soil. The modified Gaussian distribution curve provides a better fit to the settlement in sand compared to the Gaussian curve (Section 2.2.2.2, p.7).

The trough width is generally decided by i in standard Gaussian curve. As one feature of Gaussian curve, the value of vertical settlement, S_v, at the inflexion

point is fixed (when $x = i$, $S_v = 0.606S_{max}$). However, the value of i in modified Gaussian curve cannot characterise the trough width properly because the vertical location of the inflexion point is moved by the additional parameter, α. Figure 2.3 (p.9) showed that a single value of i can refer to many different shaped curves with different values of α.

Marshall et al. [2012] used x^* and x^{**} as a method to characterise the shape of the settlement trough for non-Gaussian curves with three degrees of freedom (such as the modified Gaussian curves). x^* and x^{**} is the horizontal distance from $x = 0$ to the point on fitted curve where $S_v = 0.606S_{max}$ and $0.303S_{max}$, respectively. x^* is equal to the i in Gaussian curve and they are both at $0.606S_{max}$, so that they can be used for a qualitative comparison of trough widths.

Figure 2.7 presents four kinds of curve to describe settlement troughs. The horizontal locations of inflexion points (i) for the four curves are all same, at $x = i = 3$. x^* and x^{**} is shown to well characterise the width of curves.

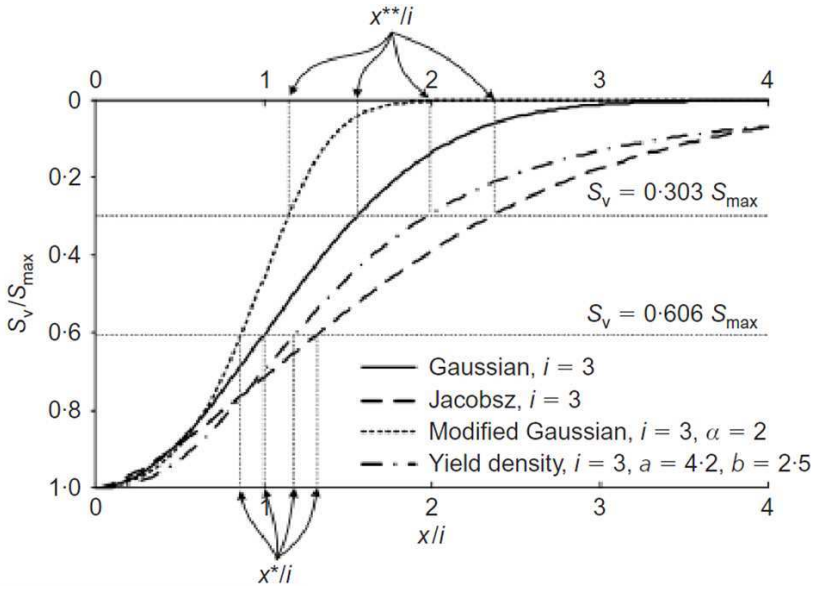

Figure 2.7: Various fitting curves with same value of i and showing location of x^* and x^{**}, after Marshall et al. [2012]

Marshall et al. [2012] analysed the results of three centrifuge tests for tunnelling in sand with a relative density of 90%. Trough width was observed to decrease

with (i) an increase of tunnel volume loss, $V_{l,t}$ (ii) an increase in depth, z and (iii) a decrease in cover/diameter ratio, C/D.

The value of i is generally expressed as $i(z) = K(z_t - z)$. For non-Gaussian, a trough width parameter K, based on x^* and x^{**}, can be calculated, and is referred to as K^* and K^{**}. The authors provided the following relationship to predict the trough width parameter based on the three tests:

$$\begin{aligned} K^* &= \left[K_s^* + (\partial x^*/\partial z)(z/z_t)\right]/(1 - z/z_t) \\ K_s^* &= K_{s,C/D}^{*int} + K_{s,C/D}^{*slope}(C/D) + K_{s,V_l}^{*slope}(V_{l,t}) \end{aligned} \tag{2.16}$$

where $K_{s,C/D}^{*int} = 0.440$; $K_{s,C/D}^{*slope} = 0.055$; K_{s,V_l}^{*slope} = -0.041; $\partial x^*/\partial z$ = -0.436; and the location of x^{**} can be found using $K^{**} = K^* + 0.29$ and $\partial x^{**}/\partial z = \partial x^*/\partial z$ - 0.20. This relation accounts for the effect of the three identified parameters and gives a generally good prediction (Figure 2.8).

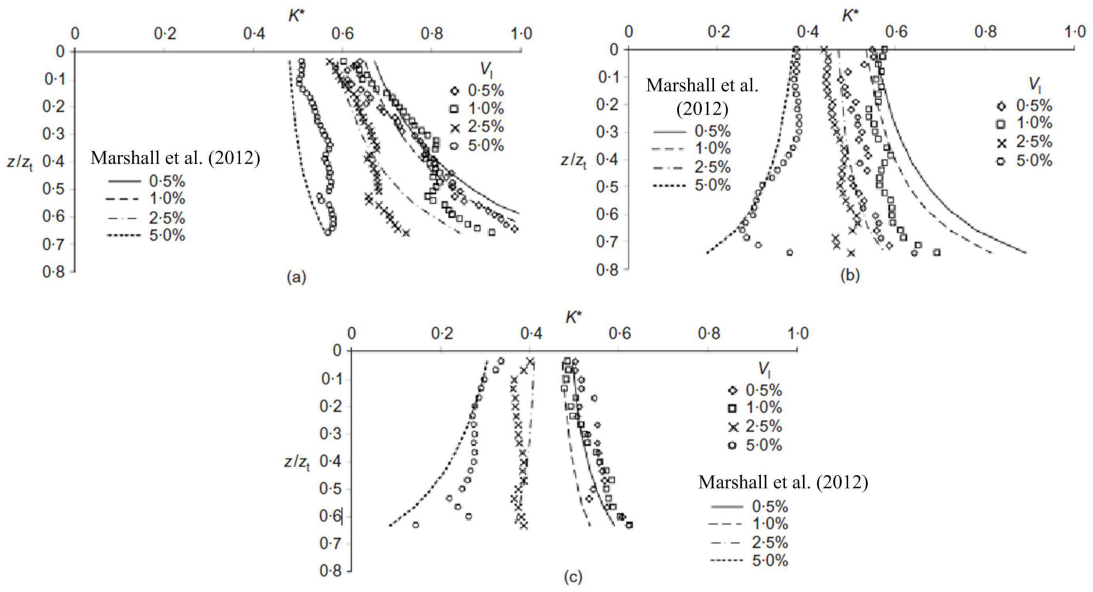

Figure 2.8: Trough width parameter against depth, compared with the prediction: (a) C/D4.4; (b) C/D2.4; (c) C/D1.3; after Marshall et al. [2012]

2.2.5 Tunnel deformation

The tunnel deformation, as the ground deformation around the tunnel section, is very important for analytical solution, centrifuge testing and numerical modelling. Some modified analytical solutions are based on using more reasonable deformation pattern of tunnel shape. The deformation pattern decides the structure of model tunnel for centrifuge tests and numerical solutions.

One of frequently-used deformation patterns is uniform convergence. Figure 2.9 shows the uniform radial convergence, where u_0 is the reduction of radius after the convergence.

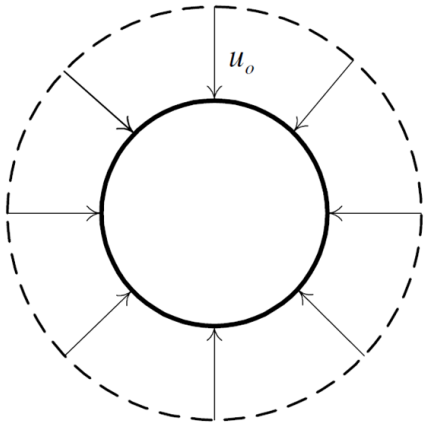

Figure 2.9: Uniform convergence

For simplification, many analytical solutions assumed that the tunnel transverse shape deformed as uniform convergence only, such as Sagaseta [1987] and Yu [2000].

Considering compressible material whose Poissons ratio is less than 0.5, another component of tunnel shape deformation is distortion (ovalisation). Some analytical solutions considered both uniform convergence and distortion in tunnel shape deformation (Figure 2.10), such as Verruijt and Booker [1996].

The third component of tunnel shape deformation is vertical translation (downward movement). Figure 2.11 shows the deformation considering both uniform convergence and vertical translation (downward movement). The dash circle is

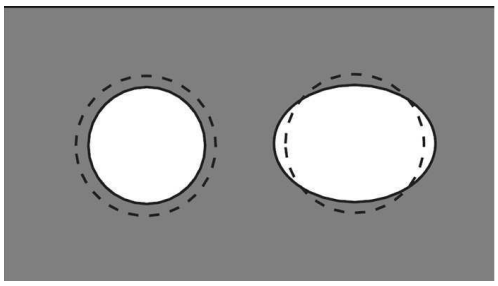

Figure 2.10: Uniform convergence and distortion (ovalisation), after Verruijt and Booker [1996]

the original tunnel shape and the solid circle is the tunnel shape after convergence and downward movement. The vectors of soil displacements around the tunnel are mostly downward in Figure 2.11.

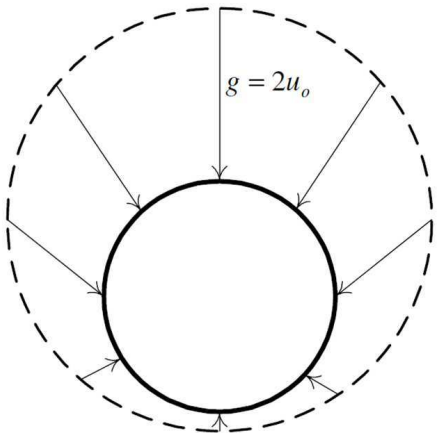

Figure 2.11: Uniform convergence and vertical translation (downward movement), after Park [2005]

The most realistic tunnel shape deformation is the combination of those three components: uniform convergence, distortion (ovalisation) and vertical translation (downward movement). Figure 2.12 illustrates the deformation modes at tunnel cavity.

Park [2005] summarised four ground deformation patterns around the tunnel section in Figure 2.13, where B.C. is boundary condition.

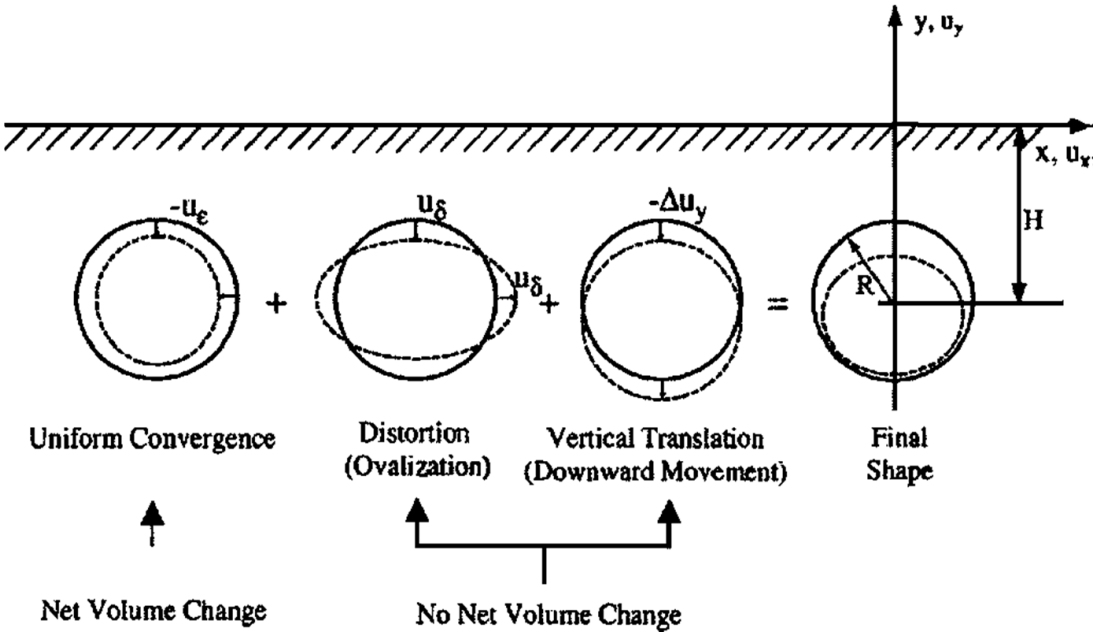

Figure 2.12: Deformed tunnel shape given by three components [Pinto and Whittle, 2006]

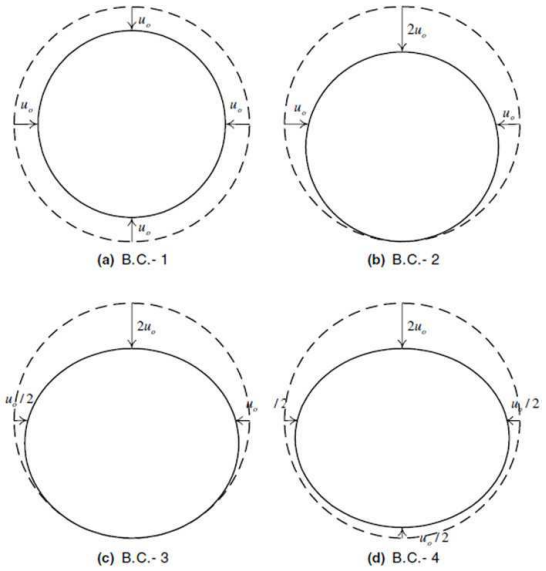

Figure 2.13: Ground deformation patterns around the tunnel section, after Park [2005]

2.2.6 Prediction of ground displacements above tunnels

Marshall [2009] distributed the prediction methods into three styles:

1. empirical relationships, such as Peck [1969]; O'Reilly, M. P. and New [1982]; Mair and Taylor [1993]; Moh et al. [1996]; Jacobsz [2002]; Vorster et al. [2005];Marshall et al. [2012];
2. closed-form solutions:
   (a) elastic solutions provided by Sagaseta [1987] and Verruijt and Booker [1996];
   (b) ribbon-sink model of New and O'Reilly [1991];
   (c) elasto-plastic solutions provided by Mair and Taylor [1993] and Yu and Rowe [1999];
3. numerical methods, including finite element (FE) and finite difference (FD).

Additionally, based on the solution of Verruijt and Booker [1996], a semi-empirical solution was provided by Loganathan and Poulos [1998]. There is a common problem in numerical solutions: the settlement trough provided by numerical solution is much wider and shallower than actual settlement trough measured in tunnelling projects. The soil behaviour changes during volume loss, but the traditional linear elastic perfectly plastic model, such as Mohr-Coulomb model, cannot model that phenomenon.

2.2.6.1 Sagaseta [1987]

An elastic solution was provided by Sagaseta [1987]. The author assumed that the behaviour of undrained soil is linear elastic, which is isotropic and homogeneous. The deformation of tunnel shape is uniform convergence. This analytical solution used either an image source for a negative image or an image sink for a positive image to balance shear or normal stresses at the surface. The steps in analysis were summarised by Sagaseta [1987] as follows and illustrated in Figure 2.14.

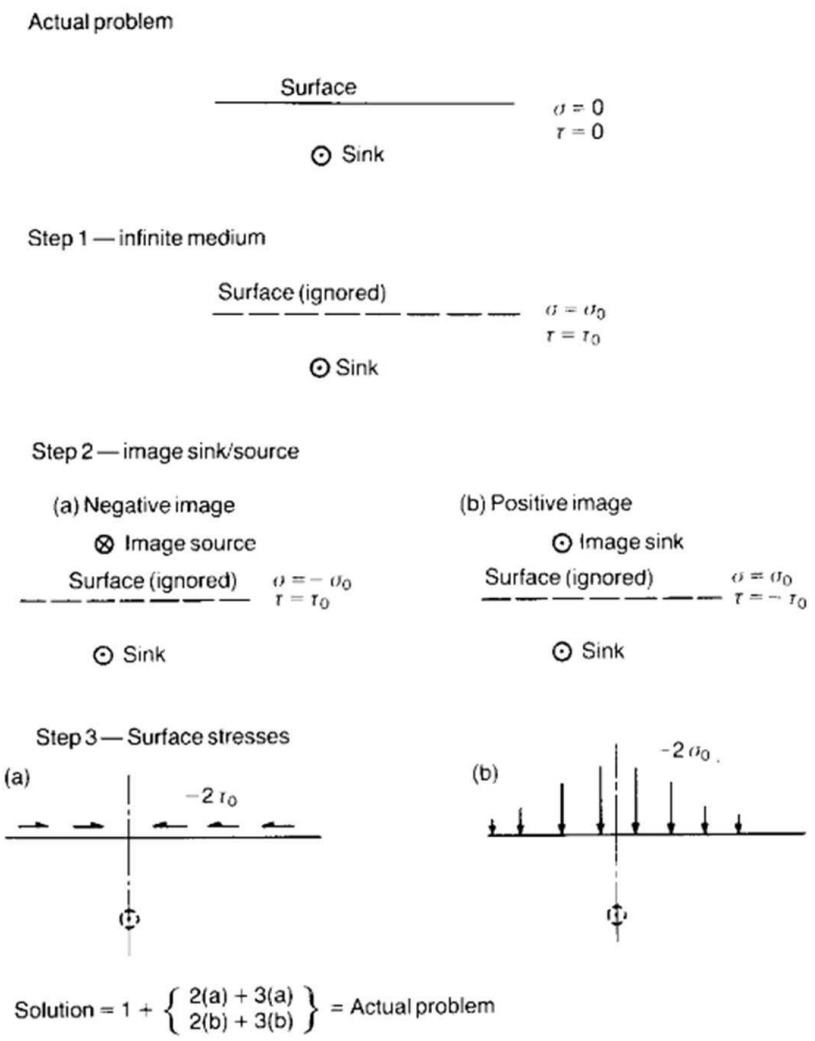

Figure 2.14: Steps in the analysis, after Sagaseta [1987]

1. The boundary effect of soil surface is ignored and the strains are calculated assuming that the sink is in an infinite medium.

2. Because the stains will produce stresses at the surface, the stress-free condition is violated. These stresses could be partially cancelled by each of the subsequent methods.

   (a) Considering a virtual source, negative mirror image of the real sink with respect to the top surface will produce opposite normal stresses

and the same shear stresses as the real sink.

(b) Considering an image sink, positive mirror image of the real sink with respect to the top surface will produce the same normal stresses and the opposite shear stresses.

The strains caused by the mirror image (a) or (b) are added to those obtained in step 1.

3. After step 2, the remaining normal or shear stresses at the soil surface are evaluated and removed. The resulting strains are added to those calculated in step 1 and step 2.

The author presented the solution for horizontal and vertical displacements at soil surface with plane strain condition (at a great distance from the tunnel face):

$$\begin{aligned} S_h &= -\frac{v}{\pi}\frac{x}{x^2+h^2} \\ S_v &= \frac{v}{\pi}\frac{h}{x^2+h^2} \end{aligned} \tag{2.17}$$

where v is the ground loss equal to the decreased cross-sectional area of tunnel, x is the horizontal offset from tunnel centreline, and h is the sink depth measured from the ground surface.

Figure 2.15 shows the final surface movements recorded in a section of the Caracas Metro in weathered schist. The solid line is the prediction by Equation 2.17. The equivalent point sink can be considered to be at depth of 10 m. As can be seen, for Equation 2.17, there is a tend to overestimate the settlement in the far field.

2.2.6.2 Verruijt and Booker [1996]

This method is an extension of the method proposed by Sagaseta [1987]. As mentioned in Section 2.2.6.1 (p.22), the assumption for Sagaseta [1987] is that the

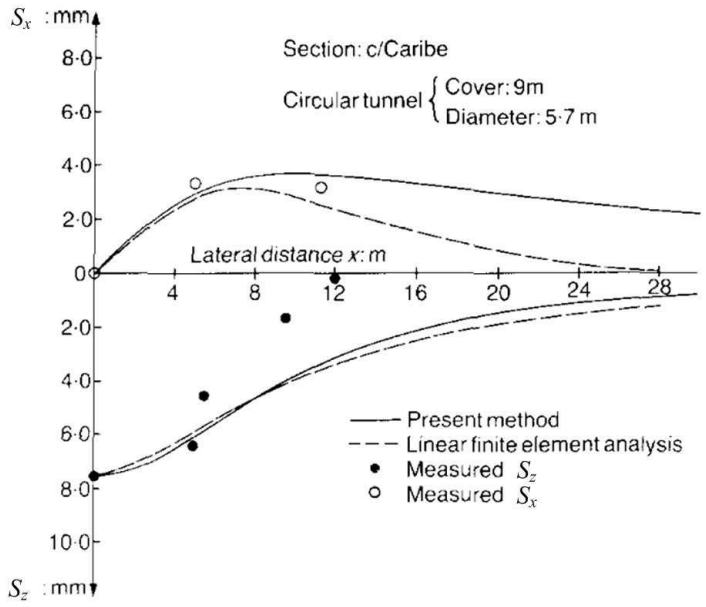

Figure 2.15: Calculated and measured final surface displacements, after Sagaseta [1987]

behaviour of soil is homogeneous incompressible (undrained) and the deformation of tunnel shape is uniform convergence. Verruijt and Booker [1996] gave the solution for the tunnels in compressible materials (with Poissons ratio less than 0.5), and that it includes the effect of ovalisation. Figure 2.10 (p.20) illustrates the uniform convergence and ovalisation.

The authors summarised this solution as three parts. The first two parts are singular elastic solutions for the points '$+h$' and '$-h$' in Figure 2.16.

The horizontal and vertical displacements for the singular parts and their images are expressed as follows:

$$\begin{aligned} u_x &= -\epsilon R^2 \left(\frac{x}{r_1^2} + \frac{x}{r_2^2} \right) + \delta R^2 \left[\frac{x(x^2 - kz_1^2)}{r_1^4} + \frac{x(x^2 - kz_2^2)}{r_2^4} \right] \\ u_z &= -\epsilon R^2 \left(\frac{z_1}{r_1^2} + \frac{z_2}{r_2^2} \right) + \delta R^2 \left[\frac{z_1(kx^2 - z_1^2)}{r_1^4} + \frac{z_2(kx^2 - z_2^2)}{r_2^4} \right] \end{aligned} \quad (2.18)$$

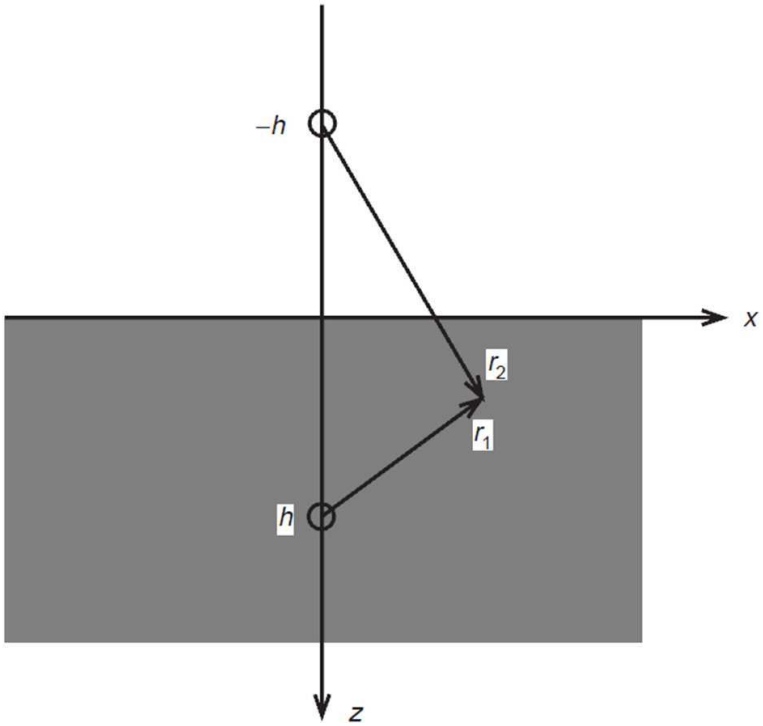

Figure 2.16: A singularity and its image, after Verruijt and Booker [1996]

where ϵ and δ are parameters indicating the relative deformation of the tunnel shape, for the uniform convergence (ϵ) and the ovalisation (δ) respectively, x, z, r_1 and r_2 are defined in Figure 2.16, $z_1 = z - h$ and $z_2 = z + h$.

As a result of the symmetry of the two solutions, both the shear stress and the vertical displacement will be zero at the soil surface but the normal stresses induced by the two singular solutions are equal. So the third part of this method is to remove the effect of normal stress on the surface. After Fourier integrals, the authors presented the displacements caused by the normal stress:

$$
\begin{aligned}
u_x &= -\frac{2\epsilon R^2 x}{m}\left[\frac{1}{r_2^2}-\frac{2mzz_2}{r_2^4}\right]-\frac{4\delta R^2 xh}{m+1}\left[\frac{z_2}{r_2^4}+\frac{mz(x^2-3z_2^2)}{r_2^6}\right] \\
u_z &= \frac{2\epsilon R^2}{m}\left[\frac{(m+1)z_2}{r_2^2}-\frac{mz(x^2-z_2^2)}{r_2^4}\right] \\
&- 2\delta R^2 h\left[\frac{x^2-z_2^2}{r_2^4}+\frac{m}{m+1}\frac{2zz_2(3x^2-z_2^2)}{r_2^6}\right]
\end{aligned} \tag{2.19}
$$

where m is a function of Poisson's ratio ($m = 1/(1-2\nu)$) and R is the tunnel radius.

The complete solution of this problem is the sum of Equations 2.18 and 2.19.

2.2.6.3 Elasto-plastic solutions using cavity expansion theory

Cavity expansion theory is the theoretical study of changes in stresses, pore pressures and movements due to the expansion and contraction of cavities [Yu, 2000]. Using cavity expansion theory in order to solve practical problems is termed cavity expansion method.

Cavity expansion theory has been used for decades to predict ground movements cased by underground tunnelling (e.g. Mair and Taylor [1993]; Yu and Rowe [1999]). Section 5.2 (p.141) will present details of the application of this theory.

2.3 Geotechnical centrifuge

2.3.1 Geotechnical centrifuge technology

The behaviour of soil is a function of current stress and stress history. The use of a geotechnical centrifuge ensures that full (prototype) scale ground stresses and behaviour are replicated within small-scale models with controlled boundary conditions and soil characteristics [Taylor, 1995]. The centrifuge can create an

acceleration field about the axis of rotation. The acceleration, a, created by the centrifuge can be calculated by the angular velocity, ω, and the distance from axis of centrifuge, r, as:

$$a = \omega^2 r \tag{2.20}$$

The level of acceleration is evaluated by g-level, N:

$$N = a/g \tag{2.21}$$

where g is the gravitational acceleration at earth surface.

Table 2.1 summarised some typical scaling laws.

Table 2.1: Centrifuge scaling laws [Taylor, 1995]

Parameter	unit	Scaling law (model/prototype)
Gravity	m/s^2	N
Length	m	$1/N$
Area	m^2	$1/N^2$
Volume	m^3	$1/N^3$
Force, Weight	$N = kg\ m/s^2$	$1/N^2$
Stress, Pressure	$Pa = N/m^2$	1
Strain	-	1
Density	kg/m^3	1
Unit weight	N/m^3	N

A number of laboratories with geotechnical centrifuge have been developed (e.g. Schofield [1980]; Ng et al. [2001]; Ma et al. [2006]; Ellis et al. [2006]). Taylor [1995] thoroughly presented the details on the subject of geotechnical centrifuge technology. The application of this technology in this research will be dealt in Chapter 3 (p.33).

2.3.2 Centrifuge tests for tunnel research

Tunnelling-induced ground movement is a complex problem because the stress-strain condition in the soil varies with position as well as the magnitude of volume loss of the tunnel. In practice, the prediction of ground displacements is based mainly on empirical relationships which do not consider intrinsic soil parameters. Prediction of ground displacements caused by tunnelling using numerical modelling provides poor results unless sophisticated constitutive models or unrealistic material parameters are used. Physical modelling using a geotechnical centrifuge can provide useful data related to tunnelling since the real behaviour of soils can be replicated.

Centrifuge technology has given significant and useful data for tunnelling in both clays (e.g. Mair [1979]; Davis et al. [1980]; Mair et al. [1993]; Grant and Taylor [2000]; Loganathan et al. [2000]; Osman et al. [2006a]; Osman et al. [2006b]) and sands (e.g. Potts [1976]; Atkinson and Potts [1977]; Kutter et al. [1994]; Marshall et al. [2012]).

The scale effects should be considered for tunnel modelling in the centrifuge. The relative size of any structural entity buried within the soil to that of the average grain size should be maximised in order to reduce scale effects. Kutter et al. [1994] investigated the collapse of cavities in sands using centrifuge testing and determined that the ratio of cavity diameter to average grain size should be greater than 350, and preferably as large as 1000. Marshall [2009] suggested that the data presented by Kutter et al. [1994] showed minimal grain size effect after a ratio of 500.

Figure 2.17 showed dimensions of the three centrifuge tests in Marshall et al. [2012]. In these tests, model tunnels were placed within the plane-strain centrifuge containers filled with dry sand (relative density, $I_d = 90\%$). The results from Test-CD2.4 are presented in Figure 2.18. The top figure presents the contours of vertical displacements of soil. A localised settlement zone is observed just above the tunnel crown and the settlements in this zone are obviously larger than that nearer the surface. The middle figure shows the contours of horizontal

displacements of soil. The magnitude of horizontal displacements is much smaller than that of vertical movements. The horizontal displacements are localised near the surface between ±50 to ±100mm offset and the tunnel shoulders. The bottom figure presents the profile of soil volumetric strain. The area near the tunnel is in a dilative mode while that nearer the surface is contractive.

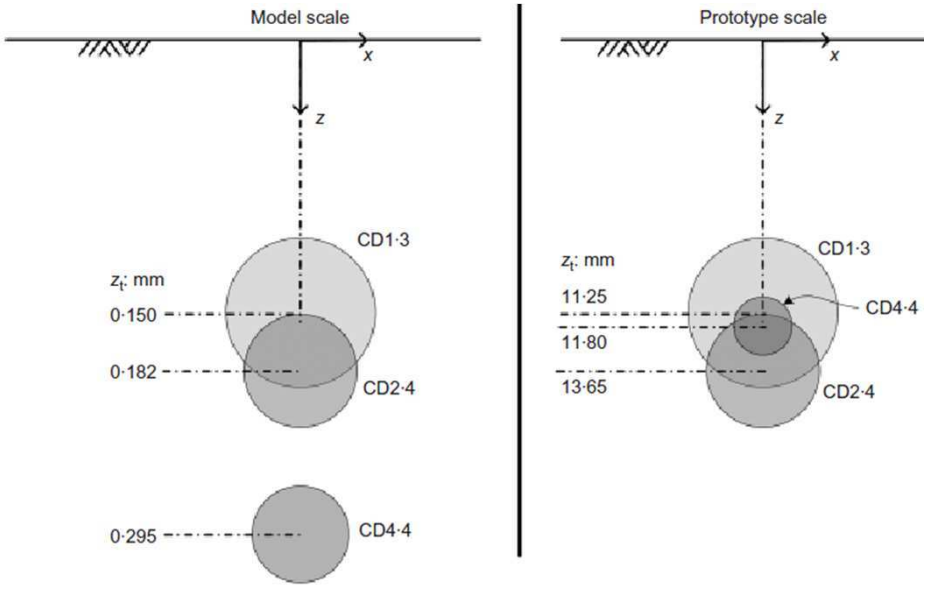

	Tunnel diameter, *D*: m*	Tunnel cover, *C*: m*	Cover to diameter, *C/D*	Acceleration, *N*
CD4·4	0·060 [2·40]	0·265 [10·60]	4·4	40
CD2·4	0·062 [4·65]	0·151 [11·32]	2·4	75
CD1·3	0·082 [6·15]	0·109 [8·18]	1·3	75

Figure 2.17: Dimensions of centrifuge tests (∗ prototype scale dimension in square brackets), after Marshall et al. [2012]

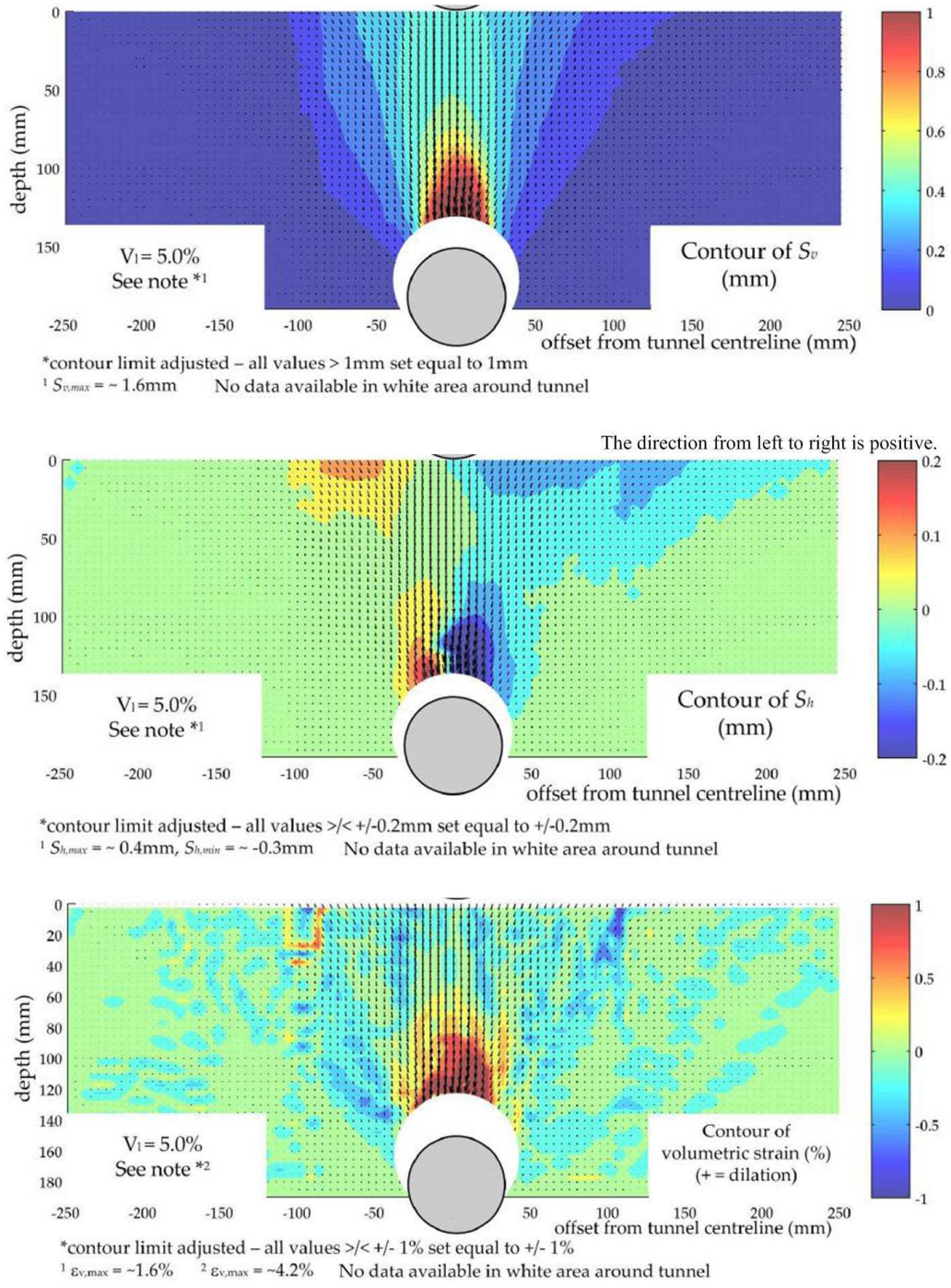

Figure 2.18: Results of the centrifuge test for tunnelling, after Marshall [2009]

Figure 2.19 illustrates the effect of cover to tunnel diameter ratio (C/D_t) on the distribution of volumetric deformation. A deep and small tunnel is characterised by low shear strains. For shallow and large tunnels, the shear strains are larger. In general, sands contract at low shear strain and dilate at high shear strain. The C/D_t ratio for the test in Figure 2.18 is 2.44 and the volumetric strain profile matches Case A in Figure 2.19.

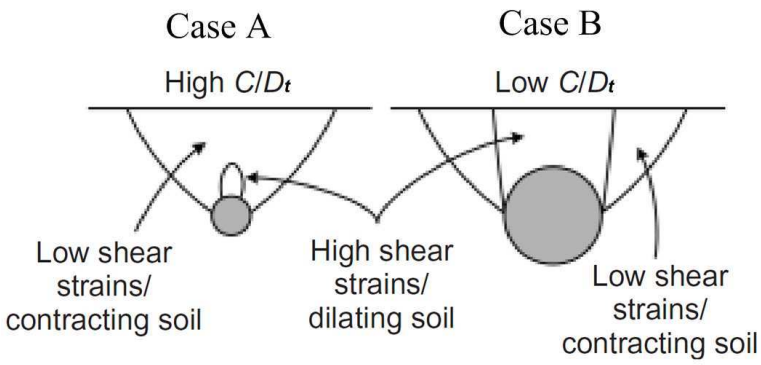

Figure 2.19: Effect of C/D_t ratio on volumetric strain, after Marshall et al. [2012]

Chapter 3

EXPERIMENTAL METHODS AND EQUIPMENT DESIGN

3.1 Introduction

The development of centrifuge model is an important part of this research. A $1/80^{th}$ scale centrifuge model was designed and manufactured. A model tunnel was placed within the plane-strain strong box filled with a dry fine-grained silica sand. The model tunnel consists of a rigid hollow aluminium cylinder sealed within a latex rubber membrane and filled with water. During a centrifuge test, the model was spun to 80 times gravity ($80g$). An actuator which controlled the piston of a water-filled hydraulic cylinder (the cylinder was connected to the water within the model tunnel) was used to extract the water within the model tunnel in order to replicate the the tunnel volume loss. The hydraulic pressure in the model tunnel was monitored with a pressure transducer. All the components were bolted on to a baseplate.

This chapter shows the development of the above experimental methods and equipment that were used for the investigation of greenfield settlements above tunnels. The details may be useful for the further research using this set of experiment. Section 3.2 introduces the Geotechnical centrifuge. Section 3.3 (p.37) provides details of the design of the centrifuge package. The subsequent sections describe the procedure of the model preparation (Section 3.4, p.66) and centrifuge tests (Section 3.5, p.75).

3.2 Geotechnical centrifuge

The Geotechnical centrifuge at the University of Nottingham [Ellis et al., 2006] comprises the following components:

- Geotechnical beam centrifuge,
- Centrifuge chamber,
- Data acquisition system (DAS).

It is a typical medium-sized beam centrifuge with one swinging cradle, which is manufactured by Broadbent©. The capability is 50 gt, as a payload of 500 kg at up to 100g at nominal radius of 1.70 m. Table 3.1 provides the specification of centrifuge.

Table 3.1: Centrifuge specification

Platform radius	2.0 m
Assumed effective radius	1.7 m
Max. size of payload	0.8 m wide (vertical in flight) 0.6 m wide (circumferential in flight) 0.9 m high (radial in flight)
Max. payload	850 kgm (500 kg at 1.7 m) up to 100g
Max. acceleration	150g (at 1.7 m)
In-flight balancing	± 50 kgm
Motor	75 kW 3 phase induction motor

The swinging payload is mainly balanced by a counterweight (Figure 3.1). The position of counterweight is adjustable for payload masses between 200 and 500 kg prior to the centrifuge spin-up . Moreover, an automatic in-flight balancing system monitors the out-of-balance force and pumps the oil in the centrifuge arms. There are oil containers in the arms at two sides of the axis. The oil is pumped from one side to the other to correct the imbalance. The centrifuge shuts down automatically in case of ± 30 kN out-of-balance force exceeded.

Figure 3.2 illustrates the centrifuge apparatus. Power slip rings are linked to the top of the DAS cabinet for AC power distribution and DC supplies on the model. Hydraulic slip rings are used to supply air and water to the model. Signals from the transducers in model are transmitted via a 'user fibre optic rotary joint'.

The centrifuge model includes two cameras in this research. A computer was mounted in the DAS cabinet and connected to cameras using USB cables. The cameras were controlled by the computer and the computer could be logged in remotely from the centrifuge control room via the fibre optic rotary joint.

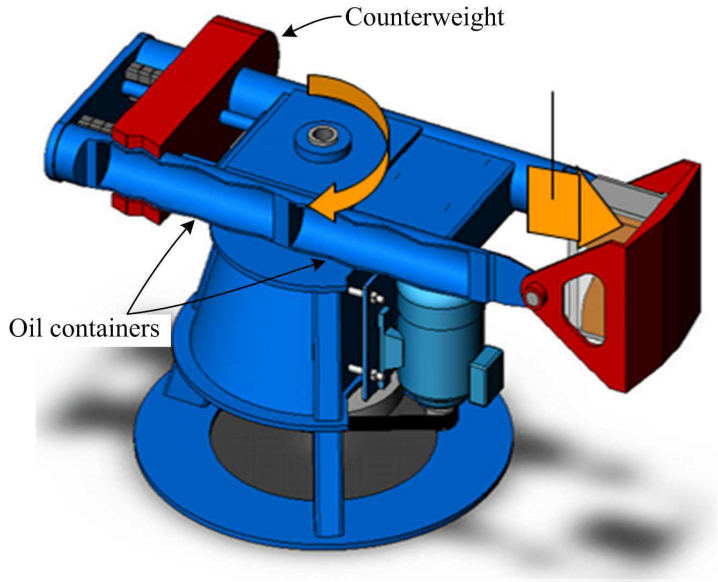

Figure 3.1: Geotechnical centrifuge at the University of Nottingham

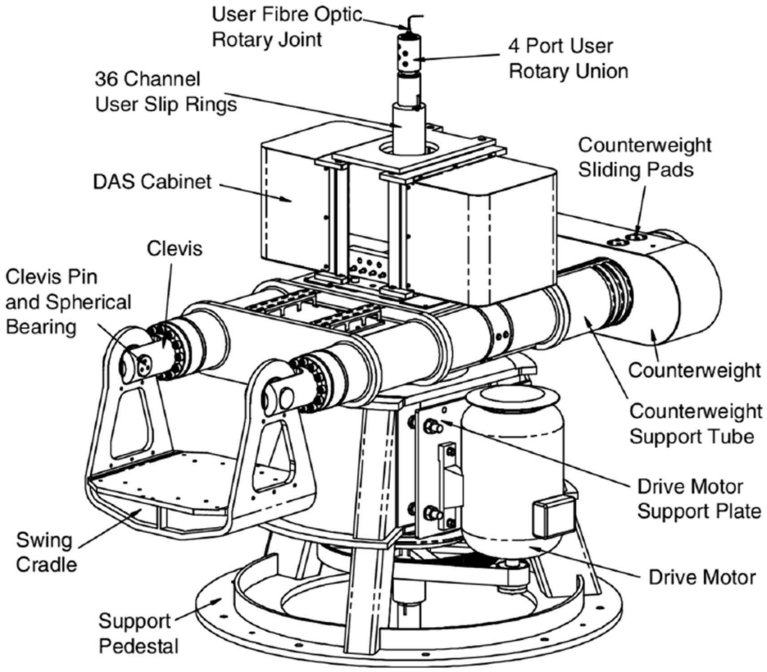

Figure 3.2: Schematic diagram of the Geotechnical centrifuge apparatus

3.3 Centrifuge package

The series of centrifuge tests were conducted in order to examine the transverse ground displacements caused by shallow tunnelling. The centrifuge package was composed of the plane-strain strong box, the soil, the model tunnel, the tunnel volume control system, and the devices for displacement measurement. The design of these components are presented in the following sections.

3.3.1 Strong box

Figure 3.3 presents the front of centrifuge package. The design of centrifuge strong box enabled the imaged-based analysis technique to measure the plain-strain soil deformations at Perspex wall. The strong box has plan dimensions of 640×260 mm and can accommodate a maximum height of soil of 500 mm. The box comprises a stainless steel U-section with front and back walls made of Perspex and aluminium, respectively.

The stainless steel U-section is bolted between the Perspex window and aluminium back wall (Figure 3.4). The U-section consists of two side walls and a bottom plate bolted and welded together. For future tests with saturated soils (the tests in this research used dry sand), nitrile rubber cords (5.7 mm diameter) were placed between the Perspex window, U-section and back wall to avoid leakage. There were five 1/8" BSPP taped holes on each side of U-section and several drainage channels on the bottom plate for pore pressure measurement and drainage. A trapezoid hole was machined on the back wall and a trapezoid aluminium ring was forced into the hole to accommodate and seal the model tunnel (Section 3.3.3.1, p.43).

In this research, the centrifuge was spun to $80g$, so it is necessary to check the strength and stiffness of centrifuge box under the high stresses experienced at $80g$. The strength of Perspex (17 MPa) is many times lower than that of aluminium (117 MPa) and stainless steel (215 MPa). The stress in Perspex at $80g$ should be lower than its strength to prevent that cracks occurs in tests, which is

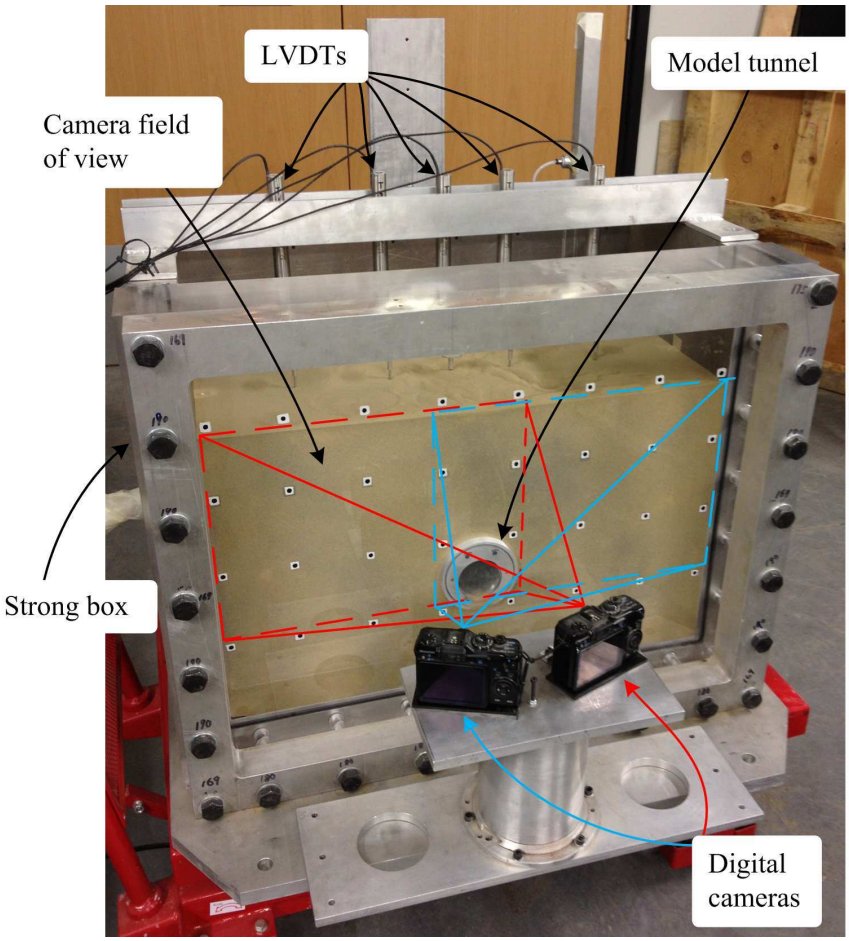

Figure 3.3: Centrifuge package (front view)

very dangerous. Moreover, the deflection of the Perspex window should be minimal to make sure that the deflection do not affect the accuracy of plane-strain displacements in the box. The thickness of the Perspex window is 100 mm, and a 100 mm diameter and 20 mm deep recess was cut into the Perspex face under the rectangle centre. In order to check the design, the unit weight of sands, γ, was set as 2.0×10^4 N/m^3 (2.0 g/cm^3). The maximum density of sand used in this research is approximately 1.6 g/cm^3. The coefficient of earth pressure K was set

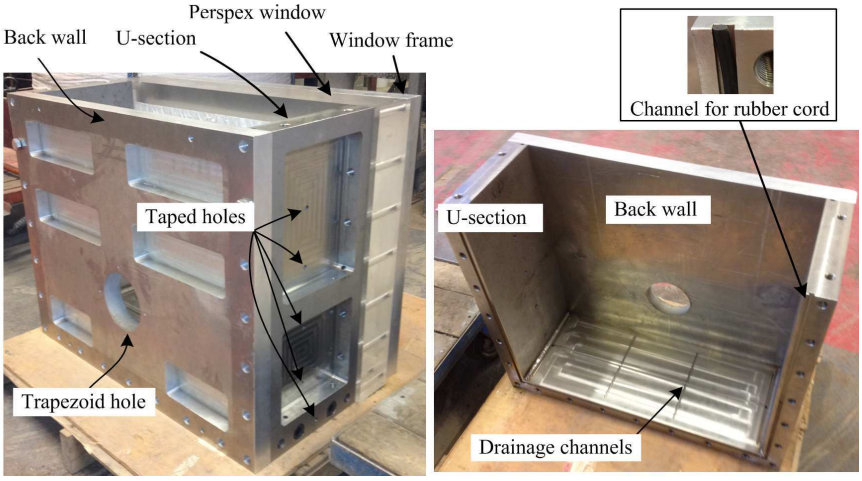

Figure 3.4: U-section and back wall of the strong box

conservatively as 1. At $1g$, the pressure on the window by saturated sands is

$$\sigma_{o,1g} = (K\gamma' + \gamma_w)z = [1 \times (2 \times 10^4 - 1 \times 10^4) + 1 \times 10^4)]z = 20z(kN) \quad (3.1)$$

where γ' is the unit weight of sands in water, γ_w is the unit weight of water and z is the depth from the surface of soil.

The acceleration in the tests was $80g$, but the acceleration for Perspex check was set as $150g$ which is the maximum capability of the centrifuge. Accordingly, the pressure on the window is

$$\sigma_{o,50g} = 150 \times \sigma_{o,1g} = 3000z(kN) \quad (3.2)$$

The two sides and bottom of the window are fixed with bolts restricting displacements in all the directions, and an aluminium window frame restricts the top displacements that are perpendicular to the face.

Finite element method (FEM) was used to estimate the stress and lateral deflection of the Perspex wall at $150g$ (nearly two times of $80g$, the acceleration in this

research). The modelling was performed using a FEM software, ABAQUS. The window boundaries were fixed by the window frame. Linear elastic model was used for Perspex with a elastic modulus of 2.5 GPa and a Poisson's ratio of 0.39 [PERSPEX, 2005].

Figure 3.5 shows results of the modelling. The maximum stress in Perspex is 4.938 MPa (tensile) at the bottom, lower than the tensile strength of Perspex, 17 MPa, so the window is very safe at $80g$. The average lateral deflection is approximately 0.2 mm at $150g$ and 0.1 mm at $80g$. The maximum lateral deflection is 0.3 mm at $80g$, which is less than 0.1% of the sand height, as suggested by Taylor [1995] to ensure minimal effect on lateral earth pressures.

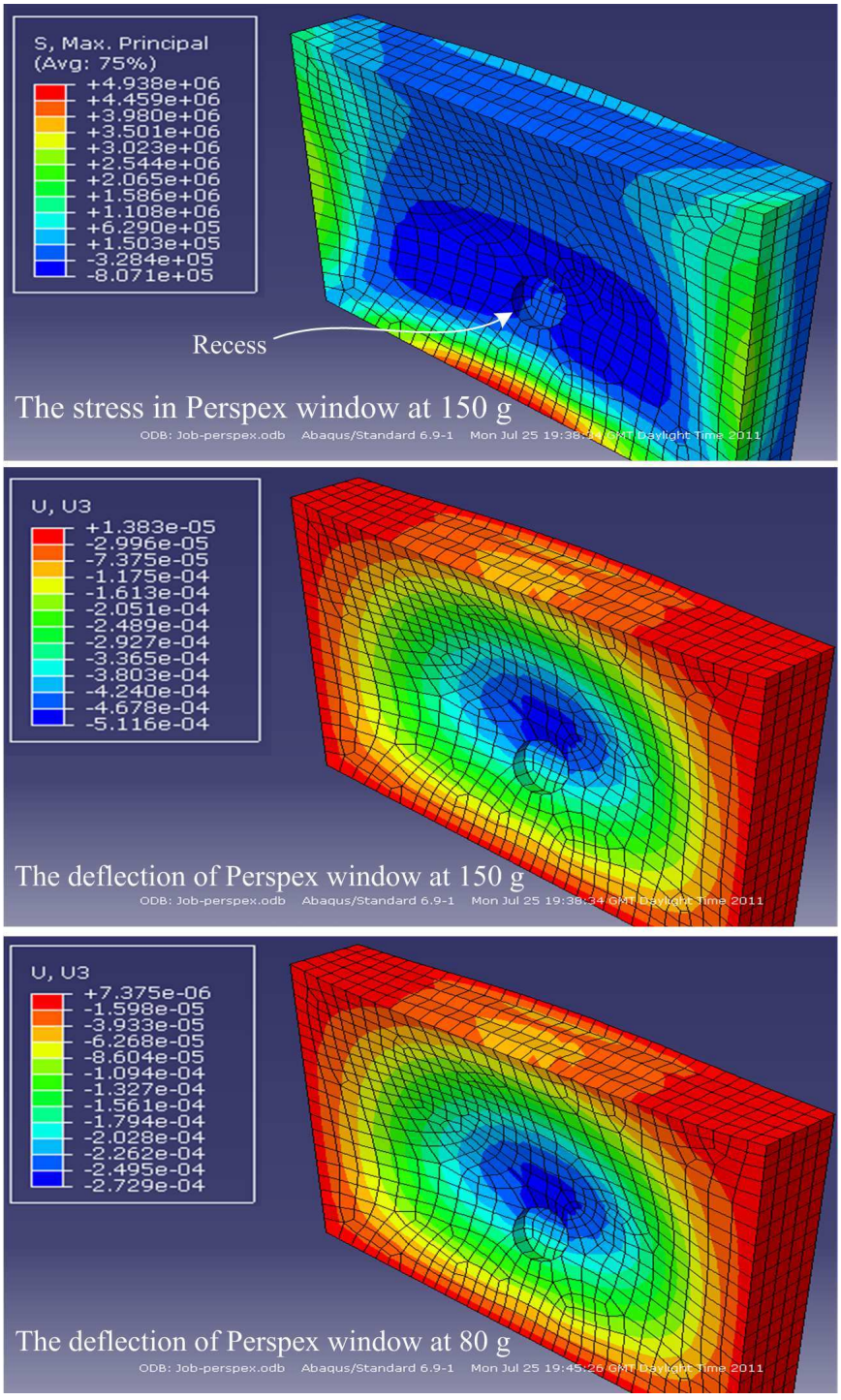

Figure 3.5: Finite element modelling of the Perspex wall

3.3.2 Soil

The soil used in the tests was Leighton Buzzard Fraction E silica sand from David Ball Group plc, which has been used extensively for physical model testing in the UK. The sand has a typical average diameter (D_{50}) of 122 μm and a specific gravity (G_s) of 2.67. The minimum and maximum void ratios (e_{min} and e_{max}) are 0.64 and 0.97, respectively. So the relationship between the density and relative density (ρ_s and I_d) is

$$\rho_s = \frac{G_s \rho_w}{1 + (1 - I_d)e_{max} + I_d e_{min}} \tag{3.3}$$

where ρ_w is the density of water.

The unit weight of the soil was varied with the relative density in the tests (Table 3.2, p.58).

Figure 3.6 illustrates the five centrifuge tests with different sandy ground conditions.

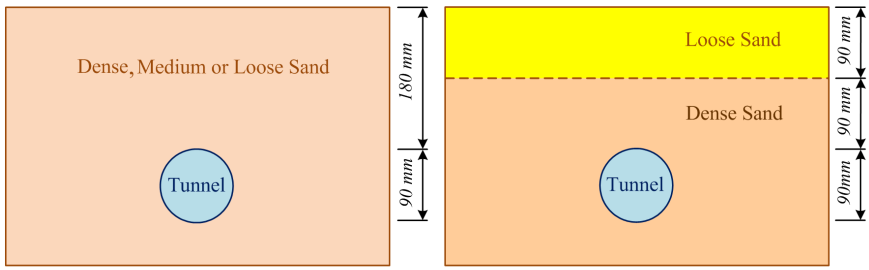

Group 1

- **Test 90**: I_d = 90% (dense sand)
- **Test 70**: I_d = 70% (medium sand)
- **Test 50**: I_d = 50% (loose sand)

Group 2

- **Test 50/90**: I_d - 50% upon 90% (loose sand upon dense sand)
- **Test 90/50**: I_d - 90% upon 50% (dense sand upon loose sand)

Figure 3.6: Tunnels in the different sandy ground conditions

3.3.3 Model tunnel

3.3.3.1 Structure of model tunnel

A model tunnel (Figure 3.7 (a)) was placed across the width of plane-strain strong box (260 mm) with its axis at a depth of 225 mm (cover to diameter ratio, C/D_t = 2). Figure 3.7 (b) illustrates the cross-section of model tunnel. The tunnel consists of a 68 mm diameter hollow inner cylinder with 88 mm diameter enlarged ends covered by a 1 mm thickness latex sleeve (supplied by Precision Dippings Marketing Ltd). So the outside diameter of the model tunnel is 90 mm, which at 80g corresponds to a prototype tunnel of 7.2 m diameter.

The annulus space between the inner cylinder and the latex sleeve was filled with water. The latex sleeve was sealed at both ends using O-rings and end plates. At the left end of model tunnel (Figure 3.7 (c)), a fitting ring tightly hooped the O-ring and secured the model tunnel within the recess of Perspex. At the right end (Figure 3.7 (d)-(g)), a trapezoid stopper ring was forced tightly by eight bolts into the annular gap of tunnel-wall to ensure a water tight seal both within the tunnel and at the tunnel-wall interfaces. Additionally, the ends of latex sleeve were compacted onto the ends of the tunnel by the end plates in order to double ensure the seal. All the components (excluding the latex sleeve) were made of aluminium.

a 1/8" BSPP taped hole was drilled on the inner cylinder. During the test, the water was extracted in order to replicate the volume loss of a tunnel. The diameter of the inner cylinder is 68 mm, thus providing more than 30% potential volume loss.

Tunnelling in sandy ground uses tunnel boring machines (TBMs) generally due to the necessary to provide face support in sand. The weight of the TBM and installed lining forces the tunnel to settle to the bottom of the excavated cavity, so deformations occur mainly above the tunnel. The model tunnel was designed as a downward eccentric cylinder (Figure 3.7 (h)) to fit expected ground deformation patterns around shallow tunnels [Loganathan and Poulos, 1998].

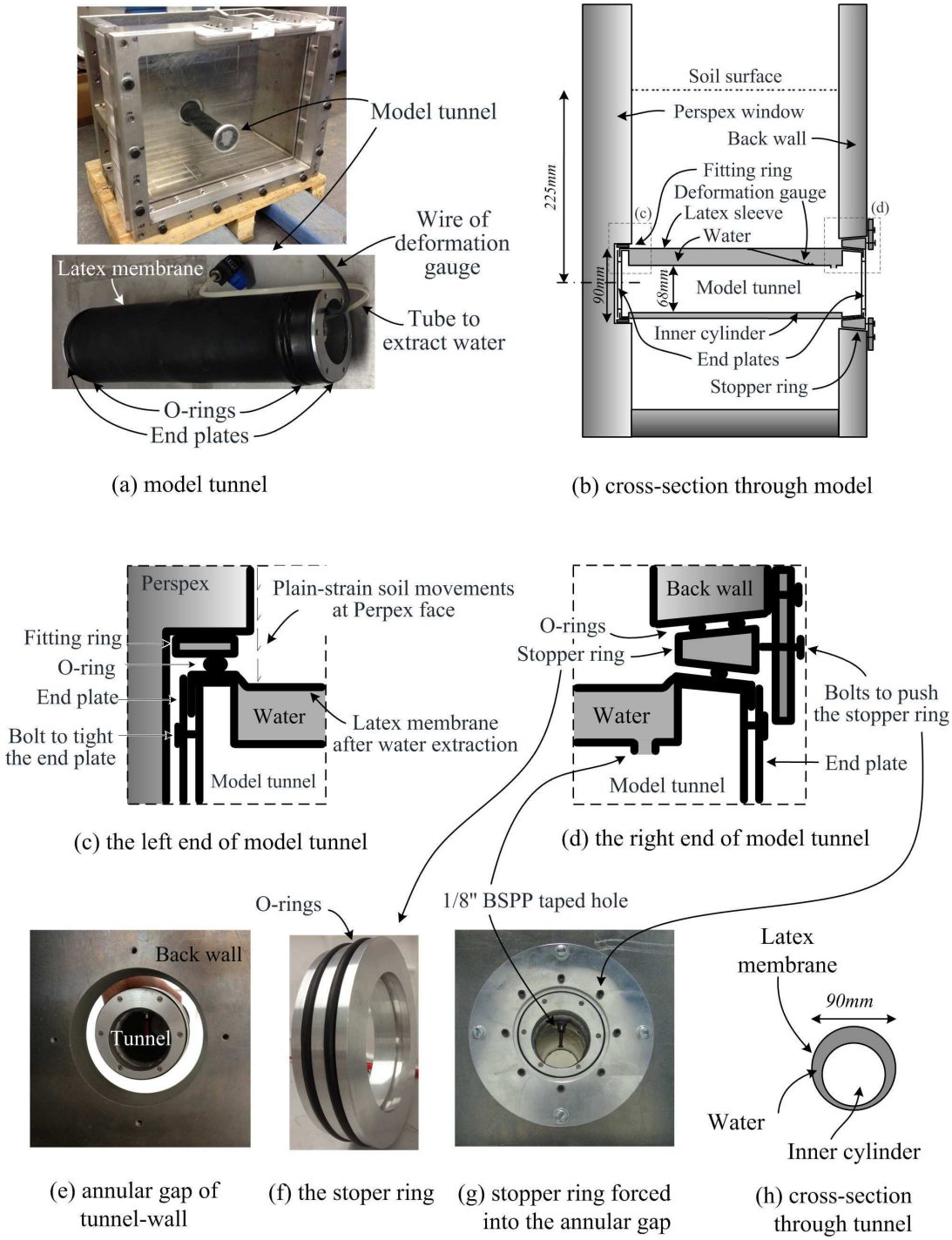

Figure 3.7: The model tunnel

The model tunnel was placed across the width of strong box to ensure the plane-strain soil displacements occurred at the Perspex wall. The inner edges of the enlarged ends (Figure 3.7 (c) and (d)) of the tunnel are set slightly inside the box walls in order to minimise any effect that the curvature of the membrane (due to its minimal stiffness) might have on obtaining plane-strain displacements at the walls.

The ratio of tunnel diameter to average grain size is 738, as mentioned in Section 2.3.2 (p.29), scale effects should be minimal as the ratio increases above 500.

3.3.3.2 Deformation gauges

The deformation (contraction) of tunnel at the crown and two sides was monitored during the centrifuge test. Because annulus space between the inner cylinder and the latex sleeve was narrower than 15 mm, it was impossible to put a normal deformation gauge (e.g. LVDT) there. Three cantilever steel strips with strain gauges in Figure 3.8 were used to monitor the tunnel deformation, which were very small and light. The steel strips were covered with the latex sleeve and bent with its contraction in the test. The strain gauges measured the bending strains on the steel strips. Because the model tunnel was filled with water, the strain gauges were coated with 5 layers of insulation and water-proof glues: (from the surface of strain gauge) 1 layer of polyurethane, 2 layers of neoprene and 2 layers of epoxy resin.

A calibration test was conducted to build the relationship between the deflection of strip and the voltage of strain gauge circuit, so the deformation of tunnel could be calculated with the slope of curves in Figure 3.9. Inevitably, the self weight of steel strip at $80g$ and the temperature affected the strain, but the increment/decrement of strain due to the self weight and the temperature were almost constant values, so they did not affect the measurement.

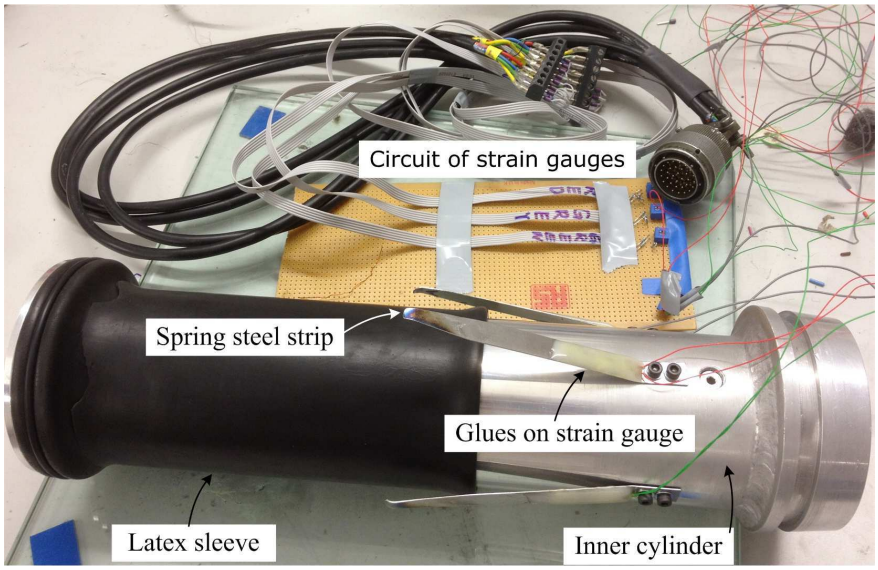

Figure 3.8: The deformation gauges

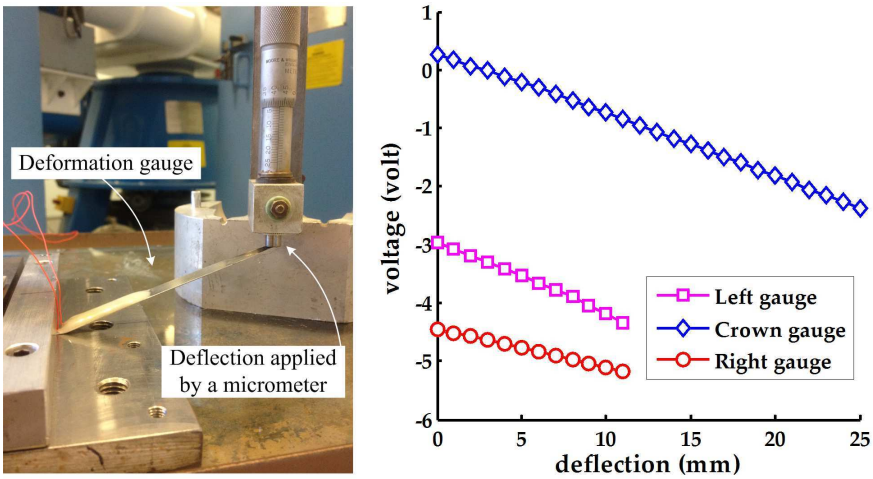

Figure 3.9: The calibration of deformation gauges

3.3.3.3 Seal test

The diameter of latex sleeve was 68 mm, same as that of the inner cylinder. During the assembly of model tunnel, if the aluminium cylinder was forced to slip into the latex sleeve, the enlarged ends and the deformation gauges may scratch the latex sleeve and cause leakage. Another method is showed in Figure 3.10.

The latex sleeve was wrapped around the inner surface of a PVC tube. The air gap between the sleeve and the inner surface of the tube was evacuated using a vacuum pump via a port opening through the tube. The aluminium cylinder was then put into the PVC tube. The vacuum port was opened so the air flowed back and the latex sleeve contracted onto the inner cylinder by its elasticity.

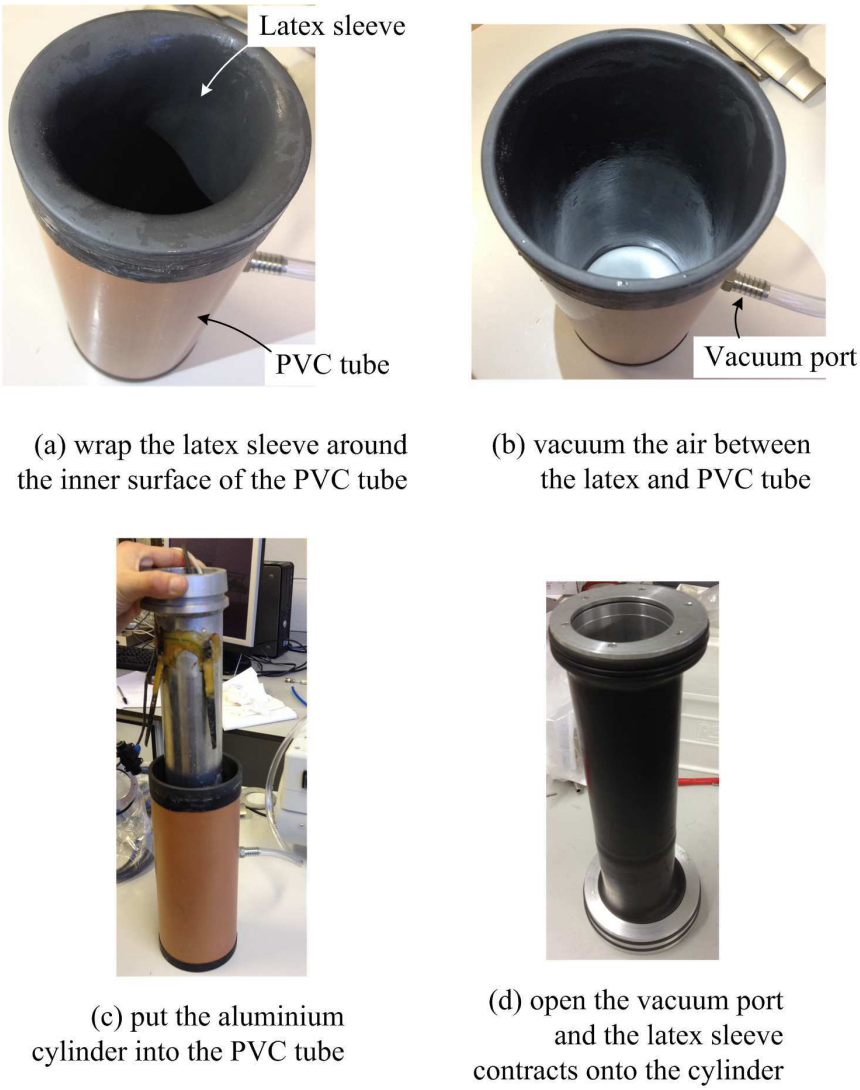

Figure 3.10: Put the aluminium cylinder into the latex sleeve

In this research, the maximum hydraulic pressure in the model tunnel was more than 250 kPa under the high stresses experienced at 80g (Section 3.3.4.3, p.55).

The model tunnel was sealed at both ends using O-rings and end plates. A seal test was conducted to check the water tight seal within the model tunnel and the water-proof of the deformation gauges. The model tunnel, a piston and a pressure gauge were connected together via pipework and filled with water (Figure 3.11). The latex sleeve was hooped by a 90 mm diameter brass tube. Then the stroke of piston was loaded to pressure the water in model tunnel to 500 kPa. The pressure was observed as a constant value for a hour, showing a good water tight seal was ensured. In the seal test, the hydraulic pressure due to the elasticity of latex sleeve was measured as 8 kPa and took account into the tunnel supporting pressure. The deformation gauges worked well during and after the seal test.

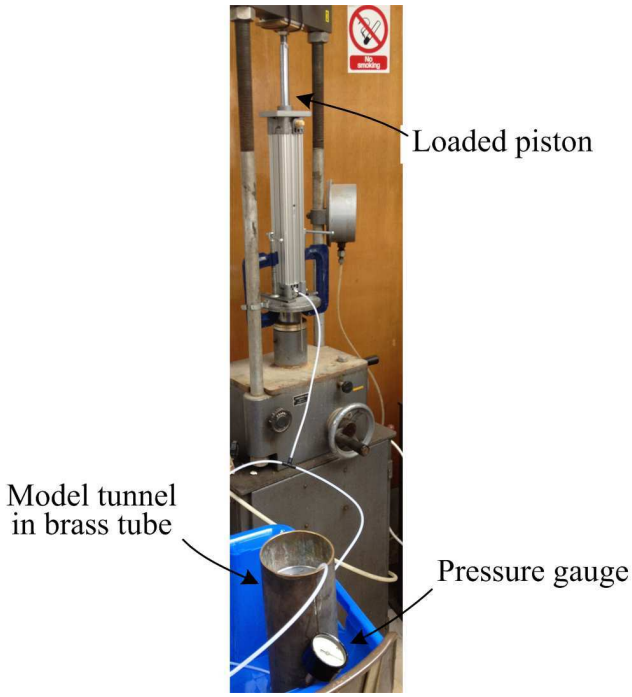

Figure 3.11: Seal test of model tunnel

In order to check the seal at the tunnel-wall interfaces, the strong box was put onto the centrifuge and filled with dyed water for observing the leakage. The acceleration in this research was $80g$ and the strong box on the centrifuge was spun-up to $100g$ in the seal tests. A camera monitored the gap between model tunnel and strong box sealed by the stopper ring (showed in Figure 3.7 (e)-(g), p.44). There was no leakage at $100g$ for half-hour.

3.3.4 Tunnel volume control system

The volume of the model tunnel was controlled using the actuator and hydraulic cylinder system. The system consists of a linear actuator, a hydraulic cylinder, an aluminium stand-pipe, a solenoid valve, a pressure sensor, pipework and aluminium joints to mount them together. A variable power supply was used to operate the system remotely allowing the piston to be raised and fluid extracted at various rates. Figure 3.12 sketches the volume control system.

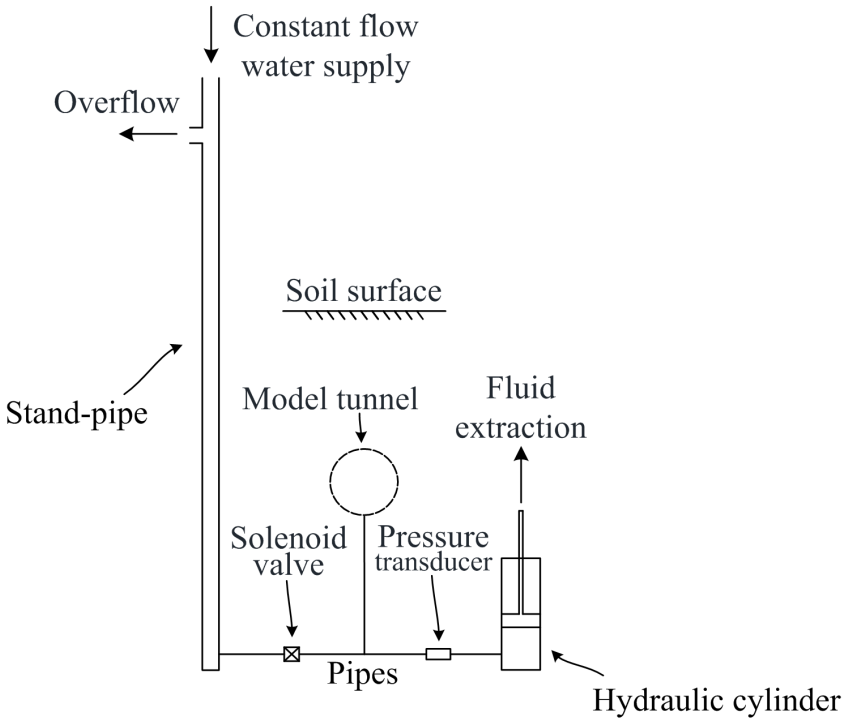

Figure 3.12: The sketch of volume control system

3.3.4.1 Actuator, hydraulic cylinder and LVDT

During the test at $80g$, the linear actuator was used to raise the piston of the hydraulic cylinder in order to extract water from the model tunnel. The actuator comprises a 24V DC electric motor which drives a stroke linearly. The stroke of the linear actuator and piston are both 300 mm and the internal diameter of

the cylinder is 50 mm. They can provide a volume loss of up to 35%. A linear variable differential transformer (LVDT) was used to measure the movement of the piston.

The tunnel volume control system was calibrated so that the volume of water extracted from the model tunnel was related to the movement of the piston directly. In this way, the volume loss of the model tunnel was related to the movement of the linear actuator. The rate of movement of the linear actuator was controlled by a variable power supply. The power supply was kept in the control room beside the centrifuge and connected to the linear actuator by the centrifuge slip rings. The calibration indicated that 10 mm of movement of the piston extracted 19634.95 mm^3 of water from the model tunnel. This volume is the 1.19% of the volume of model tunnel, as the 1.19% volume loss of tunnel. The volume loss of tunnel was conducted at the rate of 0.3% per minute that corresponds to a rate of piston movement of 28.08 mm/minute. The maximum volume loss of tunnel in this research was 10%, so the replication of tunnel volume loss during the centrifuge test took 33 minutes.

Figure 3.13 shows the volume control system at the back of strong box. The bottoms of hydraulic cylinder and linear actuator were fixed onto their bases and the bases were bolted onto the aluminium baseplate, respectively. Additionally, the actuator and cylinder were fixed together using an aluminium plate with two hoops. The LVDT was hooped and mounted onto the left side of hydraulic cylinder. The strokes of the linear actuator, the piston and the LVDT were mounted together using head joints and a threaded rod (round bar), so the movements of them were same.

3.3.4.2 Capability of volume control system

It is important to check the capability of the volume control system under the high stresses experienced at 80g. The maximum hydraulic pressure in the system was 446 kPa (Section 3.3.4.3, p.55) and the pressure range (capability) of the hydraulic cylinder was up to 1 MPa, double of the maximum value.

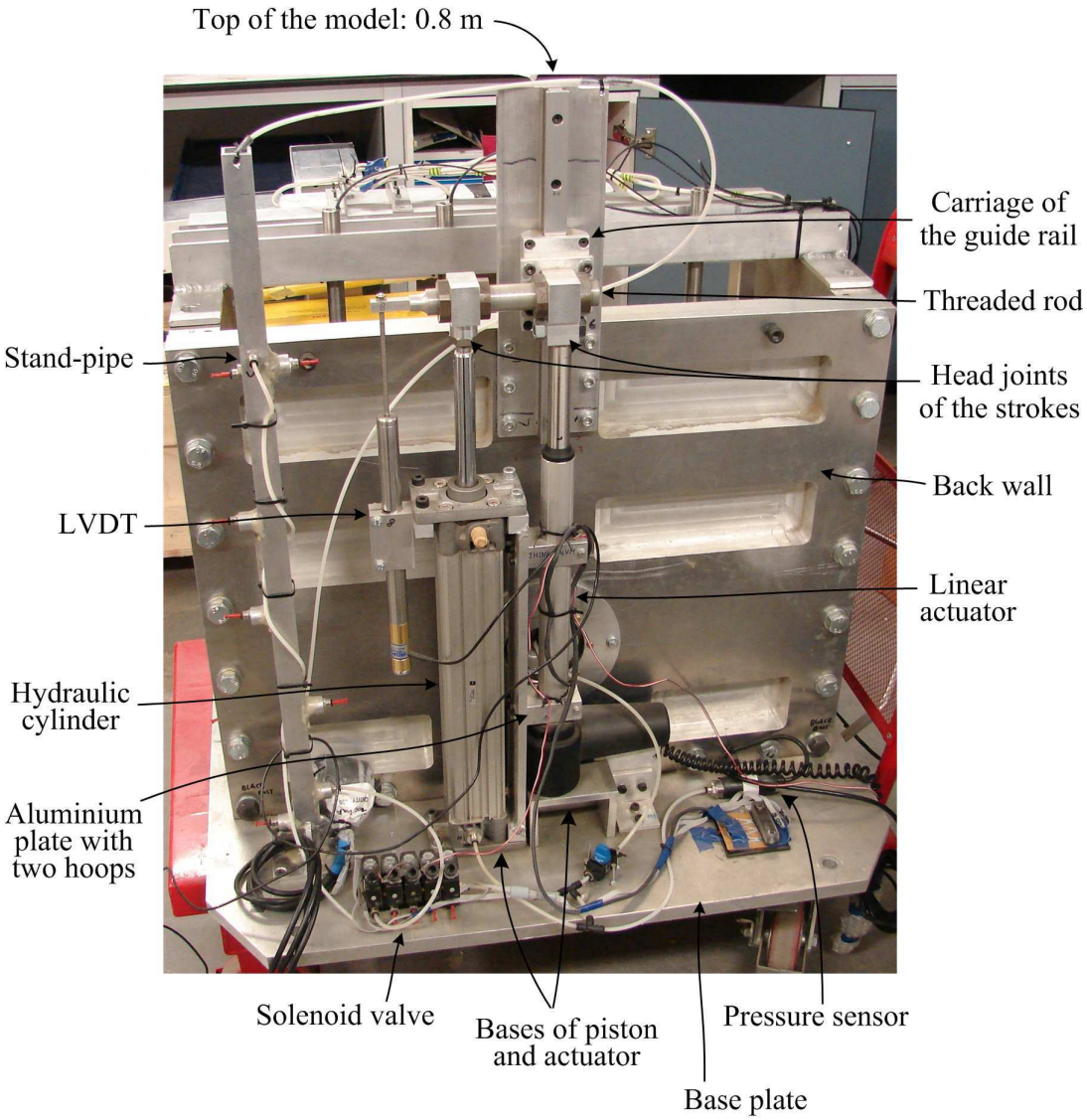

Figure 3.13: The components of volume control system

Figure 3.14 illustrates the loads on the threaded rod. The stroke of the piston was made of stainless steel and the mass of piston (including the head joints and nuts) was 1.01 kg. At $80g$, the load of piston onto the threaded rod, F_p, was 792 N, downward. The hydraulic cylinder was connected to the water within the model tunnel. The hydraulic pressure in the cylinder could force the piston upward and balance the piston, but the pressure used to decrease quickly with the volume

loss of tunnel in the test [Jacobsz, 2002; Marshall, 2009; Vorster et al., 2005], so it was ignored conservatively in the calculation. The distance between the two strokes of piston and actuator, l_1, was 70 mm, so the F_p generated a moment of 56 N·m at the head joint of the actuator. The threaded rod was made of aluminium to reduce its self weight. Considering the self weight at $80g$, the moment at the actuator head joint was 69 N·m totally, which was also the maximum moment in the threaded rod. The head joint of the actuator was bolted onto a carriage of a roller guide rail and the rail was bolted onto the back wall of the strong box (Figure 3.13). The roller guide rail restricted the movement of the system to vertical displacement only and generated a reaction moment, M_r (= 69 N·m, Figure 3.14), to balance the actuator head joint. The capability of the roller guide rail was 111 N·m, double of M_r.

The 1 inch (25.4 mm) diameter threaded rod acted as a cantilever beam in the system. Although the rod was not the best shape of beam to take the bending moment (should be I-section or rectangle) but the head joints of actuator and cylinder were easier to be fixed on the threaded rod with nuts. The bending strength of the aluminium threaded rod is

$$\begin{aligned} \sigma_{max} &= \frac{My_{max}}{I_z} = \frac{32M}{\pi D^3} \\ \Rightarrow M &= \frac{\pi D^3}{32}\sigma_{max} \end{aligned} \tag{3.4}$$

where D is the diameter of threaded rod and σ_{max} is 110 MPa for the aluminium, so the M is 177 N·m, 2.5 times of the maximum moment in the threaded rod.

The maximum shear force, $F_{s,max}$, in the threaded rod was the sum of F_p and the self weight of the rod at $80g$, 975 N totally,at the head joint of the linear actuator. The shear strength of the aluminium threaded rod is

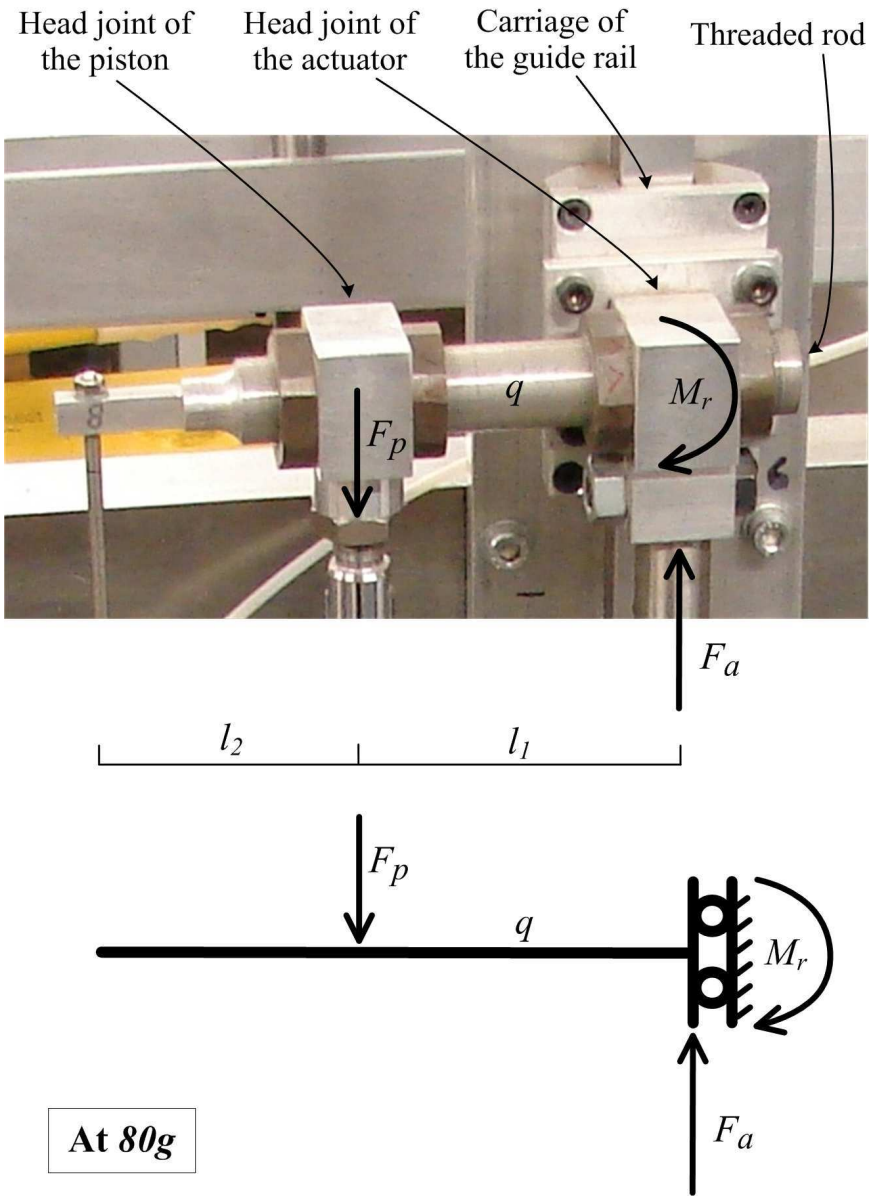

Figure 3.14: The loads on the threaded rod

$$\begin{aligned} \tau_{max} &= \frac{4}{3}\frac{F_s}{\pi R^2} \\ \Rightarrow F_s &= \frac{3}{4}\pi R^2 \tau_{max} \end{aligned} \tag{3.5}$$

where R is the radius of the threaded rod and τ_{max} is 70 MPa for the aluminium, so the shear strength, F_s, is 26588 N, 27 times of $F_{s,max}$.

The deflection and rotation (δ_p and θ_p) of the threaded rod at the head joint of the piston was due to F_p and the rod self weight (q = 2615 N/m):

$$\begin{aligned} \delta_p &= \delta_F + \delta_q = \frac{F_p l_1^3}{3EI} + \frac{q l_1^4}{8EI} \\ \theta_p &= \theta_F + \theta_q = \frac{F_p l_1^2}{2EI} + \frac{q l_1^3}{6EI} \end{aligned} \tag{3.6}$$

where E is the elastic modulus of aluminium (70 GPa) and I is the moment of inertia. δ_p and θ_p are 0.07 mm and 0.08^o, respectively.

The stroke of the LVDT was quit thin so the beam between the LVDT and piston was shaped into a small rectangular beam (l_2 in Figure 3.14). The weight of LVDT stroke and the rectangular beam were ignored, so the the deflection of the threaded rod at the LVDT stroke could be calculated by δ_p and θ_p:

$$\delta_l = \delta_p + \theta_p l_2 \tag{3.7}$$

Given that l_2 is 50 mm, δ_l is 0.14 mm. The complete derivation of Equations 3.4-3.7 can be found in a textbook on mechanics of materials.

The maximum load on the linear actuator, F_a, was the sum of the weight of the piston, the threaded rod, head joints, nuts, the guide rail carriage and the actuator stroke at $80g$. F_a was 1641 N, lower than the capability of actuator, 2000 N.

The above estimation did not consider the non-uniform acceleration in the centrifuge [Taylor, 1995] conservatively. When the piston rose up, its self weight

decreased slightly due to the lower acceleration. The top of the roller guide rail was also the top of the whole centrifuge model, 0.8 m from the bottom, lower than the 0.9 m height limit of the centrifuge model.

3.3.4.3 Constant-head stand-pipe

The model tunnel and the volume control system were filled with water carefully to avoid trapped air within the system, such as small air bubbles in the water. However, if the air did exist somewhere, during centrifuge spin-up, the trapped air within the water in the model tunnel would be compressed at high g-levels and cause unwanted volume loss of the tunnel. A constant-head stand-pipe was used to prevent the compression of the trapped air from affecting the volume of the model tunnel.

The aluminium stand-pipe was connected by pipes to the model tunnel and the hydraulic cylinder via a solenoid valve (Figure 3.12, p.49). The hydraulic pressure in the model tunnel was maintained by the constant-head stand-pipe during centrifuge spin-up. The constant pressure of the stand-pipe was set to be equal to the initial hydraulic pressure in the model tunnel. There was an overflow hole in the stand-pipe above the axis level of the model tunnel. The height of the overflow hole in the stand-pipe provided a hydraulic pressure equal the estimated soil overburden pressure at the tunnel axis (which was adjusted for different tests). Water supplied via the hydraulic slip ring was flowing to the stand-pipe continually during the spin-up process. The flow rate was controlled at 50 ccm (cm^3/min) by a water-flow meter in the centrifuge pipework.

During centrifuge spin-up the constant pressure of the stand-pipe and the hydraulic pressure in the model tunnel increased at the same rate with the g-level. The hydraulic pressure provided by the overflow hole in the stand-pipe was stably equal to the soil overburden pressure at the tunnel axis from $1g$ to $80g$. Any volume loss due to the compression of the trapped air was accounted for by the constant-head water supply from the stand-pipe to the model tunnel. Consequently, the constant-head stand-pipe ensured the trapped air within the model

tunnel and the volume control system did not affect the test results.

The connection between the stand-pipe and the model tunnel was linked by the solenoid vale with pipes. The solenoid valve was controlled remotely from the control room beside the centrifuge. The maximum operating pressure of the valve is 1200 kPa, 2.6 times of the maximum hydraulic pressure in the model at $80g$.

In a test from $1g$ to $80g$, because the elasticity of the latex membrane caused the additional tunnel pressure when initially filled with water, the solenoid value was initially closed to prevent the volume loss induced by the elasticity of the latex membrane. At approximately $5g$ the solenoid valve was opened and the model tunnel subjected to the pressure from the constant-head stand-pipe. Then the tunnel pressure increased proportionally to the overburden pressure as the centrifuge g-level increased, until $80g$ was reached. At the stage of $80g$, the solenoid valve was used to close the connection from the stand-pipe to the model tunnel. The linear actuator was then used to raise the piston of the hydraulic cylinder in order to extract water from the model tunnel.

Moreover, the stand-pipe could be used in the drainage system for the further tests with saturated sands.

The height of the overflow hole in the stand-pipe decided the hydraulic pressure subjected by the model tunnel. Because the stand-pipe was relatively high, the non-uniform acceleration in the vertical direction of the centrifuge model should be considered to decide the height of the hole. The acceleration, a, in the spinning centrifuge is

$$a = \omega^2 r \tag{3.8}$$

where ω is the angular velocity of the centrifuge and r is the radius (the distance to the centrifuge axis). When ω is 21.06 rad/s, the acceleration at the model tunnel axis is $80g$.

The weight of water in the stand-pipe varied with the acceleration along the stand-

pipe, and therefore the constant hydraulic pressure provided by the overflow hole, P_w, is the integration of the water weight along the stand-pipe:

$$P_w = \int_{R_w}^{R_t} \rho_w \omega^2 r dr \tag{3.9}$$

where R_t is radius of the model tunnel axis (the distance from the model tunnel axis to the centrifuge axis), R_w is the radius of the overflow hole and ρ_w is the density of water.

P_w was set to be equal to the estimated soil overburden pressure at the tunnel axis P_s (which was adjusted for different tests):

$$\begin{aligned} P_s &= \int_{R_s}^{R_t} \rho_s \omega^2 r dr \\ P_w &= P_s \end{aligned} \tag{3.10}$$

where R_s is the radius of the soil surface in the centrifuge and ρ_s is the density of soil (Equation 3.3, p.42).

For the layered soil in Group 2, the overburden pressure at the tunnel axis, P_{s12}, is:

$$\begin{aligned} P_{s12} &= \int_{R_{s2}}^{R_t} \rho_{s2} \omega^2 r dr + \int_{R_{s1}}^{R_{s2}} \rho_{s1} \omega^2 r dr \\ P_w &= P_{s12} \end{aligned} \tag{3.11}$$

where R_{s1} is the radius of the upper layer surface, R_{s2} is the radius of the lower layer surface (interface), ρ_{s1} and ρ_{s2} is the density of the upper and lower soil, respectively.

Substituting Equations 3.10 or 3.11 into 3.9 gives the value of R_w. R_w geometrically leads to the height of overflow hole in the constant-head stand-pipe, H_w (height from the base plate to the overflow hole). The height of the overflow hole was raised by 10 mm to account for the hydraulic pressure due to the elasticity of latex sleeve (8 kPa, Section 3.3.3.3, p.46). Table 3.2 provides the soil relative density (I_d), density (ρ_s) and H_w in the five centrifuge tests.

Table 3.2: The relative density, density of soil and the overflow hole in stand-pipe

Centrifuge test	I_d	ρ_s kg/m^3	H_w mm
Test 90	90%	1603	631
Test 70	70%	1529	611
Test 50	50%	1461	592
Test 50/90	50% upon 90%	1461/1603	617
Test 90/50	90% upon 50%	1603/1461	607

The maximum hydraulic pressure in the model tunnel was the value of P_s in Equations 3.10 for Test 90 (dense sand), 265 kPa. The maximum pressure in the centrifuge model was at the base plate level, 446 kPa.

3.3.4.4 Hydraulic pressure sensor

Figure 3.12 (p.49) and 3.13 (p.51) showed a hydraulic pressure sensor connected with the model tunnel. During the tests, the pressure sensor was used to monitor the hydraulic pressure in the model tunnel as volume loss was taking place. The pressure sensor was fastened onto the base plate of the centrifuge model, 197 mm lower than the model tunnel axis. The increment of the pressure due to the 197 mm could be integrated by the similar way as Equation 3.9, which was 181 kPa. The pressure in model tunnel was therefore equal to the sensor pressure with 181 kPa deducted.

The pressure range (capability) of the sensor (UNIK 5000, produced by General Electric) was 0-1000 kPa, more than two times of the maximum pressure in the centrifuge model. The pressure sensor and the LVDT were calibrated to measure their sensitivity of the output signal. The measurement of the hydraulic pressure

in the tests showed a $\pm$ 4% variation of the estimated value of the pressure, maybe due to the effect of high g-level on the accuracy of the pressure sensor.

3.3.5 Measuring displacements

This research is to investigate the ground movement caused by the underground tunnel. The soil displacements were measured using two methods. The main data of soil displacements were obtained using the imaged-based deformation measurement technique and examined to determine features of greenfield settlement, both surface and subsurface. The design of centrifuge strong box enabled the imaged-based analysis technique to measure the plain-strain soil deformations at Perspex window (Figure 3.3, p.38). The imaged-based data was validated against the vertical displacements of soil at the middle of strong box measured by LVDTs.

3.3.5.1 Measurement of soil displacements using PIV

The main focus of the tests was to obtain the plain-strain displacements of the surface and subsurface soil at Perspex window. Digital images were taken of the soil through the Perspex wall throughout the tests and and image analysis (GeoPIV) was performed to determine soil displacements. This method utilised the series of digital images that contained moving objects (in this research, the moving objects were the sands at the Perspex) over the given time. The measuring technique do not need the markers buried within the soil to show the displacements, which is a benefit for this research because the markers could disturb the soil and affect the soil displacements, the most important result. This method works by first using particle image velocimetry (PIV) to track the movement of patches of pixels/soil (identified by mapping pixel intensities) through a series of images. Close-range photogrammetry is then used to convert displacements in terms of pixels into a measurement of distance. This step requires that control markers at known locations are painted on the inner face of the Perspex window. Details of the development and application of GeoPIV can be found in White et al. [2003].

The PIV technique is performed with considering the errors in accuracy, precision and resolution. White et al. [2003] defined the three words as follows:

- accuracy - the systematic difference between a measured quantity and the true value;
- precision - the random difference between multiple measurements of the same quantity; and
- resolution - the smallest interval that can be present in a reading.

Take [2003] indicated that the precision was approximately 1/15th of a pixel. The precision that decide the quality of PIV result is affected by the maximum pixels of the camera, the distance from the camera to the object (or the level of zoom of the lens), the texture and lighting of the object.

The texture of the object is an important factor in determining the accuracy and precision of the PIV technique. The sufficient texture is conducive to the PIV identifying the different patches of pixels/soil effectively. The texture of clay and fine grained sand is generally poor. Increasing the size of patches could enhance the texture of each patch but reduce the number of data points of displacements. In order to improve the distinction between the grains of soil, the favourite method is to mix some fine and coloured materiel into the soil, such as dyed sands. The size of the materiel is small enough to prevent disturbing the soil.

3.3.5.2 Digital image capture for PIV analysis

In this research, two Canon PowerShot G10 14.7-megapixel 28 mm digital cameras were used to capture images of the sand behind the Perspex window during tests (Figure 3.3, p.38). The cameras were mounted onto an aluminium frame to the front of the Perspex wall. They were positioned carefully to capture the whole soil above the model tunnel and to be closest to the window. The two image areas overlapped so the displacement results from the two cameras could be merged together.

The precision of PIV is related to the distance between the camera and the object. Reducing the distance of the cameras from the Perspex wall could improve the level of precision obtained. However, the distance from any points on the Perspex wall to the lens of camera were varied. The the lens was closer to the middle of the Perspex wall (the soil above the model tunnel centreline) and relatively farther to the side of Perspex wall (soil far away from the model tunnel). The image scale was 0.09 mm/pixel at the middle and 0.12 mm/pixel at the side. Using the PIV precision of 1/15th of one pixel reported by Take [2003], the precision should theoretically be from (0.09 mm/pixel $\times$ 1/15th pixel =) 0.006 mm above the model tunnel centreline to 0.008 mm at the side. This is the attainable theoretical value of precision depended on the test conditions. In real tests, the precision of PIV results would be double of the theoretical value [Marshall, 2009] and the quality of the PIV results of the soil above the model tunnel centreline was better than that at the side (soil far away from the model tunnel). The first cause was that the cameras focused on the soil above the model tunnel centreline. The soil at side was relatively farther from the lens so it was slightly out of focus. Another cause was due to non-uniform lighting conditions on the soil behind the Perspex.

A camera test was conducted to figure out the best camera angle and height in the centrifuge package (to be closest to the object). A camera frame was designed based on the height and angle. Figure 3.15 shows the cameras that were bolted on the top of camera frame. There was a piece of rubber mat beneath each camera for shock-absorbing on the spinning centrifuge in order to ensure the image quality. Aluminium blocks were used to provide support to the telescopic camera lenses against its self weight at $80g$. The top of blocks were covered by a layer of aluminium tap that had smooth surface to allow the full range of lens movement for zoom operations. In this research, the lens zoom was generally set to the required value before centrifuge spin-up to avoid zooming at the high acceleration level. Because the cameras were placed closest to the object, the required zoom was the minimum value, 28 mm. The Fraction E silica sand used in the tests is quite fine so its texture is poor. Some of (about 1/3rd) the sand was dyed and mixed with un-dyed sand. The mixture was placed just behind

the Perspex window to enhance the texture of the soil and therefore improve the image analysis results. The lighting of the soil is also an important factor in determining the accuracy and precision of the PIV results. Both the dim lighting or the reflections within the window could hinder the image analysis. A set of fluorescent lights were positioned carefully around the front of the box to minimise reflections within the Perspex.

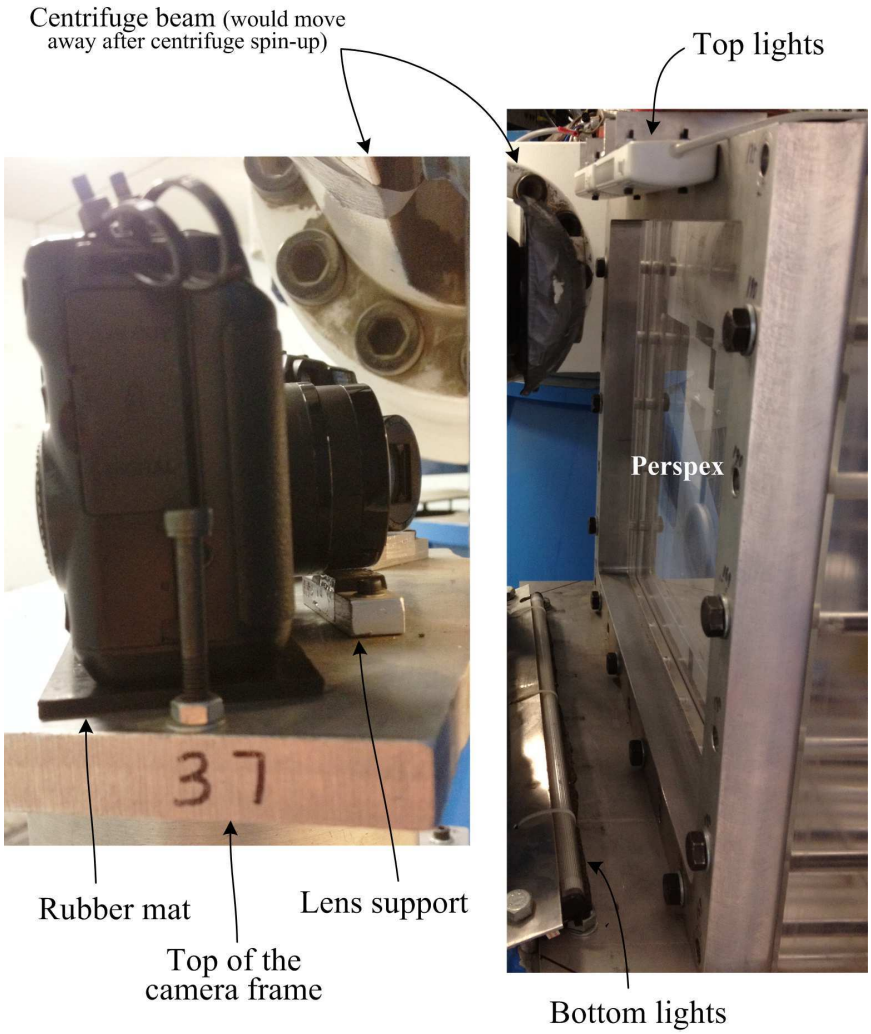

Figure 3.15: Digital image capture for PIV analysis

PIV utilises a series of photographs to map the movement of soil initially in terms of pixel movements. Control markers painted on the Perspex were used to

calibrate and map these pixel movements into real displacements. The accurate location of the control markers were measured by a calibration procedure using a photogrammetric grid (Figure 3.16), which is similar with the one used by Take [2003] and Marshall [2009]. The photogrammetric grid was firmly placed against the control markers. Because photographed area of the Perspex face was larger than the photogrammetric grid, three photographs were taken across the Perspex face. The photogrammetric grid was photographed behind the three adjacent areas that contained overlapping control markers (common points). The overlapping control markers were used to merge the marker positions from adjacent images into a global and unique axis system. Figure 3.16 is an example of 16 control markers (from r1c1 to r2c8) on the three photographs. The coordinate of the marker positions was decided by the photogrammetric grid beneath the markers, so each set of coordinates in images 1 to 3 was based on a different axis system. In order to merge the three sets of coordinate into a global and unique axis system, each image was required a rotation for this axis. In this research, the axis of image 1 was chosen as the unique axis. The rotation angle of image 2, θ, was therefore the difference of the angles of line r1c3-r2c3 in image 1 and 2 (or line r1c4-r2c4). Similarly, the rotation angle of image 3 was the accumulation of differences in image 3-2 and 2-1. Then the the coordinates were rotated using the standard rotation formulae given below:

$$\begin{aligned} x' &= x \cdot cos(\theta) + y \cdot sin(\theta) \\ y' &= y \cdot cos(\theta) - x \cdot sin(\theta) \end{aligned} \tag{3.12}$$

where (x,y) are the original coordinates of image 2 or 3 and (x',y') are the new coordinates. At last the coordinates were translated linearly such that the coordinates of all the common points were same. Some of the common points from two images could not have the same (x,y) values after the above merging process. The associated errors are averaged over the Perspex face with a maximum error in the control markers of 0.1 mm over 640 mm horizontally and 290 mm vertically, as a slight distortion in the coordinates.

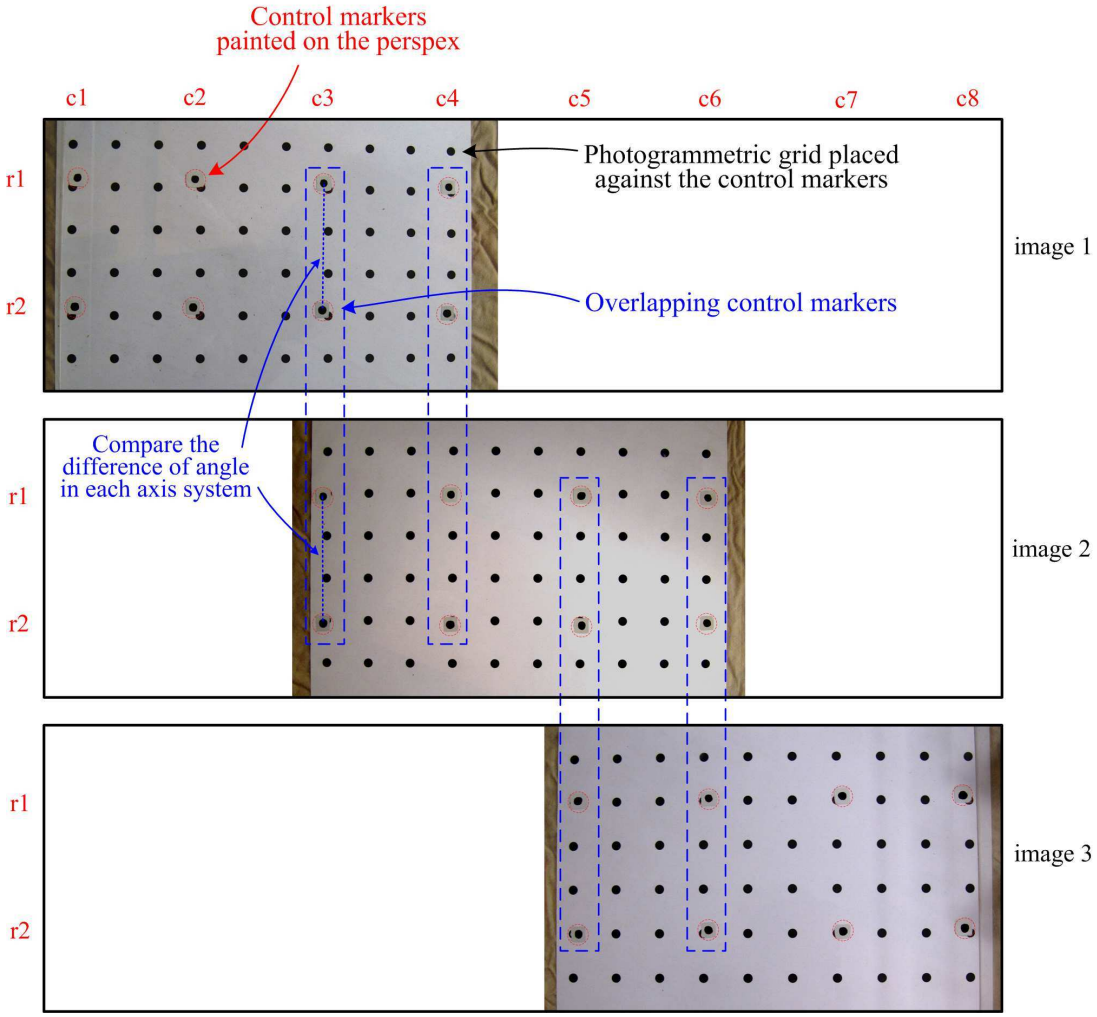

Figure 3.16: Photogrammetric calibration

During the volume loss of tunnel, the two cameras should take the image of soil at the same time, or the displacements could not coincide. A software, PSRemote©, was used to control the cameras remotely and therefore ensure the photographing at the same moment. The software could synchronise the cameras and perform the image capture timing. The timing of image capture was compared with the timing of volume loss to relate each photograph to the value of volume loss.

The software was installed in the imaging computer that was mounted on the beam centrifuge. The imaging computer could be logged in remotely from the

centrifuge control room to use the software. Because the imaging computer was on the centrifuge, the cameras could be connected to the computer directly by the USB cable. The photographs taken during the tests were saved on the memory cards in the cameras.

3.3.5.3 Vertical displacements of subsurface soil measured by LVDTs

Marshall [2009] indicated that the friction between the soil and Perspex reduced soil displacements by 10%-15% compared to tests using glass. This error was observed to be less at soil surface, presumably due to lower confining pressure. Additionally, Marshall et al. [2009] used the discrete element method (DEM) to model a centrifuge test with frictionless and frictional box walls. The simulation results indicated that wall friction tends to have a slight widening effect on the shape of the settlement trough.

Five LVDTs (Figure 3.3, p.38) were used to measure the vertical subsurface soil displacements at the middle of box width and the results were compared with the displacements measured by the cameras. The LVDT were placed 130 mm from the Perspex inner-face and at ± 200 mm, ± 80 mm and 0 mm from the tunnel centreline. Displacements at 90 mm depth from the soil surface were measured.

Subsurface attachments for the LVDTs were placed 130 mm from the Perspex inner-face during sand pouring (Section 3.4.2, p.68). This is the same attachments used by Vorster et al. [2005]. The arrangement of an attachment is illustrated in Figure 3.17 including two T-sections and a sleeve. The subsurface T-section consists of a hypodermic needle tubing with a circular pad footing at 90 mm below the soil surface. The surface T-section was placed within the sleeve after removal of the sand pouring shield. The LVDT is then suspended from a U-frame gantry above this arrangement and with the stroke of the LVDT resting on the pad footing which allows measurement of the subsurface at 90 mm depth.

Figure 3.18 shows the LVDT gantry across the box width. The gantry was made of 2"W × 2"H × 1/4"T aluminium U-frame (6082T6 aluminium alloy) with 5 hoop blocks on. Each block hooped ("held") a LVDT tightly. Due to the weight

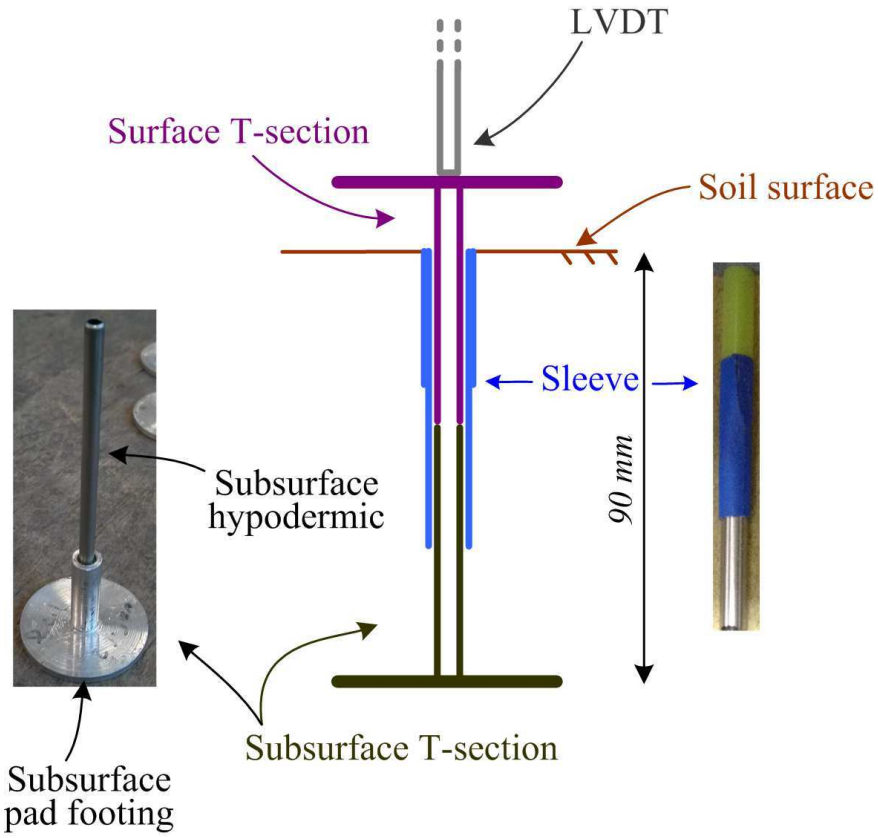

Figure 3.17: Attachment of LVDT for subsurface measurement

of 5 LVDTs and the self weight of gantry at 80g, the maximum deflection of the gantry was checked to be lower than 0.8 mm.

3.4 Model preparation

3.4.1 Sand pouring method

The data from five centrifuge tests are reported in this research(Figure 3.6, p.42), with three relative density (I_d) values of 90%, 70% and 50%. The sand was prepared using the sand pouring method. This method could ensure the soil uniformity and control the sand density. The sand density was determined by

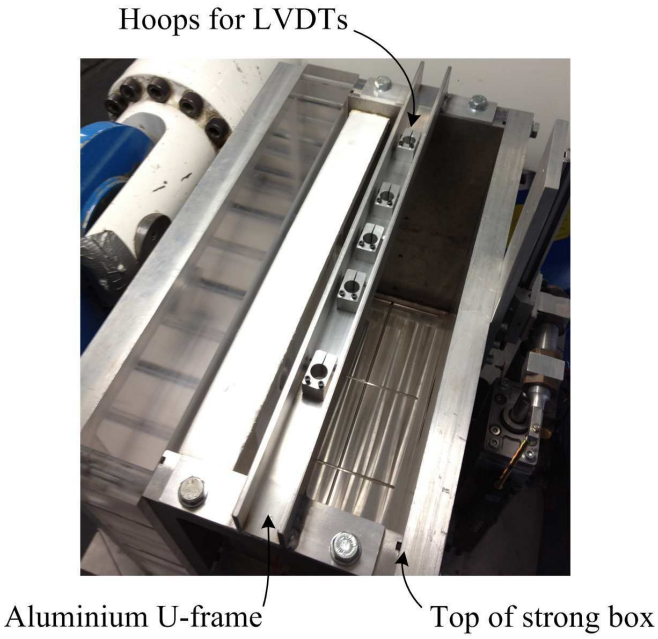

Figure 3.18: LVDT gantry

the parameters of dropping height and flow rate. With a higher dropping, the sand particle could have higher velocity and therefore more energy to compact with each other, which means that the void between sand particles is less and a higher density sample is obtained. The flow rate of sand pouring was controlled by the size of nozzle. If sand is poured at the same height but with different nozzles, the nozzle with a larger diameter will pour more sand at each moment. The sand particles will have less chance for a well redistribution in the model container due to the disturbance from other sand particles so the sample density could be looser.

For each sample preparation in this research, the height and flow rate (nozzle diameter) of sand pouring were calibrated for the target relative density. A wooden square model container (Figure 3.19) was used to collect sand poured from a metal hopper. The model container has 20 cm side length and 10 cm depth. The sand may accumulate on the edge of the container and then slip into the calibration container, so a extension made by paper cards was pasted onto the edge. The hopper was raised with the rising level of sand in the container in

order to keep a constant dropping height. The final level of sand was over the top of the container and then the paper extension was torn off and the extra sand on the top was slashed off. The total mass was measured and with the subtraction of the box self mass so the density and relative density (Equation 3.3, p.42) of poured sands could be calculated.

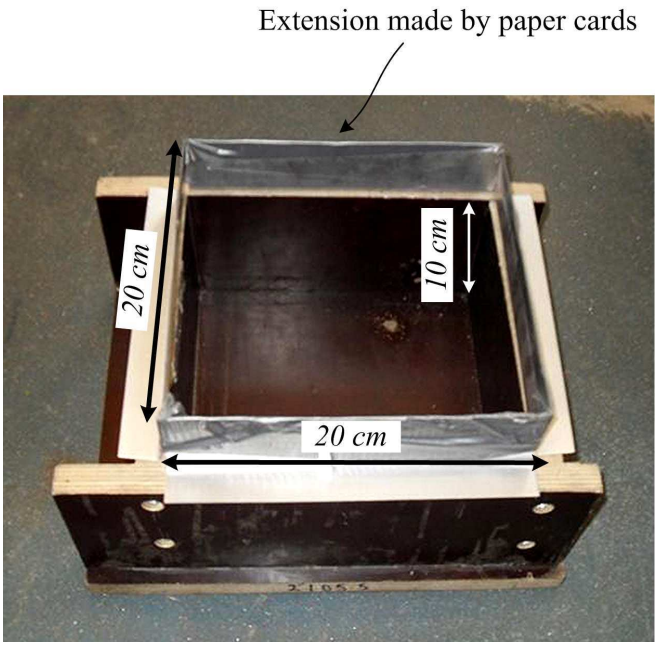

Figure 3.19: Wooden square model container

Table 3.3 summarised the experience obtained from the calibration of sand pouring: the required relative density (I_d) of sand sample, the height of pouring and the nozzle diameter. The calibration sample showed a variation of ± 4% in relative density.

3.4.2 Preparation of centrifuge model

The calibration was conducted to check the height and nozzle diameter for the I_d of each test before pouring sand into the strong box. Due to the orientation of the model tunnel across the strong box, the sands could not be poured from the top of the box. Consequently, the strong box and model tunnel were placed Perspex

Table 3.3: The calibration of sand pouring

Required I_d	Height m	Nozzle diameter mm
90%	1	5
70%	1	9
50%	0.5	9

*The data is only for the Fraction E sand and the sand pouring hopper in the University of Nottingham.

face down and the sand was poured in line with the tunnel. This method is consistent with the preparations of other similar centrifuge tests using sand, such as Jacobsz [2002], Vorster [2005] and Marshall [2009], which provides a consistent density of sand around the model tunnel. Figure 3.20 presents the top view of sand pouring. The back wall of the box was removed and a temporary wooden top was placed to prevent sands escaping from the open top.

The end of model tunnel was secured by an aluminium fitting ring within the recess of Perspex prior to the sand being poured. The fitting ring filled the annulus space between the recess and Perspex. The O-ring around the end of model tunnel was coated with silicone grease to improve the seal and prevent the sand from leaking into the recess.

When the model tunnel was placed vertically, its lower part (close to the Perspex face) had a tendency to bulge because the self weight of water in the soft latex membrane. The model tunnel was restrained by a plastic sleeve to avoid bulging. The sleeve was incrementally retracted as the sand level rose within the strong box.

The temporary wooden top was supported by two backing boards against the lateral soil pressure and the boards was clamped to the side wall of strong box. The width of backing boards controlled the final height of sand and C/D_t. The edge of wooden top was covered by foam tape to seal the sand and the deflection due to the soil pressure at $1g$ was checked to be lower than 0.1 mm. The poured sand may accumulate on the top of the vertical model tunnel and the edge of strong box and then slip onto the sample. A cup was therefore put onto the

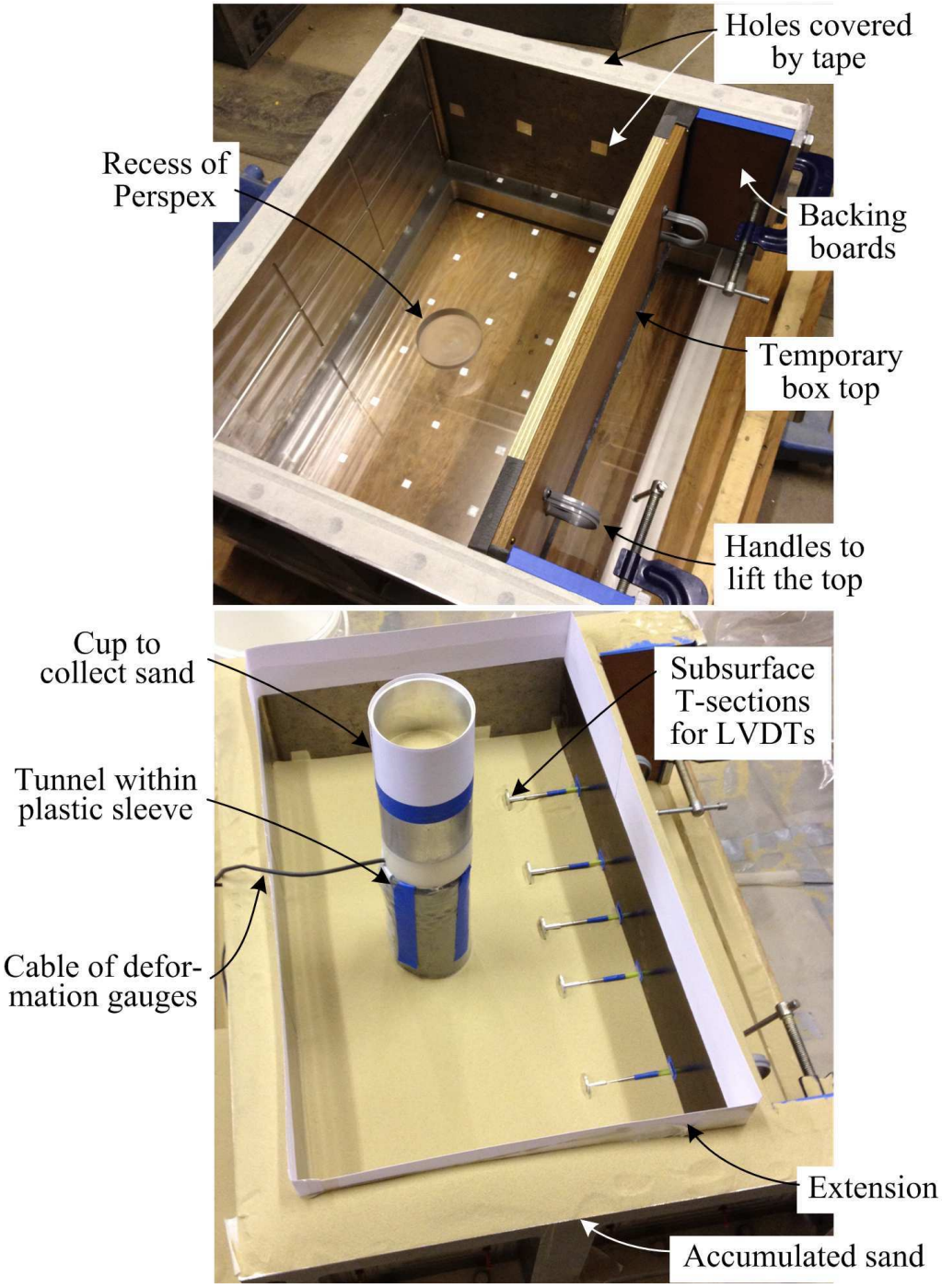

Figure 3.20: Top view of sand pouring

model tunnel to collect the sand as well as a extension was pasted onto the edge. Moreover, the drainage hole on the side wall and the threaded holes for the back wall were covered by tape to prevent the poured sand from flowing into the holes and blocking the threads.

The empty box with the model tunnel was weighed before the sand pouring. A layer of mixture (dyed and un-dyed) sand was then poured onto the Perspex face prior to the un-dyed sand being poured. The sand pouring was paused as the the level of sand reached 130 mm from the Perspex inner-face so that the subsurface T-sections and sleeves of the LVDT attachments could be inserted (Figure 3.21). The tops of sleeves was sealed with tape. The subsurface T-sections within the sleeves laid on the sand with the tapes against the temporary wooden top (the five poistions had been marked on the top previously). The sand pouring continued after that.

Small tins were put beside the strong box to check the homogeneity of the poured sand; these showed a variation of $\pm$ 3% in relative density. Similarly to the progress of calibration, the hopper was raised with the rising level of sand until the sand was over the top of strong box and then the paper extension was torn off and the extra sand on the top was slashed off. Additionally, the brush and vacuum cleaner were used to clean the extra sand on the strong box thoroughly. The strong box with sand was weighed to calculate the relative density of sample. After tearing off the tape on the threaded holes, the back wall were bolted in place and the trapezoid stopper ring was forced tightly by eight bolts into the annular gap of tunnel-wall (Figure 3.7, p.44).

The strong box was rotated slowly to its upright position with care to avoid disturbing the sand sample. The box was installed onto the base plate and the tunnel was connected to the volume control system. The whole equipments were then lifted and bolted onto the swing cradle of centrifuge. The temporary top was pulled out and the tapes on sleeves of LVDT attachments were removed to insert the surface T-sections. After that, the gantry with LVDTs was installed on the top of strong box.

The preparation of layered soil of I_d = 90% and 50% in Group 2 was slightly

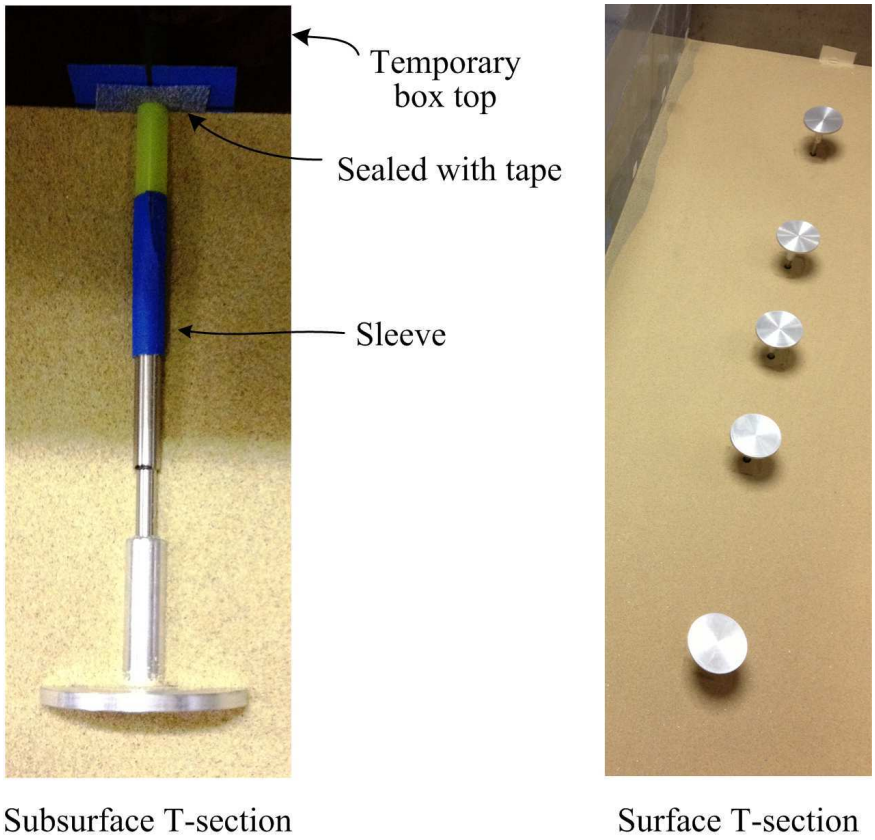

Figure 3.21: Insert the attachments of LVDT

different. For the lower layer, the strong box and model tunnel were placed Perspex face down and the temporary wooden top was palce at the interface of layers. The sand was poured in line with the tunnel (a layer of mixture firstly), which was same as the method mentioned above. After that, the strong box was rotated upright and the upper layer sand was poured from the open top of box. The upper layer sand was all mixture (dyed and un-dyed). The attachments of LVDTs was embedded during the sand pouring for upper layer and the sand was poured carefully to keep a even surface.

3.4.3 Summary of model preparation

Table 3.4 presents the results of sand pouring in the preparations of the five centrifuge tests.

Table 3.4: Sand pouring results

Centrifuge test	Required I_d	Obtained I_d
Test 90	90%	85.98%
Test 70	70%	68.30%
Test 50	50%	49.58%
Test 50/90	50%	51.30%
	90%	86.90%
Test 90/50	90%	91.31%
	50%	50.01%

To avoid complicating the analysis, the relative density of the sample was assumed to be the required value, 90%, 70% or 50%.

The procedure of model preparation was summarised in the list blow. The list may help further research with this set of experiment. The second level items of (a) were the preparation of homogeneous sand (Group 1) and items (b) were the preparation of layered sand (Group 2).

1. (after the last text) undo the connection of the strong box with the base plate and the volume control system, lift the box away and clean the sand sample;

2. remove the back wall and the model tunnel, put the strong box face down, place the temporary box top and do a calibration of sand pouring;

3. feed water into the model tunnel within the sleeve (90 mm diameter), place the model tunnel into the recess on Perspex and put the cup on the top;

4. put tins beside the strong box, weigh the empty strong box, paste the paper extension on the edge and pour a layer of mixture (dyed and un-dyed) sand;

5. (a) pour the un-dyed sand until the the level of sand reached 130 mm (check the I_d in tins during the sand pouring);

   (b) pour the un-dyed sand as the lower layer of soil until the sand was over the top of strong box (check the I_d in tins during the sand pouring);

6. (a) insert the subsurface T-sections and sleeves of the LVDT attachments;

   (b) tear off the paper extension, slash off the extra sand on the top, clean all extra sand and weigh the strong box;

7. (a) continue the sand pouring until the sand was over the top of strong box;

   (b) secure the back wall and the stopper ring in place and then rotate the strong box upright;

8. (a) tear off the paper extension, slash off the extra sand on the top, clean all extra sand, weigh the strong box;

   (b) mark the height of upper soil surface on the box walls, pull out the temporary wooden top, weigh the strong box (including the back wall and excluding the temporary wooden top now) and paste the paper extension onto the top edge of box,;

9. (a) secure the back wall and the stopper ring in place and then rotate the strong box upright;

   (b) embed the subsurface attachments of LVDT during the sand pouring of upper layer, stop pouring as the sand level reaches the mark of surface, tear off the paper extension, clean extra sand and weigh the strong box;

10. install the box onto the base plate, connect the model tunnel with the volume control system, lift and bolt the the whole equipments onto the swing cradle;

11. pull out the temporary box top (Group 1), remove the tapes on sleeves, insert the surface T-sections and installed the gantry with LVDTs;

12. electric connection from the centrifuge to the two cameras, three lights, six LVDTs, three strain gauges (on deformation gauges), one actuator (0-24 V d.c.), one pressure transducer and one solenoid valve;

13. check the power supply, signal and control system, fasten the cables and ensure that they are long enough when centrifuge spin up;

14. start to feed water into the stand pipe and remove all tools used in the centrifuge room at last.

3.5 Centrifuge test procedure

The centrifuge with the model was spun up to 201 rpm (ω = 21.06 rad/s) and therefore the acceleration at the model tunnel axis was 80g (Table 3.5). The weight of model was 400 kg totally. The position of the counterweight was adjusted to balance the centrifuge. Because the uneven distance from the centrifuge axis to the soil depths, the stress in the model varied with the depth. The stress in the upper section in the model (towards the soil surface) was underestimated and the stress in the lower section was overestimated by 6.7% and 4.8% (in homogeneous sand sample), respectively. The scaling laws in this research used 80 to determine the prototype parameters of model.

The centrifuge was spun up to 80g in steps of 10g. The electric system of model was operated by a software, LabVIEW©, in the centrifuge control room. At 5g the solenoid valve was opened so the model tunnel was connected to the pressure from the constant-head stand-pipe. A monitor above the centrifuge beam was overlooking the model and the digital cameras took a image of soil at each step. The instrumentation was also checked to ensure all signals were stable. At 80g, the solenoid valve was closed and water was extracted from model tunnel at the rate of 0.3% volume loss per minute until a maximum value of 10% volume loss was reached. The images were taken during the volume loss until the the centrifuge was spun down.

Table 3.5: Centrifuge test g-level

Parameter		Value	Unit
Centrifuge speed	rpm	201	rpm
Angular velocity = $2\pi\cdot$ rpm/60	ω	21.06	rad/s
Radius to baseplate	R	1.98	m
Offset from R to top of soil	O_{RS}	0.435	m
Height of soil	h_m	0.385	m
Radius to top of soil = $R - O_{RS}$	R_T	1.545	m
Depth where acceleration is $80g$ = depth of model tunnel axis	h_i	0.225	m
Effective radius = $R_T + h_i/2$	R_e	1.658	m
Underestimation of stress near surface	r_u	6.7	%
Overestimation of stress at base	r_o	4.8	%
g-level at h_i (depth of tunnel axis)	N	**80**	

*Some of the data are slightly different in Group 2 (layered soil).

3.6 Chapter summary

The design of centrifuge package is an important part of this research. This chapter described the development of experimental methods and equipment for the centrifuge tests. The specification of Geotechnical centrifuge was presented in Section 3.2 (p.34). The design of the centrifuge package was detailed in Section 3.3 (p.37). The procedure of the model preparation and centrifuge tests were provided in Section 3.4 (p.66) and Section 3.5, respectively. After this research, the centrifuge package has been upgraded for the further research of tunnelling beneath buried infrastructure.

Chapter 4

TUNNELLING IN SAND-THE EFFECT OF RELATIVE DENSITY

4.1 Introduction

This chapter reports the centrifuge test results in Group 1 (Figure 3.6, p.42) and analyses the effect of relative density on settlements above tunnels. The experimental methods and equipment for this research were described in Chapter 3 (p.33). The main objective of these tests was to examine the effect that relative density has on greenfield soil displacements above tunnels in sandy ground. The relative density of the sand ranged from 50% to 90% in the tests. The soil displacement data was obtained using GeoPIV and examined to determine features of greenfield settlement, both surface and subsurface. The effect that relative density has on the settlement trough shape is demonstrated and discussed. Some interesting features of tunnelling in sand were revealed in the analysis. Additionally, the data reported here serves as a baseline for comparison for the data reported in Chapter 5 (p.140), Chapter 6 (p.157), Chapter 7 (p.167) and further research for the effect of tunnelling on buried infrastructure.

The chapter consists of the following main sections:

1. The centrifuge test results are reported in Section 4.2 (p.79). The data of results is mostly observational in nature and serves as a reference for analyses provided in the next section.
2. The observational data is analysed and discussed to determine the features of settlements and examine the effect of relative density in Section 4.3 (p.116).
3. Finally, Section 4.4 (p.138) summarised the main findings.

Volume loss of tunnel ($V_{l,t}$) was taken up to 10% in each test to obtain the failed ground behaviour. The analysis in this chapter generally covers volume losses from 0% to 5% and four main stages of volume loss were specifically focused on:

1. $V_{l,t} = 1\%$, low volume loss;
2. $V_{l,t} = 2\%$, medium volume loss;

3. $V_{l,t} = 3\%$, high volume loss;

4. $V_{l,t} = 5\%$, extremely high volume loss (failure of tunnel).

The timing of image capture was compared with the timing of $V_{l,t}$ to relate each photograph to the value of $V_{l,t}$. However, those values of $V_{l,t}$ could not always exactly correspond to the four specific $V_{l,t}$. $V_{l,t}$ associated with the photographs varied within a range of $\pm$ 0.1% of the specific $V_{l,t}$ and are assumed to be the specific values for reporting purposes.

4.2 Centrifuge test results

Three centrifuge tests were completed in Group 1 to investigate the tunnelling in homogeneous sand. The tests were identical in all aspects except the relative density of the soil sample, varied from 90%, 70% to 50%, and therefore are referred to as Test 90, Test 70 and Test 50, respectively. The objective of those tests was to study the effect of the relative density on ground displacements caused by tunnelling. It will be presented that some interesting differences were observed between the tests. Relevant dimensional parameters of the tests were showed in Figure 3.6 (p.42). The cover, C, is 180 mm, measured from soil surface to tunnel crown. Given 90 mm tunnel diameter, the cover to diameter ratio, C/D_t, is 2.0. All results in this research are presented using model scale unless prototype scale stated. The model scale could be covered to prototype scale by a centrifuge scaling factor, N, of 80. Consequently the centrifuge models represent a 7.2 m diameter tunnel with 14.4 m soil covering its crown and C/D_t remains 2.0.

4.2.1 Assessment of sand densification and boundary effects

4.2.1.1 Sand densification caused by high g-level

The stress in soil sample increased by 80 times during the centrifuge spin-up. The high stress could densify the sand, especially the loose sand ($I_d = 50\%$, for Test 50). An assessment of the densification in loose sand was carried out by comparing PIV displacement data from $1g$ to $80g$. The settlement at soil surface shows that the average relative density increased by 0.96%. Figure 4.1 presents vertical displacement contours for Test 50 from $1g$ to $80g$ before the volume loss of tunnel, as a result of densification. The PIV displacement vectors are also shown as a reference. The magnitude of displacement increases with height due to the accumulation of densification-induced settlement. The average settlement at surface is 0.81 mm. The surface settlement above the tunnel centreline (0.9-1.0 mm) is more than that at side (0.5-0.6 mm) by 0.4 mm, due to the boundary effect. The vertical displacement above the tunnel centreline decreases sharply at the depth between 120-140 mm.

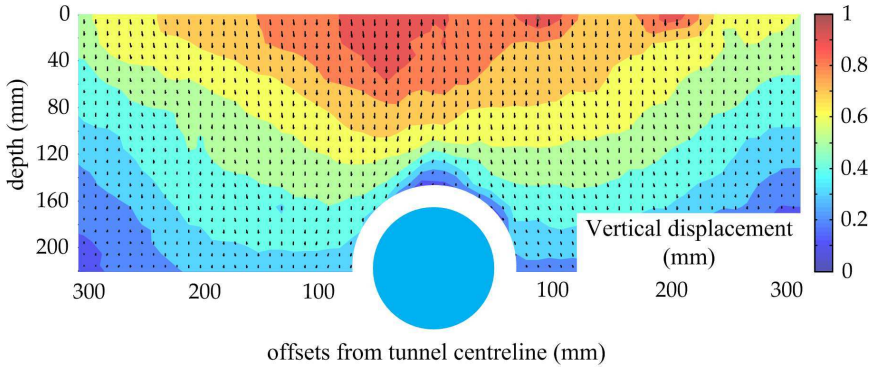

Figure 4.1: Vertical displacement contours for Test 50 - from $1g$ to $80g$

The $1g$-$80g$ displacements of sand around the model tunnel are illustrated by a vector field scaled up by 20 times in Figure 4.2. The black arrows are the PIV displacement vectors and the red arrows indicates the trends of movements. Above depth 120 mm, the sand moved downwards in parallel directions. The

reaction of model tunnel started to restrict the downward displacements at the depth between 120-140 mm. Beneath this area, the displacements were diverted towards the shoulder and side of the model tunnel.

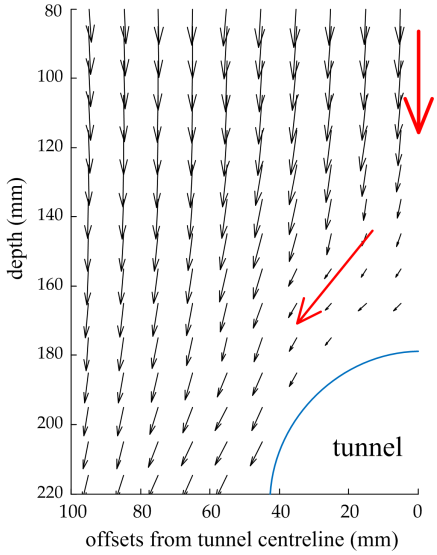

Figure 4.2: The PIV displacement vectors around tunnel for Test 50 - from 1g to 80g

Figure 4.3 illustrates the increment of relative density from 50% during spin-up (1g-80g). The contours were calculated based on the PIV displacement field. The restriction on sand displacements at the depth between 120-140 mm above the tunnel crown causes the concentration of sand, as the maximum increment of relative density (4%-5%). Moreover, the displacements diverted towards the shoulders and sides of tunnel cause 1.5%-3% increment of relative density in these area.

Consequently, the densification of sand during the centrifuge spin-up is limited and the effects are minimal.

4.2.1.2 Boundary effects on PIV data

The friction between the soil and Perspex inevitably reduced soil displacements to some extend. The vertical subsurface (90 mm depth) soil displacements at

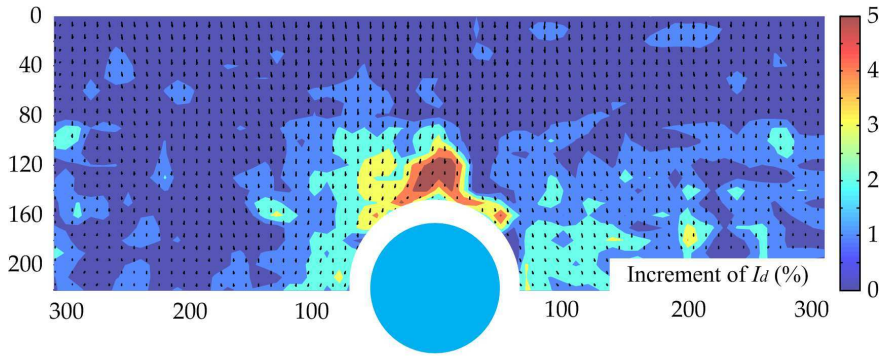

Figure 4.3: I_d increment contours for Test 50 - from $1g$ to $80g$

the middle of box width were measured by five LVDTs and are compared with the obtained PIV results in order to assess the boundary effects (Section 3.3.5.3, p.65).

The PIV displacements directly above the tunnel centreline at 90 mm depth are compared with the subsurface (LVDT) data in Figure 4.4. The LVDT data generally agree with the PIV data. However, the PIV values mostly are less than the LVDT data, which is due to some friction loss at the Perspex face.

In Group 1, the maximum ratios of PIV displacements to LVDT values are 0.90, 0.88 and 0.85 for Test 90, 70 and 50, respectively. All the maximum ratios are at high or extremely high volume loss of tunnel. The ratios were calculated over the rang of tunnel volume loss from 0.5% to 5%. The displacements of volume loss lower than 0.5% are micro and could not be measured reasonably well by cameras.

Figure 4.5 presents a comparison between PIV and LVDT subsurface settlement profiles at 5% volume loss. The reduction of PIV displacements is maximum in Test 70 and 50 at this stage (12% - 15%), but even so, there is no significant discrepancy between PIV and LVDT displacements as well as the curves describe the effects of relative density clearly.

The natural variability of soil behaviour should be taken into account when considering Figure 4.4 and 4.5. The plan-strain model means a uniform settlement

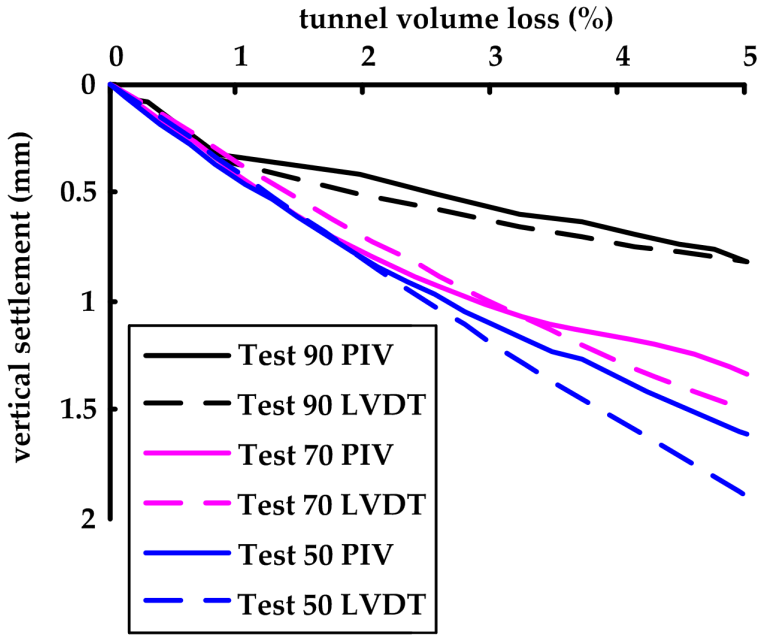

Figure 4.4: Vertical soil displacements above tunnel centreline at 90 mm depth - Group 1

trough through the width of the plane-strain strong box. The sand sample was assumed to be a homogeneous material but the real sand, as a granular material, does not always behave homogeneously. The non-uniformity of trough shapes at Perspex and middle width could result in some of the PIV-LVDT differences.

The results are similar to the previous investigation of the boundary effects on PIV data (Section 3.3.5.3, p.65).

Furthermore, Section 4.2.3.1 (p.86) reports that the displacements faraway from the model tunnel are micro, so the boundary effects of the side walls are minimal.

4.2.2 Tunnel pressure

The hydraulic pressure in the model tunnel was monitored by the pressure sensor (Section 3.3.4.4, p.58) during the tests. Figure 4.6 presents the relationship between tunnel pressure with volume loss for Group 1. The pressure is in nor-

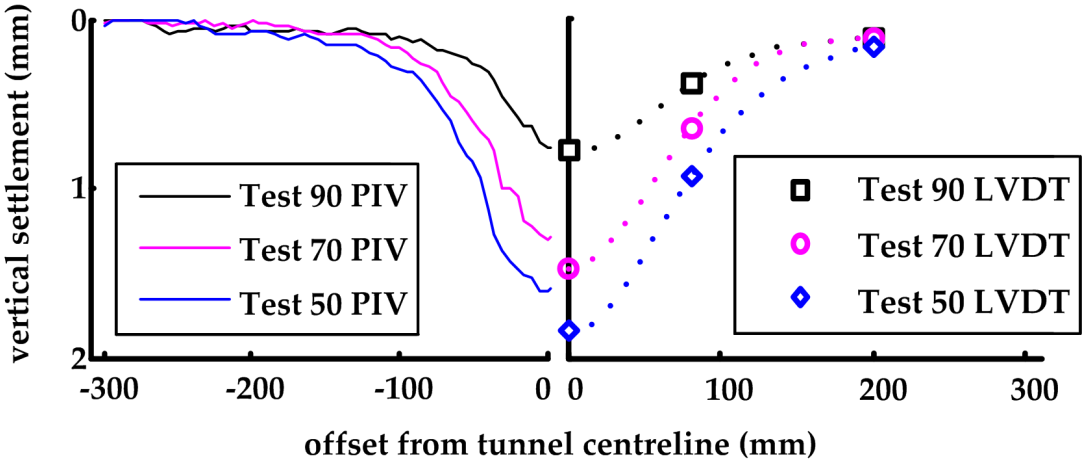

Figure 4.5: Comparison of PIV and LVDT subsurface settlement profiles at 5% volume loss - Group 1

malised form for comparison of different tests to examine the effect of relative density:

$$\sigma_{norm} = \sigma_t/(\rho g N D_t) \tag{4.1}$$

where σ_t is the pressure in model tunnel, ρ is the soil density, g is 9.81m/s^2, N is the centrifuge g-level, and D_t is the diameter of the model tunnel (90 mm).

Almost identical variation of normalised pressure with volume loss is observed in the three tests with different relative densities. The extraction of water from the tunnel during the experiment resulted in a reduction in the tunnel pressure. As presented in Figure 4.6 the normalised tunnel pressure shows a sharp initial drop from approximately 2.5 at 0% volume loss to 0.8 at 1% volume loss. After that there is little reduction in the pressure until the normalised pressure remains relatively stable at 0.5. This behaviour is similar to that found by Marshall [2009], Vorster [2005] and Jacobsz [2002].

The scope of this research is concerned with pre-collapse soil displacements induced by tunnelling so that 10% is the maximum volume loss of tunnel. The

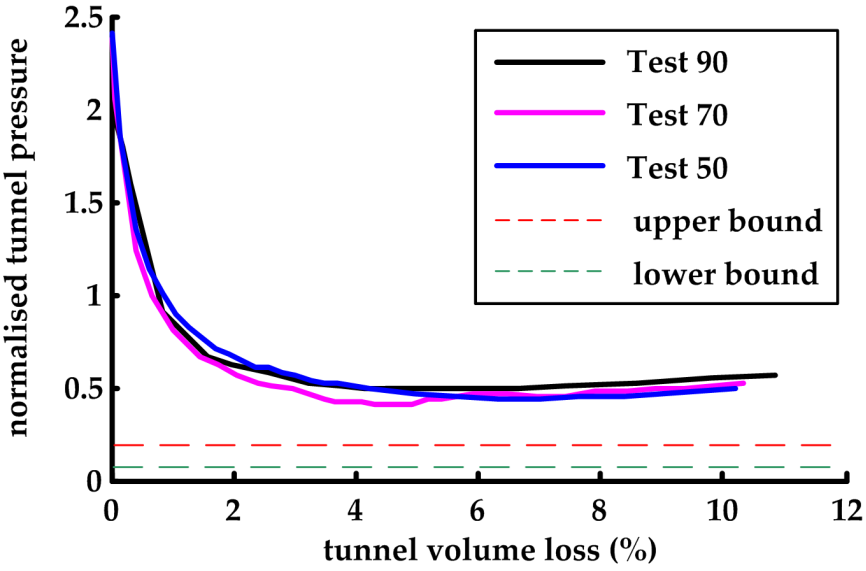

Figure 4.6: Normalised tunnel pressure with volume loss - Group 1

ultimate tunnel pressure is above the upper and lower bound predicted by Atkinson and Potts [1977] for tunnel collapse.

4.2.3 Soil displacements

This section gives the displacements data of soil in Group 1. The data was obtained using GeoPIV (introduced in Section 3.3.5, p.59) to analysis the photographs of soil behind the Perspex wall taken during the process of tunnel volume loss. The displacements are illustrated in form of coloured contours. The contours of Test 90, 70 and 50 are put together for comparison in each main stage of volume loss.

The displacements in the soil are generally regular. For example, the vertical displacements are larger near the model tunnel. There are, however, some abnormally large movements in PIV data at the two sides of sample (near the side wall of box), which are attributed to that the soil sample at two sides is not high definition in images because of the long distance to the camera. The other errors associated with merging PIV data from adjacent images are found in some of the

figures. As a result, some distortion in the data where the images overlapped is evident.

4.2.3.1 Vertical soil displacements

Contours of vertical displacements in Group 1 are shown in Figure 4.7-4.10 (p.88-91) for 1%, 2%, 3% and 5% tunnel volume loss. Note that the scale of colour bar of the contours is not constant in the figures for varying volume losses. Some of the displacement vectors are also shown as a reference. The vectors are scaled up by 25, 20, 15 and 10 times in the four figures for varying volume losses, respectively. The observations from the figures are summarised as below:

- The value of displacement generally increases with tunnel volume loss in all the three tests.
- The distribution of settlement narrows with the increasing volume loss in each test.
- At low volume loss of 1% (Figure 4.7, p.89), the soil above the tunnel moves downwards as a rigid body in a chimney like shape. The 'chimney' mechanism described by various authors for tunnelling in sands develops vertically above the tunnel. The magnitude of settlement at the soil surface does not differ much from that near the tunnel crown. The values of displacement in the chimney are all around 0.25-0.5 mm in the three tests. The settlement trough in dense sand (Test 90) is a little wider.
- At medium to high volume losses of 2% to 3% (Figure 4.8-4.9, p.89-90), there is a localised settlement zone directly above the tunnel crown from which a small flame of settlement contours propagate. The settlements in this zone are substantially larger than that nearer the surface. The displacements in loose sand (Test 50) and medium sand (Test 70) are significantly higher than that in dense sand as well as the settlements in loose sand are relatively higher than that in medium sand. Moreover, the major

settlements are mostly in the area between ± 100 mm offset from tunnel centreline; the settlements outside of this area are substantially smaller.

- At extremely high volume loss of 5% (Figure 4.10, p.91), the values of localised displacements in all the three tests are approximately same.There is not much development of the surface settlement in dense sand from 3% to 5% volume loss and the centre surface settlements stay around 0.4-0.5 mm (note the different scales of colour bars). In dense and medium sand, the settlements extend from the localised settlement zone towards the surface with sharp decreasing magnitude at about 100-130 mm depth, but in loose sand, the magnitude of settlements decreases gradually from the tunnel crown towards the surface. Consequently, the localisation of settlements above the tunnel is severer in dense and medium sand than that in loose sand. Additionally, the difference of displacements in loose and medium sand is enlarged. The magnitude of displacements in loose sand is evidently larger than that in medium sand at this stage.

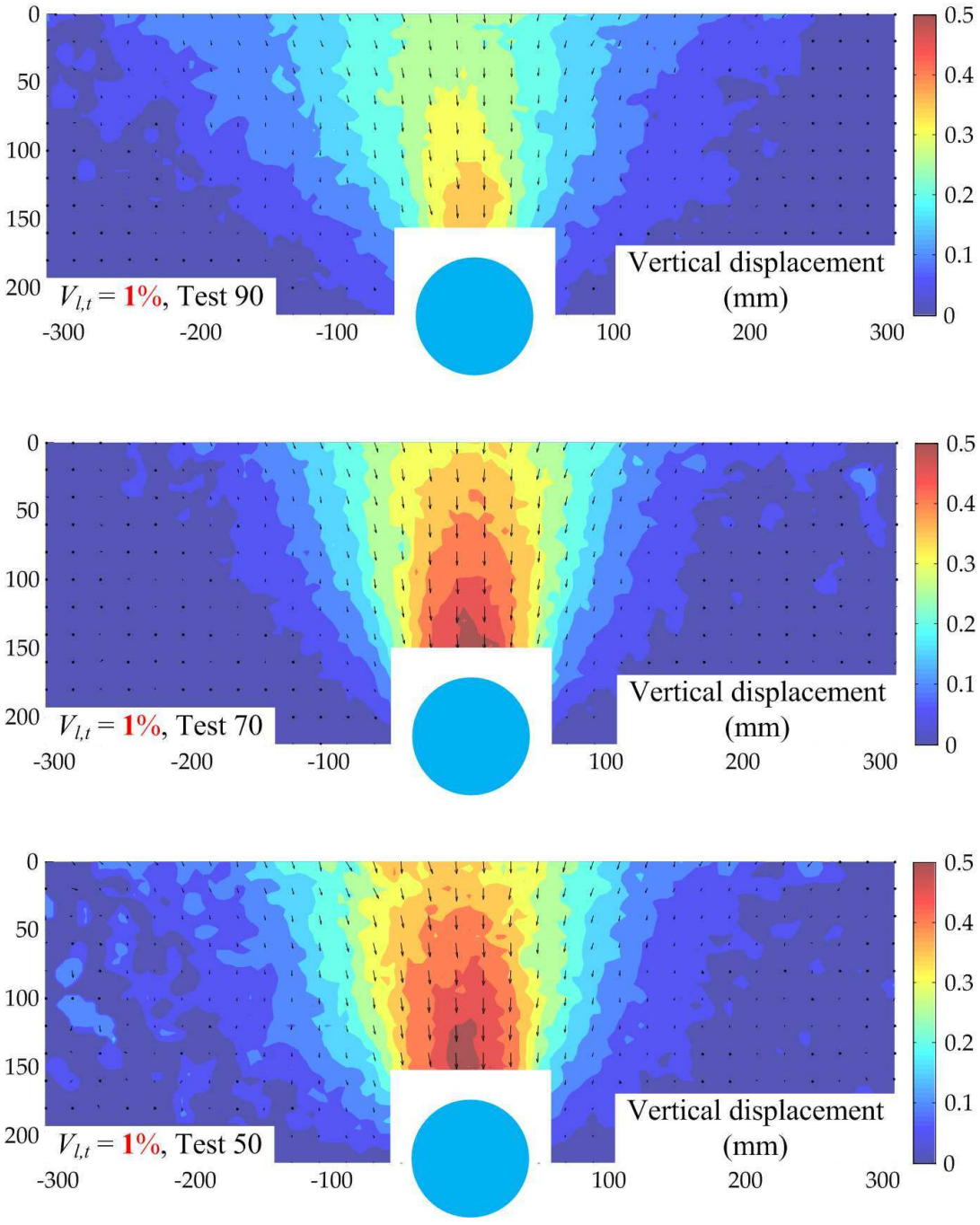

Figure 4.7: Vertical displacement contours - $V_{l,t}$ = 1%, Group 1

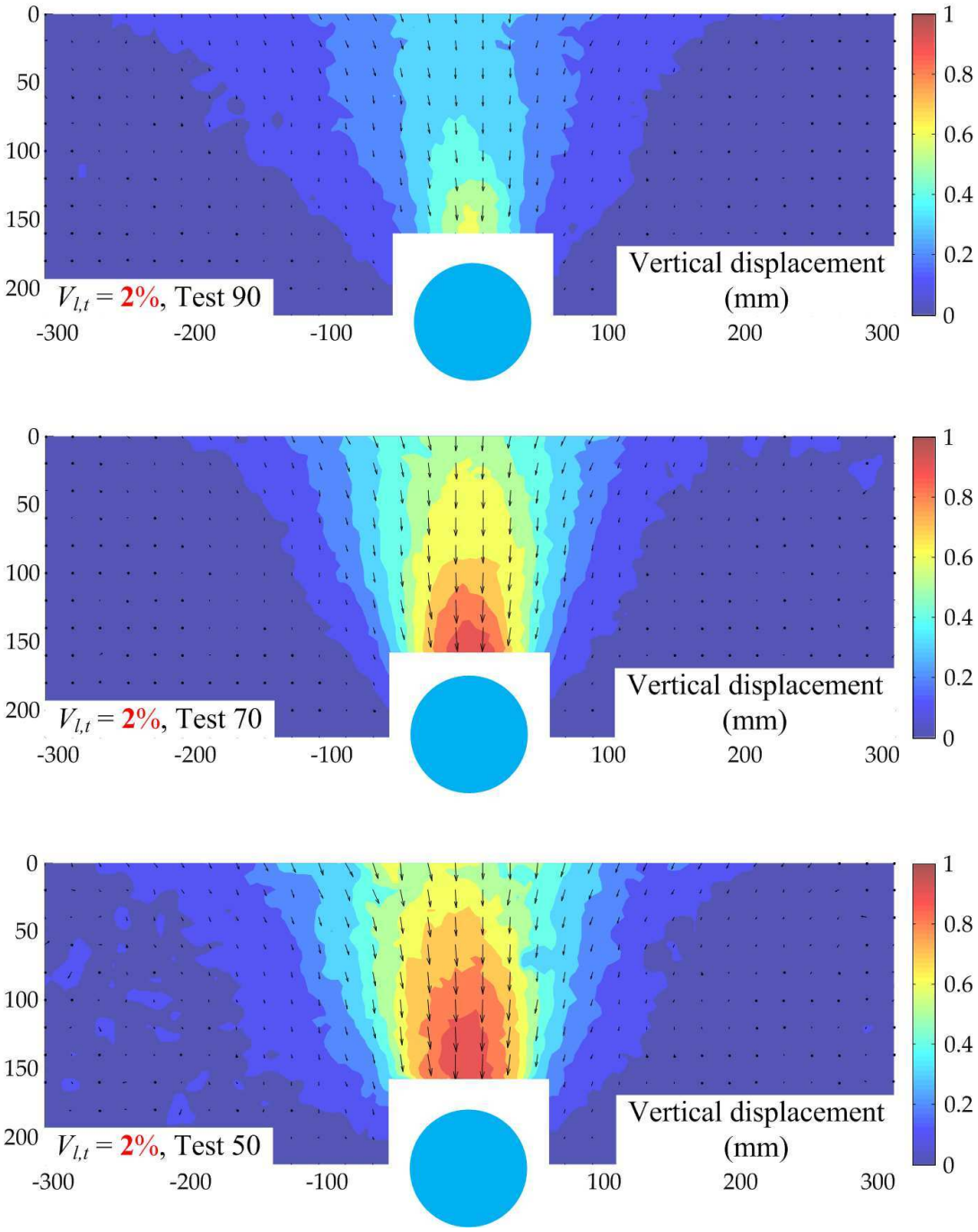

Figure 4.8: Vertical displacement contours - $V_{l,t} = 2\%$, Group 1

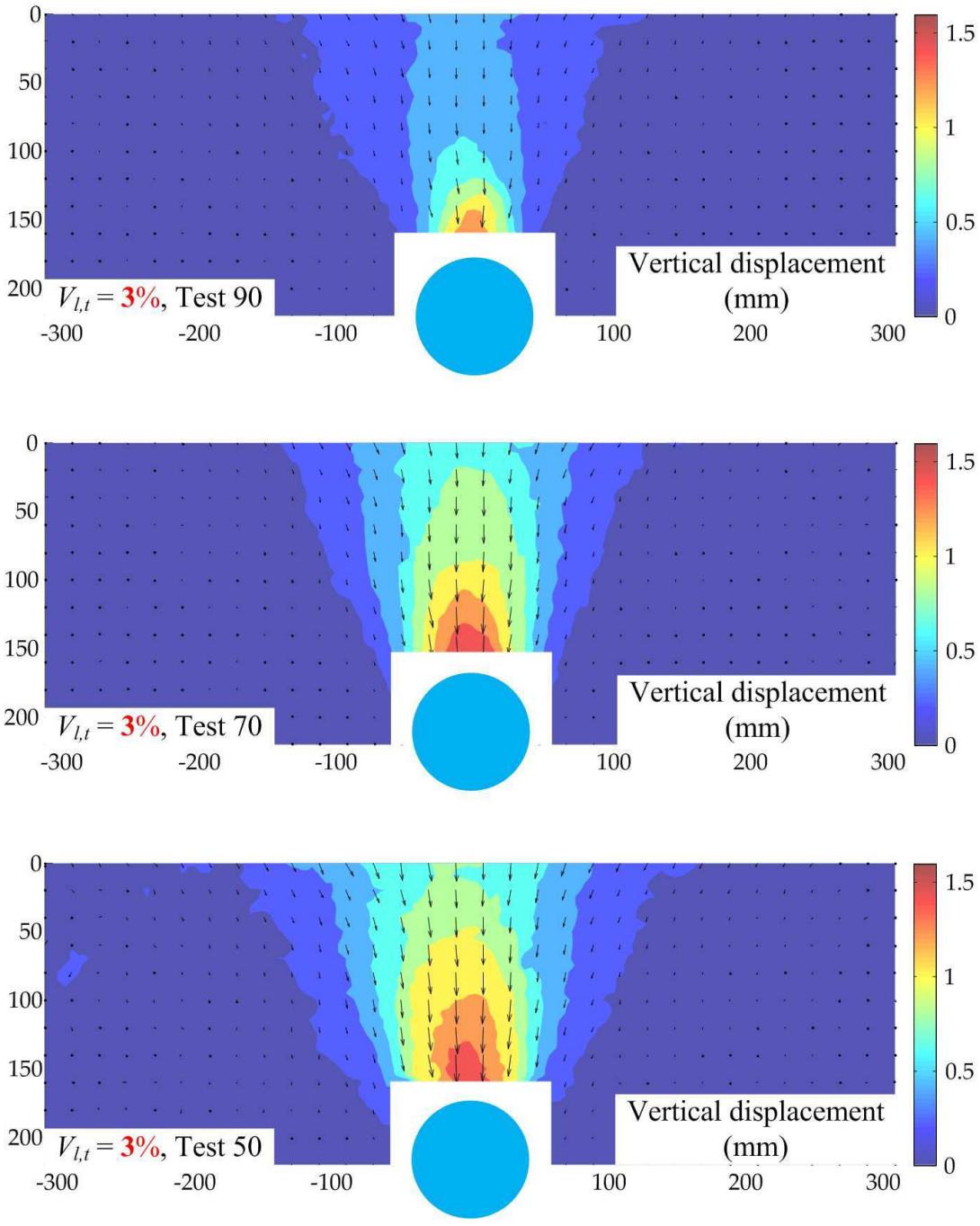

Figure 4.9: Vertical displacement contours - $V_{l,t}$ = 3%, Group 1

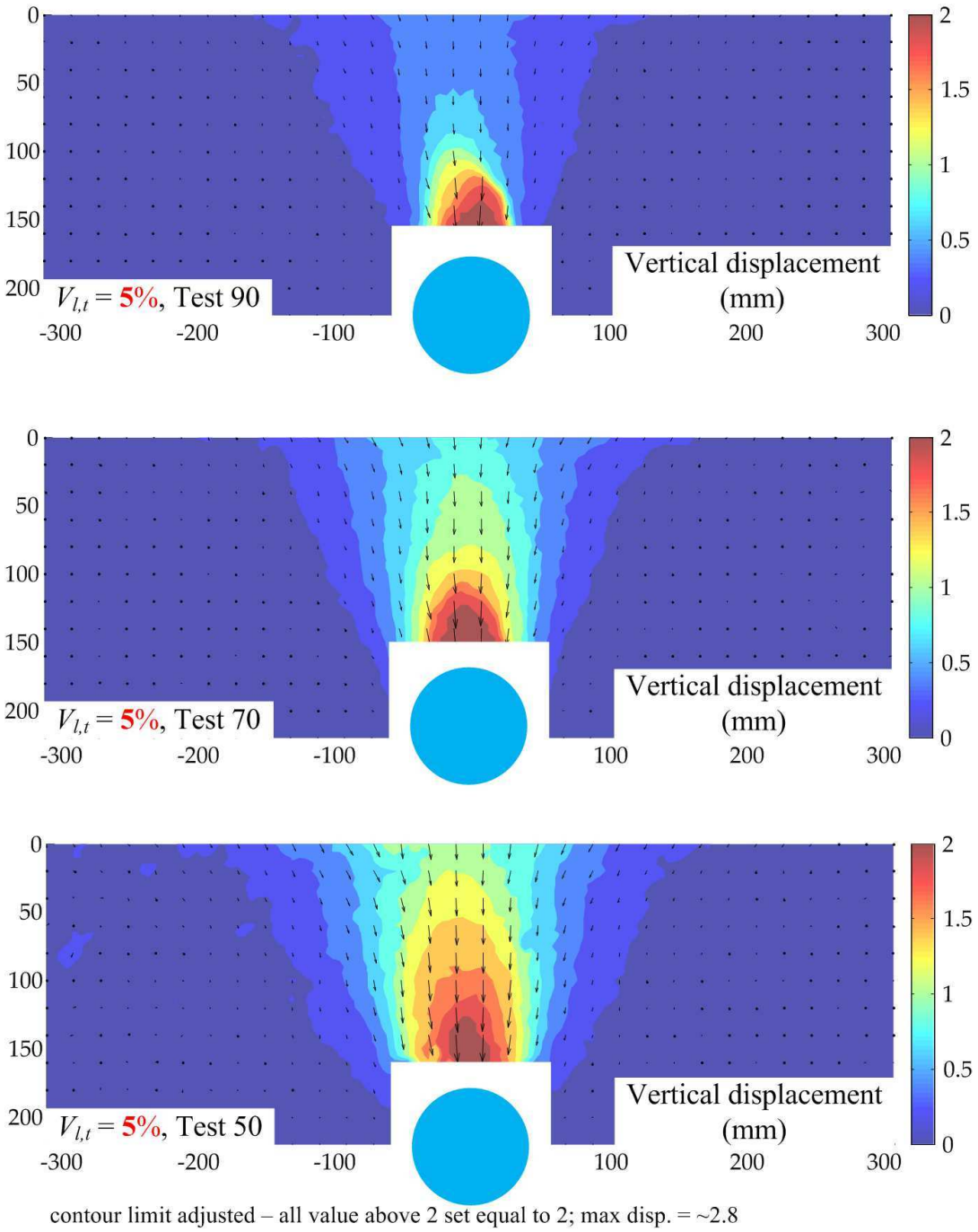

Figure 4.10: Vertical displacement contours - $V_{l,t} = 5\%$, Group 1

4.2.3.2 Horizontal soil displacements

Contours of horizontal displacements in Group 1 are presented in Figure 4.11-4.13 (p.94-96) for 1%, 3% and 5% tunnel volume loss in a similar fashion as that showed for the vertical displacements. The direction from left to right is positive in the contours. The soil displacements should theoretically be symmetrical in this model, but the real sand does not always behave as desired due to the natural variability. The magnitude of horizontal displacements is quite small and therefore the sand could not perform the symmetry in the contours accurately. The following observations are made from the three figures:

- All the horizontal movements are towards the model centreline. The magnitude of horizontal movements is much lower than that of vertical movements.
- The horizontal displacements are generally localised near the surface between ±50 to ±100mm offset and the tunnel shoulders.
- Similar to the vertical mechanisms, there is an increasing and narrowing of the horizontal displacements with volume loss in all the three tests.
- The magnitude of displacement is higher in looser sand in each stage of volume loss.
- At 1% volume loss (Figure 4.11, p.94), the horizontal displacements are mostly near the soil surface between ±50 to ±100mm offset in all the three tests (the trends at 2% volume loss are very similar to those at 1%).
- At 3% volume loss (Figure 4.12, p.95), the magnitude of horizontal displacements near the tunnel shoulders develops and is approximately equal to that near surface in Test 90. The shoulder displacements are slightly lower than the surface displacements in Test 70. But the major zones of horizontal displacements still occur near the surface in Test 50.
- At 5% volume loss (Figure 4.13, p.96), the horizontal displacements near the tunnel shoulders dominate in Test 90. The magnitudes of displacements

in the two zones (near surface and tunnel shoulders) are similar in Test 70. The major displacements localise near surface in Test 50 as before.

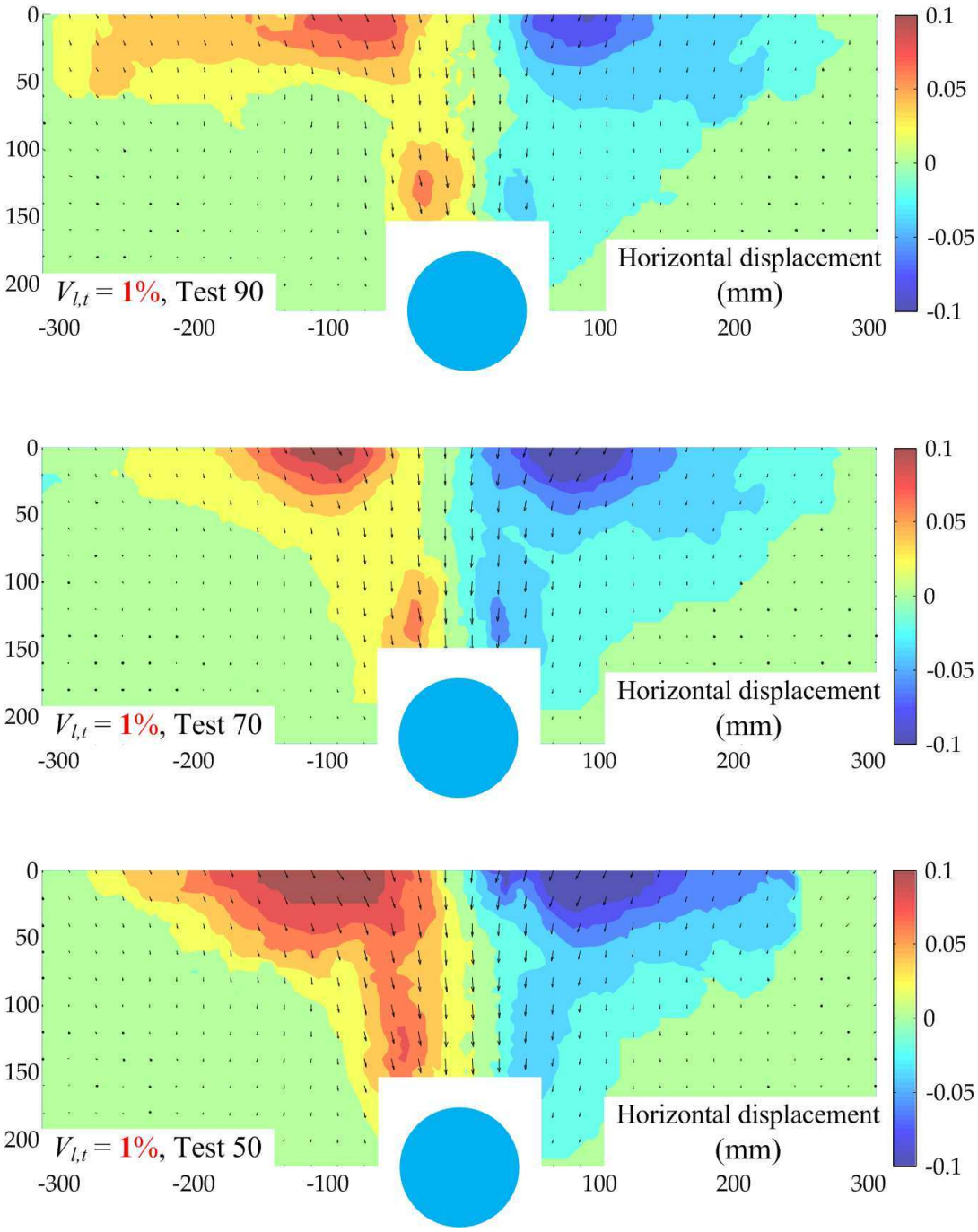

Figure 4.11: Horizontal displacement contours - $V_{l,t}$ = 1%, Group 1

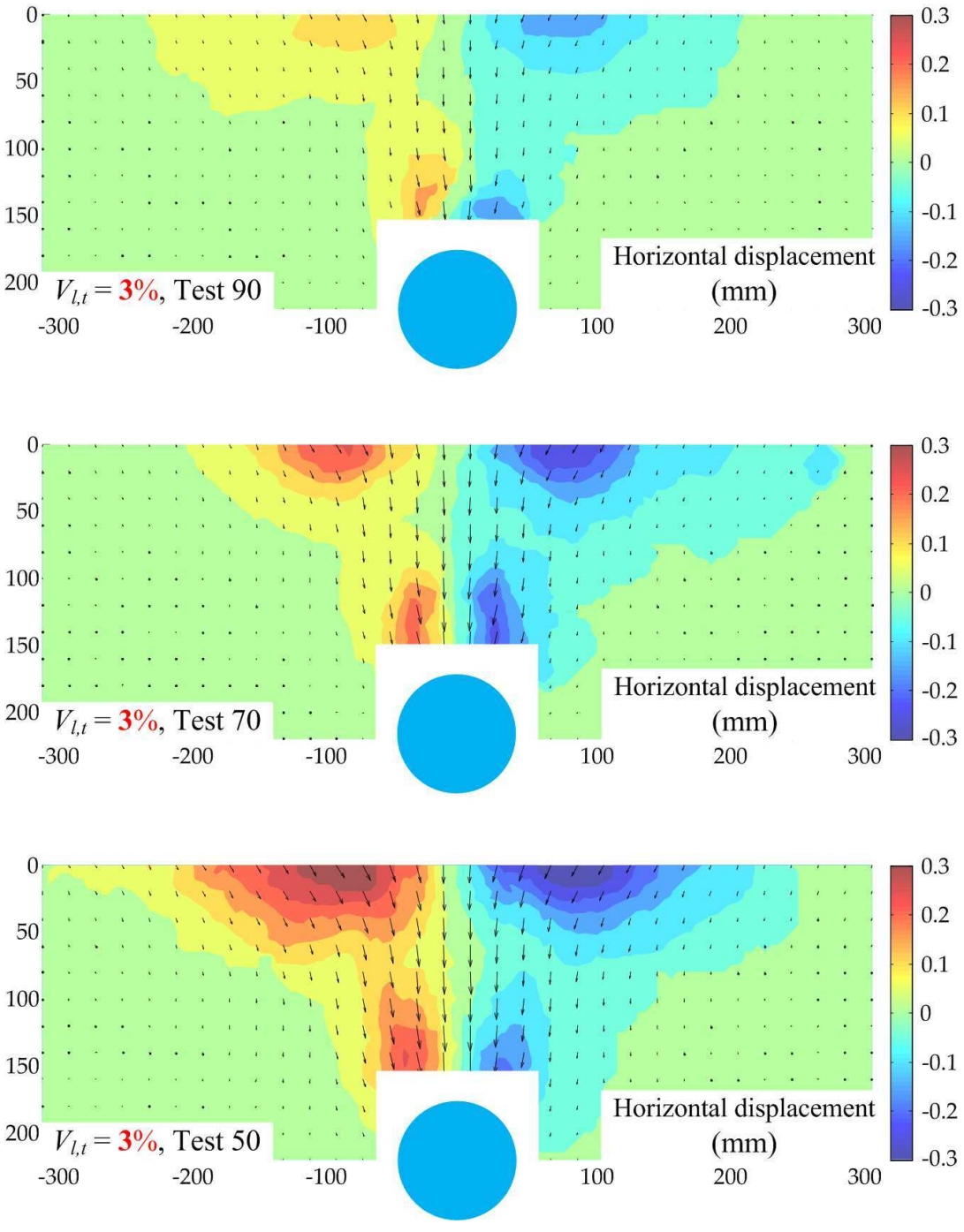

Figure 4.12: Horizontal displacement contours - $V_{l,t} = 3\%$, Group 1

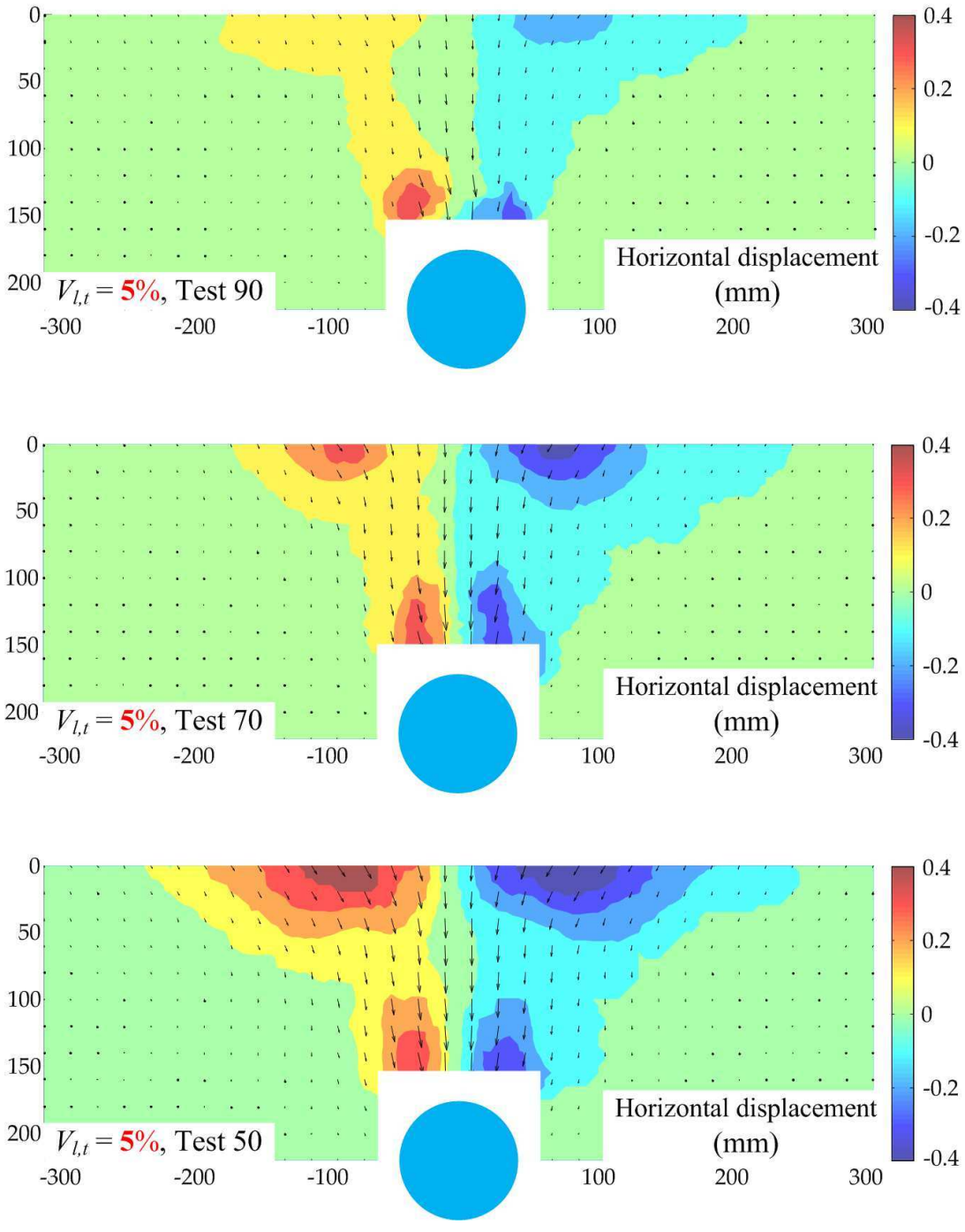

Figure 4.13: Horizontal displacement contours - $V_{l,t} = 5\%$, Group 1

4.2.4 Soil strains

This section presents the contours of volumetric strain and shear strain distributions within the soil behind the Perspex at each stage of volume loss. The PIV displacement data was used to calculate the strains. Some of the displacement vectors are again shown in the contours as a reference. As before, the scale of vectors varied with tunnel volume loss.

The Mohr circle of strain is shown in Figure 4.14, where ϵ_{xx} and ϵ_{zz} are axial strains in x and z directions, respectively, ϵ_{xz} is shear strain and γ is engineering shear strain. The data of soil displacements was input into a mechanics computation program, FLAC (ITASCA^{TM}), to calculate the stain data. The ϵ_{xx}, ϵ_{zz} and ϵ_{xz} were calculated using the meshing and calculation abilities of the program and determined volumetric strain and engineering shear strain, as presented in the subsequent sections.

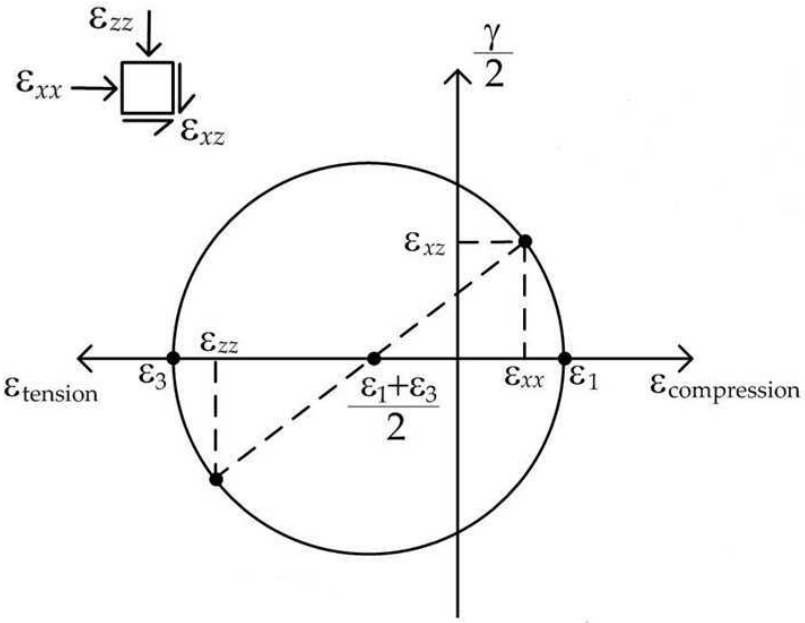

Figure 4.14: Mohr circle of strain

4.2.4.1 A comment on strain error

The values of strain are sensitive to errors in PIV data. Some of 'patches' in the following colour contours may be attributed to the errors but not real strain. These patches are associated with the level of scatter in the displacement data at the side of Perspex wall, far away from the cameras and lights. A large zone of soil strain exhibiting similar values in contours is less likely due to the errors and more likely to represent real strain. Consequently, statements on stain contours focus on large zones of strain exhibiting similar values.

The PIV displacement results were obtained from two cameras. The two image areas overlapped (Figure 3.3, p.38) so the PIV displacements data from the two cameras could be merged together. Merging together displacements data may result in some of 'thin strips' in the overlapped area in strain contours, as another type of error. Figure 4.15 compares the engineering shear strain (γ) contours calculated by merged data and half data (from one camera only). The contours are almost identical except several errors in the overlapped area.

The PIV technology needs control markers painted on the Perspex and used to calibrate and map image pixel movements into real displacements. The control markers shaded the soil behind it so the real displacement data there were lost. The lost displacement data was estimated by several nearest displacement data to obtain a complete PIV result and therefore the estimated values are similar to the nearest values. However, the strain is associated with the variation of displacements in soil (strain is zero if displacements are same everywhere, as a moving rigid body). As a result of similar displacement values, a row of control markers at 70 mm depth from soil surface caused a reduction of strains around that depth in the subsequent contours.

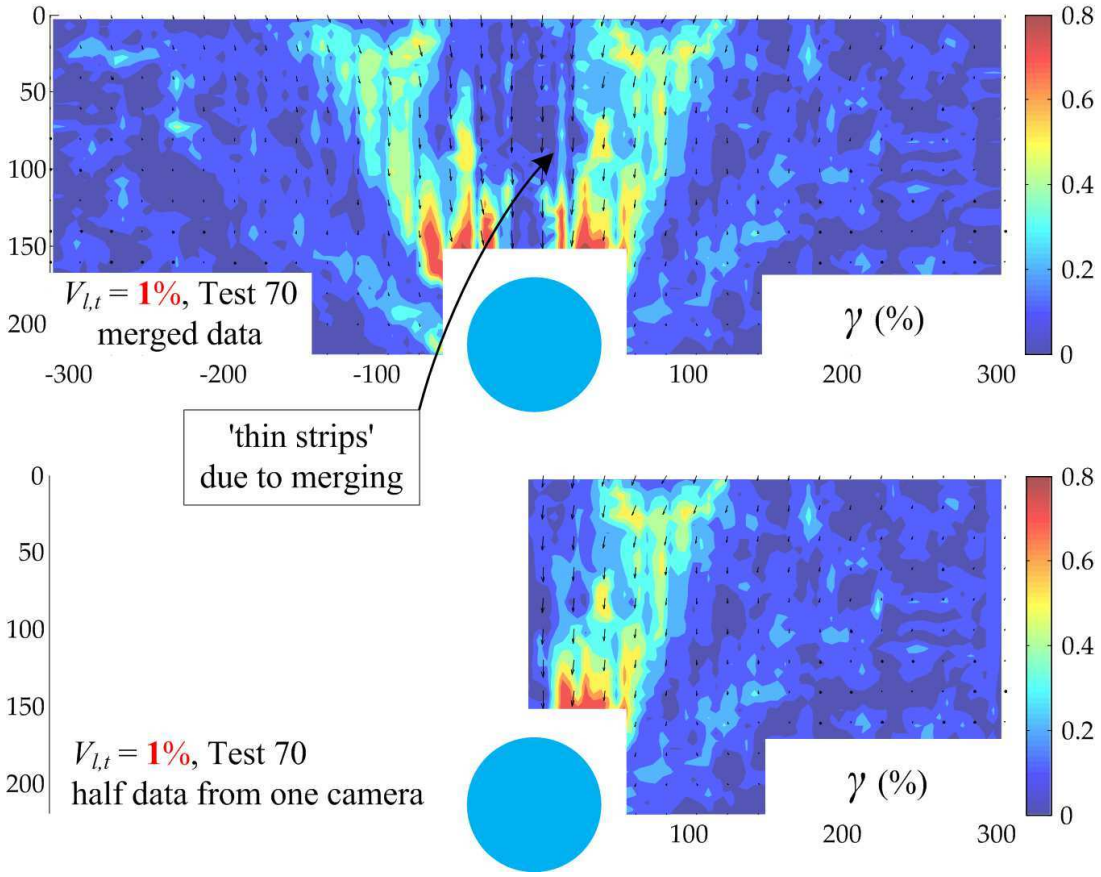

Figure 4.15: Shear strain contours from two (merged) cameras and one (right) camera only

4.2.4.2 Volumetric strain

Volumetric strain, ϵ_v, was

$$\epsilon_v = \epsilon_{xx} + \epsilon_{yy} + \epsilon_{zz} \tag{4.2}$$

where ϵ_{yy}, the strain parallel to the model tunnel, was assumed to be zero in this plane-strain model.

Figure 4.16-4.19 (p.102-105) show the volumetric strain in the soil for Group 1 at a tunnel volume loss of 1%, 2%, 3% and 5%. The PIV displacement vectors that

were used to calculate strains are also partially shown as a reference. The scale of colour bar of the contours is not constant in the figures for varying volume losses. The observations from the figures are summarised as below:

- Generally, the dilation zones in sand are above the tunnel crown and the contraction zones are above the tunnel shoulders (two sides of tunnel).
- At low volume loss of 1% (Figure 4.16, p.102), there is no significant difference in the ϵ_v contours for all the three tests. The volumetric contraction concentrated at two troughs, a narrow one and a wide one, which are indicated by white dash lines. All the troughs extend from the tunnel to the soil surface with decreasing magnitudes of contraction. The distance between two troughs (one narrow and one wide) are wider in denser sand (with higher relative density). The next section will show that these contraction troughs are associated with the shear bands developing within the soil. The dilation in the chimney zone above the tunnel is small and scattered. The average values of volumetric strain in these zones are about 0.1% in all the three tests. This observation relates well to that made in Section 4.2.3.1 (p.86) regarding that the soil above the tunnel moves downwards as a almost rigid body in a chimney like shape.
- At medium volume loss of 2% (Figure 4.17, p.103), the contraction troughs are wider and more evident in all the three tests. The size and magnitude of contraction zones in looser sand (with lower relative density) are obviously greater. Large dilation is observed and the distributions of dilation zones are different in the three tests. In dense and medium sand, large dilation is localised above the tunnel crown, but in loose sand, dilation zone extends from the tunnel crown towards the surface with similar magnitudes (note that the strain reduction around 70 mm depth probably is attributed to the control markers there). The different distribution of dilation zones in Test 50 could be associated with the larger contraction in loose sand. Presumably the large contraction in the troughs at two sides leads to the soil at centre 'extending' towards the troughs and causes dilation. The last two strain profiles in Figure 4.17 compare the horizontal strain, ϵ_{xx}, in dense

and loose sand. ϵ_{xx} near surface in loose sand, as an horizontal 'extension', was significantly higher than that in dense sand, which partly support the presume.

- At high volume loss of 3% (Figure 4.18, p.104), the magnitude of contraction is lower than that of dilation in dense sand and there is not much development of contraction troughs except those near tunnel shoulders. In medium sand, the magnitude of contraction in the wide trough stopped growing but that in the narrow trough increased (note strain reduction around 70 mm depth due to control markers). In loose sand, the contraction troughs kept developing. The magnitude of dilation have grown obviously in all the three test and the distribution of dilation zones is constant in each test.

- At extremely high volume loss of 5% (Figure 4.19, p.105), the trends are very similar to those at 3%. The distance between two troughs are narrower in looser sand from 1% to 5% volume loss.

- The cover to tunnel diameter ratio (C/D) is 2.0 for this centrifuge model. The volumetric deformations observed in this research are more similar to Case B in Figure 2.19 (p.32).

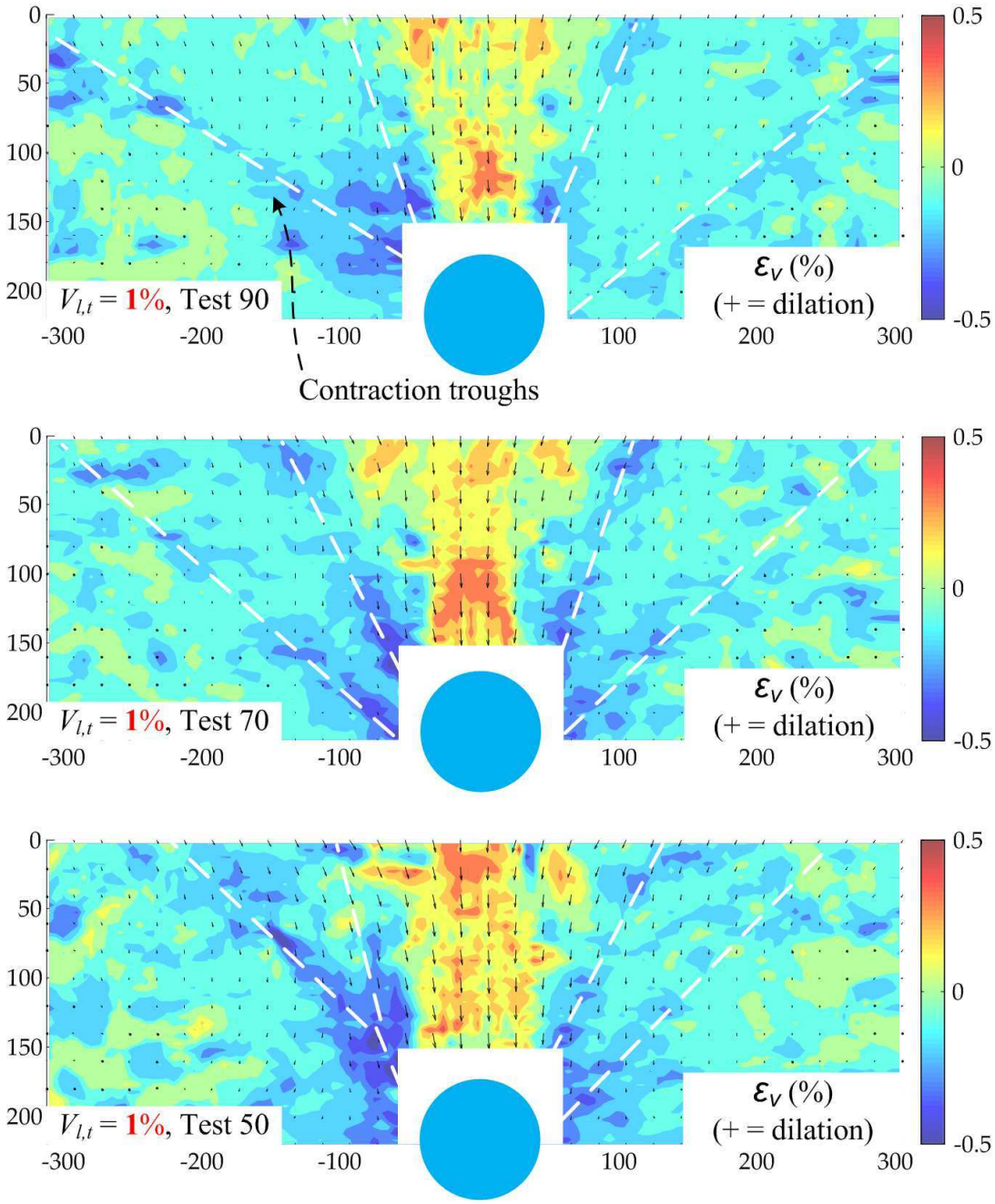

Figure 4.16: Volumetric strain - $V_{l,t}$ = 1%, Group 1

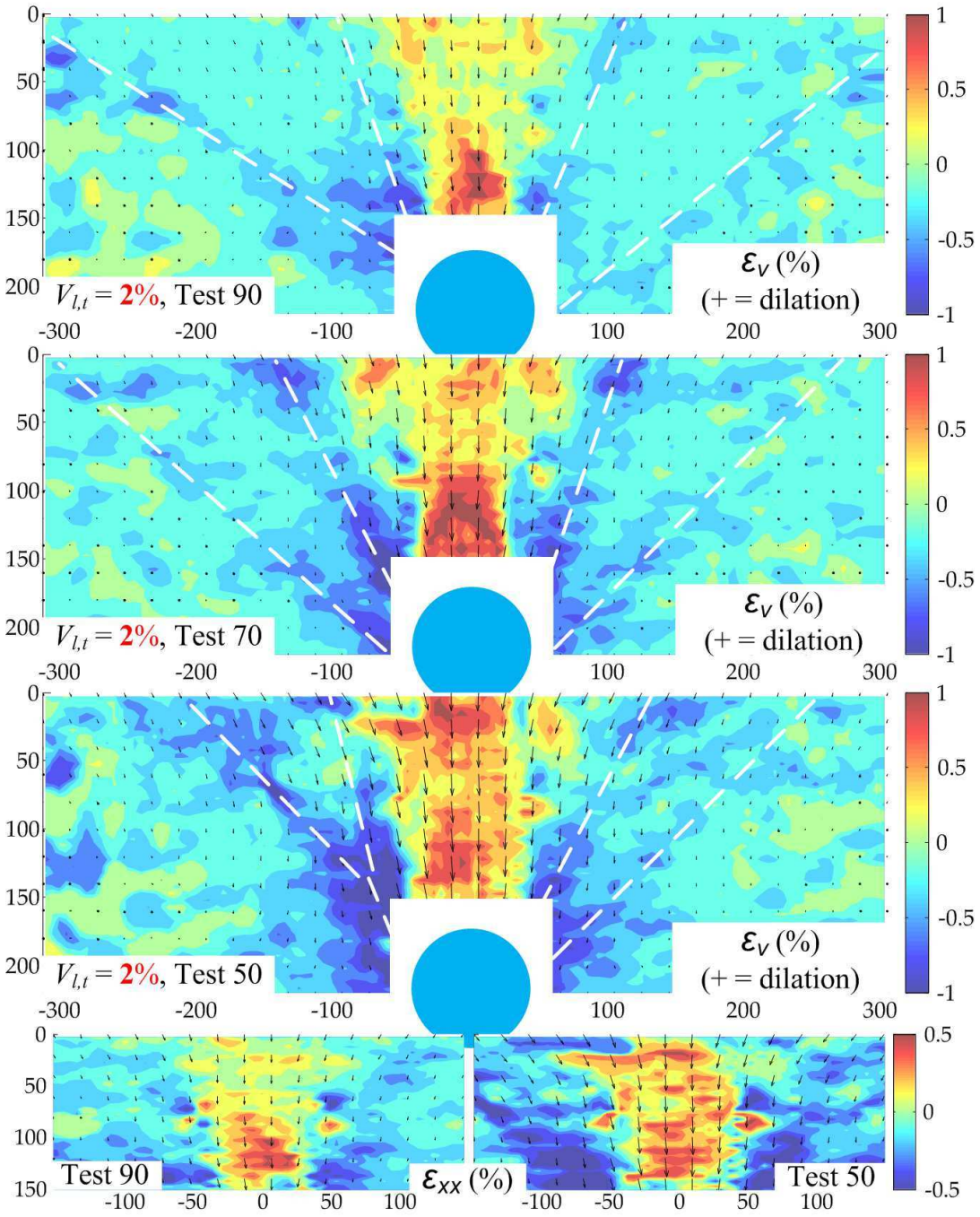

Figure 4.17: Volumetric strain - $V_{l,t}$ = 2%, Group 1

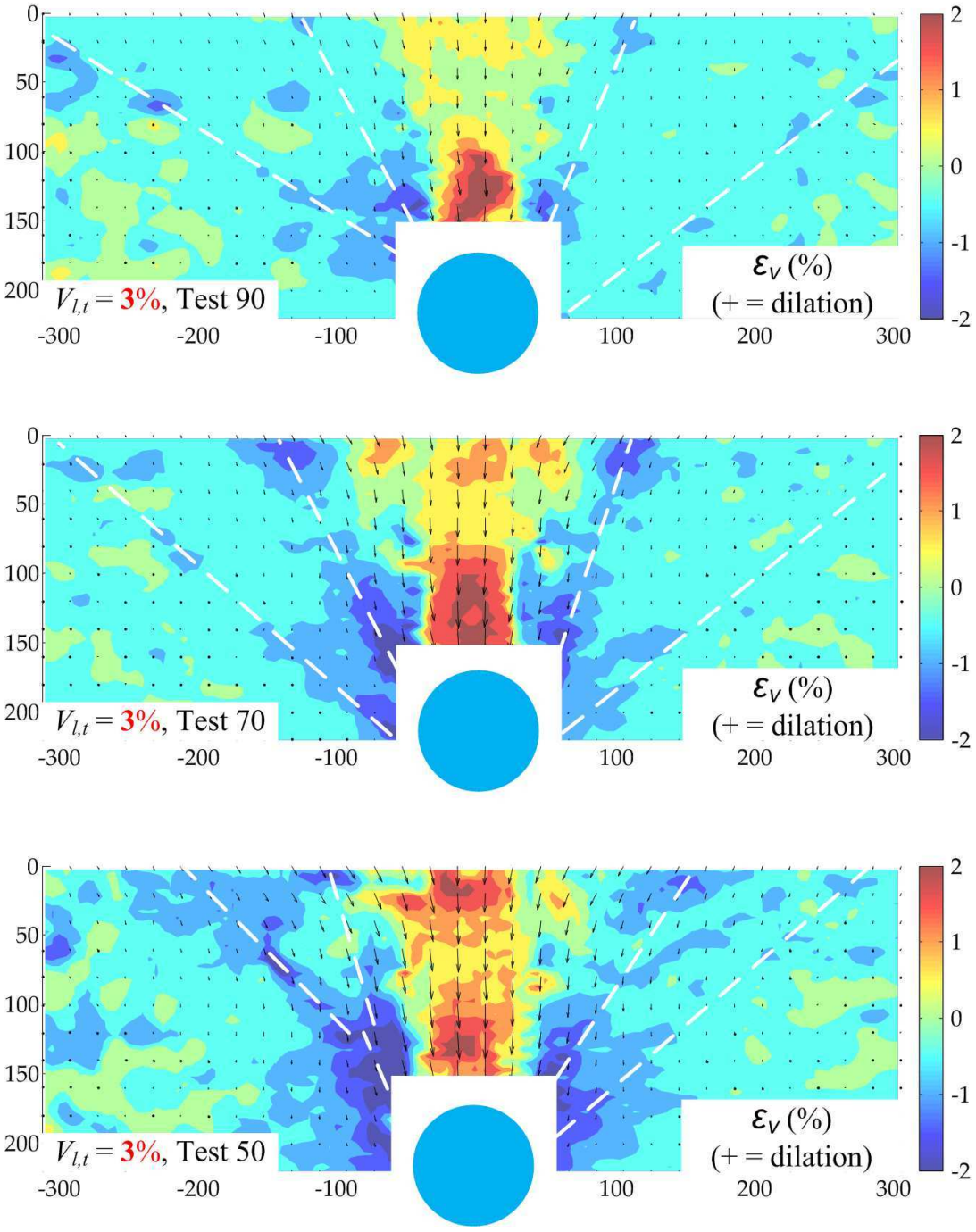

Figure 4.18: Volumetric strain - $V_{l,t} = 3\%$, Group 1

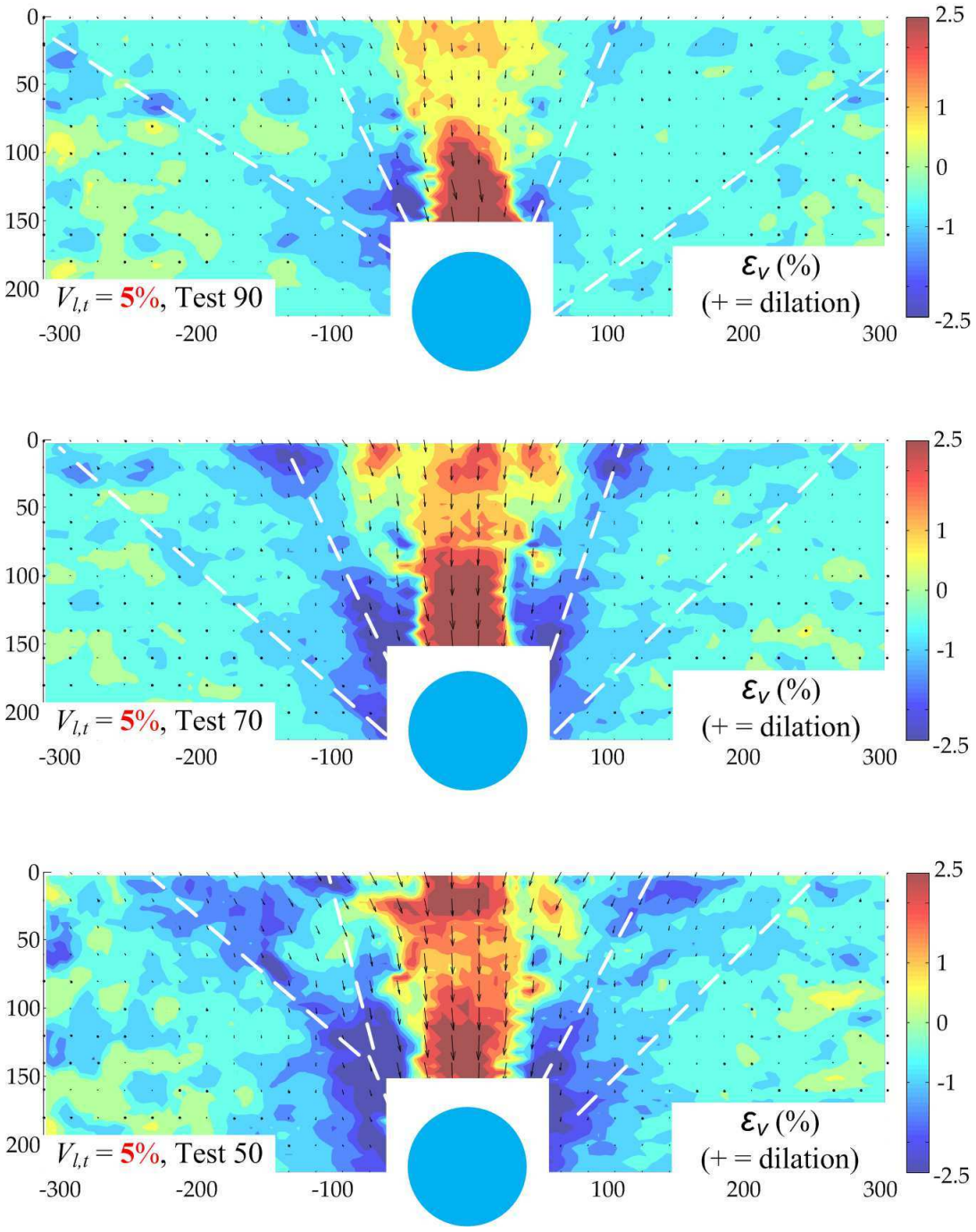

Figure 4.19: Volumetric strain - $V_{l,t} = 5\%$, Group 1

4.2.4.3 Shear strain

The volumetric strain contours in Section 4.2.4.2, p.99 gave useful information regarding soil volumetric change with different relative densities and volume losses. Additionally, it is useful to look at the shear strains for a better understanding of the mechanism and effect of relative density.

Engineering shear strain, γ, can be calculated by

$$\gamma = \sqrt{(\epsilon_{xx} - \epsilon_{zz})^2 + (2\epsilon_{xz})^2} \tag{4.3}$$

on plane-strain conditions. The term 'shear strain' implies engineering shear strain in this discussion.

Figure 4.20-4.23 (p.108-111) show the shear strain within the soil for Group 1 at a tunnel volume loss of 1%, 2%, 3% and 5%. The observations from the figures are summarised as below:

- Generally, the large shear strain zones in sand are above the tunnel shoulders (two sides of tunnel).
- At low volume loss of 1% (Figure 4.20, p.108), there is no significant difference in the shear strain profiles for all the three tests. The profiles at 1% agree well with the volumetric strain profiles (Figure 4.16, p.102). Again, two sets of shear bands in each test are visible; one narrow and one wide (indicated by white dash lines). The main shear bands extend near-vertically from the tunnel shoulders towards the soil surface. The distance between two sets of shear bands are wider in denser sand (with higher relative density). This data relates well to the idea that the soil above the tunnel moves downwards as a almost rigid body in a chimney like shape, creating the near-vertical shear bands.
- At medium volume loss of 2% (Figure 4.21, p.109), the shear bands are wider and more evident in all the three tests. The shear bands extend

from the tunnel to the soil surface with decreasing values of shear strain. Large shear strain is localised above the tunnel shoulders, witch is associated with the localisation of large vertical displacements above tunnel crown (Figure 4.8, p.89). The size and magnitude of shear zones in looser sand (with lower relative density) are obviously greater, relating to larger settlements in looser sand.

- At high volume loss of 3% (Figure 4.22, p.110), there is not much development of shear bands in dense sand except those near tunnel shoulders. In medium sand, the magnitude of main shear bands (near centre) increased but that of shear bands at two sides stopped growing. In dense sand, the shear bands kept developing (note the different scales of colour bars).

- At extremely high volume loss of 5% (Figure 4.23, p.111), the trends of γ development are very similar to those at 3%. The large shearing zone above the tunnel indicates the growth of soil failure. The size and magnitude of shear bands in looser sand are again noted to be larger.

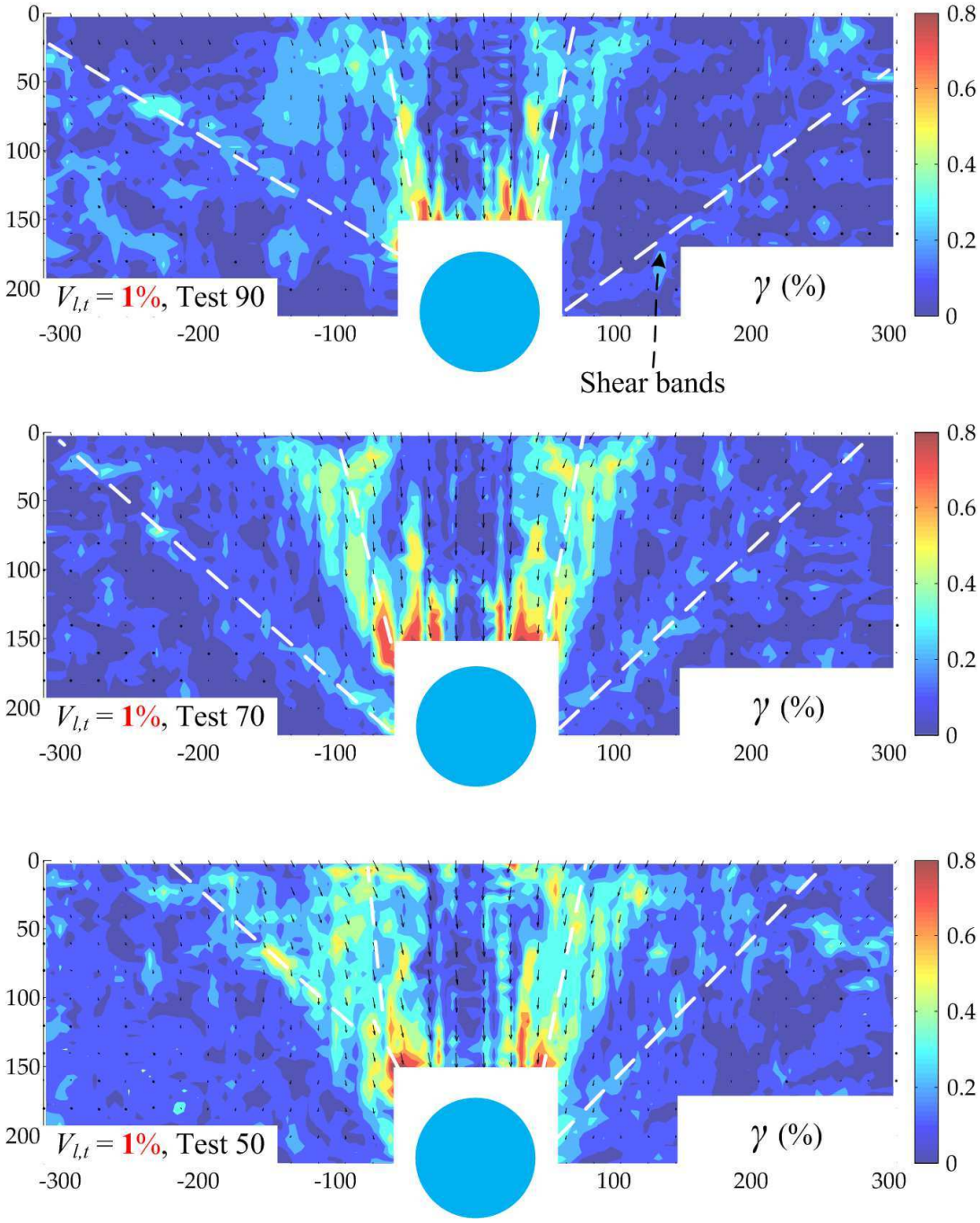

Figure 4.20: Engineering shear strain - $V_{l,t} = 1\%$, Group 1

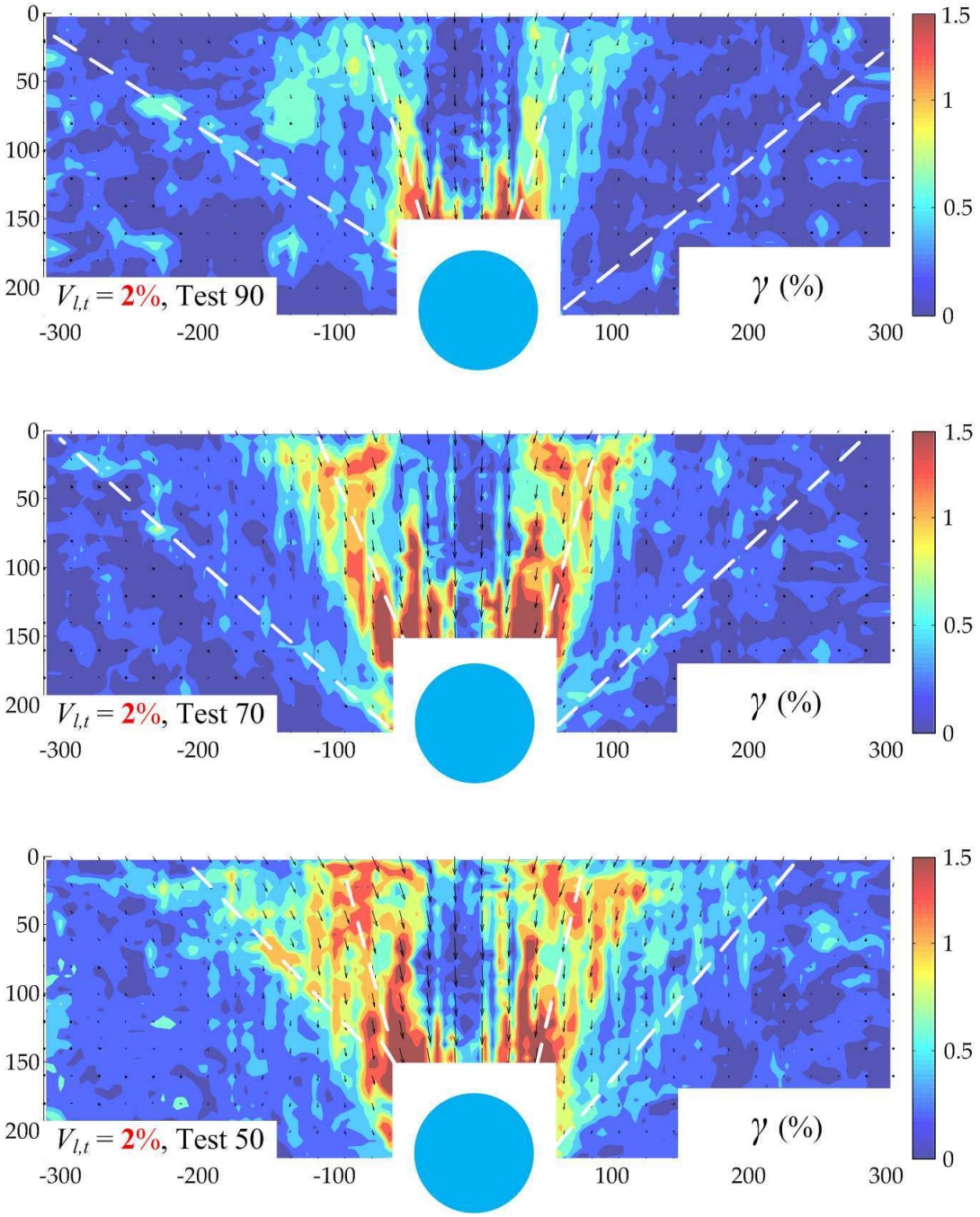

Figure 4.21: Engineering shear strain - $V_{l,t} = 2\%$, Group 1

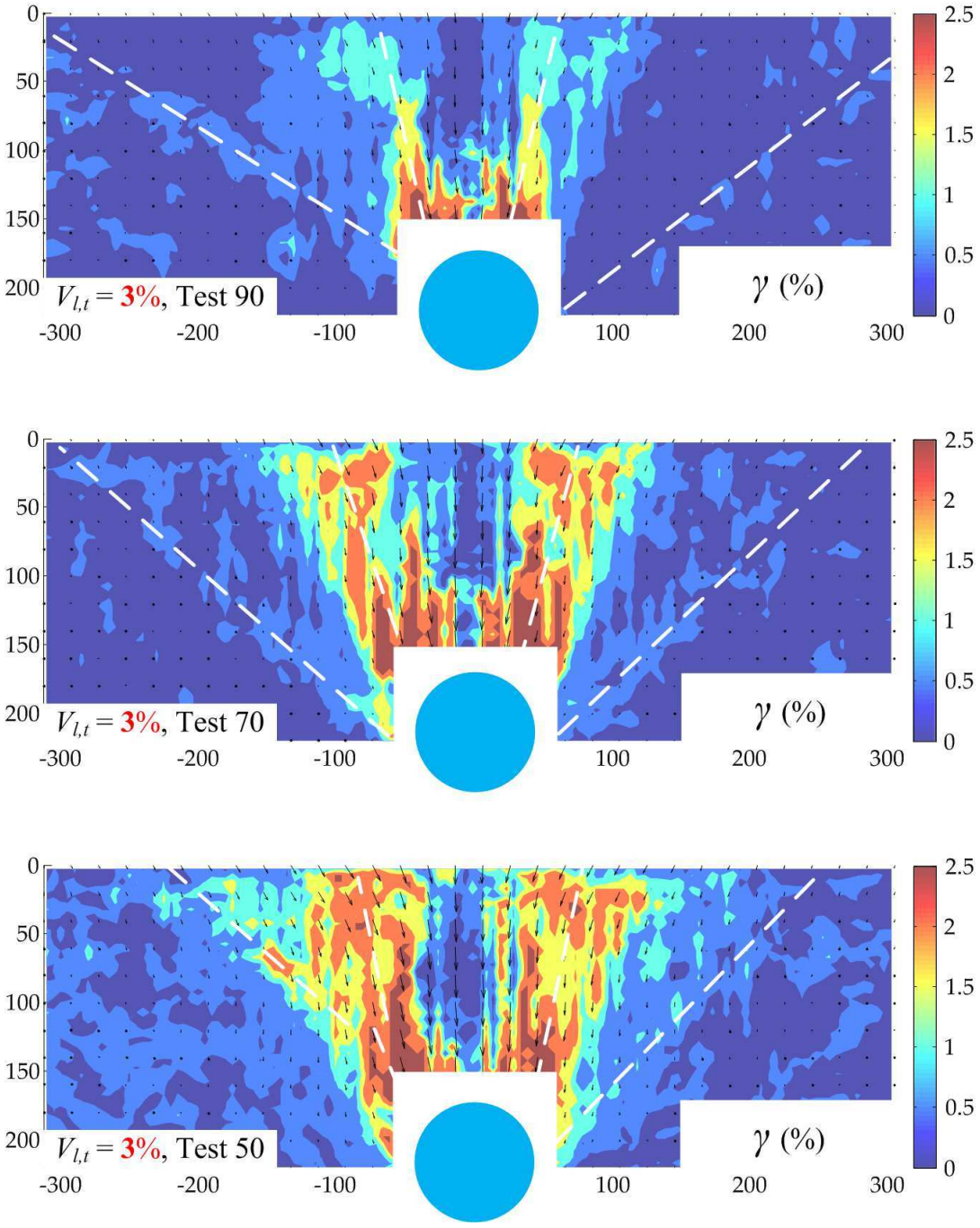

Figure 4.22: Engineering shear strain - $V_{l,t} = 3\%$, Group 1

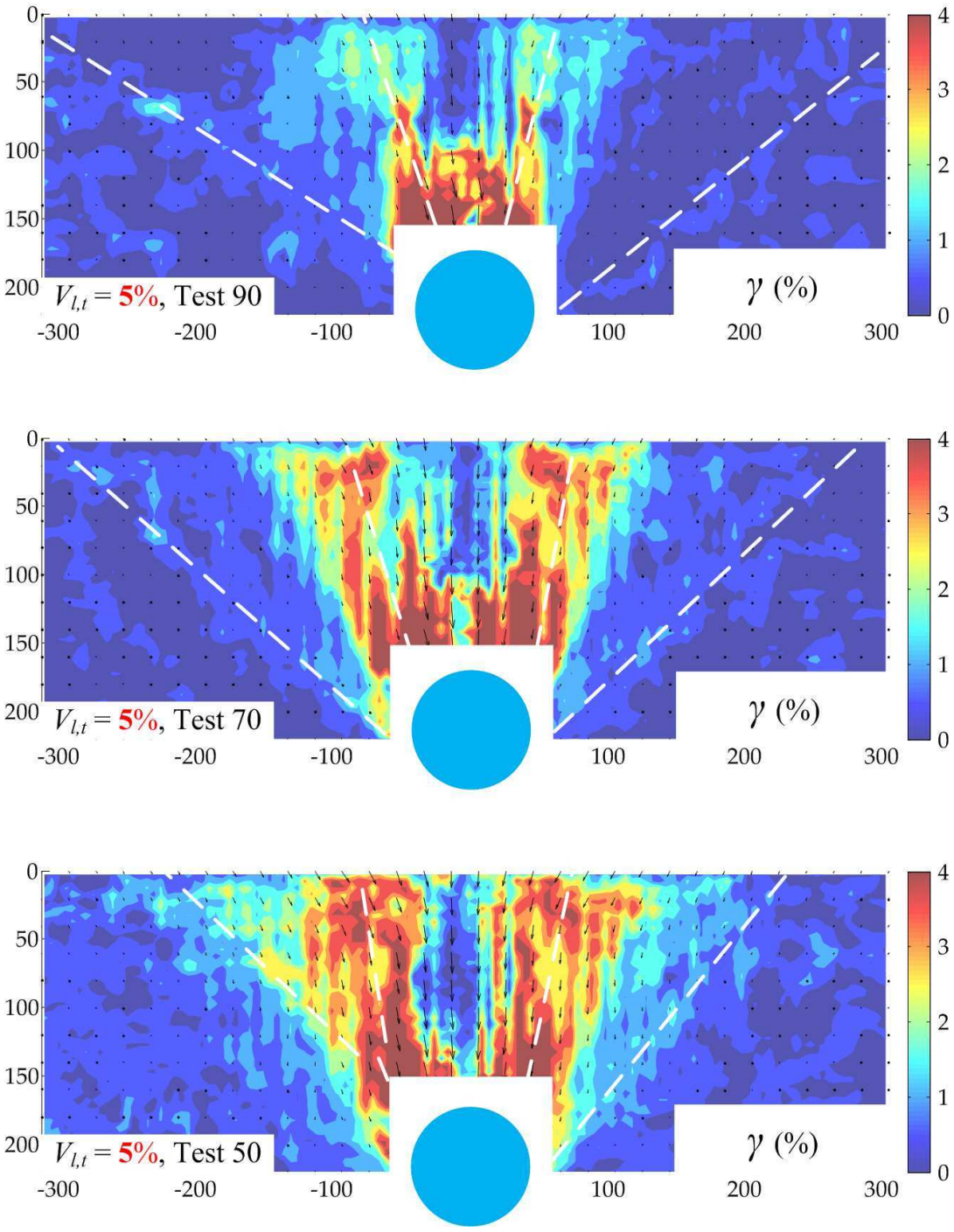

Figure 4.23: Engineering shear strain - $V_{l,t} = 5\%$, Group 1

4.2.5 Settlement trough profiles

Figure 4.24 shows the surface settlement trough profiles for the three tests at a volume loss of 1, 3, and 5%. The labels, '90', '70' and '50' means Test 90, Test 70 and Test 50, respectively. The magnitude of settlement increases with an decrease of relative density and the major settlements are mostly in the area between ± 100 mm offset from tunnel centreline, which relates well to the displacement contours. The settlement data was fitted by Gaussian curve and modified Gaussian curve for further analysis in Section 4.3 (p.116).

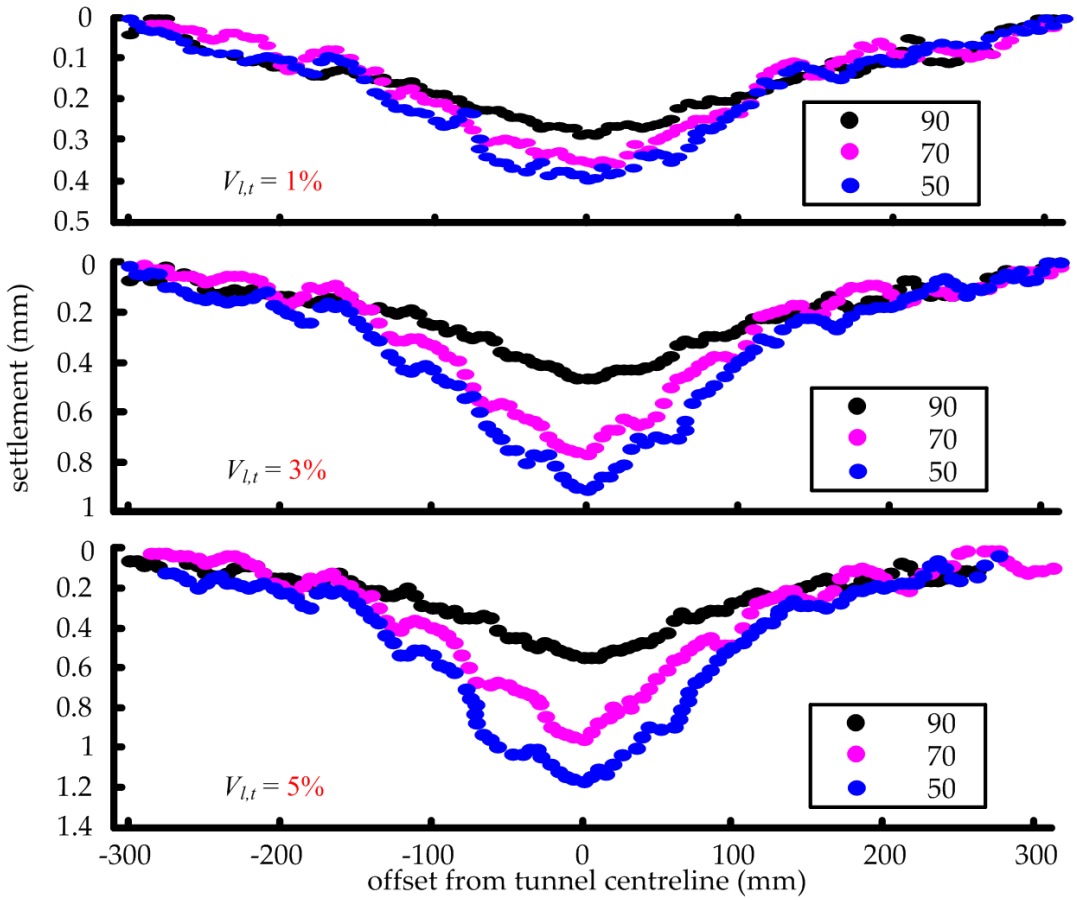

Figure 4.24: Settlement trough profiles for Group 1

4.2.6 Tunnel deformation

The deformation (contraction) of tunnel at the crown and sides was monitored by cantilever steel strips with strain gauges (Figure 3.8, p.46). Figure 4.25 presents the tunnel deformation at crown and side (average value) during the tests. The displacements increase almost linearly with the tunnel volume loss. The displacement at crown is larger in denser sand but that at side is greater in looser sand.

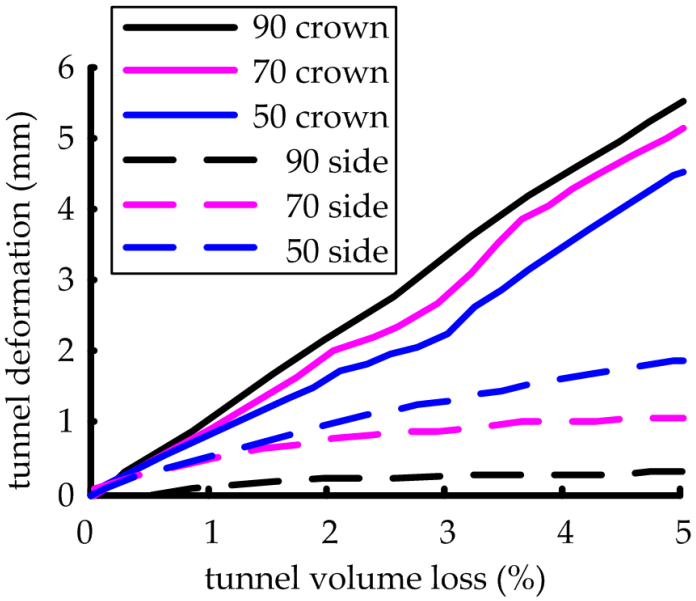

Figure 4.25: Tunnel deformation at crown and side - Group 1

Figure 4.26 compares the ratio of displacement at crown to side in Group 1. The ratio is relative constant with tunnel volume loss and significantly higher in dense sand so that the tunnel deformation is localised at crown in dense sand.

The tunnel deformation is generally considered as the sum of several fundamental components: a uniform radial displacement, an ovalisation of the tunnel and a downward uniform movement (mentioned in Section 2.2.5, p.19). A downward ellipse (Figure 4.27) is used to describe the deformed tunnel shape and fitted to the displacement data at tunnel wall. In Figure 4.27, c is the displacement measured at model tunnel crown and s is the average displacement at sides.

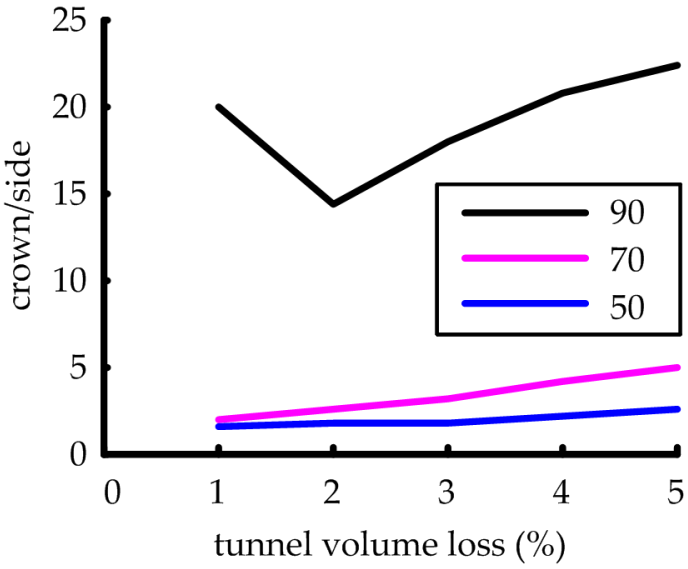

Figure 4.26: Ratio of displacement at crown to side - Group 1

Because the weight of the tunnel boring machines and installed lining forces the tunnel to settle to the bottom of the excavated cavity, the displacement at bottom (d) is assumed to be micro.

The equation of ellipse in Figure 4.27 is

$$\begin{aligned} x^2/a^2 + (y + c/2)^2/b^2 &= 1 \\ a &= (r - s)/\sqrt{1 - c^2/(2r - c)^2} \\ b &= 45 - c/2 \\ Area &= \pi ab \\ V_{l,t}[\%] &= [1 - Area/(\pi r^2)] \cdot 100 \end{aligned} \tag{4.4}$$

where r is the original radius of model tunnel, 45 mm.

The tunnel volume loss estimated by the ellipse model is compared to the volume loss measured in the tests (by volume of water extraction) in Figure 4.28. The model overestimates the tunnel volume loss to some extent.

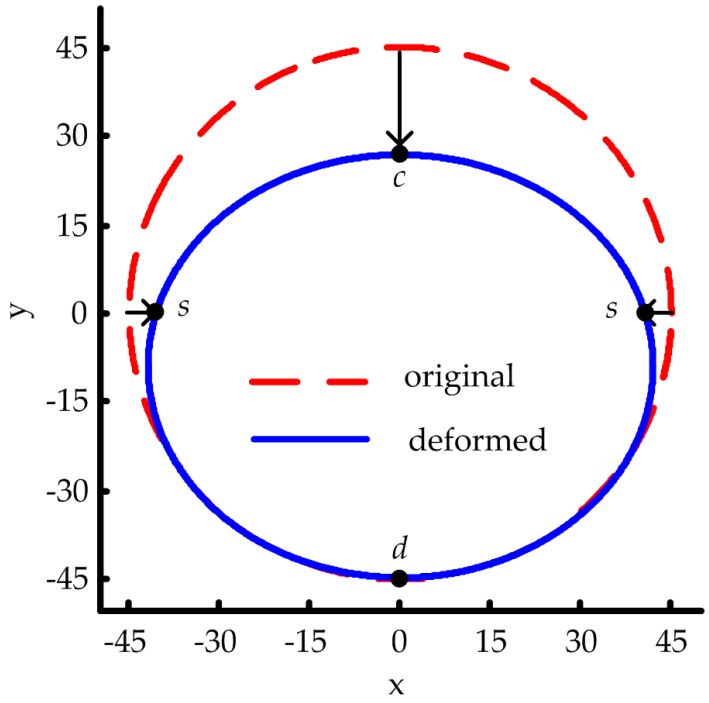

Figure 4.27: Model of deformed tunnel shape

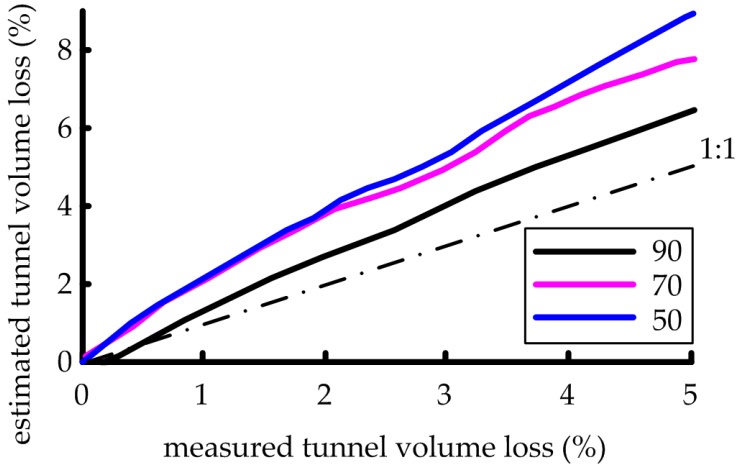

Figure 4.28: Comparison of estimated and measured tunnel volume loss

The overestimation probably is a result of that the deformation gauge 'stuck' into sand a bit due to its elasticity (Figure 4.29). The further research could use soft and light-weight material instead of spring steal.

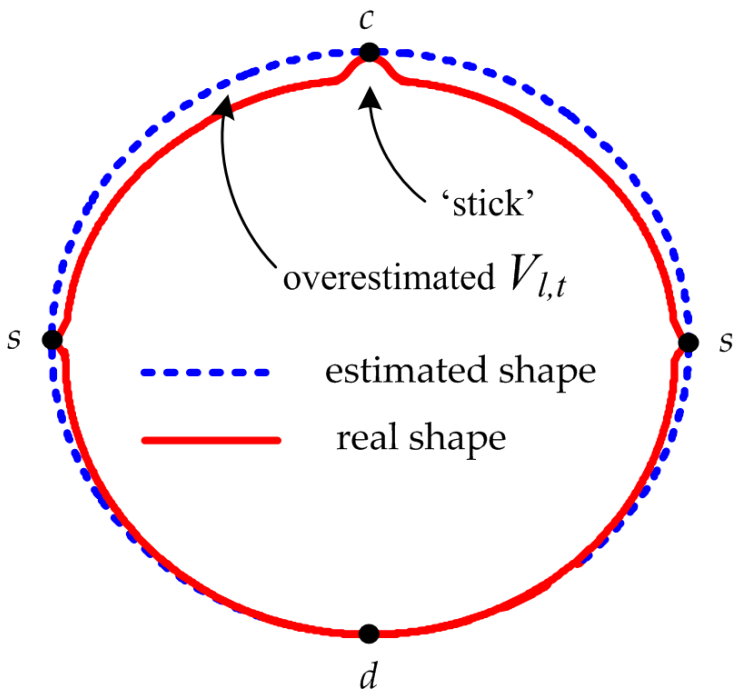

Figure 4.29: Overestimated tunnel volume loss

Additionally, the deviation (overestimation) may partly be attributed to the natural variability of soil behaviour (irregularly deformed tunnel shape) and the electrical noisy in the centrifuge signal system. Because the strain gauge is quite sensitive, the output signal from strain gauge is susceptible to electrical noisy.

4.3 Analysis and discussion of results

A further analysis and discussion are provided by this section for centrifuge Test 90, 70 and 50. The presented results in Section 4.2 (p.79) showed the differences of soil movements in the three tests. At low volume loss of 1%, two main shear bands extend near-vertically from the tunnel shoulders towards the soil surface and the chimney-shaped zone between shear bands does not show large volumetric change. Soil above model tunnel moves vertically downwards as a rigid body in all the three tests. At higher volume losses, the greater volumetric deformation

in medium (70) and loose (50) sand causes higher magnitude of settlements than that in dense (90) sand. The soil displacements in loose sands become larger than that in medium sand after 3% volume loss.

4.3.1 Fitting curves to settlement trough data

In order to analyse and compare the settlement trough shape, and for the evaluation of the effect of tunnelling on buildings and other infrastructure, it is useful to fit a curve to settlement data. The transverse settlement trough is generally described as a Gaussian distribution curve (Equation 2.1, p.7) with two degrees of freedom. Using the Gaussian curve, the settlement trough can be defined by the two variables S_{max} and i (inflexion point). To obtain a better fit to settlements in sands, a modified Gaussian curve (Equation 2.3, p.8) was suggested by Vorster et al. [2005], with an additional variable, α (n is a function of α). The modified Gaussian curve provides an additional degree of freedom compared to the Gaussian curve, which makes it more versatile for fitting to settlement data, however it adds the complexity of another unknown variable. The curves were fitted by Matlab© using a least squares regression technique.

Figure 4.30 shows examples of the Gaussian and modified Gaussian curves fitted to the surface settlement data at 3% volume loss for the three centrifuge tests. 'G' in the figure labels means Gaussian distribution curve and 'mG' means modified Gaussian curve. The evaluation of quality of fit is based on the coefficient of determination, R^2 (values closer to 1 indicate a better fit). The value of i is noted to be less for the modified Gaussian curve compared to the Gaussian curve.

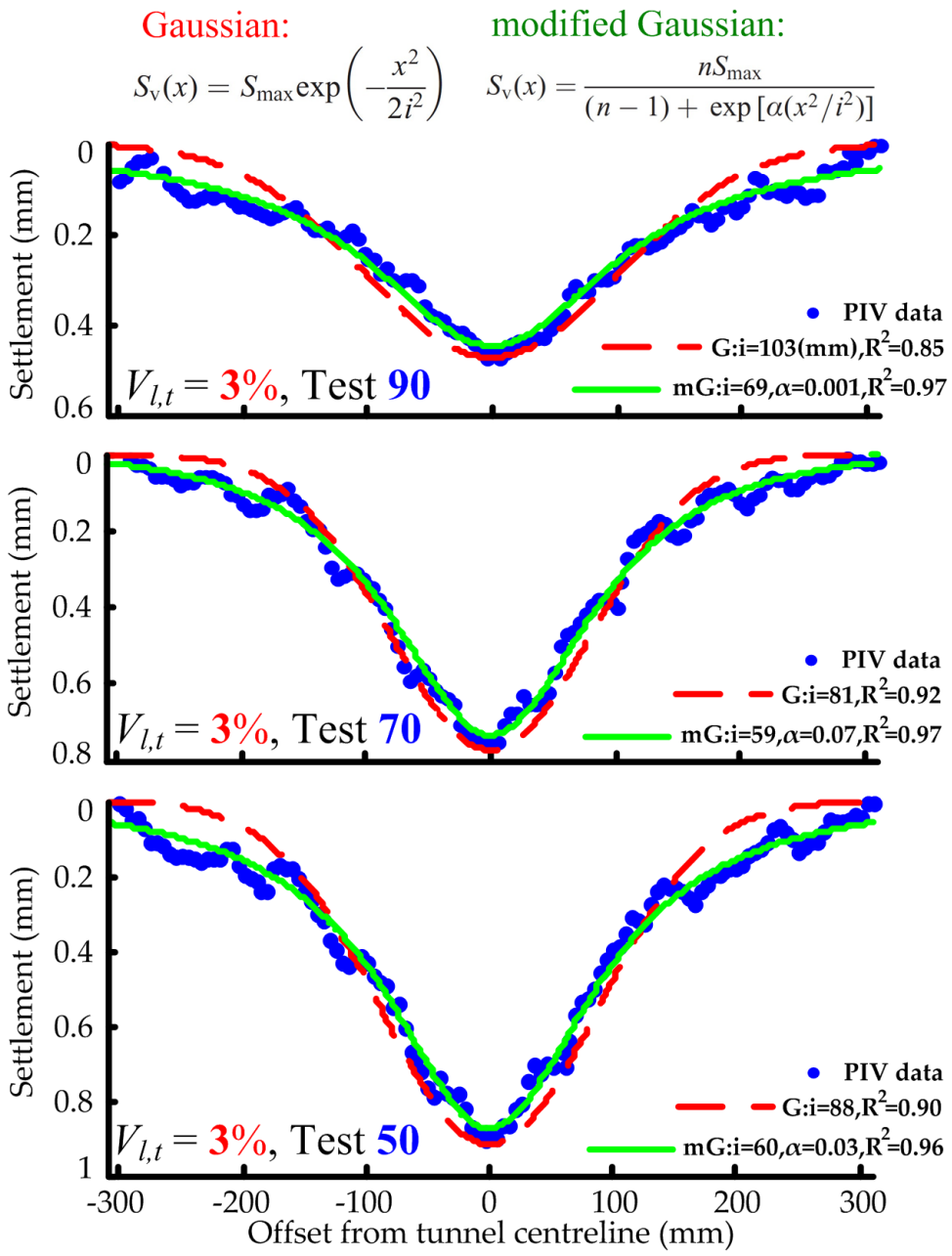

Figure 4.30: Fitting curves to PIV settlement data - Group 1

Figure 4.31 presents the coefficient of determination for the Gaussian and modified Gaussian curves at each volume loss for surface data and for data at a depth of 90 mm (depth/tunnel axis depth, $z/z_t = 0.4$). The modified Gaussian curve is shown to provide an equally good or better fit to the displacement data, especially in Test 90.

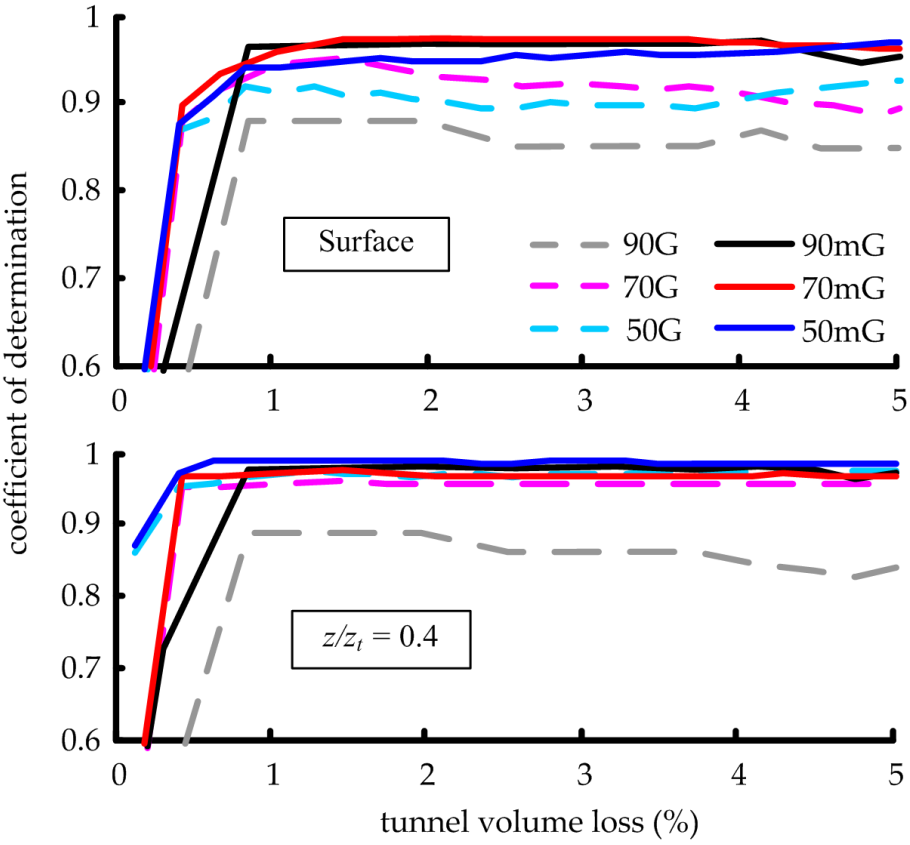

Figure 4.31: Quality of fit with $V_{l,t}$ - Group 1

The trend of R^2 with depth at $V_{l,t} = 1$, 3 and 5% is presented in Figure 4.32. The modified Gaussian curve provides a better fit than Gaussian curve at an arbitrary depth and in each test. Large decrement of modified Gaussian R^2 is observed at $z/z_t > 0.5$, especially in Test 90 at $V_{l,t} = 3$ and 5 % (but still higher than that of standard Gaussian). The decrement of R^2 is associated with several anomalies of fitting parameter i and α at $z/z_t > 0.5$ (will be showed in subsequent sections).

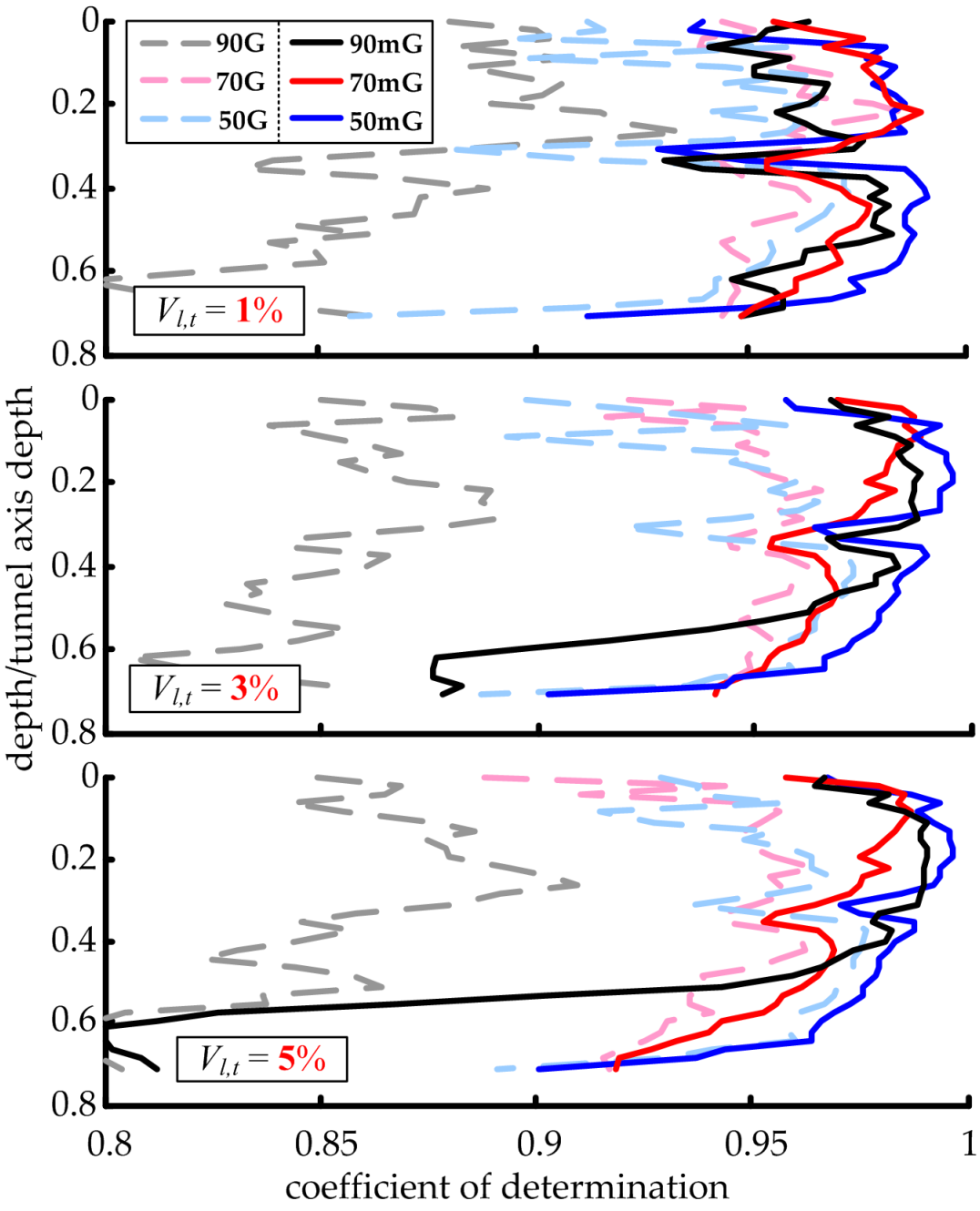

Figure 4.32: Quality of fit with depth - Group 1

To sum up, the modified Gaussian curve is shown to provide a better fit to the surface and subsurface displacement data in sand with various relative densities. The modified Gaussian curve is defined by three variables, S_{max}, i and α. The trends of these parameters with relative density, tunnel volume loss and depth will be examined in the following sections.

4.3.2 S_{max}

Figure 4.33 (a) presents the variation of S_{max} with tunnel volume loss for Group 1. The values of S_{max} increase linearly with $V_{l,t}$ at 0-1% and do not vary with relative density and depth, as a result of 'chimney' mechanism at low volume loss. Then the growth rate of S_{max} in dense sand decreases at $V_{l,t}$ = 1% so that the values of S_{max} in medium and loose sand become relatively larger. The growth rate of S_{max} in medium sand decreases at $V_{l,t}$ = 2-3% and therefore the value of S_{max} in loose sand become relatively larger after that. The decrease of S_{max} growth rate in the tests probably relates to the development of contraction (volumetric strain) within the soil (Section 4.2.4.2, p.99).

The variation of S_{max} with depth is presented in Figure 4.33 (b). The maximum settlement was nearly constant from surface to subsurface in each test at $V_{l,t}$ = 1%. At higher volume losses of 3% and 5%, the values of S_{max} increase linearly with depth at z/z_t = 0-0.4 as well as the values and growth rates of S_{max} are higher in looser sand. Blow the depth of z/z_t = 0.45 (when $V_{l,t}$ = 3 and 5%), S_{max} of Test 90 and 70 starts to increase rapidly with depth, indicating the severer localisation of settlement above the tunnel in dense and medium sand (mentioned in Section 4.2.3.1, p.86).

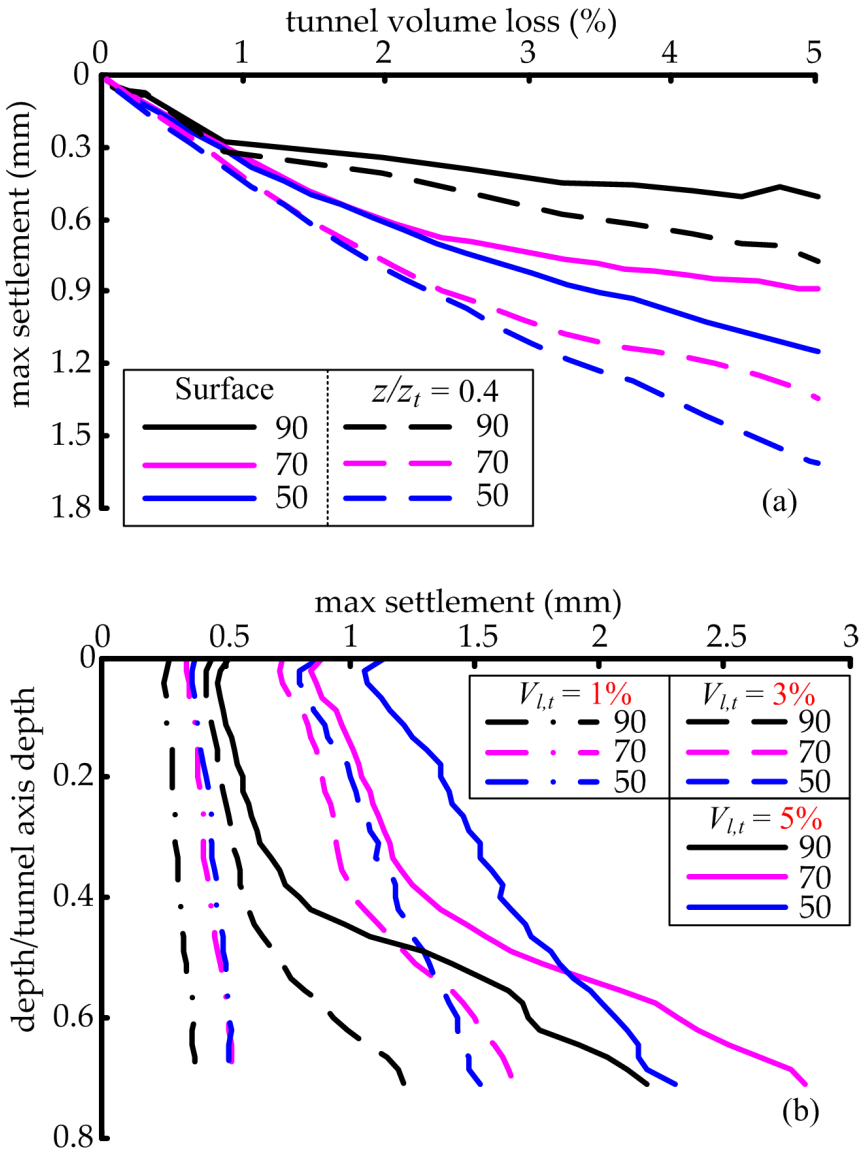

Figure 4.33: Variation of S_{max} with $V_{l,t}$ and depth - Group 1

4.3.3 x^* and x^{**} method to study trough shape

Modified Gaussian curves were fitted to the settlement trough data from Test 90, 70 and 50. Section 2.2.4.3 (p.16) introduced x^* and x^{**} as a method to characterise the shape of the settlement trough for non-Gaussian curves with three degrees of freedom (such as the modified Gaussian curves). x^* and x^{**} is the horizontal distance from $x = 0$ to the point on fitted curve where $S_v = 0.606S_{max}$ and $0.303S_{max}$, respectively. x^* is equal to the i in Gaussian curve and they are both at $0.606S_{max}$, so that they can be used for a qualitative comparison of trough widths.

Figure 4.34 (p.125) shows the variation of x^* and x^{**} with depth when $V_{l,t} =$ 1, 3 and 5%. Also included is the data from a similar centrifuge test conducted by Marshall [2009] ('90CD2.4' in the figure). The centrifuge test used the same sand as that in this research but with a different C/D_t ratio, 2.44 (C/D_t in this research is 2.0). The values of x^* and x^{**} decrease approximately linearly with depth (as did the data on which the Mair et al. [1993], equation is based). The data show that the decrement rate of values with depth is not significantly different in sand with different I_d, and there is a slight decrease of values with volume loss, as Marshall et al. [2012] have found.

The values near surface in dense sand (90 and 90CD2.4) are larger than that in loose (50) and medium (70) sand, but decrement rates of the values with depth in dense sand are higher than that in loose and medium sand. At depths approaching the tunnel, x^* and x^{**} in dense sand become similar to that in both medium and loose sand when $V_{l,t} = 1\%$. x^* and x^{**} in dense sand become smaller than that in medium and loose sand at depths approaching the tunnel when $V_{l,t}$ = 3 and 5%. Note that the anomaly (sharp increase) of the values at $z/z_t > 0.5$ when $V_{l,t} = 5\%$ in Test 90 is possibly associated with bad fitting quality there (mentioned in Section 4.3.1, p.117).

The effects of relative density on trough width are complex, which is affected by both magnitude and distribution of displacements. At depths near soil surface, Figure 4.34 showed that: the trough width in dense sand > that in loose sand >

that in medium sand. The vertical displacement contours (Section 4.2.3.1, p.86) indicated that the ground displacements were mainly near the tunnel centreline and the magnitude of displacements in dense sand are significantly smaller than that in medium and loose sand, so that the settlement trough in dense sand is wider. The magnitude of displacements in loose sand is relatively larger than that in medium sand but the trough width near surface in the medium sand is slightly narrower, so that the displacements in medium sand is more localised and the distribution of displacements in loose sand is wider. The volumetric deformation contours (Section 4.2.4.2, p.99) showed that the contraction in the wide trough in loose sand was larger than that in medium sand, even when the wide trough in medium sand stopped growing after $V_{l,t} = 3\%$. Probably the wider contraction in loose sand caused the wider distribution of settlements.

At the depths approaching the tunnel, the settlement trough is narrower in denser sand, indicating the severer localisation of settlement above the tunnel in dense and medium sand (Section 4.2.3.1, p.86).

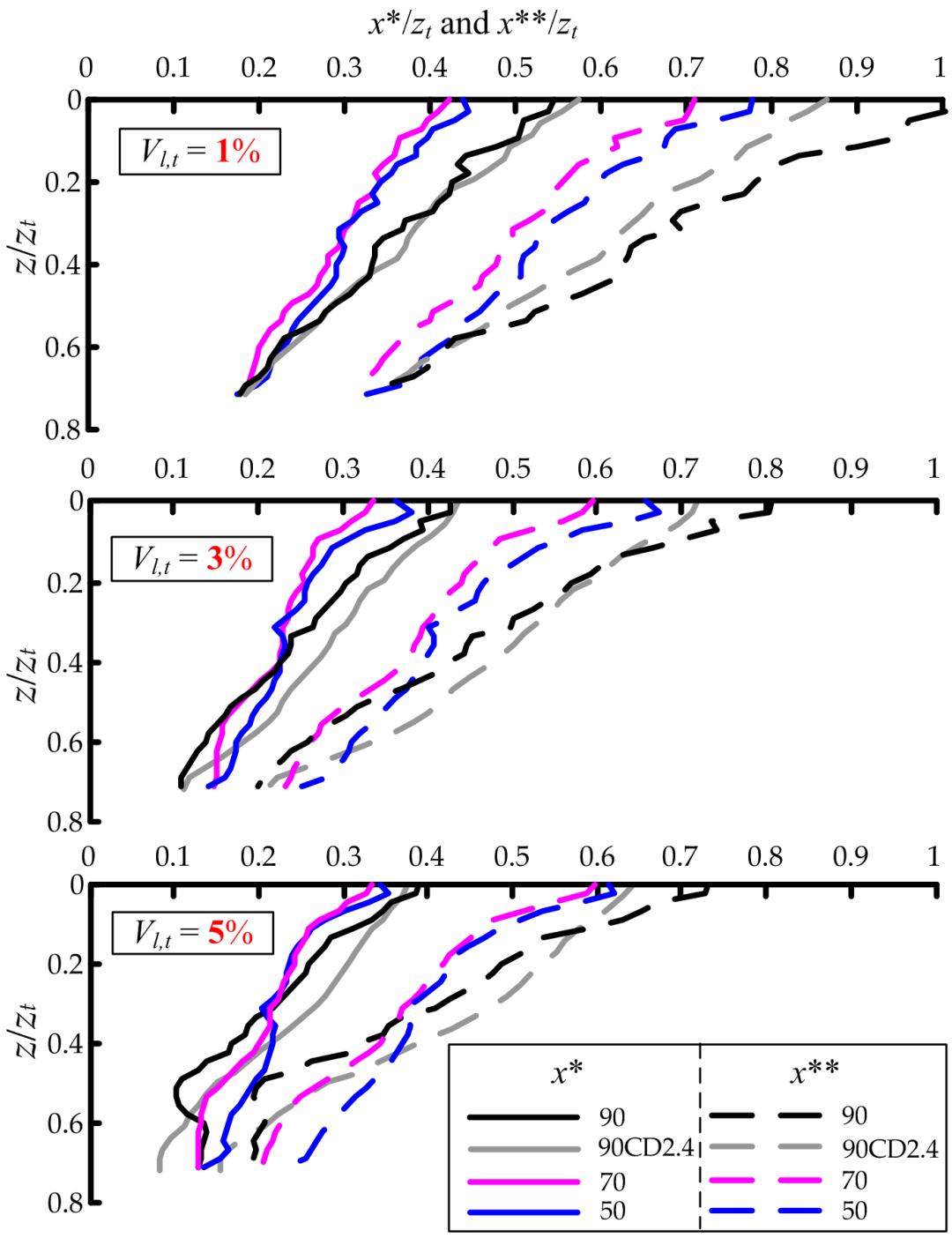

Figure 4.34: Variation of x^* and x^{**} with depth (normalised by tunnel depth, z_t) - Group 1

The value of i is generally expressed as $i(z) = K(z_t - z)$, where K is referred to as the trough width parameter, z_t is tunnel axis depth and z is an arbitrary depth. It should be noted that these relationships are based on fitting the Gaussian curve to settlement data, do not consider the effect of tunnel size or magnitude of volume loss, and should not be used at depths very close to the tunnel. For non-Gaussian, a trough width parameter K, based on x^* and x^{**}, can be calculated, and is referred to as K^* and K^{**}.

Marshall et al. [2012] provided the following relationship to predict the trough width parameter, based on the data from three centrifuge tests for tunnelling in dense sand:

$$\begin{aligned} K^* &= \left[K_s^* + (\partial x^*/\partial z)(z/z_t)\right]/(1 - z/z_t) \\ K_s^* &= K_{s,C/D}^{*int} + K_{s,C/D}^{*slope}(C/D) + K_{s,V_l}^{*slope}(V_{l,t}) \end{aligned} \tag{4.5}$$

where $K_{s,C/D}^{*int}$ = 0.440; $K_{s,C/D}^{*slope}$ = 0.055; K_{s,V_l}^{*slope} = -0.041; $\partial x^*/\partial z$ = -0.436; and the location of x^{**} can be found using $K^{**} = K^* + 0.29$ and $\partial x^{**}/\partial z = \partial x^*/\partial z$ - 0.20.

Figure 4.35 presented the variation of trough width parameter, K^*, with depth at the three values of tunnel volume loss. The data for dense sand was compared with the prediction using Equation 4.5. The agreement is generally good. Equation 4.5 captures the variable nature of the settlement trough shape caused by tunnelling in dense sand as it is affected by depth, tunnel volume loss and C/D_t ratio.

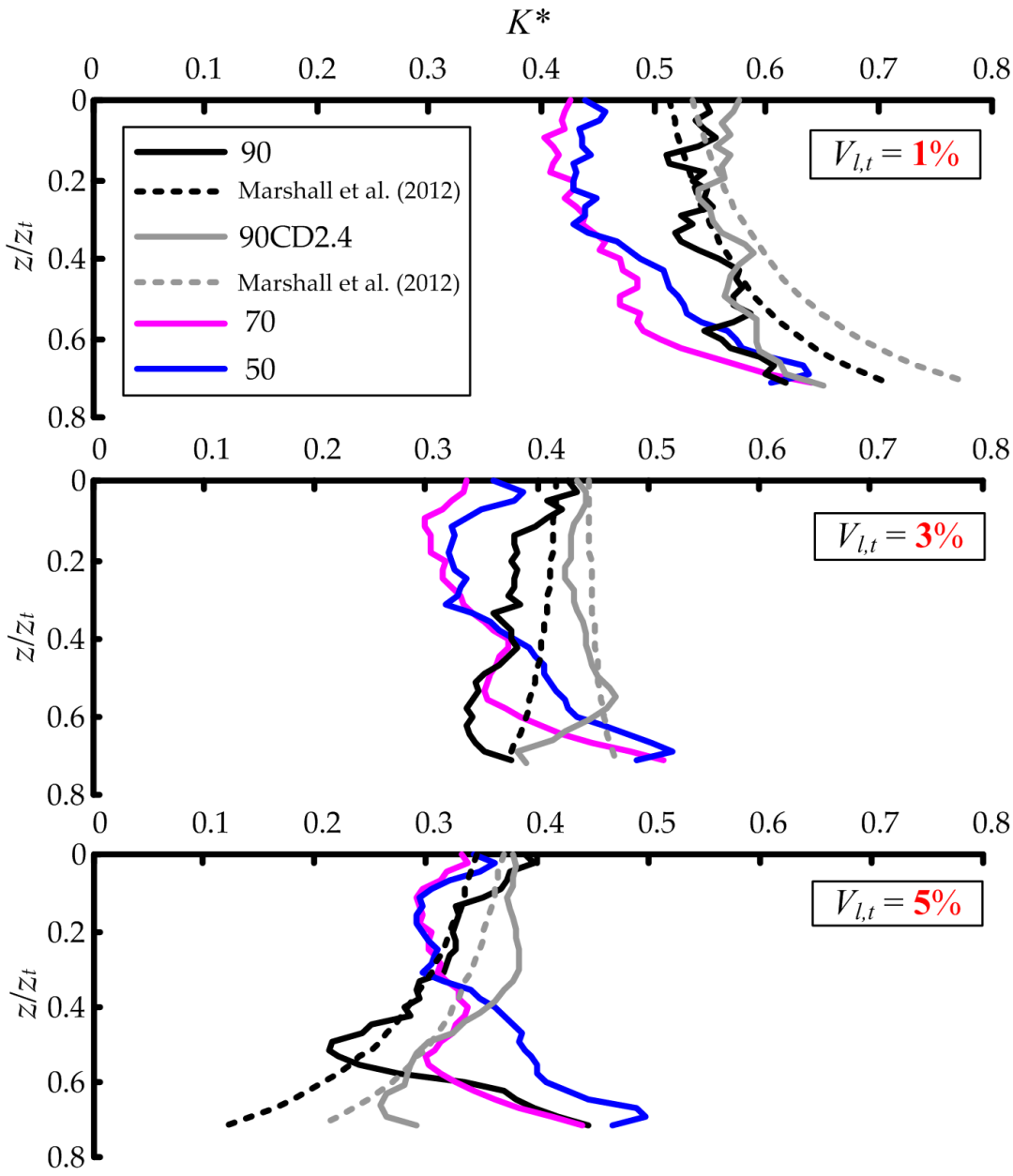

Figure 4.35: Trough width parameter against depth - Group 1

4.3.4 α

Figure 4.36 presents the trend of α with tunnel volume loss at surface and 90 mm depth. Note that α calculated at $V_{l,t} < 0.2\%$ were not included in the Figure because it was felt that they were unreliable as a result of the scatter in the data at small volume losses. The variation of α is small (0.001-0.2). Considering that an α value of 0.5 corresponds to the standard Gaussian curve, the inflexion points of settlement troughs in sand are generally higher than that in Gaussian curve (usually has a good fit to settlement in undrained clay).

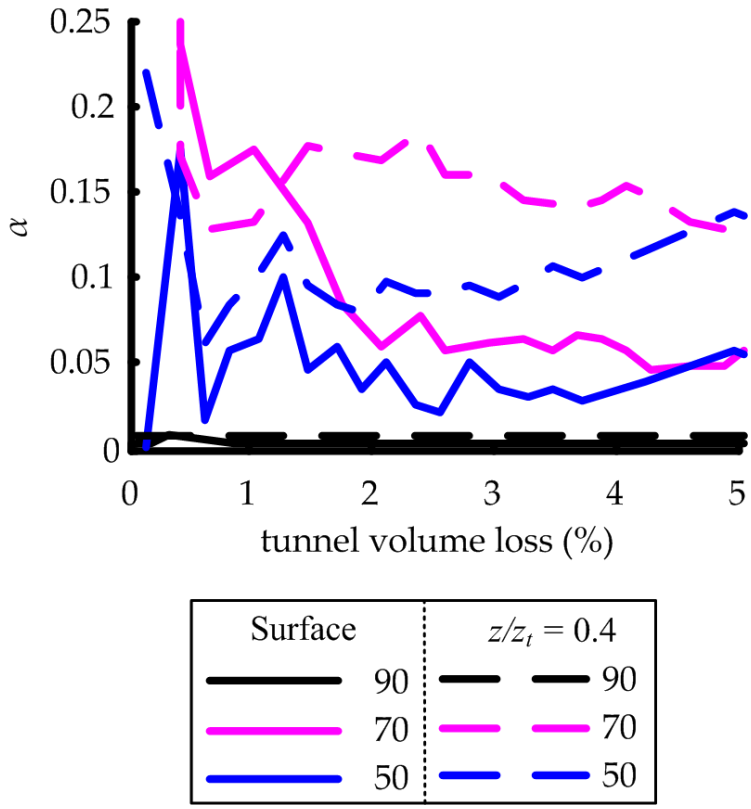

Figure 4.36: Variation of α with $V_{l,t}$ - Group 1

Figure 4.37 shows the trend of α with normalised depth at 1%, 3% and 5% tunnel volume loss. The values of α are mostly lower than 0.2. The anomalies (sharp increase) of α at $z/z_t > 0.5$ in several curves are possibly associated with bad fitting quality there (Section 4.3.1, p.117).

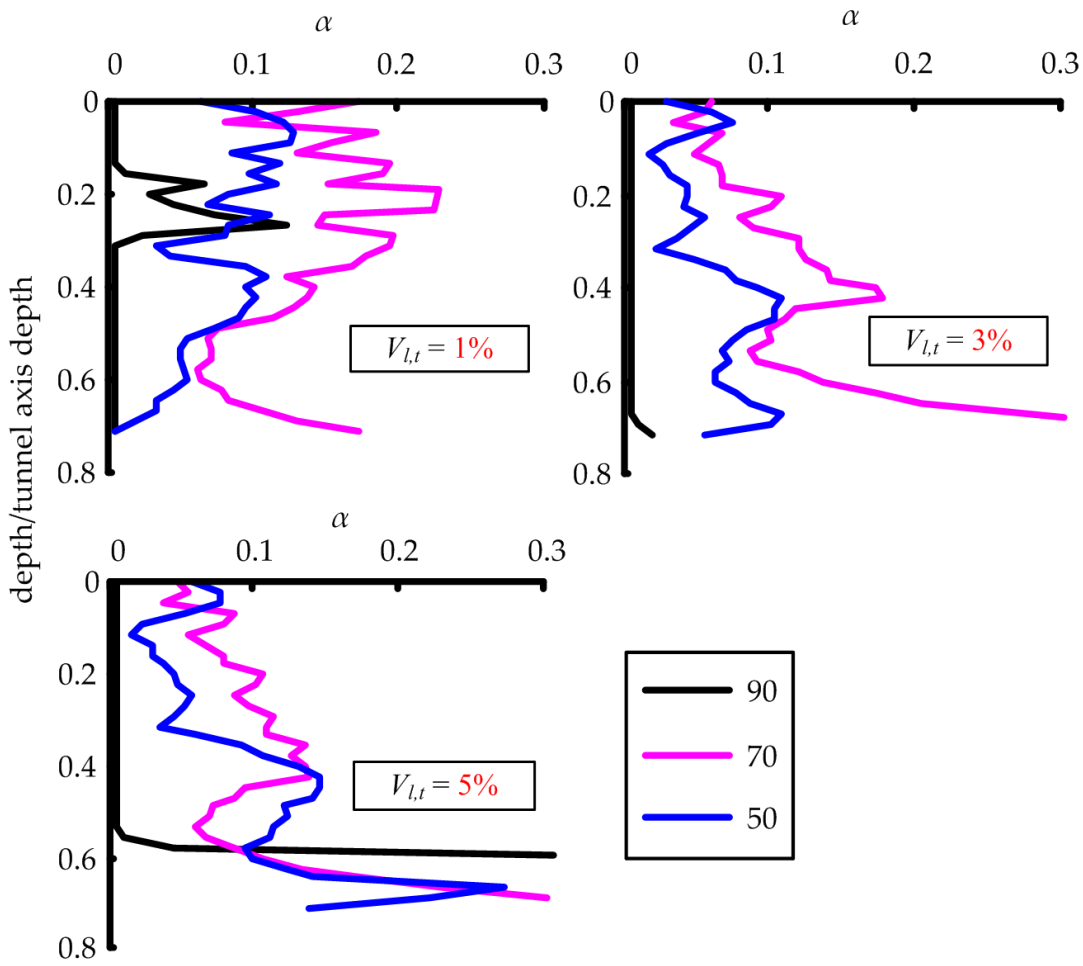

Figure 4.37: Variation of α with depth - Group 1

4.3.5 Slope and curvature

Figure 4.38 (a) presents the surface settlement trough (described by modified Gaussian curve) normalised by the maximum settlement at the tunnel centreline. The settlement trough is wider in dense sand. The lower trough width may cause a larger slop and curvature in settlement trough which will impact on the bending strains within buried infrastructure, such as pipelines [Marshall et al., 2010b]. The slope of the modified Gaussian curve is determined as the first derivative of the curve function, $S_v(x)$:

$$Slope = \frac{dS_v(x)}{dx} = \frac{-2nx}{\left[(n-1) + exp\left(\alpha x^2/i^2\right)\right]^2} \cdot \frac{\alpha S_{max} exp\left(\alpha x^2/i^2\right)}{i^2} \tag{4.6}$$

where n and α were introduced in Section 2.2.2.2 (p.7).

The curvature of the modified Gaussian curve is the second derivative of the curve function:

$$Curvature = \frac{d^2 S_v(x)}{dx^2} = u'vx + uv'x + uv \tag{4.7}$$

where u, u', v and v' is the functions of x:

$$\begin{aligned} u &= \frac{-2nx}{\left[(n-1) + exp\left(\alpha x^2/i^2\right)\right]^2} \\ v &= \alpha S_{max} \cdot exp\left(\alpha x^2/i^2\right)/i^2 \\ u' &= \frac{8\alpha nx \cdot exp\left(\alpha x^2/i^2\right)}{i^2\left[(n-1) + exp\left(\alpha x^2/i^2\right)\right]^3} \\ v' &= v \cdot 2\alpha x/i^2 \end{aligned} \tag{4.8}$$

Figure 4.38 (b and c) show the slop and curvature in the settlement trough. The maximum slop is at the inflexion point (i) and the maximum curvature is at the tunnel centreline.

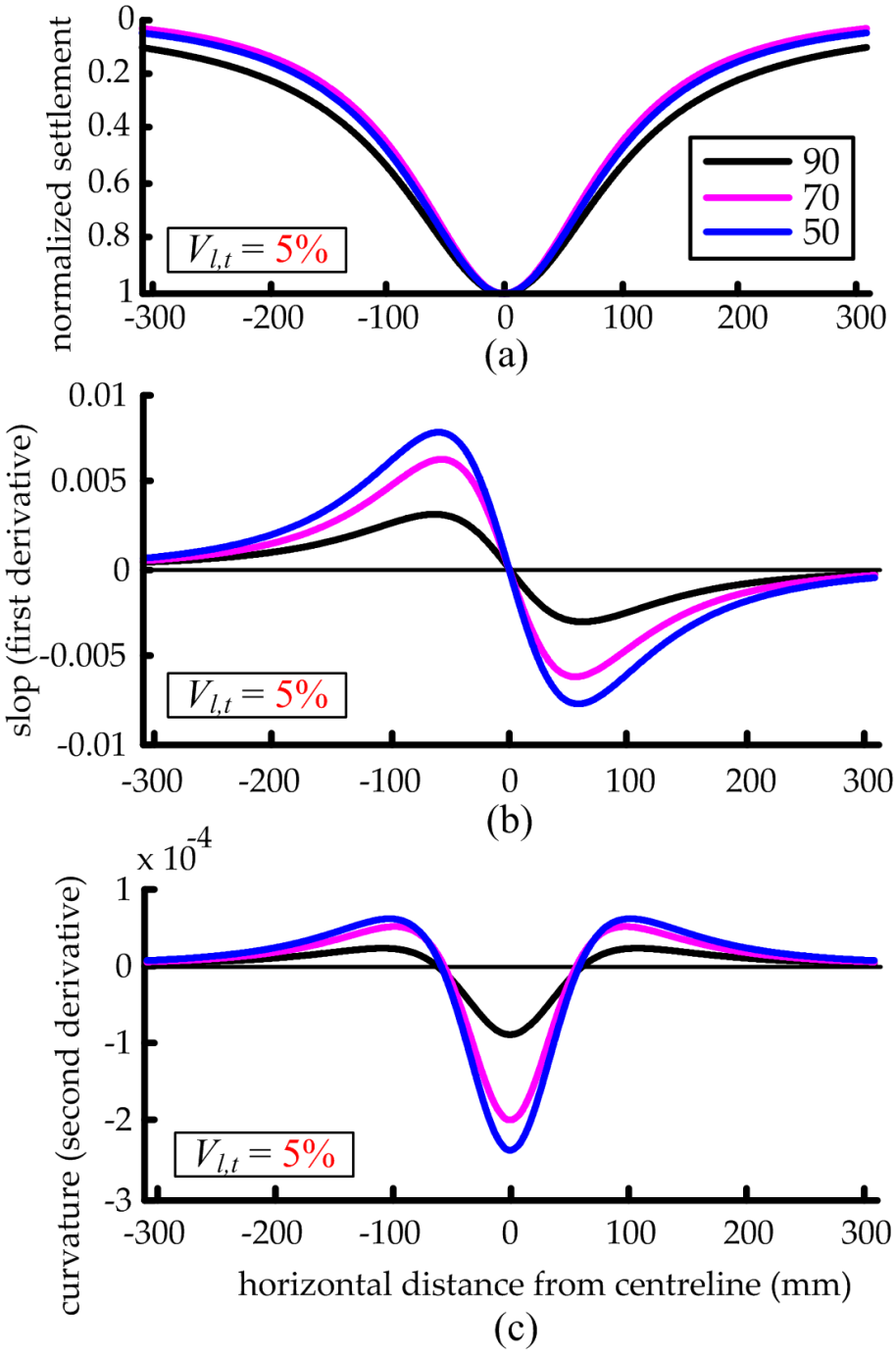

Figure 4.38: Normalised settlement trough and slope/curvature of settlement trough

Figure 4.39 presents the variation of maximum slop and curvature with $V_{l,t}$ at surface and $z/z_t = 0.4$. The values of maximum slop generally increase linearly with $V_{l,t}$ and do not vary with relative density in each depth before $V_{l,t} = 0.8\%$. Then the growth rate of maximum slop in dense sand decreases at 0.8% so that the values of maximum slop in medium and loose sand become relatively larger. The growth rate of maximum slop in medium sand decreases at 3-4% and therefore the value of maximum slop in loose sand becomes relatively larger after that.

The trend of maximum curvature with $V_{l,t}$ are mostly similar to those of maximum slop. The growth rate of maximum curvature in dense sand at $z/z_t = 0.4$ is not constant and its value is lower than those in medium and loose sand throughout $V_{l,t} = 0$-5%.

The variation of maximum slop and curvature with $V_{l,t}$ relates well to the trend of S_{max} with $V_{l,t}$ (Section 4.3.2, p.121).

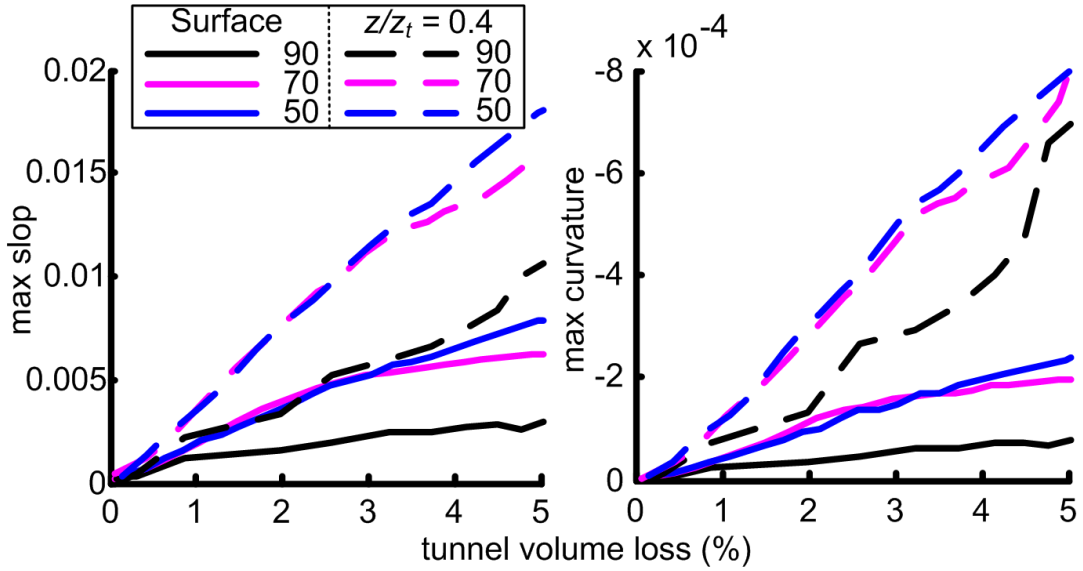

Figure 4.39: Variation of maximum slop and curvature with $V_{l,t}$ - Group 1

Figure 4.40 shows the trends of maximum slop and curvature with depth at $V_{l,t}$ = 1, 3 and 5%. The variation of maximum slop and curvature with depth is quite small at 1%, as a result of 'chimney' mechanism at low volume loss. At higher volume losses of 3% and 5%, the values of maximum slop and curvature increase almost linearly with depth at z/z_t = 0-0.4 as well as the values are higher in looser sand. Blow the depth of z/z_t = 0.45 (when $V_{l,t}$ = 3 and 5%), maximum slop and curvature in Test 90 and 70 start to increase rapidly with depth, probably caused by the severer localisation of settlement above the tunnel in dense and medium sand at high volume loss (Section 4.2.3.1, p.86).

Note that the anomaly of maximum curvature at $z/z_t > 0.55$ when $V_{l,t}$ = 5% in Test 90 is possibly associated with bad fitting quality there (mentioned in Section 4.3.1, p.117).

The variation of maximum slop and curvature with depth relates well to the trend of S_{max} with depth (Section 4.3.2, p.121), showing that S_{max} is an important factor for slop and curvature in this research.

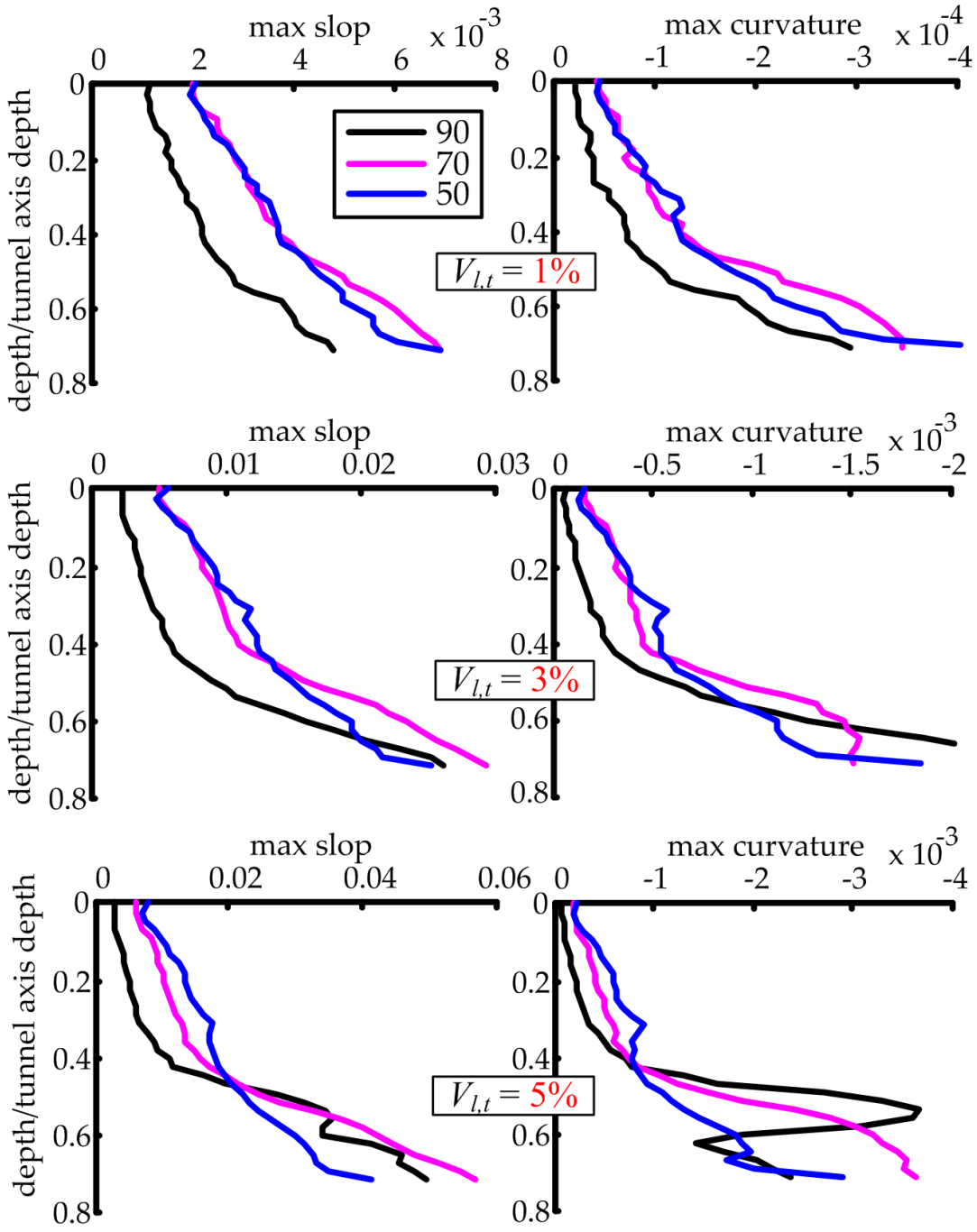

Figure 4.40: Variation of maximum slop and curvature with depth - Group 1

4.3.6 Variation of soil volume loss with tunnel volume loss

The research thus far has focused on the variation of trough parameters with tunnel volume loss, $V_{l,t}$. Tunnel volume loss is convenient to use, however, it is not practical for real tunnels, because it cannot be directly calculated. Engineers need to evaluate the volume loss experienced by the soil. Soil volume loss, $V_{l,s}$, is equal to the area of settlement trough of soil divided by initial cross-sectional area of tunnel. Soil volume loss is not equal to tunnel volume loss, because of the volumetric changes that occur in the soil.

Figure 4.41 (a) compares the soil volume loss and tunnel volume loss from the three tests. The area of surface settlement curve from PIV data was calculated to determine soil volume loss. The 1:1 line indicates $V_{l,s} = V_{l,t}$. When a point on the curves is above the 1:1 line ($V_{l,s} > V_{l,t}$), the volume of soil is lower than its original volume, so the soil is contracted due to the tunnelling. When a point on the curves is below the 1:1 line ($V_{l,s} < V_{l,t}$), the volume of soil is higher than its original volume, so the soil is dilated due to the tunnelling. Because boundary friction of Perspex wall had some effect on PIV displacements, the values of $V_{l,s}$ are slightly underestimated in the curves.

In order to analyse trends in $V_{l,s}$-$V_{l,t}$ curves, polynomial curves are fitted to $V_{l,s}$-$V_{l,t}$ curves. The first derivative of $V_{l,s}$-$V_{l,t}$ functions (polynomial fit) in Figure 4.41 (b) is the slope of tangent line on $V_{l,s}$-$V_{l,t}$ curves. When the slope of tangent is greater than 1, the soil volume loss is increasing faster than the tunnel volume loss, so the soil is in an overall state of contracting. When the slope of tangent is less than 1, the tunnel volume loss is increasing faster than the soil volume loss, so the soil is in an overall state of dilating.

Note that the contraction/dilation in Figure 4.41 (a) and Figure 4.41 (b) is different. The contraction/dilation in Figure 4.41 (a) is a concept of 'accumulation', which means the volume of soil is lower or higher than its original ($V_{l,t} = 0\%$) volume. The contraction/dilation in Figure 4.41 (b) is a concept of 'instant', which means the soil is generally contracting or dilating at the 'instant' of a $V_{l,t}$. Moreover, the volumetric stain contours in Section 4.2.4.2 (p.99) showed that

contraction and dilation occurred simultaneously at an arbitrary volume loss and therefore the contraction/dilation in Figure 4.41 implies an overall state of soil behaviour.

Figure 4.41 (a) shows the difference between the soil and tunnel volume loss is little at low volume loss in all the three tests, indicating small volumetric strain within the sand. After $V_{l,t} = 1\%$, the soil volume loss is obviously higher in looser sand. This relates well to the larger magnitude of contraction in looser sand observed in the volumetric strain contours (Section 4.2.4.2, p.99). Figure 4.41 (b) shows that the sand starts with contracting from $V_{l,t} = 0\%$ and then becomes dilating at $V_{l,t} = 0.5$, 1.1 and 1.5% in Test 90, 70 and 50, respectively. The change from contraction to dilation occurs later in looser sand. After that, the volume of sand becomes larger than its original volume at $V_{l,t} = 1.4$, 2.5 and 3.3% in Test 90, 70 and 50, respectively (Figure 4.41 (a)). This is associated with the large and fast-growing dilation observed in the volumetric strain contours at higher volume loss (Section 4.2.4.2, p.99): the development of dilation zone compensates for the contractive soil and effectively reduces the soil volume loss.

For real tunnelling, the actual tunnel volume loss can not be measured directly. Soil volume loss from surface settlement data was generally used to determine the tunnel volume loss. For this case, given a value of soil volume loss and assuming constant soil volume conditions, the value of tunnel volume loss would be overestimated or underestimated.

The relationship of $V_{l,s}$-$V_{l,t}$ will be further analysed with cavity expansion method in Chapter 5 (p.140).

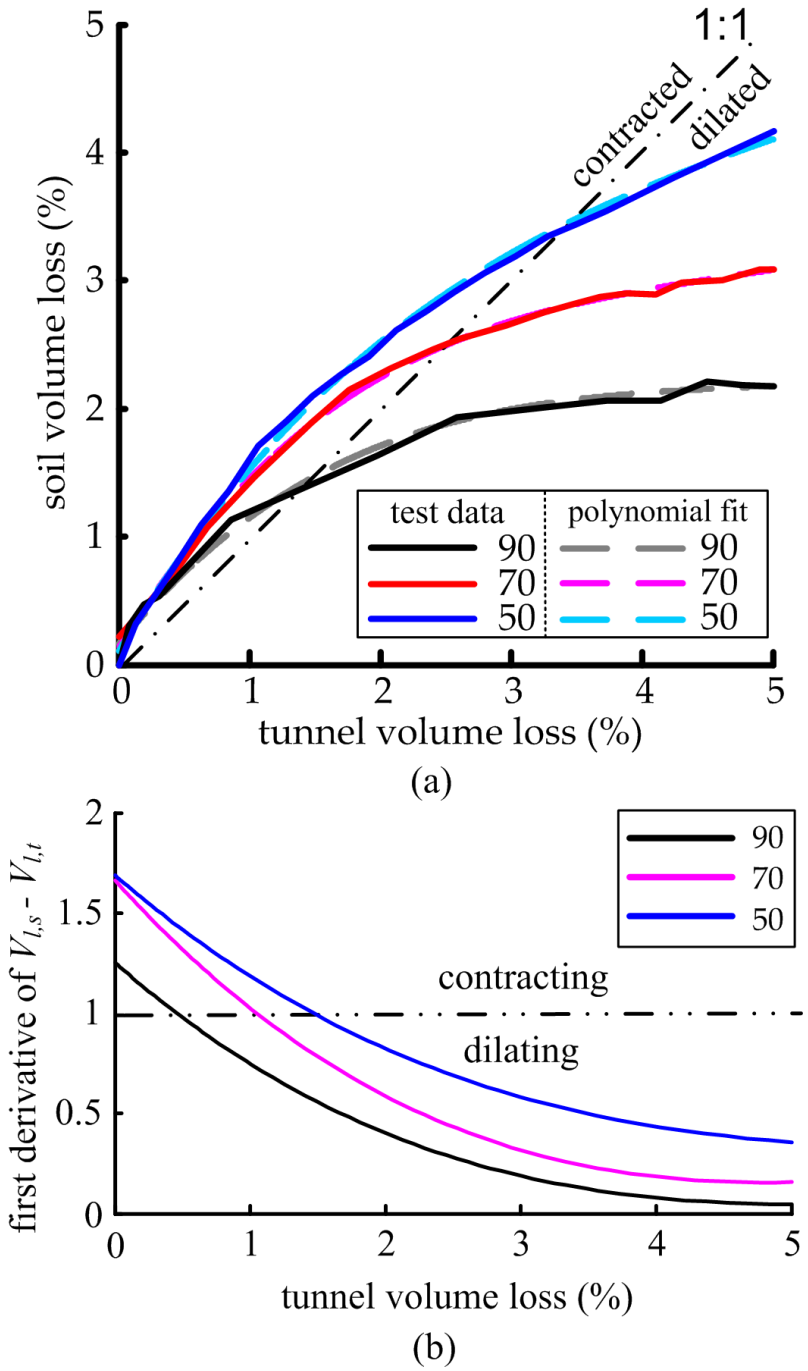

Figure 4.41: Volume loss calculated from soil displacements compared to tunnel volume loss - Group 1

4.4 Chapter summary

This chapter presented three geotechnical centrifuge tests undertaken to investigate the effect of relative density on displacements above the tunnels in sands. The relative density was found to affect the magnitude and shape of ground settlements. The following conclusions can be drawn:

1. The trends of normalised tunnel pressure with $V_{l,t}$ (Section 4.2.2, p.83) were almost same in the three tests: a sharp initial dropping and then remaining stable.

2. The contours of soil displacements and stains were presented in Section 4.2.3 (p.85) and 4.2.4 (p.97). The magnitudes of displacements and strains decreased with an increase in the relative density of the sand.

3. The ratio of tunnel deformation (Section 4.2.6, p.113) at crown to side was higher in denser sand.

4. The modified Gaussian curve provided a better fit to the settlement data compared to the Gaussian curve (Section 4.3.1, p.117).

5. Tunnelling in sand with lower relative density resulted in higher S_{max} (Section 4.3.2, p.121).

6. The settlement trough near surface in dense sand was wider than that in loose and medium sand (Section 4.3.3, p.123). Equation 4.5 (p.126) well predicted the trough width in dense sand. The values of α were mostly lower than 0.2 (Section 4.3.4, p.128).

7. The larger slop and curvature were observed in looser sand mostly in Section 4.3.5 (p.130).

8. The results in this Chapter indicated that the localisation of settlement above the tunnel is severer in denser sand.

9. $V_{l,s}$-$V_{l,t}$ relationship in Section 4.3.6 (p.135) indicated that the soil was in an overall state of contraction initially and then in an overall state of dilation

with increasing $V_{l,t}$ in each test. The change from contraction to dilation occurred later in looser sand.

The results of this chapter can have implication to the evaluation of the effect of tunnelling on buried infrastructure.

Chapter 5

VOLUMETRIC DEFORMATION WITH CAVITY EXPANSION METHODS

5.1 Introduction

Cavity expansion theory studies the stress and displacement fields around cavities embedded in linear or non-linear media. It is a simple theory which has found many applications in geotechnical engineering. In particular, it has been widely used to analyse problems relating to pile foundations, in-situ testing, underground tunnelling and wellbore instability.

Section 5.2 (p.141) reviews the literature using cavity expansion theory for underground tunnelling. Section 5.3 (p.148) further analyses the relationship of $V_{l,s}$-$V_{l,t}$ and the volumetric deformation within sand using cavity expansion methods. Note that a tension positive notation is used in this chapter.

5.2 Cavity expansion methods and underground tunnelling

Cavity expansion theory is concerned with the theoretical study of changes in stresses, pore pressures and displacements due to the expansion and contraction of cylindrical or spherical cavities [Yu, 2000]. Using cavity expansion theory in order to solve practical problems is termed cavity expansion method. Cavity expansion and contraction in soil or rock is a fundamental problem in theoretical geomechanics primarily because it provides a useful tool to model many complex geotechnical problems.

Analysis of the expansion and contraction of cavities in soil and rock provides a surprisingly versatile and accurate geomechanics approach for study of important problems in geotechnical engineering [Yu, 2000]. Among them are the axial and lateral capacity of pile foundations, interpretation of pressuremeter and cone penetration tests for determining soil state and properties, and analysis of stability and deformations associated with underground excavation and tunnelling.

Underground tunnelling involves the removal of soil masses from their initial

locations. This action reduces the initial stresses which existed in the area of tunnelling (from p_0 to p, in Figure 5.1, p.143). Therefore, it is probably reasonable to assume that the underground tunnelling can be modelled by the unloading of a cavity from p_0 to p. Cavity expansion theory has been used for decades to predict ground displacements cased by underground tunnelling (e.g. Mair and Taylor [1993]; Yu and Rowe [1999]).

It is assumed that an unbound Mohr-Coulomb medium contains a single cylindrical or spherical cavity (the cylindrical cavity could model the tunnel in this research). Initially the radius of the cavity (tunnel) is a_0 as well as a hydrostatic pressure p_0 acts throughout the soil. The soil is assumed to be homogeneous. The supporting pressure (pressure on the tunnel wall) is then decreased quite slowly and therefore the dynamic effects could be ignored. The distribution of stress and displacement within the soil during the unloading is presented here.

Elastic response

As the supporting pressure p is reduced from p_0, the soil deformation is firstly at purely elastic. The stresses and displacement in the elastic zone are shown to be as follows:

$$\sigma_r = -p_0 - (p - p_0)(\frac{a}{r})^{1+k} \tag{5.1}$$

$$\sigma_\theta = -p_0 + \frac{p - p_0}{k}(\frac{a}{r})^{1+k} \tag{5.2}$$

$$u = r - r_0 = \frac{p - p_0}{2kG}(\frac{a}{r})^{1+k} r \tag{5.3}$$

where a is the current cavity radius, r is an arbitrary distance from the cavity centre (tunnel axis), r_0 is the initial distance (when $p = p_0$), k is the cavity expansion parameter (= 1 for cylindrical cavity solution; = 2 for spherical cavity solution), and G is the shear stiffness/modulus.

Elastic-plastic stress fields

For unloading cavities, the Mohr-Coulomb yield equation takes the form:

$$\alpha\sigma_r - \sigma_\theta = Y \tag{5.4}$$

where $\alpha = (1 + sin\phi)/(1 - sin\phi)$ and $Y = 2Ccos\phi/(1 - sin\phi)$ in which C and ϕ is soil cohesion and friction angle, respectively.

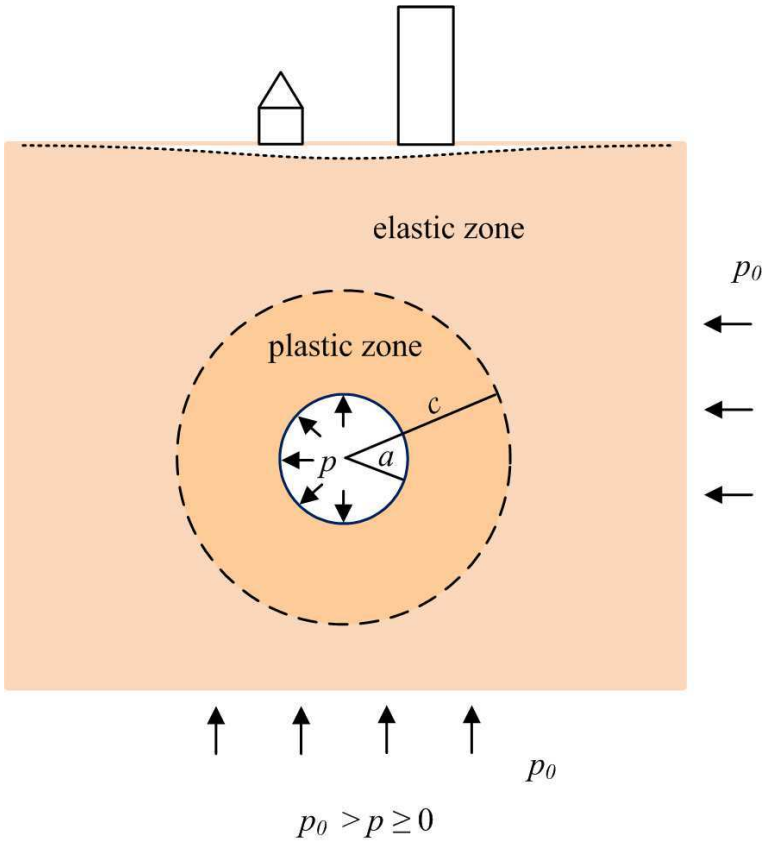

Figure 5.1: Action of underground tunnelling

After initial yielding at the cavity wall, a plastic zone will form within the region $a \leq r \leq c$ with a further reduction in the tunnel pressure p.

The stresses in the elastic zone are shown to be of the form:

$$\sigma_r = -p_0 - Br^{-(1+k)} \tag{5.5}$$

$$\sigma_\theta = -p_0 + \frac{B}{k} r^{-(1+k)} \tag{5.6}$$

On the other hand, the stresses in the plastic zone must satisfy equilibrium and yield condition. They are shown to be as follows:

$$\sigma_r = \frac{Y}{\alpha - 1} + Ar^{k(\alpha-1)} \tag{5.7}$$

$$\sigma_\theta = \frac{Y}{\alpha - 1} + A\alpha r^{k(\alpha-1)} \tag{5.8}$$

The continuity of stresses at the elastic-plastic interface ($r = c$) is used to calculate the constants A and B:

$$A = -\frac{(1+k)\left[Y + (\alpha-1)p_0\right]}{(\alpha-1)(1+k\alpha)} c^{(1-\alpha)k} \tag{5.9}$$

$$B = \frac{k\left[(1-\alpha)p_0 - Y\right]}{1+k\alpha} c^{1+k} \tag{5.10}$$

Applying $\sigma_r = -p$ at the cavity wall ($r = a$) can lead to the following relation between the supporting pressure p and the plastic radius c:

$$\frac{c}{a} = \left\{ \frac{(1+k\alpha)\left[Y + (\alpha-1)p\right]}{(1+k)\left[Y + (\alpha-1)p_0\right]} \right\}^{\frac{1}{k(1-\alpha)}} \tag{5.11}$$

Elastic-plastic displacements

In the elastic zone, the displacement is shown to be:

$$u = r - r_0 = \frac{(1-\alpha)p_0 - Y}{2G(1+k\alpha)}(\frac{c}{r})^{1+k}r \tag{5.12}$$

Therefore, the displacement at the elastic-plastic interface should be:

$$u_{r=c} = c - c_0 = \frac{(1-\alpha)p_0 - Y}{2G(1+k\alpha)}c \tag{5.13}$$

For the unloading of cavities, the non-associated Mohr-Coulomb flow rule is expressed as:

$$\frac{\dot{\epsilon}_r^p}{\dot{\epsilon}_\theta^p} = \frac{\dot{\epsilon}_r - \dot{\epsilon}_r^e}{\dot{\epsilon}_\theta - \dot{\epsilon}_\theta^e} = -k\beta \tag{5.14}$$

where $\dot{\epsilon}_r^p$ and $\dot{\epsilon}_\theta^p$ is the variation of plastic strain, and β is a simple function of dilation angle ψ:

$$\beta = \frac{1+sin\psi}{1-sin\psi} \tag{5.15}$$

Note that the flow rule for the soil is associated if $\beta = \alpha$.

It is difficult to solve Equation 5.14 analytically if the elastic strains are included. However, with ignoring the elastic contribution in the plastic deformation zone, the solution can be considerably simplified. By adopting the logarithmic strains ($\epsilon_r = ln(dr/dr_0)$ and $\epsilon_\theta = ln(r/r_0)$), the flow rule (5.14) can be integrated to give the following equation:

$$r^{k\beta}dr = r_0^{k\beta}dr_0 \tag{5.16}$$

Equation 5.16 can be integrated over the interval $[c, r]$ to give:

$$r^{1+k\beta} - c^{1+k\beta} = r_0^{1+k\beta} - c_0^{1+k\beta} \tag{5.17}$$

Note that c (plastic radius) is the current distance from tunnel axis to the soil at current elastic-plastic interface, and c_0 is the original distance from tunnel axis to the soil which would form the current elastic-plastic interface. c and c_0 refer to the same soil with different locations and $c_0 > c$ due to the cavity contraction.

Because c_0 can be linked to c by the elastic displacement solution (5.13), Equation 5.17 determines the displacement field in the plastic zone. At the tunnel wall, the relation reduces to:

$$a^{1+k\beta} - a_0^{1+k\beta} = c^{1+k\beta} - c_0^{1+k\beta} \tag{5.18}$$

The complete derivation of Equations 5.1-5.18 can be found in Yu [2000].

As an analytical solution, cavity expansion method assumes that an unbound soil medium contains a cavity (tunnel). Yu [2000] compared the analytical prediction against the centrifuge test results for tunnelling in clay reported by Mair [1979]. The comparison showed that solutions for contracting cavities in an infinite soil medium were less accurate for modelling the behaviour of soils far away from the tunnel wall, however, the cavity unloading solutions gave more accurate predictions for displacements around the tunnel. The discrepancy far away from the tunnel wall is, to a large extent, due to the effect of the free ground surface that is not accounted for in cavity unloading in an infinite soil mass. To take into account the effect of free ground surface, the elastic solutions proposed by Sagaseta [1987] and Verruijt and Booker [1996] (introduced in Section 2.2.6.1 and 2.2.6.2, p.22-24) for displacements due to the unloading of a cavity in a half space can be used.

Soil volume loss

Klar [2013] proposed an approximated relation for the volume loss at soil surface,

$V_{l,s}$ (Section 4.3.6, p.135). This relation uses the elastic solution by Verruijt and Booker [1996], but with an artificially enlarged 'tunnel' radius equal to the elastic-plastic interface radius in the cavity expansion method (c in Figure 5.1, p.143). Hence the 'tunnel' is enlarged to include the whole plastic zone. The region out of the 'tunnel' is purely elastic for the solution [Verruijt and Booker, 1996] that leads to a volume loss at soil surface:

$$V_{l,s}\,[\%] = 2(c_0^2 - cc_0)/a_0^2 \cdot 100 \tag{5.19}$$

Adopting the relation 5.19 and the large strain (logarithmic strain) relations of cavity contraction (Equation 5.13 and 5.18), Marshall [2013] linked the soil volume loss to the tunnel volume loss as:

$$V_{l,s} = \frac{2\,[Y + p_0(\alpha - 1)]}{Y + p_0(\alpha - 1) + 2G(\alpha + 1)} \left(\frac{(1 - V_{l,t})^{\frac{-(\beta+1)}{2}} - 1}{(1 + \frac{Y + p_0(\alpha-1)}{2G(\alpha+1)})^{\beta+1} - 1} \right)^{\frac{2}{\beta+1}} \tag{5.20}$$

Figure 5.2 compares the relationship using Equation 5.20 for a range of values of dilation angle against the data from three centrifuge tests in sand reported in Marshall [2013]. The figure also includes the relationship of $V_{l,s} - V_{l,t}$ established by Klar [2013] using the small strain relations. For $\psi = 0$, the predicted soil volume loss and tunnel volume loss are identical. For positive or negative dilation angle, the predicted soil volume loss is smaller or larger than that of tunnel, respectively. However, most centrifuge tests in Figure 5.2 and 4.41 (p.137) indicated that the soil volume loss was greater than the tunnel volume loss (soil was contracted) initially but then became less (soil was dilated) at higher tunnel volume loss. This discrepancy indicates that the dilation angle may not be a constant value during the cavity contraction.

It is useful to examine the variation of dilation angel with tunnel volume loss[1] to evaluate the effect of tunnelling on the soil dilatancy. After that, more factors (e.g. relative density of soil) could be considered. This research develops a method to

[1]This research tried to establish an analytical model using a variable parameter (describing dilatancy) which could be defined as a function of shear strain, but it was shown to be difficult.

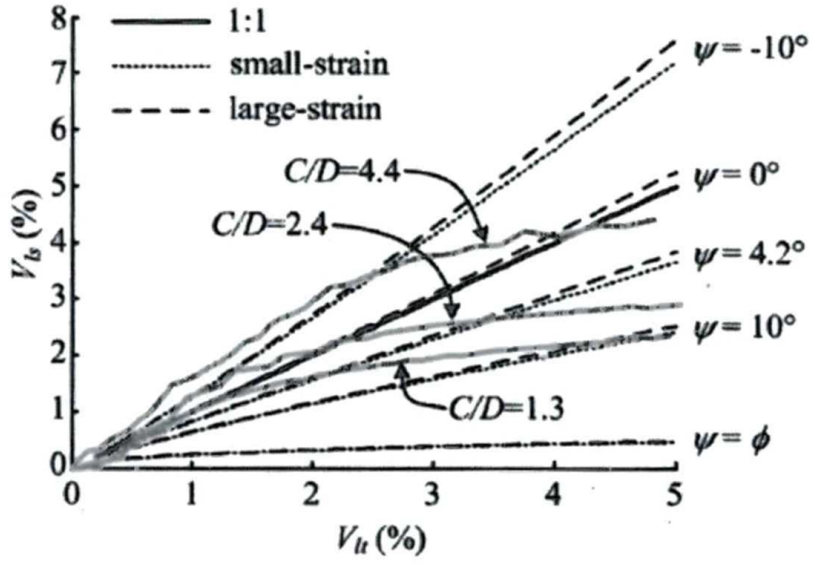

Figure 5.2: Surface volume loss compared to tunnel volume loss and effect of dilation angle, after Marshall [2013]

examine the trend of dilation angel with tunnel volume loss and illustrates the effect of relative density on that using the data from centrifuge tests in Chapter 4 (p.77).

5.3 Trend of dilation angel with tunnel volume loss

As it is difficult to be solved analytically, a numerical method is used here to calculate the dilation angel (ψ) at an arbitrary volume loss ($V_{l,t}$). The progress of tunnel volume loss is divided into N steps. In each small step, the initial values and final values are denoted by subscript '1' and '2', respectively (not meaning the step 1 and 2). The dilation angle of the soil for each step is $\psi_{rep,i}$. $\psi_{rep,i}$ is a value of dilation angle representing the overall state of dilatancy within the soil at step i.

Solution

For unloading cylindrical cavities ($k = 1$), the non-associated Mohr-Coulomb flow rule can be expressed as:

$$\frac{\dot{\epsilon}_r^p}{\dot{\epsilon}_\theta^p} = \frac{\dot{\epsilon}_r - \dot{\epsilon}_r^e}{\dot{\epsilon}_\theta - \dot{\epsilon}_\theta^e} = -\beta_{rep} \tag{5.21}$$

where β_{rep} is a function of ψ_{rep} (Equation 5.15, p.145).

Ignoring the elastic contribution in the plastic zone and adopting the logarithmic strains (as Equation 5.16, p.145), the flow rule in each step can be as follows:

$$\frac{\dot{\epsilon}_r}{\dot{\epsilon}_\theta} = \frac{\epsilon_{r,2} - \epsilon_{r,1}}{\epsilon_{\theta,2} - \epsilon_{\theta,1}} = \frac{ln\frac{dr_2}{dr_0} - ln\frac{dr_1}{dr_0}}{ln\frac{r_2}{r_0} - ln\frac{r_1}{r_0}} = -\beta_{rep,i} \tag{5.22}$$

$\Longrightarrow$

$$r_2^{\beta_{rep,i}} dr_2 = r_1^{\beta_{rep,i}} dr_1 \tag{5.23}$$

Equation 5.23 can be further integrated over the interval $[c, a]$ (from tunnel radius to plastic radius) to give:

$$a_2^{1+\beta_{rep,i}} - a_1^{1+\beta_{rep,i}} = c_2^{1+\beta_{rep,i}} - c_1^{1+\beta_{rep,i}} \tag{5.24}$$

In order to solve the $\beta_{rep,i}$ (the function of $\psi_{rep,i}$), it is necessary to know a_2, a_1, c_2 and c_1 in Equation 5.24. a_1 and a_2 is the initial and final radius of tunnel in each step, respectively, which can be derived from the values of tunnel volume loss. c_2 is the final radius of plastic zone in each step and can be solved by the relationship 5.11 (p.144) between the supporting pressure p_i and the plastic radius c_2:

$$\frac{c_2}{a_2} = \left\{ \frac{(1+\alpha)\left[Y + (\alpha - 1)p_i\right]}{2\left[Y + (\alpha - 1)p_0\right]} \right\}^{\frac{1}{1-\alpha}} \tag{5.25}$$

The supporting pressure of tunnel in centrifuge tests was measured by the pressure sensor (Section 4.2.2, p.83).

Adopting Equation 5.19 (p.147), c_1 can be determined by c_2 and soil volume loss:

$$V_{ls,i} - V_{ls,i-1}\,[\%] = 2(c_1^2 - c_2 c_1)/a_0^2 \cdot 100 \tag{5.26}$$

The soil volume loss was measured in the centrifuge tests and compared with tunnel volume loss in Section 4.3.6 (p.135).

With the values of a_2, a_1, c_2 and c_1, the dilation angel in each step of volume loss can be solved by Equation 5.24.

$\psi_{rep} - V_{l,t}$ for the centrifuge test 90, 70 and 50 in Group 1 is analysed numerically. The tunnel contraction (V_{lt} = 0%-5%) is divided into 30 steps (V_{lt} for each step = 0.167%). The value of α, as a simple function of friction angle ($\alpha = (1+sin\phi)/(1-sin\phi)$), is used to determine the plastic radius in this solution. The friction angles are assumed constant in the plastic zone around the cavity. However, the numerical analysis for cavity expansion in sand published by Collins et al. [1992] showed that the friction angles varied during the soil approaching critical state and suggested that the appropriate angles for analysis should be average values between the initial (maximum) state and final (critical) state. Thus $\bar{\phi}' = 0.5(\phi'_{max} + \phi'_{cv})$, where ϕ'_{cv} is the critical state friction angle. The work of Bolton [1986, 1987] can be used to link the friction angle for plane-strain to I_d (relative density) and p' (mean effective stress) as follows:

$$\phi'_{max} - \phi'_{cv} = 5I_R \tag{5.27}$$

where

$$I_R = 5I_d - 1 \tag{5.28}$$

for $p' < 150kPa$ and

$$I_R = I_d \left[5 - ln \frac{p'}{150} \right] - 1 \tag{5.29}$$

for $p' > 150kPa$.

This relation do not consider the anisotropy of sand. Using this relation, the effect friction angles for cavity expansion solution is:

$$\bar{\phi'} = 0.5(\phi'_{max} + \phi'_{cv}) = \phi'_{cv} + 2.5I_R \tag{5.30}$$

The value of ϕ'_{cv} for plane-strain was taken as 30° here [Bolton, 1987].

Results

The plastic radius calculated by Equation 5.25 (p.149) is presented in Figure 5.3. The radius increases rapidly at low volume loss and then remains relatively stable, which is associated with the decrease of tunnel pressure, p (Section 4.2.2, p.83). Using the estimation proposed by Bolton [1986, 1987], the value of $\bar{\phi}'$ is less in looser sand with lower I_d. Hence the plastic zone in looser sand is larger. The relation determines the value of c_2 in the solution 5.24 (p.149).

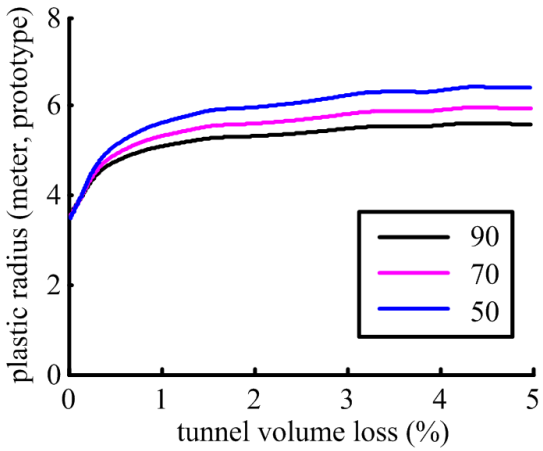

Figure 5.3: Plastic radius with tunnel volume loss

Figure 5.4 (a) shows the trend of dilation angle with tunnel volume loss solved by this numerical method. The negative values of dilation angle are indicative of the decreasing volume of soil. The sand in all the three tests starts with contracting from $V_{l,t} = 0\%$ and then becomes dilating at $V_{l,t} = 0.5$, 1.1 and 1.5% in Test 90, 70 and 50, respectively. The transition of dilation angle from negative to positive occurs later in looser sand. At an arbitrary volume loss, the dilation angle is presented to be relatively higher in denser sand.

The variation of dilation angle with volume loss is compared with that of the slop of $V_{l,s} - V_{l,t}$ (Figure 5.4 (b), also mentioned in Section 4.3.6, p.135). The transitions of states from 'contracting' to 'dilating' in the two figures matches well.

Some of calculated dilation angles at $V_{l,t} < 0.6\%$ are anomalous or even not

real numbers. This solution ignores the elastic contribution and therefore the volumetric deformation is all attributed to the dilatancy in plastic zone. However, the plastic zone is quite small at low volume loss (or underestimated) so that the calculated dilation angle is too large (negative).

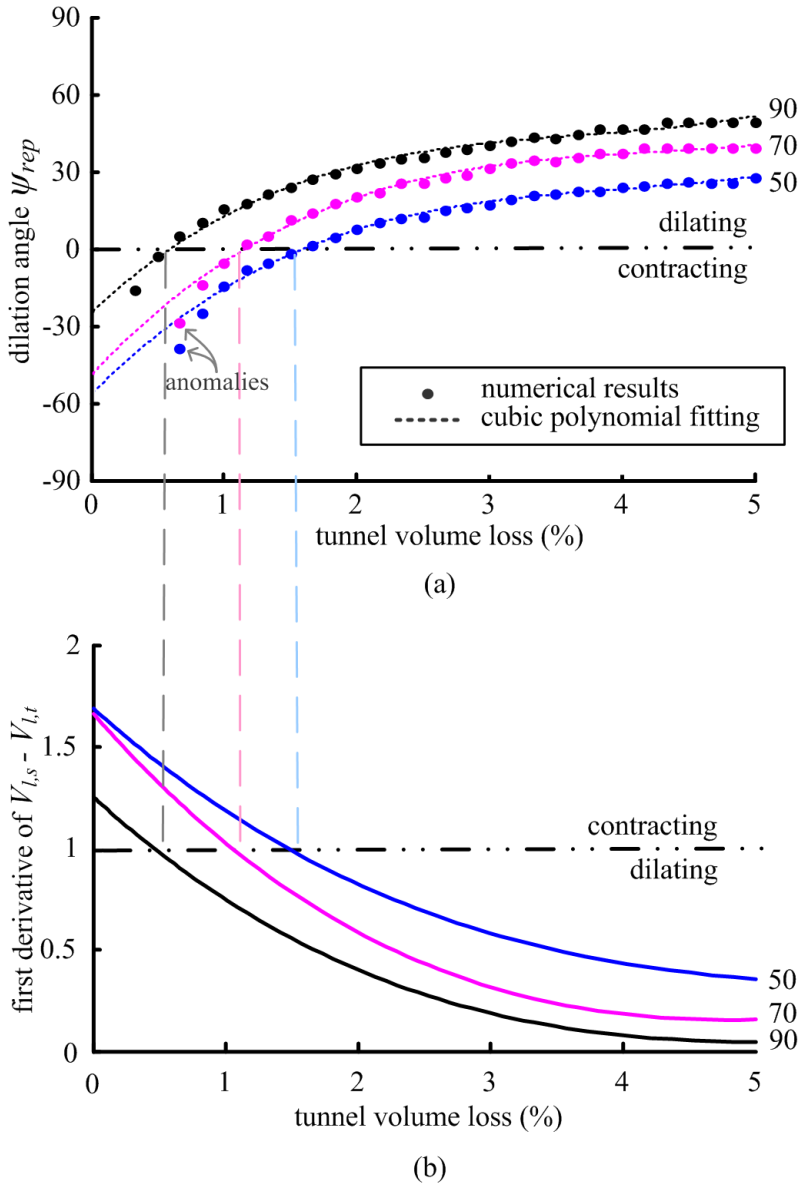

Figure 5.4: Trend of dilation angel with tunnel volume loss

Zhao [2008] performed a series of standard triaxial compression tests on the same

Fraction E sand that was used in this research. The sand was at a relative density of 70% and at a confining stress, $p'_0 = 100$, 200 or 400 kPa. A standard triaxial compression was then conducted, during which only the major principal stress changes. Figure 5.5 presents the variation of volumetric strain and dilation angle with shear strain in the three triaxial tests.

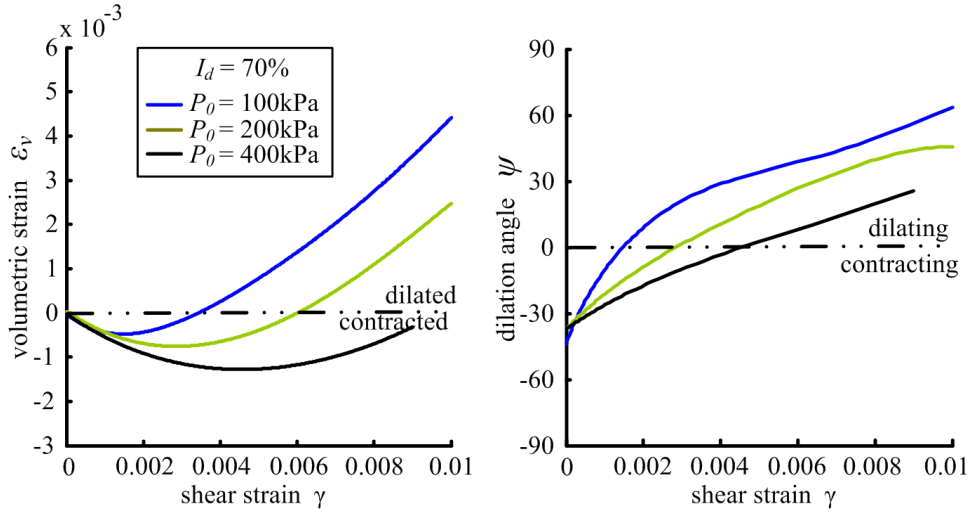

Figure 5.5: Triaxial tests on Fraction E sand by Zhao [2008]

The trend of $\psi - \gamma$ from the triaxial tests looks similar to that of $\psi_{rep} - V_{l,t}$ from the numerical solution in Figure 5.4. It is probably reasonable to assume a a linear relation between γ and $V_{l,t}$. The values of γ are multiplied by a empirical parameter, $T_{\gamma-Vl}$, in order to fit $\psi - \gamma$ curves to $\psi_{rep} - V_{l,t}$ data from Test 70. The fitting method is to match the points of $\psi = 0$. The quality of fit is evaluated by the coefficient of determination, R^2 (values closer to 1 indicate a better fit), showed in Figure 5.6. The curve of $\psi - \gamma$ at $p'_0 = 100$ kPa performed better then the others and this value of p'_0 is near the half value of overburden pressure in Test 70 (255 kPa at tunnel axial level).

The triaxial test can not replicate the plane-strain condition in the centrifuge tests, but considering the difficulty and complex of a plane-strain test on sand (e.g. the simple shear test), it is probably acceptable to adopt the data from triaxial test.

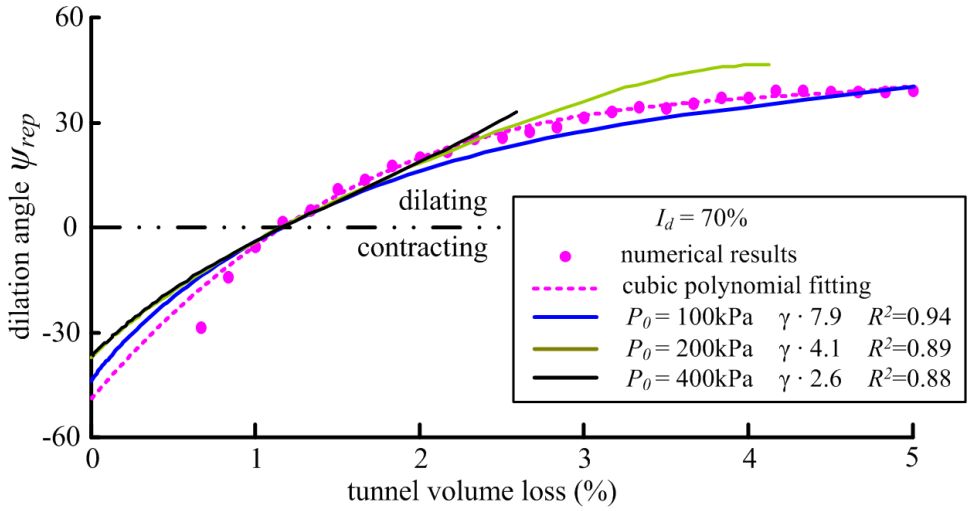

Figure 5.6: Fit $\psi - \gamma$ curves to $\psi_{rep} - V_{l,t}$ data

5.4 Chapter summary and further work

This chapter studied the volumetric deformation of sand caused by tunnelling. The cavity expansion method and the half-space elastic solution were used to examine the trend of dilation angle with tunnel volume loss. The following is a summary of the most pertinent findings:

1. The size of plastic zone was relatively steady after $V_{l,t} = 2\%$.
2. The soil was contracting initially and then dilating with the progress of tunnel contraction in each test.
3. The 'contracting-dilating' transition occurs later in looser sand.
4. The dilation angle generally increased with an increase in the relative density of sand.
5. The $\psi_{rep} - V_{l,t}$ data was compared against the test results of $\psi - \gamma$, and it was validated that the volumetric deformation within the ground was due to the shear strain in the soil around tunnel.

More triaxial tests could be performed on sand at a range of relative density and p'_0. The relations of $\psi - \gamma$ could be fitted to the $\psi_{rep} - V_{l,t}$ data for Test 90, 70 and 50 in order to examine if there is a constant value of the fitting parameter, $T_{\gamma-Vl}$. Furthermore, this solution may be inversely used to predict the relation of $V_{l,s} - V_{l,t}$ by that of $\psi - \gamma$ (or $\epsilon_v - \gamma$) from triaxial or other in-situ tests. This method requires one empirical parameter, $T_{\gamma-Vl}$. The relation of $p - p_0$ that determines the plastic radius is almost identical for sand with varied relative densities.

Note that the applicability of the solution in this Chapter is somewhat limited. As mentioned previously, the cavity expansion method is a solution for contracting cavities in an infinite soil medium, so that this method is more accurate for deep tunnels with larger C/D_t ratios but less accurate for lower C/D_t ratios.

Chapter 6

DISCRETE ELEMENT METHOD

6.1 Introduction

The discrete element method (DEM) has been shown to be a suitable method for the analysis of tunnelling induced ground displacement [Bym et al., 2012; Marshall et al., 2009, 2010a] as it can replicate complex soil behaviour using only inter-particle contact models. This chapter evaluates the capability of DEM to accurately predict the effect of relative density. DEM models were developed to simulate the three plane-strain geotechnical centrifuge experiments in Group 1. Three DEM simulations were conducted with particle relative densities of 90%, 70% and 50%. The DEM models were developed using PFC^{3D} and made to replicate the conditions of the centrifuge experiments, including geometry, boundary conditions, and elevated gravity. The tunnel and volume loss (water extraction) were represented in the DEM models using designated subroutines created to replicate the membrane behaviour.

A comparison of the magnitude and shape of ground displacements measured in the centrifuge and DEM analyses is provided. Data related to the volumetric behaviour of the soil and DEM samples is also provided, as well as a discussion on how this affects ground settlements. Because soil above the tunnel moves downwards as a rigid body in a chimney-like fashion at low volume loss, the effect of relative density and volumetric deformation on settlements at low volume loss is small. The research focuses on the ground displacements at 3% tunnel volume loss.

The research presented in this chapter are collaborations between Bo Zhou, Itai Elkayam and Alec M. Marshall. The DEM model was mainly created by Itai Elkayam.

6.2 DEM model

The DEM code PFC^{3D} of ITASCA^{TM} was used for the solution of the equations of motion of the particles. The PFC^{3D} model was created as a replica of the

physical conditions of the centrifuge model (same tunnel depth and diameter) and was also tested under the same gravity conditions ($80g$). A uniform particle size with radius of 2.5 mm was used to represent the Fraction E sand used in the centrifuge tests. The particle size effect was evaluated in Marshall et al. [2009] and the 2.5 mm diameter was shown to give good results for a similar problem with reasonable model run times. The Hertz-Mindlin contact and slip models [Itasca, 2008; Mindlin and Deresiewicz, 1953] with properties corresponding to quartz (density $\rho = 2600kg/m^3$, shear stiffness $G = 31 \cdot 10^7 kPa$, Poisson's ratio $\nu = 0.27$, and inter-particle friction coefficient $\mu = 0.5$) were used in the simulations. The boundaries were assumed to be frictionless in all the simulations.

Normally consolidated samples were prepared by (i) dropping the balls first under $1g$ to fill the box, (ii) reducing the the friction coefficient to a relatively low value and compacting the particles using a horizontal wall until the desired relative density was achieved, and (iii) increasing the friction and gravity to the required values and cycling to reach equilibrium. Upon reaching equilibrium, the relative density and coefficient of lateral earth pressure at rest ($K_0 = 0.5$) were verified. The relative density was calculated, in the DEM models, using the same maximum and minimum void ratios as in the centrifuge tests (for Fraction E sand), resulting with the same void ratios for the DEM and centrifuge models. As in the centrifuge test, three DEM tests were conducted on samples with relative density (I_d) values of 90%, 70% and 50% for comparison with the centrifuge test. The models contained 293600, 304081, and 315101 particles for the the $I_d = 50\%$, 70%, and 90% tests, respectively. The $I_d = 70\%$ model is shown in Figure 6.1.

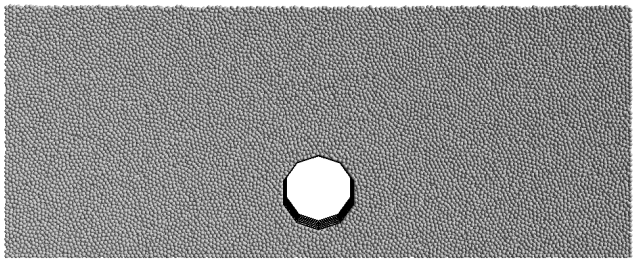

Figure 6.1: The DEM model of $I_d = 70\%$

The tunnel membrane and water extraction process, representing the tunnel and

volume loss in the centrifuge, were modelled using 50 wall elements that could move only in the radial direction, according to the following equations:

$$\begin{aligned} \bar{v}_i^{t+\Delta t/2} &= \bar{v}_i^{t-\Delta t/2} + \frac{\Delta F_i - 0.8\,|\Delta F_i|\, sgn\left(\bar{v}_i^{t-\Delta t/2} \cdot \hat{n}_i\right)}{M_{w,i}} \Delta t \cdot \hat{n}_i \\ \Delta F_i &= \left(P_w^t + \rho_w g\,(z_i - z_t)\right) \cdot A_i + \bar{F}_{g,i}^t \cdot \hat{n}_i \\ P_w^t &= P_w^{t-\Delta t} + \frac{K_w}{V_0}\left(Q - \sum_{i=1}^{N} A_i \bar{v}_i^{t-\Delta t/2} \cdot \hat{n}_i\right) \Delta t \end{aligned} \tag{6.1}$$

where $\bar{v}_i$ is the velocity of each of the N walls which make up the membrane, ΔF_i is the out-of-balance force in the radial direction of the tunnel, $F_{g,i}$ is the particle force acting on wall i, P_w is the water pressure at the axis level of the tunnel (at depth z_t), $\hat{n}_i$ is the outer normal vector to the each of the N walls, Δt is the explicit scheme time step, $M_{w,i}$ is the mass of each wall defined to keep the critical time step as that defined by PFC^{3D}, A_i is the area of each wall, z_i is the depth to the centre of wall i, and ρ_w is the water mass density. Because the latex membrane does not contribute to the stiffness of the system, but simply transfers water pressure to the model tunnel, this representation ($\bar{v}_i$) of the independent radial motion of the walls is accurate. P_w is responsible for the simulation of fluid extraction under a constant volumetric rate of Q (negative value for water extraction). K_w is the water stiffness, and V_0 is the initial volume of water in the tunnel.

6.3 Result and comparison

Excavation of underground tunnels can lead to shear strains within the surrounding ground. The shear strain causes dilation or contraction in drained soils, depending on the magnitude of shear strain and the soil type. The complicated variation of shear strain in the soil leads to difficulty in the prediction of the magnitude and shape of the resulting settlement trough [Marshall et al., 2012]. Moreover, the relationship between shear and volumetric strain are dependant on the characteristics of the soil, the confining pressure, and the relative den-

sity. This section presents data from the three centrifuge experiments and three DEM simulations in which the only variable that was changed was the relative density of the sand/particles: dense $I_d = 90\%$, medium dense $I_d = 70\%$ and loose $I_d = 50\%$. The results of the centrifuge tests and the DEM simulations are compared to evaluate the ability of the DEM method to replicate real trends in soil behaviour during the tunnelling process.

Figure 6.2 presents contours of vertical displacement from the ground surface to the tunnel crown at a tunnel volume loss, $V_{l,t} = 3\%$ for the three centrifuge tests and DEM simulations. A localized zone of large settlement is observed above the tunnel crown in this Figure. In both the centrifuge and DEM tests, the general trend of magnitude of settlements increases from $I_d = 90\%$ to 70% and 50%. This trend illustrates the effect of volumetric strain behaviour (contraction/dilation) on the tunnelling induced settlements. There is generally good agreement between the centrifuge and DEM results for $I_d = 90\%$ and 70% except that the settlements at the surface are slightly lower in the DEM analysis. For $I_d = 50\%$, the comparison between centrifuge and DEM results is not as good. The DEM settlements are considerably larger than for the centrifuge test. The DEM particles experienced a greater degree of volumetric contraction than the real sand in the centrifuge tests. This will be demonstrated later in discussing the relative values of soil volume loss between the tests. There may also have been an effect of the boundaries in the DEM analysis since the distance from the tunnel to the model boundary, with respect to particle diameters, was much less for the DEM simulation than the centrifuge test. Vertical displacements did not go to zero at the lateral boundaries of the DEM model, and therefore the symmetric nature of the model (due to the frictionless lateral boundaries) could have had an influence on measured displacements.

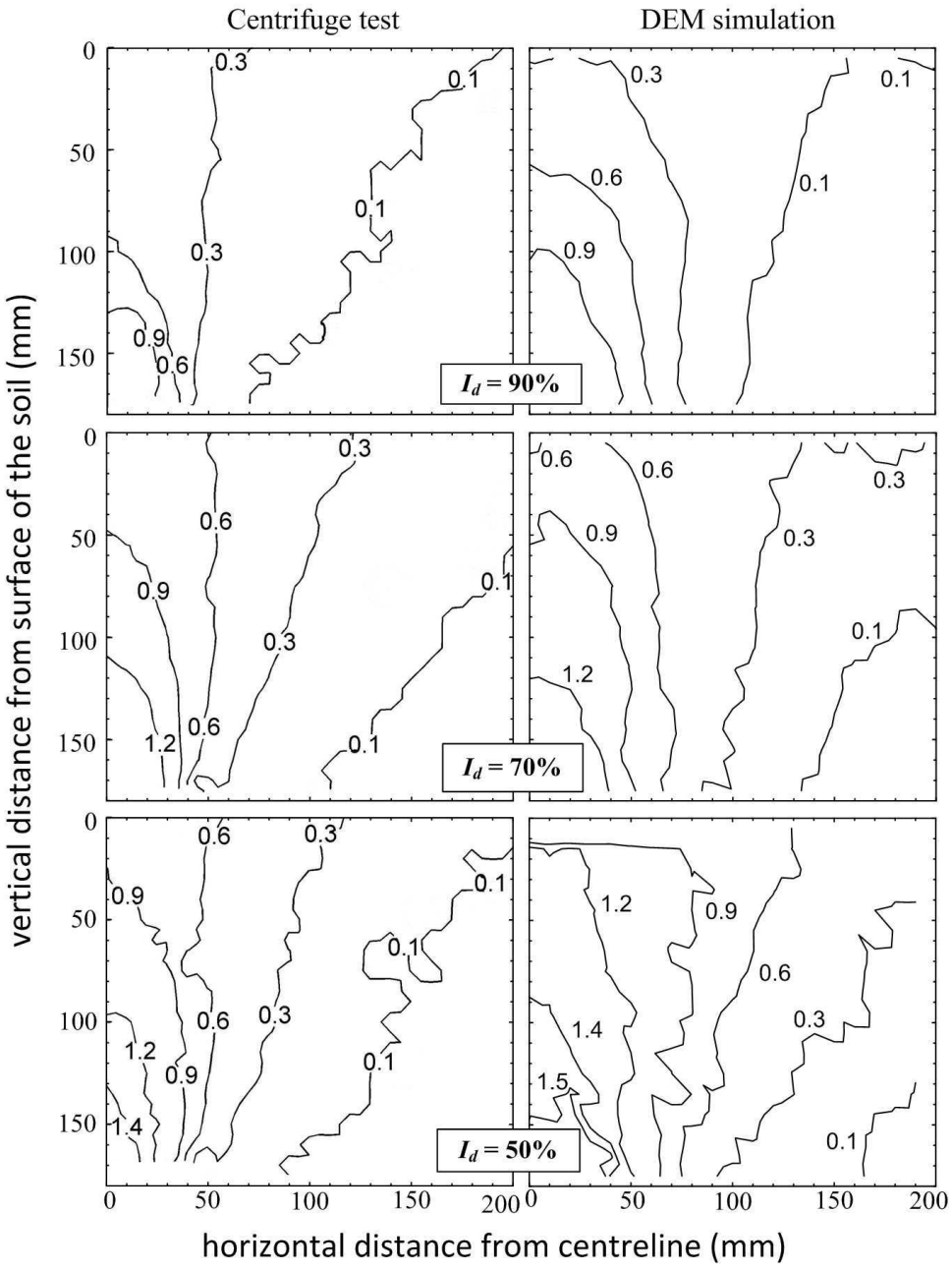

Figure 6.2: Contours of vertical displacement when $V_{l,t} = 3\%$

The variation of S_{max} (above the tunnel centreline) with depth at $V_{l,t} = 3\%$ is presented in Figure 6.3. There is generally good agreement between the centrifuge and DEM data. The value of S_{max} increases approximately linearly with depth and decreases with an increase of relative density. The slope of S_{max} with depth is slightly less steep in the denser samples. The DEM S_{max} value near the ground surface for the loosest sample is larger than that of the centrifuge test, again illustrating that the DEM sample experienced greater levels of volumetric contraction than the real soil.

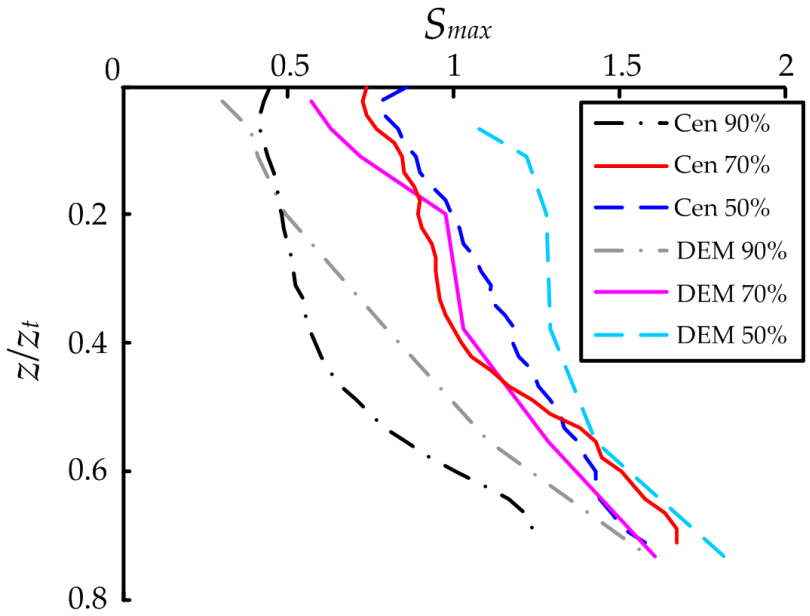

Figure 6.3: Variation of S_{max} with depth ($V_{l,t} = 3\%$)

In order to analyse and compare the settlement trough shape, and for the evaluation of the effect of tunnelling on buildings and other infrastructure, it is useful to fit a curve to settlement data. A modified Gaussian curve can often provide a better fit to observed settlements above tunnels in sands than the standard Gaussian curve. The modified Gaussian curve was fitted to the settlement data from the centrifuge and DEM tests using a least-squares method in order to evaluate the trough shape parameters.

The trough width parameter, K^*, was used to characterise the shape of the

settlement trough ($K^* = x^*/(z_t - z)$, Section 4.3.3, p.123). Figure 6.4 shows the variation of K^* with depth when $V_{l,t} = 3\%$ for the DEM and centrifuge data. Also included is the trend obtained using Equation 4.5 (p.126). The values of K^* are noted to remain relatively constant $(0.3 - 0.5)$ with depth in all the three centrifuge tests and the DEM simulation of initial $I_d = 90\%$. However, the values of K^* in DEM 70 and 50 increase steeply with depth at z/z_t of $0.2 - 0.8$, which means the values of x^* don't decrease as quickly with depth for these tests. This indicates that the shape of the settlement trough does not change as quickly with depth and therefore the DEM results for these tests don't give a good prediction of the transition of settlement trough shape with depth, especially at depths approaching the tunnel.

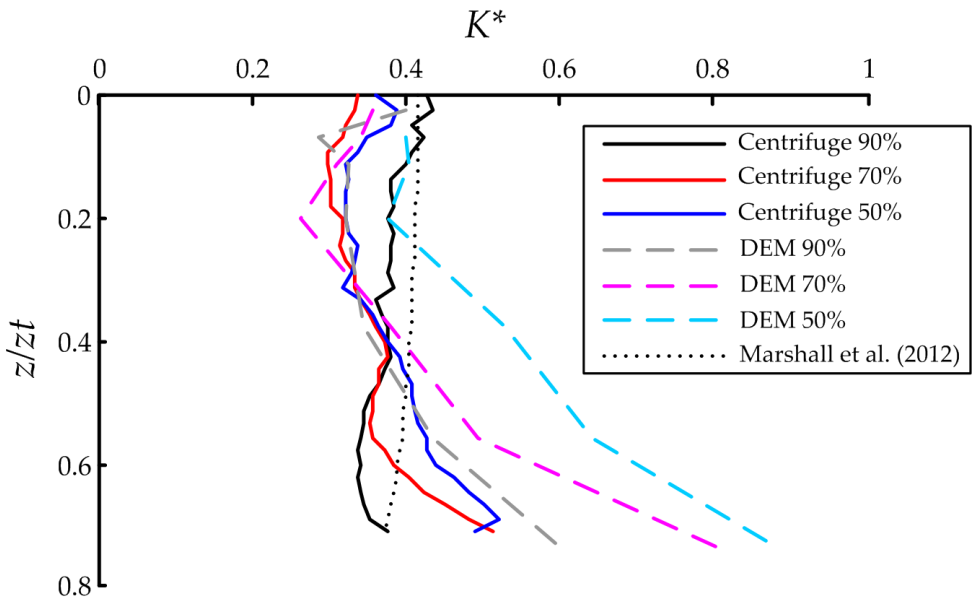

Figure 6.4: Variation of K^* with depth at $V_{l,t} = 3\%$

Figure 6.5 shows the settlements near the ground surface at $V_{l,t} = 3\%$ for the centrifuge and DEM data. Note that the data is from 'near' the ground surface (at $z/z_t = 0.07$) because of some abnormal displacements of the DEM particles at the surface. Both the centrifuge tests and the DEM simulations indicate that the settlement in dense sands is significantly lower than that in looser sands. The agreement between the centrifuge and DEM data for $I_d = 90\%$ and 70% are better

than that of $I_d = 50\%$. As discussed earlier, for sands the volume loss experienced by the soil ($V_{l,s}$) may not equal the volume loss of tunnel ($V_{l,t}$) because of the volumetric changes that occur in the soil during shear. At this stage of $V_{l,t} = 3\%$, the values of $V_{l,s}$ for $I_d = 90\%$ and 70% from both centrifuge and DEM data are all less than $V_{l,t} = 3\%$, so they indicate that the soil is dilated due to the tunnelling. In comparison, the values of $V_{l,s}$ for $I_d = 50\%$ from both centrifuge and DEM data are all more than 3%, so they indicate that the soil is contracted due to the tunnelling. The DEM model was generally able to replicate the trend of change of soil volume loss with relative density, however the magnitudes of soil volume loss did not agree very well with the centrifuge test data.

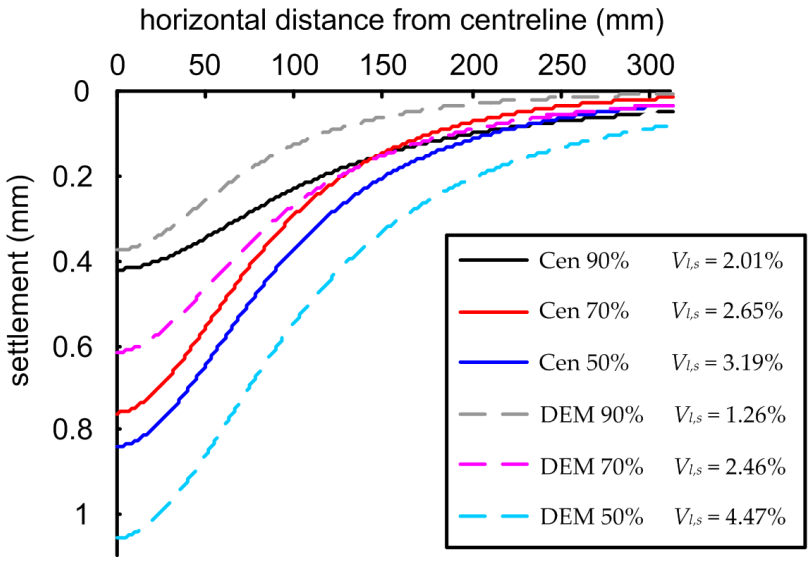

Figure 6.5: Comparison of settlement troughs (z/z_t=0.07, $V_{l,t} = 3\%$)

Figure 6.6 shows the profiles of normalised vertical settlements S_v/S_{max} near the ground surface ($z/z_t = 0.07$) for $V_{l,t} = 3\%$. Note that when $x = x^*$, $S_v = 0.606S_{max}$. The centrifuge tests indicate that the settlement trough for $I_d = 90\%$ is wider than that for $I_d = 50\%$ and 70%. The trend from the DEM data, however, does not agree with this and shows that the trough becomes narrower as relative density increases.

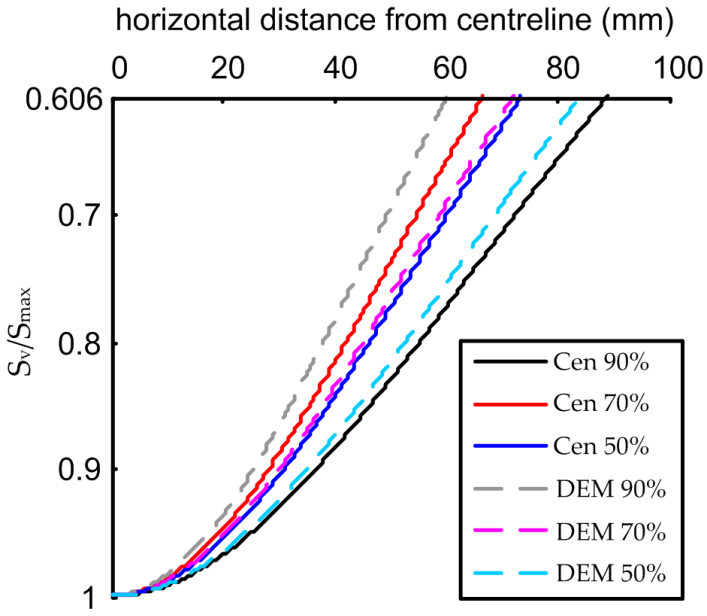

Figure 6.6: Comparison of normalised settlement troughs ($z/z_t = 0.07$, $V_{l,t} = 3\%$)

6.4 Chapter summary

This chapter presented data related to tunnelling-induced ground displacements in sands with different relative densities and compared centrifuge test and DEM simulation data. Reasonable agreement was obtained in the vertical displacements for $I_d = 90\%$ and 70% as well as the general trend of the effect of I_d on settlement, where the magnitude of settlement at the ground surface was shown to decrease as relative density was increased. Nevertheless, the settlement in the loose sample from the DEM simulation was larger and wider than that of the centrifuge test. The DEM analysis over-predicted the magnitude of contraction of the soil in the loose sample tests, which had an impact on the DEM predictions of settlement trough shape. The DEM simulations were not able to replicate the trend of settlement trough width with relative density. One possible reason may be the the definition of relative density in DEM, as the void ratio range may much narrow compared to that of real sand. Further research can be done in order to examine the use of different particle sizes as well as particle shape.

Chapter 7

TUNNELLING IN LAYERED SAND

7.1 Introduction

This chapter reports the centrifuge test results in Group 2 (Figure 7.1) and examines the effect of stratification on settlements above tunnels. The experimental methods and apparatus for this research were described in Chapter 3 (p.33). The soil sample was stratified with different relative densities (I_d = 90% or 50%) and the thickness of each layer above the model tunnel is equal to the tunnel diameter, 90 mm, so the cover to diameter ratio, C/D_t = 2.0. The soil movement data was obtained by GeoPIV and analysed to determine features of greenfield settlement, both surface and subsurface. The data from tests in Group 2 was compared with that form Group 1 (Figure 7.1). The interaction of two layers and its effect on the settlement trough shape are demonstrated and discussed. Some interesting features of tunnelling in layered sand were revealed in the analysis.

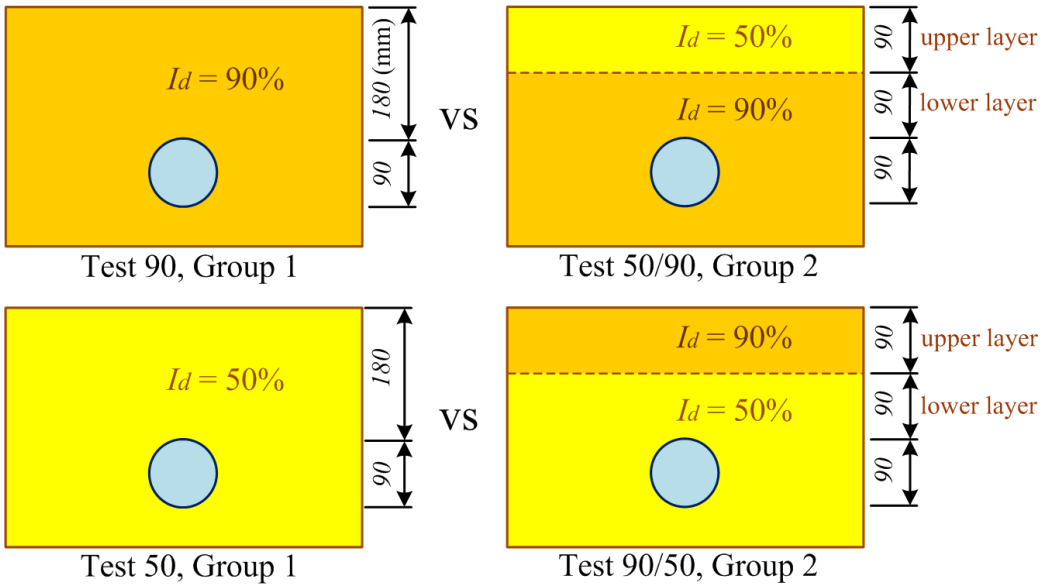

Figure 7.1: Comparison between Group 1 and Group 2

The centrifuge test results are reported in Section 7.2 (p.169) and then the data is analysed to determine the features of settlements in Section 7.3 (p.182). Because the soil above the tunnel moves downwards as a rigid body in a chimney-like shape at low volume loss, the effect of relative density and volumetric deformation on settlements at low volume loss is not obvious. The research mainly forces on the

displacements at 3% tunnel volume loss.

Most previous research assumed a homogeneous ground, but for real cases, tunnels are often constructed in layered ground. Selby [1988] and New and O'Reilly [1991] suggested that the trough width (i) of the surface settlement trough for layered ground could be simply estimated from the trough width parameter (K) for each layer and the thickness of each layer. For example, i for a two-layered ground would be calculated as:

$$i = K_1 z_1 + K_2 z_2 \tag{7.1}$$

where K_1 is the trough width parameter for the soil type in layer 1 of thickness z_1 and K_2 is the trough width parameter for soil type 2 for thickness z_2. This prediction do not consider the interaction of layers. Field observation at ground surface suggested that for sands overlain by clays layers wider settlement trough were obtained than that in sand alone [Ata, 1996; Atahan et al., 1996]. There is, however, less evidence for cohesionless soils overlying clays. Grant and Taylor [1996] used centrifuge tests to study the ground movements cased by a tunnel in soft clay overlain by sand. In this case the settlement trough was observed to be wider than that in soft clay only, which did not agree with the narrowing estimated by Equation 7.1. This is probably a result of the overlying sand layer being significantly stiffer than the soft clay [Mair and Taylor, 1997]. The relative stiffness should be considered for the interaction of soil layers.

7.2 Centrifuge test results

Two centrifuge tests were completed in Group 2 to investigate the tunnelling in layered sand. The tests were identical in all aspects except the relative density of the soil sample: loose sand overlying dense sand (Test 50/90) and dense sand overlying loose sand (Test 90/50). In comparison with Test 50/90, Test 90/50 is uncommon in real cases. The research on both tests nevertheless is useful in understanding the mechanism of tunnelling in layered sand.

Relevant dimensional parameters of the tests were showed in Figure 7.1 (p.168). The cover, C, is 180 mm (= 90 mm + 90 mm), measured from soil surface to tunnel crown. Given 90 mm tunnel diameter, the cover to diameter ratio, C/D_t, is 2.0. All results in this research are presented using model scale unless prototype scale stated.

7.2.1 Tunnel pressure

During the tests, the pressure sensor (Section 3.3.4.4, p.58) measured the variation of tunnel pressure with volume loss. Figure 7.2 presents the tunnel pressure normalised by its initial value.

The variation of p/p_0 are almost identical for the Test 90, 70 and 50 in Group 1 with homogeneous sand sample. The relation for Test 50/90 is generally same with that for Group 1 at $V_{l,t}$ = 0%-3.5%, while there are small increases in tunnel pressure after $V_{l,t}$ = 3.5%. The increases indicated the evidence of soil collapse in Test 50/90, as the loading recovery stage in the ground reaction curve (Figure 2.4, p.11). The value of p/p_0 for Test 90/50 is relatively higher then that for all the other tests. The dense sand in upper layer acted as a surcharge loading onto the tunnel.

7.2.2 Soil displacements

This section presents the displacements data of soil in Group 2. The data was obtained using the GeoPIV technology (introduced in Section 3.3.5, p.59) to analysis the photographs of soil behind the Perspex wall taken during the tests. The displacements are illustrated in form of coloured contours. The contours for Test 50/90 and 90/50 are compared with that for Test 90 and 50, respectively, in the following two subsections.

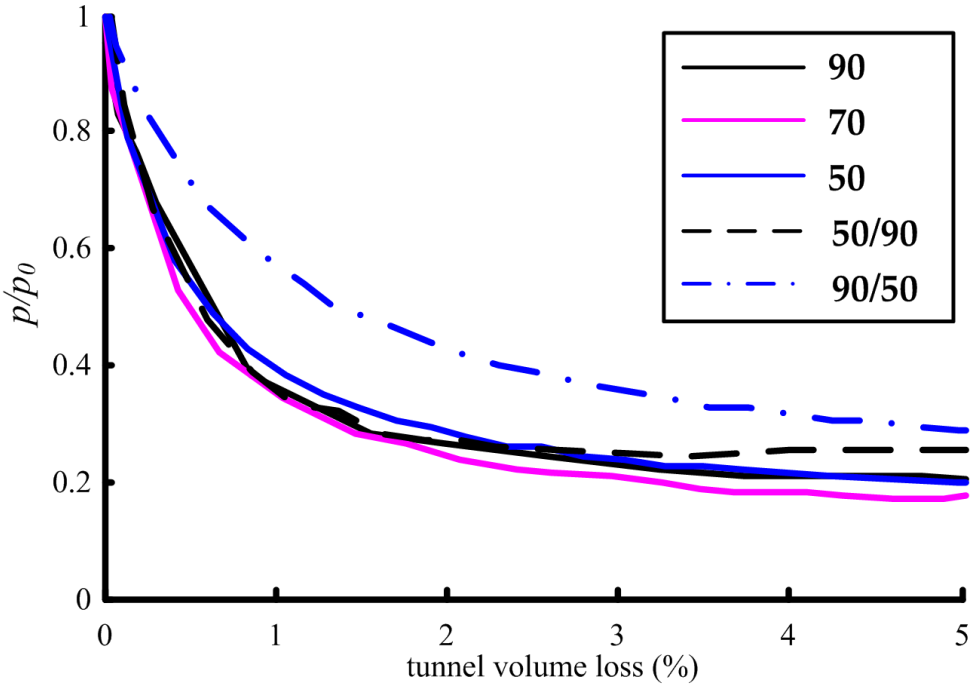

Figure 7.2: p/p_0 with volume loss - Group 2

7.2.2.1 Vertical soil displacements in Test 50/90

Contours of vertical displacements for Test 90 and 50/90 are shown in Figure 7.3 (p.173). Some of the displacement vectors are also shown as a reference and the vectors are scaled up by 15 times. The ratio of settlements for Test 50/90 to 90 is presented in the third profile.

The major settlements are mostly in the area between ± 100 mm offset from tunnel centreline in Test 90 and 50/90. The localised settlement zone directly above the tunnel crown is observed for both of tests. The displacement ratio in centre above the interface (x between ± 80 mm, y = 0 - 90 mm) is about 1.5-2.0, and the ratio in centre beneath the interface is approximate 1.2-1.4, while the ratio at two sides is less than 1, about 0.4-0.8 (narrower settlement trough). The greater displacements in centre and smaller movements at sides indicate a narrower settlement trough for Test 50/90.

There probably are two reasons for the narrowing. Firstly, it has been found that

the settlement trough near ground surface in loose sand is narrower than that in dense sand (Section 4.3.3, p.123). Secondly, the density, stiffness and strength of loose sand is lower than that in dense sand, so that the performance of lower layer in Test 50/90 may fall somewhere between Test 90 and Test 90_{CD1} (Figure 7.4, p.174). Marshall et al. [2012] showed that the trough width decreases with C/D_t ratio and therefore the trough width in Test 50/90 is lower than that in Test 90.

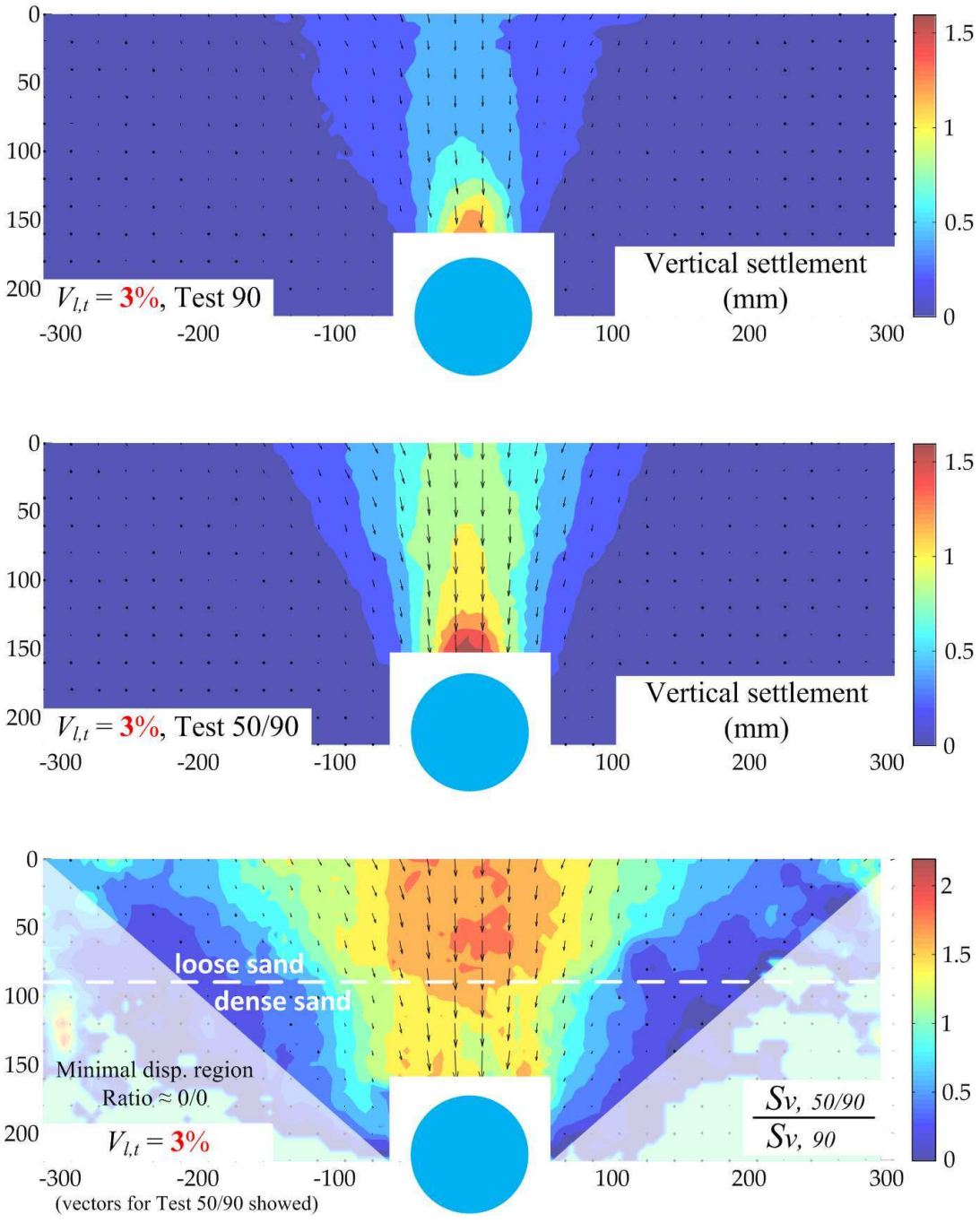

Figure 7.3: Vertical displacement contours - $V_{l,t}$ = 3%, Test 90 and 50/90

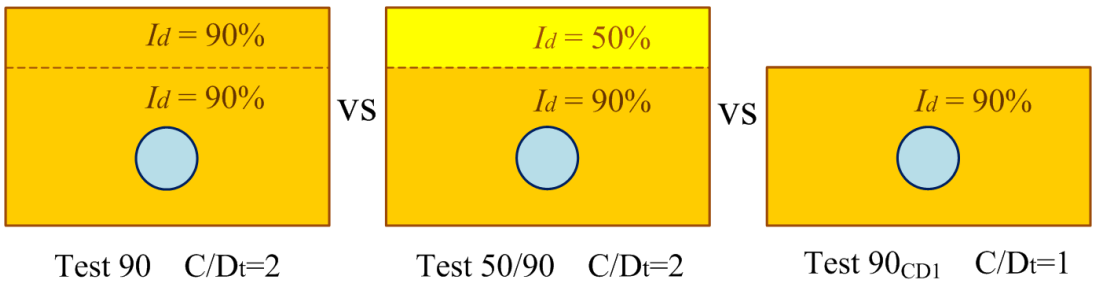

Figure 7.4: Assumption on the effect of loose upper layer

7.2.2.2 Vertical soil displacements in Test 90/50

Contours of vertical displacements for Test 50 and 90/50 are presented in Figure 7.5 (p.175). Some of the displacement vectors are also shown as a reference and the vectors are scaled up by 15 times. The ratio of settlements for Test 90/50 to 50 is presented in the third profile.

The distribution of the ground movements in Test 90/50 is obviously wider than that in Test 50 and the magnitude of displacement in Test 90/50 is larger. There is no much variation and obvious localisation of the displacements above the tunnel for Test 90/50. The third profile shows that the values of settlement just above the tunnel crown are almost same in the two tests. The displacement ratio in centre from 110 mm depth to surface is around 1.25 while the ratio at two sides is larger, about 1.4-1.7. The larger increase of settlement at sides indicates a wider settlement trough for Test 50/90.

Test 50/90 simulated the tunnelling in loose sand overlain by dense sand with greater stiffness. Similarly, the tunnelling in soft clay overlain by much stiffer sand was modelled by centrifuge tests showing a wider settlement trough (mentioned in Section 7.1, p.168).

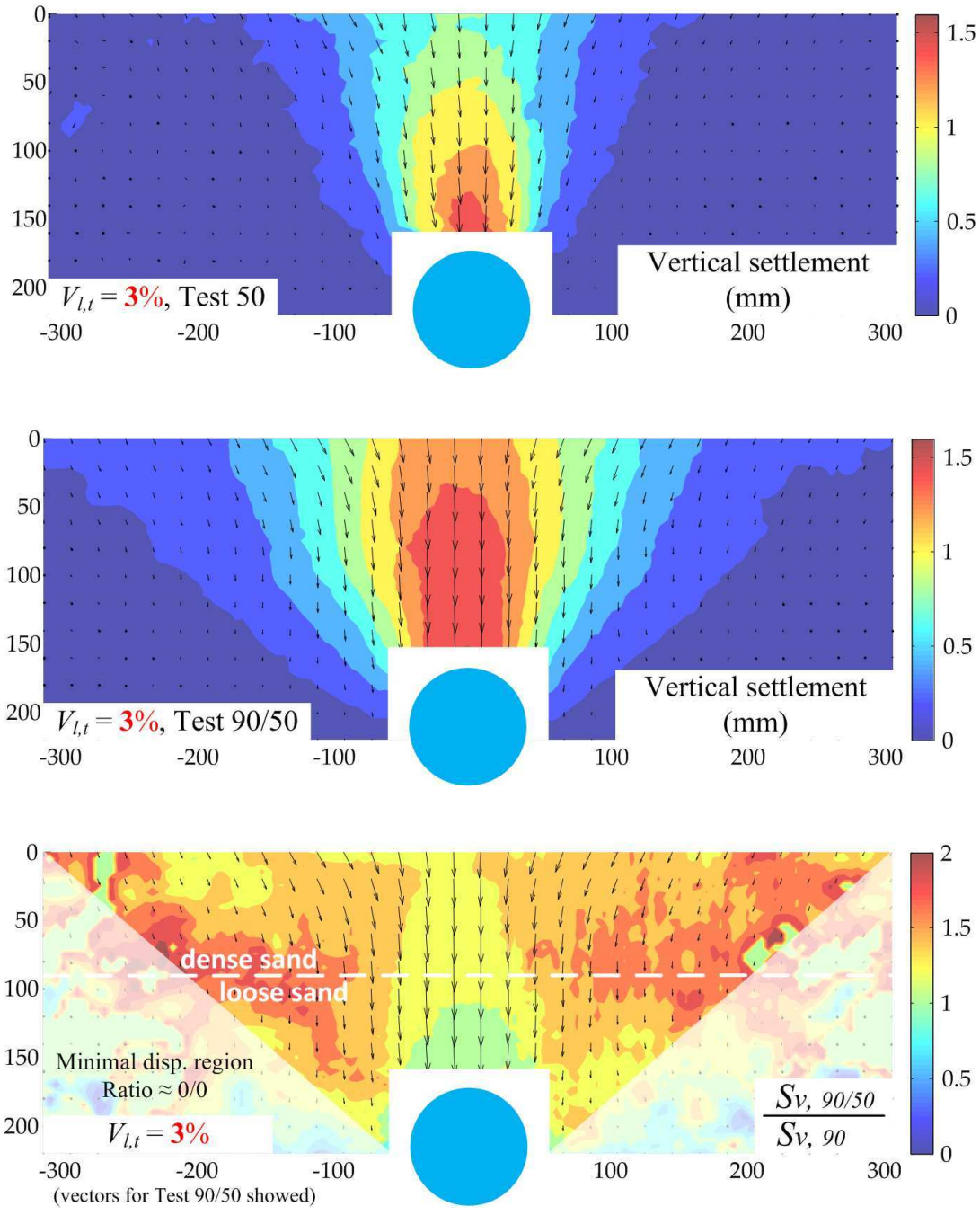

Figure 7.5: Vertical displacement contours - $V_{l,t}$ = 3%, Test 50 and 90/50

7.2.3 Soil strains

This section presents the contours of engineering shear strain and volumetric strain distributions within the soil behind the Perspex window. The definitions of engineering shear strain (γ) and volumetric strain (ϵ_v) were introduced in Section 4.2.4 (p.97). The term 'shear strain' implies engineering shear strain in this discussion. The PIV displacement data was used to calculate the strains. The data of soil displacements was input into the mechanics computation program, FLAC (ITASCA^{TM}), to calculate the stain data. Section 4.2.4.1 (p.98) evaluated the errors in strain profiles.

Again, the stain contours for Test 50/90 and 90/50 are compared with that for Test 90 and 50, respectively, in the following two subsections. The PIV displacement vectors that were used to calculate strains are presented as a reference.

7.2.3.1 Soil strains in Test 50/90

Figure 7.6 shows the shear strain in the soil for Test 90 and 50/90. The distribution of the shear bands in Test 50/90 is obviously narrower than that in Test 90. Two sets of shear bands in Test 90 are visible; one narrow and one wide (both indicated by white dash lines). However, only one set of shear band is visible above the tunnel in Test 50/90. The distance of the two shear bands above the tunnel in Test 50/90 is closer than that in Test 90 and the shear bands in Test 50/90 extend almost vertically from the tunnel shoulders towards the soil surface. The closer and vertical shear bands relate well to the narrower settlement trough in Test 50/90 (Section 7.2.2.1, p.171).

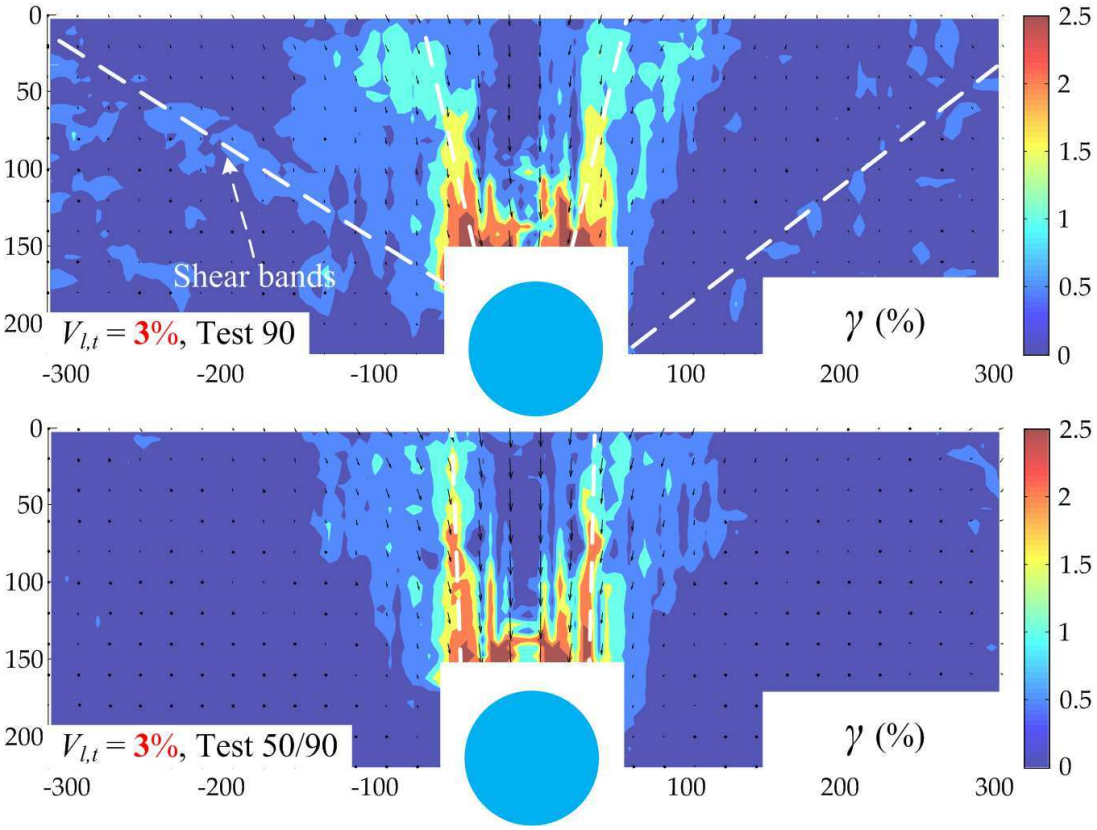

Figure 7.6: Shear strain - $V_{l,t}$ = 3%, Test 90 and 50/90

Figure 7.7 shows the volumetric strain in the soil for Test 90 and 50/90. The distribution of the volumetric strain in Test 50/90 is obviously narrower than that in Test 90. The volumetric contraction in Test 90 concentrated at two troughs, a narrow one and a wide one, which are indicated by white dash lines. There is, however, only one narrow contraction trough is visible in Test 50/90. In comparison with the volumetric strain for Test 90, the magnitude of both contraction and dilation in Test 50/90 is smaller. Section 7.2.4 (p.181) will show that the lower magnitude and narrower distribution of volumetric strain for Test 50/90 are associated with its feature of settlement trough compared to Test 90.

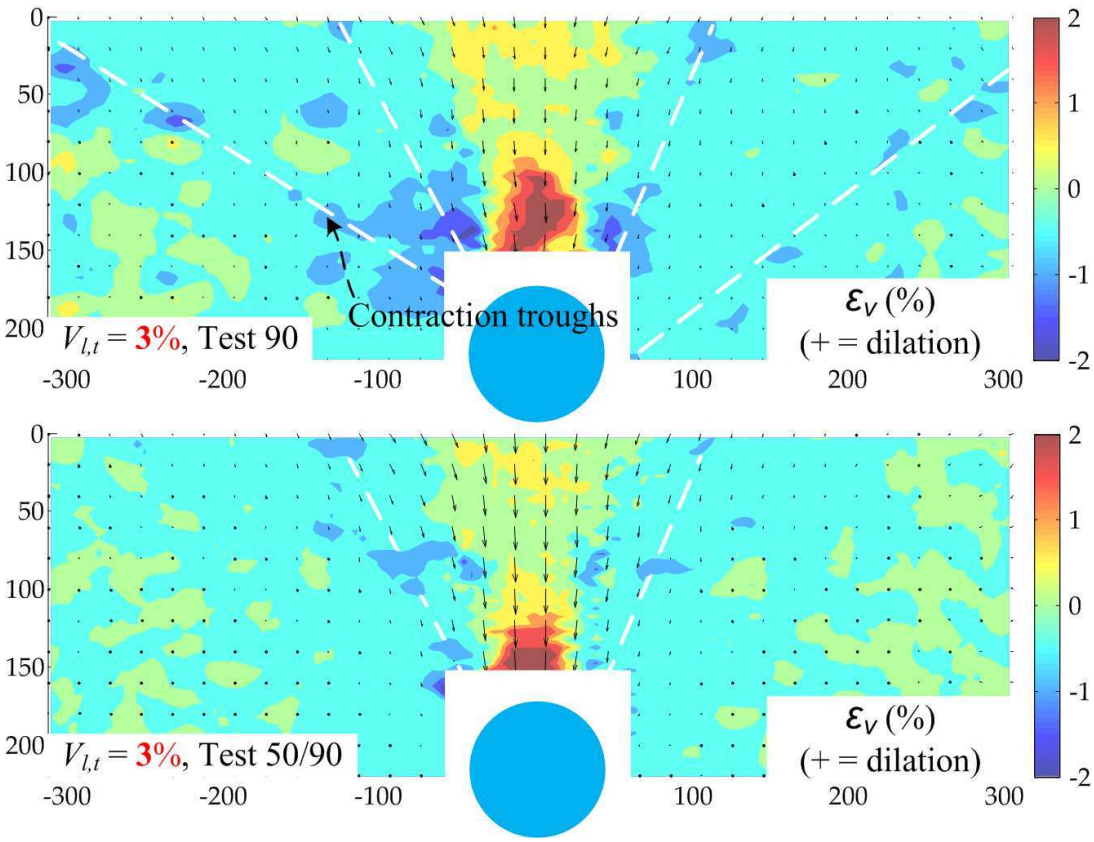

Figure 7.7: Volumetric strain - $V_{l,t}$ = 3%, Test 90 and 50/90

7.2.3.2 Soil strains in Test 90/50

Figure 7.8 presents the shear strain in the soil for Test 50 and 90/50. The magnitude of shear strain in Test 90/50 is significantly lower than that in Test 50. There are two sets of shear bands in Test 50 but only one set of shear band in Test 90/50.

The distribution of settlement for Test 90/50 was found to be quite wider than that for Test 50 in Section 7.2.2.2 (p.174). Because the dense sand in upper layer is stiffer than the loss sand in lower layer, the stiffer upper layer may restrict the development of shear band and extend the distribution of ground movements.

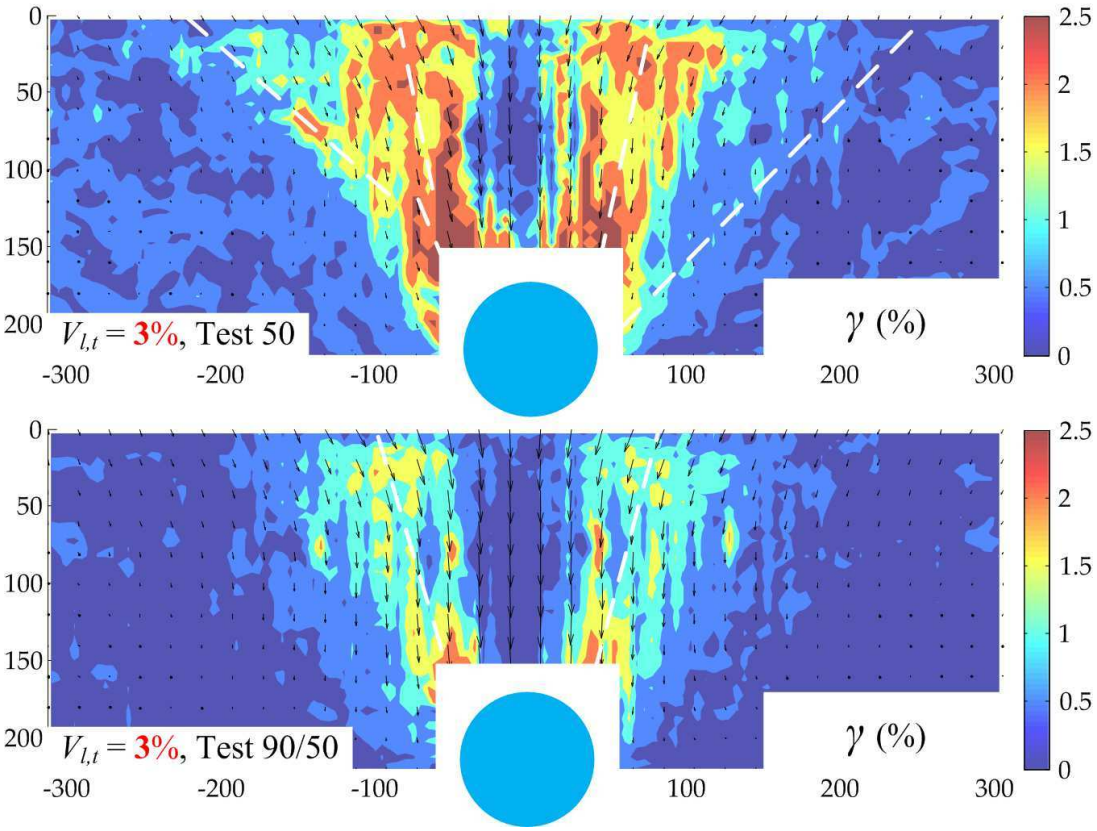

Figure 7.8: Shear strain - $V_{l,t}$ = 3%, Test 50 and 90/50

Figure 7.9 shows the volumetric strain in the soil for Test 50 and 90/50. The volumetric deformation within the sand is due to the development of shear strain, so that the smaller shear strain leads to the lower magnitude of volumetric strain. The magnitude of contraction for Test 90/50 are relavitly lower than that for Test 50 and the contraction zones for Test 90/50 is mainly in the lower layer with loose sand. Again, there is only one contraction trough in Test 90/50. In comparison with the large dilation zone in Test 50, the dilation for Test 90/50 nearly 'disappeared'. The 'disappeared' dilation is associated with the greater settlement in Test 90/50. Moreover, the micro volumetric deformation above the tunnel relates well to the small variation of the value of displacements observed in the contour profile (Section 7.2.2.2, p.174).

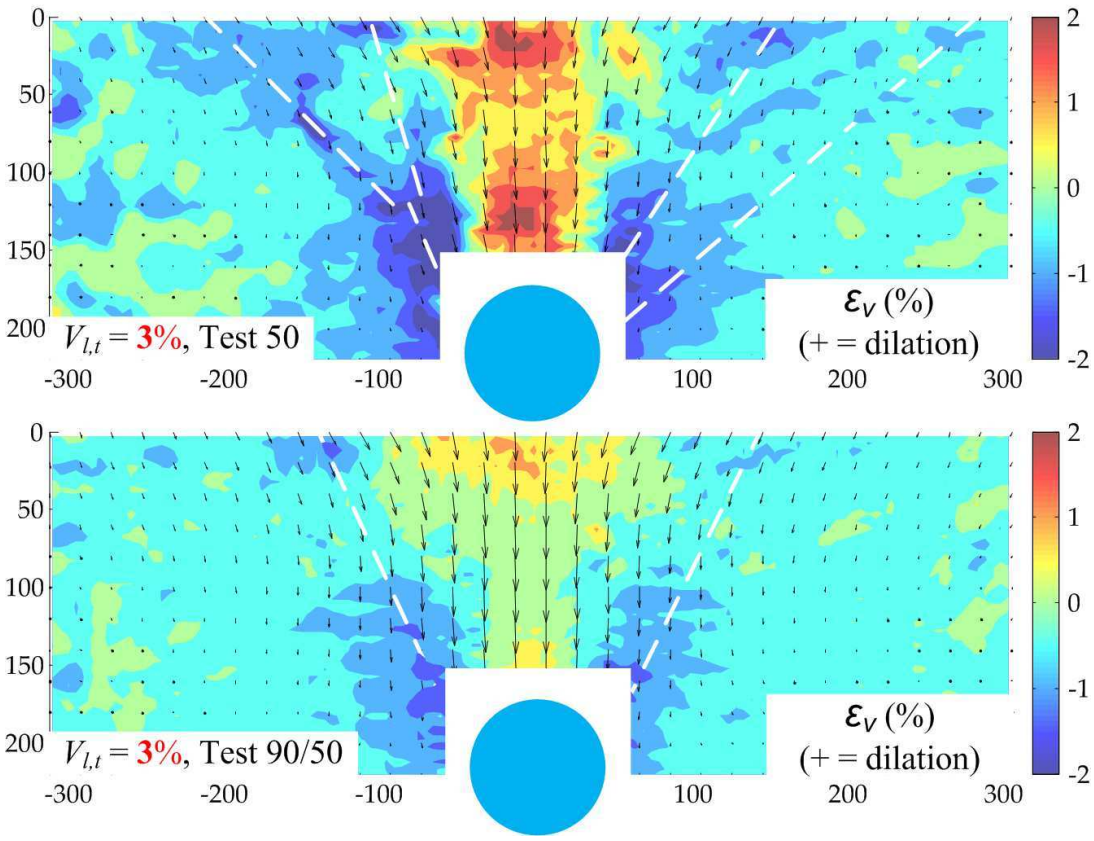

Figure 7.9: Volumetric strain - $V_{l,t}$ = 3%, Test 50 and 90/50

7.2.4 Settlement trough profiles

Figure 7.10 shows the surface settlement trough profiles for Test 90, 50/90, 50 and 90/50.

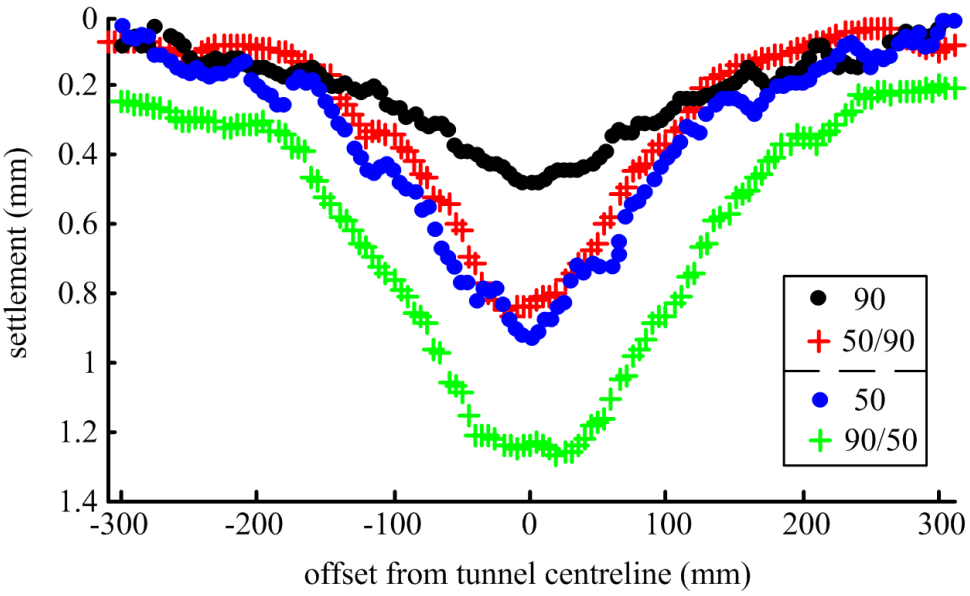

Figure 7.10: Settlement trough profiles for Group 2 ($V_{l,t} = 3\%$)

The settlement trough for Test 50/90 is narrower than that for Test 90. The value of displacements for Test 50/90 is larger between ± 120 mm offset but smaller outside of this area. In comparison with the settlement for Test 90, the greater settlement in centre and less settlement at sides for Test 50/90 are associated with its smaller dilation in centre and smaller contraction at sides (Section 7.2.3.1, p.177), respectively.

Both the trough width and the magnitude of settlement in Test 90/50 is larger than that in Test 50. In comparison with the volumetric deformation for Test 50, the strain contours for Test 90/50 (Section 7.2.3.2, p.179) showed that the decrease of dilation in 90/50 sand is considerably higher than that of contraction, leading to a larger soil volume loss at ground surface. Additionally, the values of settlement in centre (between ± 30 mm offset) are nearly uniform, probably due to the effect of stiffer upper layer. The settlement trough for Test 90/50 is

too wide and excesses the boundary of strong box. The value of soil movements along the steel side wall is about 0.25 mm at ground surface. The friction of steel against sand is lower than the friction between sand, so that the boundary effect may enhance the settlement in Test 90/50.

7.3 Analysis and discussion of results

A further analysis and discussion are provided by this section for tunnelling in layered sand. The presented results in Section 7.2 (p.169) showed soil movements affected by the interaction of two layers with different relative densities. The trough width of settlement in dense sand overlain by loose sand is narrower than that in dense sand with the same C/D_t ratio, which is like the feature for tunnelling with lower C/D_t ratio (Figure 7.4, p.174). The development of shear strain and volumetric strain is restricted for the tunnelling in loose sand overlain by dense sand and leads to the wider settlement trough. The magnitudes of dilation for Test 50/90 and 90/50 are significantly less than that for Test 90 and 50, respectively, and result in the greater settlements.

7.3.1 Fitting curves to settlement trough data

In order to analyse and compare the shape of settlement trough, it is useful to fit a curve to settlement data. The transverse settlement trough is generally described as a Gaussian distribution curve. Using the Gaussian curve, the settlement trough can be determined by the two variables, S_{max} and i (inflexion point). A better fit to settlements in sands could be obtained by a modified Gaussian curve, with an additional variable, α. The modified Gaussian curve has an additional degree of freedom compared to the Gaussian curve, which is more versatile for fitting to settlement data. The curves were fitted by Matlab© using a least squares regression technique.

Figure 7.11 shows the examples of the Gaussian and modified Gaussian curves fitted to the surface settlement data at 3% volume loss for Test 50/90 and 90/50.

'G' in the figure label means Gaussian distribution curve as well as 'mG' means modified Gaussian curve. The quality of fit is evaluated by the coefficient of determination, R^2 (values closer to 1 indicate a better fit). The modified Gaussian curve is shown to provide a better fit to the displacement data, while it could not describe the nearly-uniform settlement between ± 30 mm offset for Test 90/50. Additionally, the value of i is noted to be lower for the modified Gaussian curve compared to the Gaussian curve.

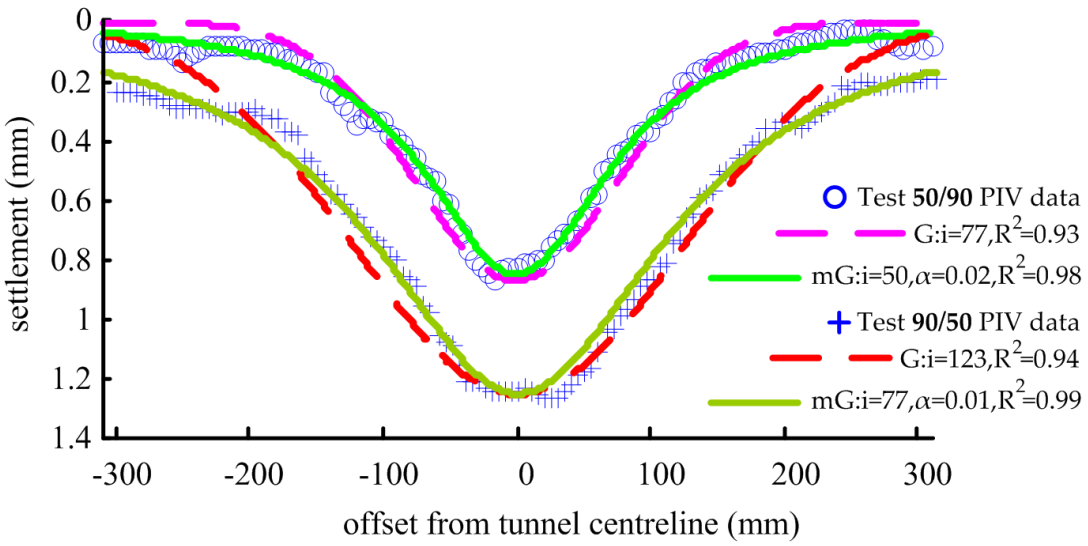

Figure 7.11: Fitting curves to PIV settlement data - $V_{l,t} = 3\%$, Group 2

The trend of R^2 for the Gaussian and modified Gaussian curves with depth is presented in Figure 7.12. The depth is normalised by the tunnel axial depth, as z/z_t $(z/225mm)$. The modified Gaussian curve provides a better fit than Gaussian curve at an arbitrary depth for tunnelling in layered sand.

7.3.2 S_{max}

Figure 7.13 compares the variation of S_{max} with depth for Test 50/90 and 90/50 to that for Test 90 and 50, respectively. The maximum settlement is almost constant from surface to subsurface in each test at $V_{l,t} = 1\%$, as a result of 'chimney' mechanism at low volume loss. At higher volume losses of 3% and

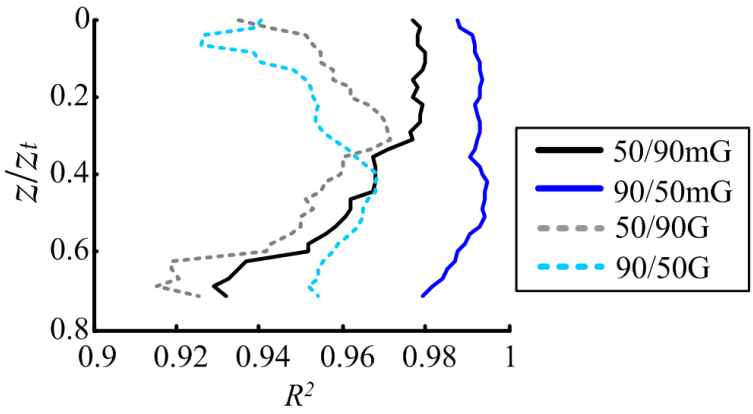

Figure 7.12: Quality of fit with depth - $V_{l,t} = 3\%$, Group 2

5%, the values of S_{max} for Test 90 and 50/90 start to increase rapidly blow the depth of $z/z_t = 0.45$ (Test 90) or 0.55 (Test 50/90), both indicating the severer localisation of settlement just above the tunnel within dense sand (mentioned in Section 7.2.2.1, p.171). The variation of S_{max} with depth for Test 50 and 90/50 is mostly linear. There is no much variation of S_{max} at $V_{l,t} = 3\%$ for Test 90/50. The differences of the S_{max} for both Test 90 vs 50/90 and Test 50 vs 90/50 become smaller at $z/z_t > 0.5$ (the interface of layers is at $z/z_t = 0.4$). Moreover, no dramatical variation of S_{max} is observed at the interface for Test 50/90 and 90/50, which could be attributed to the interaction of two layers.

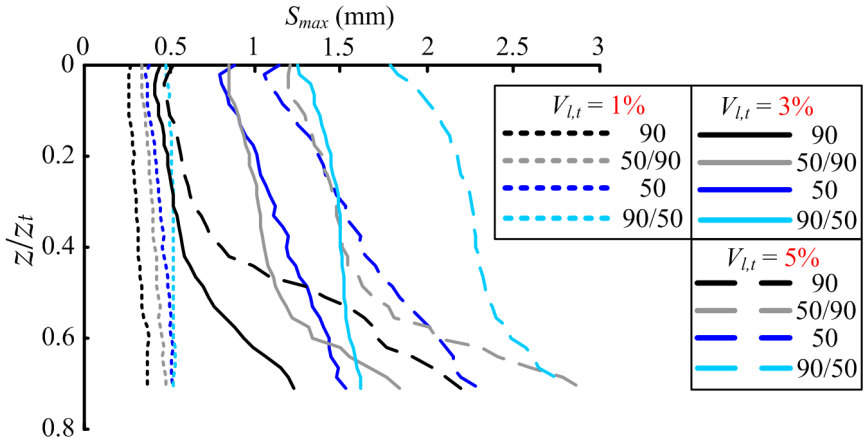

Figure 7.13: Variation of S_{max} with $V_{l,t}$ and depth - Group 2

7.3.3 x^* and x^{**} method to study trough shape

The trough width is generally decided by the value of i in standard Gaussian curve. However, the value of i in modified Gaussian curve cannot characterise the trough width properly because the vertical location of the inflexion point is affected by the additional parameter, α. Marshall et al. [2012] used x^* and x^{**}, as the location of $S_v = 0.606S_{max}$ and $0.303S_{max}$, respectively, to characterise the shape of the settlement trough for non-Gaussian curves.

Figure 7.14 presents the trends of x^* and x^{**} with depth for Test 90, 50/90, 50 and 90/50. The values of x^* and x^{**} for Test 50/90 are relatively lower than that for Test 90, indicating a narrower trough due to the effect of loose upper layer. The values for the two tests become similar at the depths approaching the tunnel, so that the trough width in the localisation zone of settlements in dense sand is not affected by the stratification. The values of x^* and x^{**} for Test 90/50 are obviously larger than that for Test 50. The restriction from the stiffer upper layer may extend the distribution of displacements.

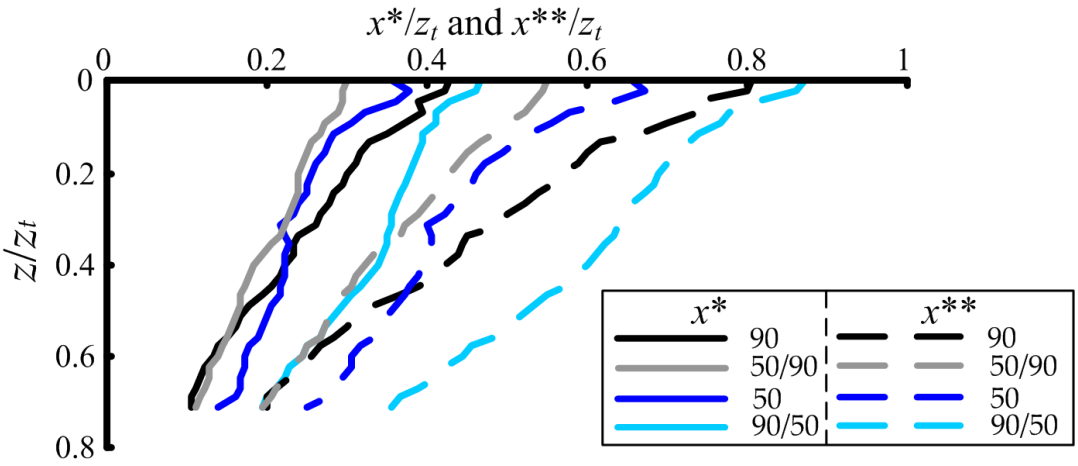

Figure 7.14: Variation of x^* and x^{**} with depth (normalised by tunnel depth, z_t) - $V_{l,t} = 3\%$, Group 2

The value of i is generally expressed as $i(z) = K(z_t - z)$, where K is referred to as the trough width parameter. For non-Gaussian curves, a trough width parameter K, based on x^* and x^{**}, can be calculated, and is referred to as K^* and K^{**}.

Figure 7.15 presented the variation of trough width parameter, K^*, with depth for Test 90, 50/90, 50 and 90/50. The value of K^* for Test 90/50 is obviously greater than the others. Marshall et al. [2012] suggested a relation to predict K^* (in dense sand) considering the effect of depth, C/D_t and $V_{l,t}$ (Equation 4.5, p.126). The figure also includes the predicted K^* for Test 90 and Test 90_{CD1} (Figure 7.4, p.174). The depth of $z/z_t = 0.4$ is the location of the interface for layers in Test 50/90 and also the surface of soil sample in Test 90_{CD1}. A relatively better fit to K^* for the lower layer of Test 50/90 was obtained by the prediction for Test 90_{CD1}.

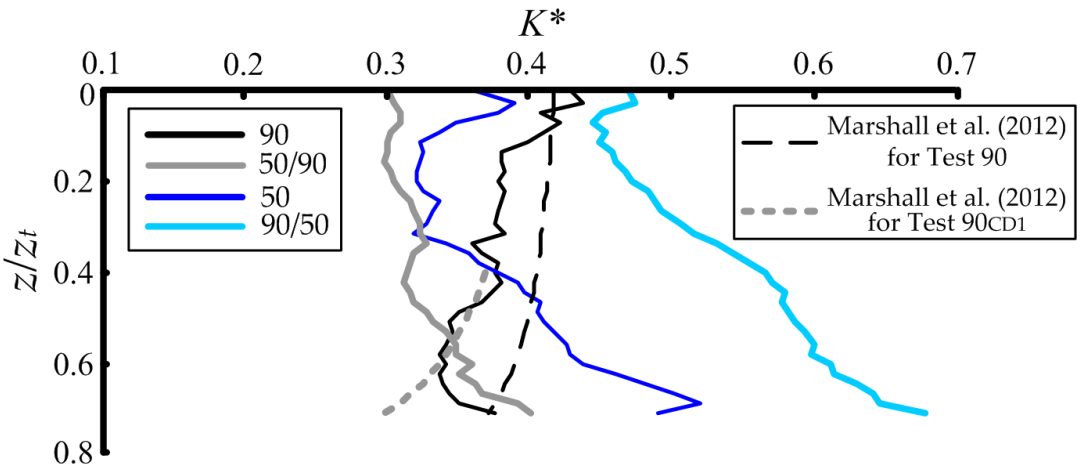

Figure 7.15: Trough width parameter against depth - $V_{l,t} = 3\%$, Group 2

Selby [1988] and New and O'Reilly [1991] used the values of K for the soil type in each layer to estimate the trough width for layered ground (mentioned in Section 7.1, p.168). Although this method ignores many factors (e.g. the interaction of layers and the effect of C/D_t), it is useful to evaluate if the value of K (or K^*) for layered ground could be estimated by that values observed in homogeneous soil of related types, because it is quite simple. K^* for Test 50/90 and 90/50 is estimated by K^* for Test 90 and 50 in Figure7.16. K^*_{50} at z/z_t = 0-0.4 and K^*_{90} at z/z_t = 0.4-0.8 are used for $K^*_{50/90}$. K^*_{90} at z/z_t = 0-0.4 and K^*_{50} at z/z_t = 0.4-0.8 are used for $K^*_{90/50}$. The estimation for the value of K^* in Test 50/90 is showed to be generally good. This method, however, underestimate the value of K^* in Test 90/50 as the effect of stiffer upper layer.

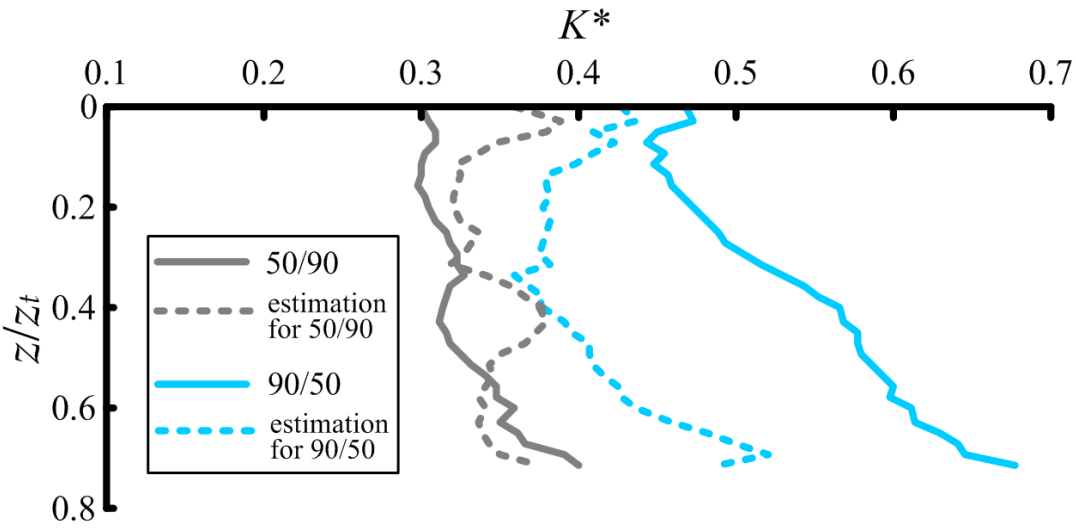

Figure 7.16: Trough width parameter for Group 2 estimated by that for Group 1

7.3.4 Slope and curvature

The slop and curvature of settlement trough will impact on the bending strains within underground pipelines and cause leakage. Figure 7.17 compares the trends of maximum slop and curvature with depth for Test 50/90 and 90/50 to that for Test 90 and 50, respectively. The values of slop and curvature are calculated by Equation 4.6-4.8 (p.130).

The values of maximum slop and curvature for Test 50/90 are larger than than that for Test 90 at an arbitrary depth. The values for Test 50/90 increase almost linearly with depth at z/z_t = 0-0.55, but blow the depth of z/z_t = 0.55, the values start to increase rapidly with depth, probably caused by the localisation of settlement just above the tunnel. The variation of maximum slop and curvature with depth for Test 50/90 relates well to the trend of S_{max} with depth (Figure 7.13, p.184), indicating that S_{max} is an important factor, which is same with that found in Group 1 (Section 4.3.5, p.130).

The value of S_{max} for Test 90/50 is larger than that for Test 50, but the maximum slop and curvature for Test 90/50 are generally smaller than that for Test 50. Although the greater magnitude of displacements could raise the values of slop

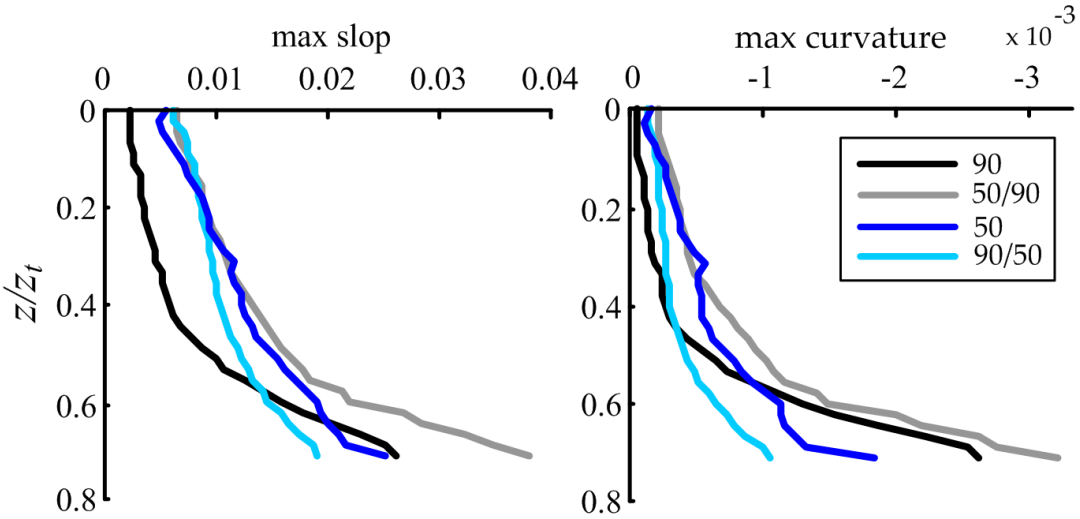

Figure 7.17: Variation of maximum slop and curvature with depth - $V_{l,t} = 3\%$, Group 2

and curvature, the larger trough width for Test 90/50 reduces the values. It should be noted that the modified Gaussian curve did not provide a good fit to the nearly-uniform settlement data in centre for Test 90/50 (Section 7.3.1, p.182), so that the maximum curvature calculated by the fitted curves for Test 90/50 may not accurately represent the true curvature.

7.3.5 Variation of soil volume loss with tunnel volume loss

The research thus far has focused on the tunnel volume loss, $V_{l,t}$. Soil volume loss, $V_{l,s}$, is equal to the area of settlement trough within soil divided by initial cross-sectional area of tunnel. Soil volume loss is not equal to tunnel volume loss, as a consequence of the volumetric changes that occur in the soil. Figure 7.18 (a) compares the soil volume loss to tunnel volume loss and Figure 7.18 (b) presents the slope of tangent line on $V_{l,s}$-$V_{l,t}$ curves. Because the boundary friction of Perspex window had some effect on PIV data, the values of $V_{l,s}$ are slightly underestimated in the curves.

Figure 7.18 (a) shows the soil volume loss for Test 50/90 and 90/50 is larger

than that for Test 90 and 50, respectively. The soil volume loss for Test 90/50 is approximately double of the tunnel volume loss. This relates well to the considerable decrease (or 'disappearance') of contraction for Test 50/90 and 90/50, observed in the contours of volumetric strain (Section 7.2.3, p.176). The decrease of contraction dominates the volumetric deformation. Note that the settlement for Test 90/50, to some extent, is enhanced by the boundary effect of side wall (discussed in Section 7.2.4, p.181).

Figure 7.18 (b) shows that the sand starts with contracting from $V_{l,t} = 0\%$ and then becomes dilating at $V_{l,t} = 0.5$, 1.2, 1.5 and 4.1% for Test 90, 50/90, 50 and 90/50, respectively. The change from contraction to dilation occurs later in the stratified sand compared with the related homogeneous sand.

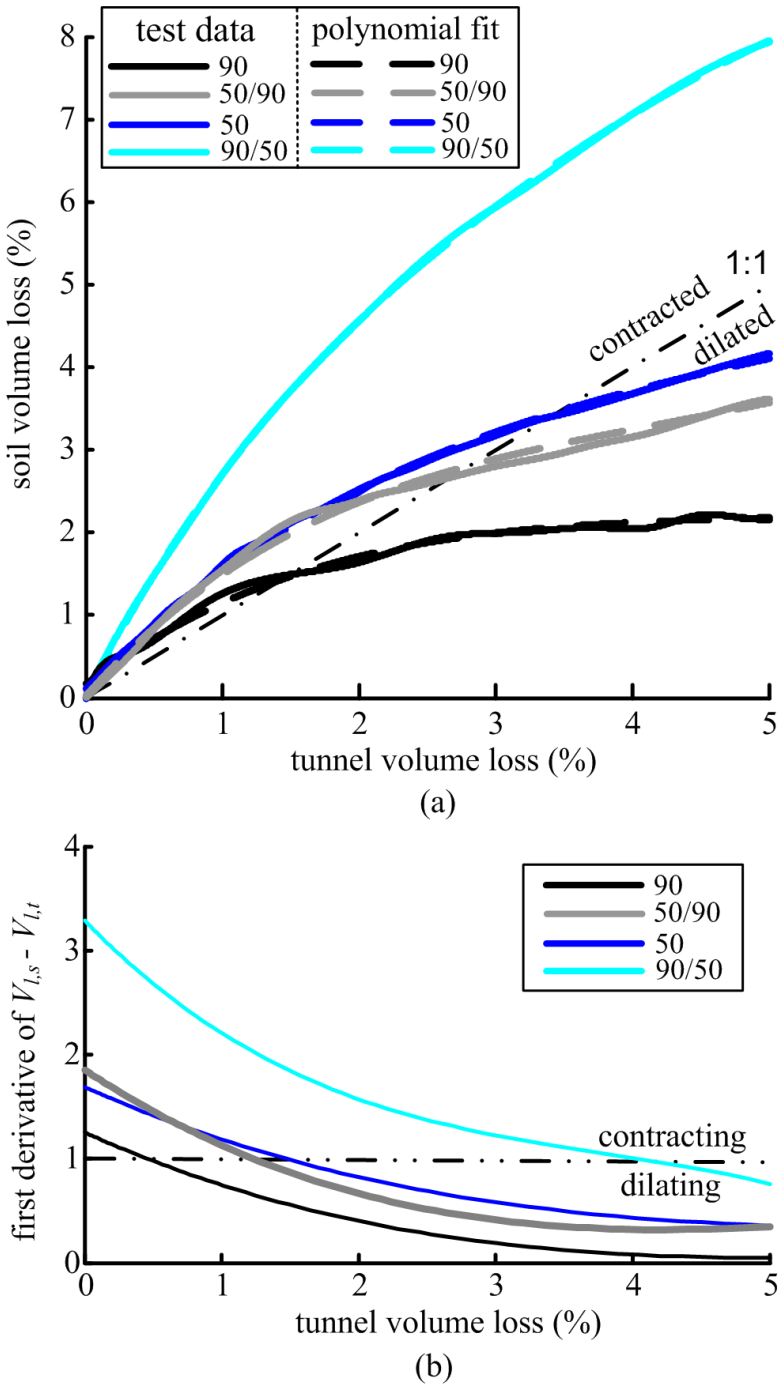

Figure 7.18: Volume loss calculated from soil displacements compared to tunnel volume loss - Group 2

7.4 Chapter summary

This chapter presented two geotechnical centrifuge tests undertaken to investigate the effect of stratification on displacements above the tunnels in sands. The layers with different relative densities were found to affect the magnitude and shape of ground settlements. The following conclusions can be drawn:

1. The contours of soil displacements and stains were presented in Section 7.2.2 (p.170) and 7.2.3 (p.176). The distribution of settlements and stains for loose sand overlying dense sand was narrower than that for dense sand only with the same C/D_t ratio. The development of strains was restricted for the tunnelling in loose sand overlain by dense sand and led to the wider settlement trough than that in loose sand alone. The stratification caused the decrease of dilation above the tunnel and the greater magnitude of settlements in both tests.

2. The modified Gaussian curve provided a better fit to the settlement data in layered sand compared to the Gaussian curve (Section 7.3.1, p.182).

3. The localisation zone of large displacements just above the tunnel was observed in dense sand for tests with both homogeneous sample and layered sample (Section 7.3.2, p.183).

4. The trough width parameter for loose sand overlying dense sand could be approximately estimated by the values observed in tests with loose sand and dense sand only. The trough width parameter for dense sand overlying loose sand, however, was significantly larger than that found in the other tests (Section 7.3.3, p.185).

5. In comparison with the related test in Group 1, the greater settlements caused severer slop and curvature for loose sand overlying dense sand, but that the values of slop and curvature were lower for dense sand overlying loose sand, as a result of the wider settlement trough (Section 7.3.4, p.187).

6. The magnitude of soil volume loose was found to be quite large for tunnelling in loose sand overlain by dense sand (Section 7.3.5, p.188).

Chapter 8

CONCLUSIONS AND RECOMMENDATIONS

8.1 Conclusions

This thesis, in conjunction with Marshall et al. [2012], provides a relatively complete investigation for tunnelling in sands: the effect of size, depth, volume loss and relative density on greenfield displacements. High quality displacement data was obtained using the image-based technique on centrifuge tests. Marshall et al. [2012] showed that the trough width decrease with (i) increasing tunnel volume loss, (ii) increasing depth and (iii) decreasing C/D_t ratio. The following findings can be drawn, based on the centrifuge tests for the both researches:

1. The modified Gaussian curve provided a better fit to the settlement data in sand compared to the Gaussian curve. The modified Gaussian curve has three degrees of freedom and the Gaussian curve has two.

2. Tunnelling in sandy ground with lower relative density (I_d) caused the larger magnitudes of displacements and strains.

3. The ratio of tunnel deformation at crown to side was obviously higher in denser sand.

4. The settlement trough near surface ($z/z_t < 0.3$) in sand with $I_d \geq 90\%$ was wider than that with $I_d \leq 70\%$.

5. The value of trough width in layered soil could be approximately estimated by the values observed in the related homogeneous soil if the lower layer is stiffer than the upper layer.

6. The slop and curvature of settlement trough generally increased with a decrease of relative density.

7. Large displacements were localised just above the tunnel in sand with $I_d \geq 70\%$ when $V_{l,t} > 2\%$. The severe localisation of settlements led to the low trough width and large slop and curvature.

8. The dilation zones in sand were above the tunnel crown and the contraction zones were above the tunnel shoulders (two sides of tunnel). The sand was

initially in an overall state of contraction and then in an overall state of dilation. The change from contraction to dilation occurred later in sand with lower relative density.

Another contribution of this research is the development of centrifuge model. Expect measuring the soil movements and tunnel pressure, the deformation of tunnel shape was monitored in this centrifuge model. Moreover, the strong box passed the seal test at 100 times gravity. The drainage holes and channels were designed for soil with ground water. The centrifuge model has been upgraded for the further research of tunnelling beneath infrastructure.

This research developed a solution for the volumetric deformation using cavity expansion theory. This solution examined the trends of soil dilatancy with tunnel volume loose, which is different from most previous solutions for underground tunnelling. Additionally, this solution investigated the possibility of using laboratory or field tests to estimate the soil volume loss.

It is difficult to find appropriate data from real cases for the comparison with test results. The tunnelling in real cases is usually more complex due to the soil stratification and ground water. Alternatively, the test results were compared to the prediction by discrete element method (DEM). DEM can replicate complex soil behaviour using only inter-particle contact models. Reasonable agreement was obtained in tunnelling-induced displacements for $I_d = 90\%$ and 70% as well as the general trend of the effect of relative density on settlement.

8.2 Applicability of results

It should be noted that, for real cases, the term 'dense sand' usually refers to $I_d = 100\% - 67\%$ and 'medium dense sand' refers to $I_d = 66\% - 33\%$. The relative density of 90%, 70% and 50% are termed dense, medium and loose (sand) in this research, respectively. The displacement data reported in this thesis will not be unique and depend on the soil type in real cases. The results, however,

illustrated the mechanism of tunnelling-induced displacements and the effect of relative density on that.

The results showed that the magnitude of ground displacements is considerably larger in sand with $I_d \leq 70\%$ when $V_{l,t} > 1\%$. The volume loss of tunnel and the decrease of supporting pressure, consequently, should be controlled at a low level as tunnelling trough sands with low relative density (or layers with loose sand). Earth pressure balance (EPB) tunnelling machine technologies are suggested to be used for this case.

Both this research and Marshall [2009] found the localisation zone of large displacements in sand with $I_d \geq 70\%$ when $V_{l,t} > 2\%$. This zone is usually just above the tunnel and below $z/z_t = 0.5$. Underground structure in this zone should get adequate attention by tunnelling engineers.

The tunnel deformation due to unloading was mainly at the crown for sand with $I_d = 90\%$. The deformation at two sides was micro. For sand with $I_d \leq 70\%$, however, considerable deformation at sides was observed, which is about 1/2 - 1/3 of that at crown. This feature should be considered during the design, construction and displacement monitoring of the lining for shallow tunnels.

Furthermore, the greenfield displacements data could be used for the research on tunnelling beneath infrastructure.

8.3 Further research

Further centrifuge tests using medium and loose sand with different C/D_t ratios could examine the relation between settlement trough shape and C/D_t. After that, the parameter values ($K^{*int}_{s,C/D}$, $K^{*slope}_{s,C/D}$, K^{*slope}_{s,V_l} and $\partial x^*/\partial z$) predicting trough width (Equation 4.5, p.126) could be calibrated for sand with lower relative density.

The researches thus far have focused on the tunnelling in dry sand. It is also of interest to consider the ground water. The subsurface water table will lead

to three layers of sand: dry sand on top, unsaturated sand above the water table and saturated sand below the water table. Centrifuge tests with subsurface water table in sand sample could evaluate the effect of pore pressure (positive or negative) on ground movements.

Further triaxial tests could be performed on the same sand used at a range of relative density and stress path. The triaxial test can not replicate the plane-strain condition in the centrifuge tests, but it is worth examining if the volumetric strain data from triaxial tests could be used to estimate volumetric deformation within the soil above tunnels.

Tunnelling is not only limited to greenfield condition. Tunnels constructed in urban areas generally are close to structures, such as buried pipelines, foundations or roads. Thus the problem of tunnelling near to or beneath existing infrastructure is a frequent practical issue for engineers. The analysis of soil-structure interaction is suggested.

References

Ata, A. A. (1996). Ground settlements induced by slurry shield tunnelling in stratified soils. In *Proceedings International Conference North American Tunneling*, volume 96, pages 43–50. 169

Atahan, C., Leca, E., and Guilloux, A. (1996). Performance of a shield driven sewer tunnel in the Val-de-Marne, France. In *Proceedings International Symposium on Geotechnical Aspects of Underground Construction in Soft Ground, London, RJ Mair & RN Taylor Eds*, pages 641–646. 169

Atkinson, J. H. and Potts, D. M. (1977). Stability of a shallow circular tunnel in cohesionless soil. *Géotechnique*, 27(2):203–215. 12, 29, 85

Attewell, P. B., Yeates, J., and Selby, A. R. (1986). Soil movements induced by tunnelling and their effects on pipelines and structures. x, 6

Bolton, M. D. (1986). The strength and dilatancy of sands. *Géotechnique*, 36(1):65–78. 150, 152

Bolton, M. D. (1987). Discussion on the strength and dilatancy of sands. *Géotechnique*, 37(2):219–226. 150, 151, 152

Bowers, K. H., Hiller, D. M., and New, B. M. (1996). Ground movement over three years at the heathrow express rail tunnel. In *Geotechnical aspects of underground construction in soft ground - preprint volume of proceedings from an international symposium held at City University, London, UK, 15-17 April 1996*, pages 647–652. 7

Bym, T., Marketos, G., Burland, J. B., and O'SULLIVAN, C. (2012). Use of a two-dimensional discrete-element line-sink model to gain insight into tunnelling-induced deformations. *Géotechnique*, 63(9):791–795. 158

Celestino, T. B., Gomes, R., and Bortolucci, A. A. (2000). Errors in ground distortions due to settlement trough adjustment. *Tunnelling and Underground Space Technology*, 15(1):97–100. 8

Clough, W. and Schmidt, B. (1981). Design and performance of excavations and tunnels in soft clay. *Soft Clay Engineering*, pages 567–634. 13, 16

Collins, I. F., Pender, M. J., and Yan, W. (1992). Cavity expansion in sands under drained loading conditions. *International Journal for Numerical and Analytical Methods in Geomechanics*, 16(1):3–23. 150

Davis, E. H., Gunn, M. J., Mair, R. J., and Seneviratine, H. N. (1980). The stability of shallow tunnels and underground openings in cohesive material. *Géotechnique*, 30(4):397–416. 29

Ellis, E., Cox, C., Yu, H., Ainsworth, A., and Baker, N. (2006). A new geotechnical centrifuge at the University of Nottingham, UK. In *Physical Modelling in Geotechnics - 6th ICPMG - Ng, Zhang & Wang (eds)*, pages 129–133. 28, 34

Grant, R. J. and Taylor, R. N. (1996). Centrifuge modelling of ground movements due to tunnelling in layered ground. In *Proceedings International Symposium on Geotechnical Aspects of Underground Construction in Soft Ground, RJ Mair & RN Taylor Eds., London.* 169

Grant, R. J. and Taylor, R. N. (2000). Tunnelling-induced ground movements in clay. In *Proceedings of the ICE - Geotechnical Engineering*, volume 143, pages 43–55. 15, 29

Iglesia, G. R., Einstein, H. H., and Whitman, R. V. (1999). Determination of vertical loading on underground structures based on an arching evolution concept. In *Geo-Engineering for Underground Facilities*, pages 495–506. ASCE. 11

Itasca (2008). *PFC3D Ver. 4.0- User Manual*. Minneapolis, MN, USA. 159

Jacobsz, S. W. W. (2002). The effects of tunnelling on piled foundations. *Ph.D. Thesis, Cambridge University*. 11, 22, 52, 69, 84

Jacobsz, S. W. W., Standing, J. R. R., Mair, R. J. J., Hagiwara, T., and Sugiyama, T. (2004). Centrifuge modelling of tunnelling near driven piles. *Soils and Foundations*, 44(1):49–56. 8

Klar, A. (2013). Discussion of "Tunnel-Pile Interaction Analysis Using Cavity Expansion Methods" by Alec M. Marshall. *Journal of Geotechnical and Geoenvironmental Engineering*, 139(11):2001–2002. 146, 147

Kutter, B., Chang, J., and Davis, B. (1994). Collapse of cavities in sand and particle size effects. In C. F. Leung, F. Lee and Tan, T., editors, *Centrifuge 94*, Singapore. Balkema. 29

Loganathan, N., Poulos, H. G., and Stewart, D. P. (2000). Centrifuge model testing of tunnelling-induced ground and pile deformations. *Géotechnique*, 50(3):283–294. 29

Loganathan, N. and Poulos, H. G. G. (1998). Analytical prediction for tunneling-induced ground movements in clays. *Journal of Geotechnical and Geoenvironmental Engineering*, 124(9):846–856. 22, 43

Ma, X. F., He, Z. M., Zhu, H. H., and Lin, M. (2006). Development of a new geotechnical centrifuge at Tongji University in Shanghai. *Proc. 6th IC Physical Modelling in Geotechnics*, pages 151–156. 28

Mair, R. J. (1979). Centrifugal modelling of tunnel construction in soft clay. *PhD Thesis Cambridge University*. 29, 146

Mair, R. J. (2008). Tunnelling and geotechnics: new horizons. *Géotechnique*, 58(9):695–736. 11

Mair, R. J., Gunn, M. J., and O'Reilly, M. P. (1982). Ground movement around shallow tunnels in soft clay. *Tunnels and Tunnelling International*, 14(5). 13

Mair, R. J. and Taylor, R. N. (1993). Prediction of clay behaviour around tunnels using plasticity solutions. In *Predictive Soil Mechanics: Proceedings of the Wroth Memorial Symposium Held at St. Catherine's College*, pages 449–463, Oxford. Telford, Thomas. 22, 27, 142

Mair, R. J. and Taylor, R. N. (1997). Bored tunnelling in the urban environment. In *14th International conference on soil mechanics and foundation engineering*, pages 2353–2385. 5, 10, 14, 169

Mair, R. J., Taylor, R. N., Bracegirdle, A., and Bracegirdle, N. (1993). Subsurface settlement profiles above tunnels in clay. *Géotechnique*, 43(2):315–320. 14, 15, 29, 123

Marshall, A., Farrell, R., Klar, A., and Mair, R. (2012). Tunnels in sands: the effect of size, depth and volume loss on greenfield displacements. *Géotechnique*, 62(5):385–399. 2, 6, 9, 17, 22, 29, 123, 126, 160, 172, 185, 186, 193

Marshall, A. M. (2009). Tunnelling in sand and its effect on pipelines and piles. *Ph.D. Thesis, Cambridge University*. 7, 11, 22, 29, 52, 61, 63, 65, 69, 84, 123, 195

Marshall, A. M. (2013). Closure to "Tunnel-pile interaction analysis using cavity expansion methods" by Alec M. Marshall. *Journal of Geotechnical and Geoenvironmental Engineering*, 139(11):2002–2004. 147

Marshall, A. M., Elkayam, I., and Klar, A. (2009). Ground behaviour above tunnels in sand-DEM simulations versus centrifuge test results. In *Euro: Tun 2009, Proceedings of the 2nd International Conference on Computational Methods in Tunnelling, Bochum, Germany*, pages 9–11. 65, 158, 159

Marshall, A. M., Elkayam, I., Klar, A., and Mair, R. J. (2010a). Centrifuge and discrete element modelling of tunnelling effects on pipelines. In *Physical Modelling in Geotechnics-Proceedings of the 7th International Conference on Physical Modelling in Geotechnics 2010, ICPMG 2010*, volume 1, pages 633–637. 158

Marshall, A. M., Klar, A., and Mair, R. (2010b). Tunneling beneath buried pipes: View of soil strain and its effect on pipeline behavior. *Journal of Geotechnical and Geoenvironmental Engineering*, 136(12):1664–1672. 130

Martos, F. (1958). Concerning an approximate equation of the subsidence trough and its time factors. In *International strata control congress, Leipzig*, pages 191–205. 7

Mindlin, R. D. and Deresiewicz, H. (1953). Elastic Spheres in Contact under Varying Oblique Forces. *Journal of Applied Mechanics*, 20:327–344. 159

Moh, Z. C., Hwang, R. N., and Ju, D. H. (1996). Ground movements around tunnels in soft ground. In R. J. Mair and R. N. Taylor, editor, *Geotechnical Aspects of Construction in Soft Ground*, pages 725–730, London. Balkema. 15, 22

New, B. M. and O'Reilly, M. P. (1991). Tunnelling induced ground movements: predicting their magnitude and effects. In *Proceeding of the 4th International Conference on Ground Movements and Structures, Jul 8-11*, pages 671–697, Cardiff, Wales. Pentench Press Ltd. 14, 22, 169, 186

Ng, C. W. W., Van Laak, P., Tang, W. H., Li, X. S., and Zhang, L. M. (2001). The Hong Kong geotechnical centrifuge. In *Proceedings of the 3rd international conference soft soil engineering, Hong Kong*, pages 225–230. 28

O'Reilly, M. P. and New, B. M. (1982). Settlements above tunnels in the United Kingdom - their magnitude and prediction. In *Tunnelling 82, Papers Presented at the 3rd International Symposium*, London, England, Brighton, England. Inst of Mining and Metallurgy. 13, 14, 22

Osman, A. S., Bolton, M. D., and Mair, R. J. (2006a). Predicting 2D ground movements around tunnels in undrained clay. *Géotechnique*, 56(9):597–604. 29

Osman, A. S., Mair, R. J., and Bolton, M. D. (2006b). On the kinematics of 2D tunnel collapse in undrained clay. *Géotechnique*, 56(9):585–595. 29

Park, K. H. (2005). Analytical solution for tunnelling-induced ground movement in clays. *Tunnelling and underground space technology*, 20(3):249–261. 20

Peck, R. B. (1969). Deep excavations and tunnelling in soft ground. In *7th International Conference on Soil Mechanics and Foundation Engineering*, pages 225–290, Mexico City. 7, 22

PERSPEX (2005). *Workshop Handbook*. Lucite International UK LTD, Cleveland, UK. 40

Pinto, F. and Whittle, A. J. (2006). Discussion of "Elastic solution for tunneling-induced ground movements in clays" by K. H. Park. *International Journal of Geomechanics*, 6(1):72–73. x, 21

Potts, D. M. (1976). Behaviour of lined and unlined tunnels in sand. *Ph.D. thesis, Cambridge University*. 29

Sagaseta, C. (1987). Analysis of undrained soil deformation due to ground loss. *Géotechnique*, 37(3):301–320. 19, 22, 24, 146

Schmidt, B. (1969). *Settlements and ground movements associated with tunneling in soil*. PhD thesis, University of Illinois at Urbana-Champaign. 7

Schofield, a. N. (1980). Cambridge Geotechnical Centrifuge Operations. *Géotechnique*, 30(3):227–268. 28

Selby, A. R. (1988). Surface movements caused by tunnelling in two-layer soil. *Geological Society, London, Engineering Geology Special Publications*, 5(1):71–77. 14, 169, 186

Take, W. A. (2003). *The influence of seasonal moisture cycles on clay slopes*. PhD thesis, University of Cambridge. 60, 61, 63

Taylor, R. N. (1995). *Geotechnial centrifuge technology*. CRC Press, London. 27, 28, 40, 54

Verruijt, A. and Booker, J. R. (1996). Surface settlements due to deformation of a tunnel in an elastic half plane. *Géotechnique*, 46(4):753–756. 19, 22, 25, 146, 147

Vorster, T. E., Klar, A., Soga, K., and Mair, R. J. (2005). Estimating the effects of tunneling on existing pipelines. *Journal of Geotechnical and Geoenviromental Engineering*, pages 1399–1410. 8, 22, 52, 65, 117

Vorster, T. E. B. (2005). The effect of tunnelling on buried pipes. *Ph. D. dissertation, Cambridge University, Cambridge, UK*. 11, 69, 84

White, D. J., Take, W. A., and Bolton, M. D. (2003). Soil deformation measurement using particle image velocimetry (PIV) and photogrammetry. *Géotechnique*, 53(7):619–631. 59, 60

Yu, H.-S. (2000). *Cavity expansion methods in geomechanics*. Kluwer Academic, Dordrecht, Netherlands. 19, 27, 141, 146

Yu, H. S. and Rowe, R. K. (1999). Plasticity solutions for soil behaviour around contracting cavities and tunnels. *International Journal for Numerical and Analytical Methods in Geomechanics*, 23:1245–1279. 22, 27, 142

Zhao, Y. (2008). *In situ soil testing for foundation performance prediction*. PhD thesis, University of Cambridge. 153